Directed Assembly of Single-Molecule and Single-Chain Magnets: From Mononuclear High-Spin Iron(II) Complexes to Cyano-Bridged Chain Compounds

By

Thomas David Harris II

A dissertation submitted in partial satisfaction of the

requirements for the degree of

Doctor of Philosophy

in

Chemistry

in the

Graduate Division

of the

University of California, Berkeley

Committee in charge:

Professor Jeffrey R. Long, Chair
Professor Kenneth N. Raymond
Professor Thomas M. Devine

Fall 2010

Abstract

Directed Assembly of Single-Molecule and Single-Chain Magnets: From Mononuclear High-Spin Iron(II) Complexes to Cyano-Bridged Chain Compounds

By

Thomas David Harris II

Doctor of Philosophy in Chemistry

University of California, Berkeley

Professor Jeffrey R. Long, Chair

The work herein describes the design, synthesis, and characterization of magnetic molecules and chain compounds, with an emphasis on probing slow magnetic relaxation. Chapter 1 presents an extensive survey of the literature of cyano-bridged single-molecule and single-chain magnets, focusing on a building block approach wherein simple cyanometalate precursor complexes direct the assembly of larger architectures. Specific synthetic strategies to obtain multinuclear clusters and chain compounds of desired structure and magnetic properties are outlined in detail. Finally, perspectives on the future directions in the field are presented.

Chapter 2 exemplifies the utility of the building block approach in generating high-nuclearity cyano-bridged clusters. It describes the design and synthesis of the facially-capped tricyanide building unit, $[TpCr(CN)_3]^-$, as its incorporation into the face-centered cubic cluster $[Tp_8(H_2O)_6Cu_6Cr_8(CN)_{24}]^{4+}$. Ferromagnetic exchange between Cr^{III} and Cu^{II} ions gives rise to an $S = 15$ spin ground state, one of the highest yet observed for a cyano-bridged cluster. In addition, the formation of this cluster is accompanied by a linkage isomerism of 12 of the 24 cyanide ligands, providing the first example of a molecule undergoing partial cyanide isomerism.

Chapter 3 presents a survey of actinide-containing molecules that have demonstrated evidence of magnetic exchange coupling. The strong magnetic anisotropy characteristic of these elements marks them as promising candidates for single-molecule magnets, however the spin-orbit coupling that gives rise to this anisotropy also complicates analysis of exchange interactions. Current methods for extracting coupling information in these systems are outlined in detail. In addition, molecules that bear exchange-coupled centers but as of yet have not been thoroughly characterized are presented.

Chapter 4 describes a detailed investigation of a series of iron(II) pyrrolide complexes of formulae $[(tpa^{R})Fe]^{-}$, representing the first examples of transition metal-based mononuclear single-molecule magnets. Static magnetic measurements and high-field EPR spectroscopy reveal the presence of exceptionally strong uniaxial anisotropy in the complexes. Moreover, dynamic magnetic measurements carried out in a small dc field demonstrate that this anisotropy leads to slow relaxation in the complexes. In addition, this relaxation dynamics is probed through Mössbauer spectroscopy, which reveals that the phenomenon occurs in zero applied field in at least two complexes.

Chapter 5 describes the synthesis and characterization of a series of cyano-bridged single-chain magnets. Reaction of the $S = {}^{3}/_{2}$, high-anisotropy building unit $[ReCl_4(CN)_2]^{2-}$ with $[M(DMF)_6]^{2+}$ (M = Mn, Fe, Co, Ni) is shown to direct the formation of the chain compounds $(DMF)_4MReCl_4(CN)_2$. Dc susceptibility measurements uncover the presence of intrachain antiferromagnetic (Mn) and ferromagnetic (Fe, Co, Ni) exchange. Most importantly, ac susceptibility measurements reveal that all of the chain compounds exhibit slow magnetic relaxation at low temperature. Notably, the Fe congener displays significant magnetic hysteresis at low temperatures, thus demonstrating classical magnet-like behavior in a one-dimensional system.

Chapter 6 describes the synthesis the incorporation of $[ReCl_4(CN)_2]^{2-}$ into the zig-zag chain compound $(Bu_4N)[TpCuReCl_4(CN)_2]$, which is found to demonstrate the strongest ferromagnetic exchange yet observed through cyanide. The strong coupling arises from judicious selection of Re^{IV} and Cu^{II} ions, whose molecular orbitals interact through the cyanide bridge such that orbital overlap is minimized. Moreover, the compound is shown to display metamagnetic behavior, and the complete magnetic phase diagram is elucidated through a combination of experimental and theoretical analysis. Finally, the anisotropy tensors of the Re^{IV} centers are shown to cancel, leading to a small effective chain anisotropy and thus the absence of single-chain magnet behavior.

Chapter 7 concludes this work by demonstrating that $[ReCl_4(CN)_2]^{2-}$ can also be employed in the assembly of molecular magnets, as it presents the synthesis and characterization of two linear trinuclear clusters of formulae $[(PY5Me_2)_2M_2ReCl_4(CN)_2]^{2+}$ (M = Mn, Ni; $PY5Me_2$ = 2,6-bis(1,1-bis(2-pyridyl)ethyl)-pyridine). Dc susceptibility measurements reveal the presence of antiferromagnetic exchange in the Mn congener, while ferromagnetic exchange is observed in the Ni analogue. In addition, dc magnetization experiments show the presence of axial magnetic anisotropy in both clusters.

Chapter 1: An Overview of Cyano-Bridged Single-Molecule and Single-Chain Magnets

Contents

1.1. Introduction
1.2. A Building-Block Approach to Cyano-Bridged Coordination Compounds
    1.2.1. The Cyanide Ligand
    1.2.2. Cyanide Bridge-Forming Reactions
    1.2.3. Magnetic Superexchange Coupling through a Cyanide Bridge
    1.2.4. Mononuclear Cyanometalate Building Units
1.3. Raising the Relaxation Barrier by Controlling Magnetic Parameters
    1.3.1. Spin Ground State (*S*)
    1.3.2. Axial Zero-Field Splitting Parameter (*D*)
    1.3.3. Superexchange Interaction (*J*)
1.4. Cyano-Bridged Single-Molecule Magnets
    1.4.1. Trinuclear Clusters
        1.4.1.1. Linear M_2M' Clusters
        1.4.1.2. A Bent MM'_2 Cluster
    1.4.2. Tetranuclear Clusters
        1.4.2.1. An Arch-Like $M_2M'_2$ Cluster
        1.4.2.2. An $M'M_2M'$ Cluster
        1.4.2.3. A T-Shaped M_3M' Cluster
        1.4.2.4. Square $M_2M'_2$ Clusters
    1.4.3. Pentanuclear Clusters
        1.4.3.1. Star-like M_4M' Clusters
        1.4.3.2. Trigonal Bipyramidal $M_3M'_2$ Clusters
    1.4.4. Hexanuclear Clusters
        1.4.4.1. An Extended Square $M_4M'_2$ Cluster
    1.4.5. Heptanuclear Clusters
        1.4.5.1. A Trigonal Prismatic MM'_6 Cluster
        1.4.5.2. A C_3-Symmetric M_6M' Cluster
    1.4.6. Higher-Nuclearity Clusters
        1.4.6.1. Simple Cubic $M_4M'_4$ Clusters
        1.4.6.2. Face-Centered Cubic $M_6M'_8$ Clusters
        1.4.6.3. A Wheel-Like $M_6M'_6$ Cluster
        1.4.6.4. An Extended Trigonal Bipyramidal $M_7M'_2$ Cluster
        1.4.6.5. Centered, Face-Capped Octahedral $M_9M'_6$ Clusters
1.5. Cyano-Bridged Single-Chain Magnets
    1.5.1. Chain Compounds Incorporating $[M(CN)_n]^{x-}$ Units
    1.5.2. Chain Compounds Incorporating $[LM(CN)_2]^{x-}$ Units
    1.5.3. Chain Compounds Incorporating $[LM(CN)_3]^{x-}$ Units
    1.5.4. Chain Compounds Incorporating $[LM(CN)_4]^{x-}$ Units

1.5.5. Chain Compounds Incorporating $[LM(CN)_6]^{x-}$ Units
1.6. Future Directions in Cyano-Bridged Single-Molecule and Single-Chain Magnets
1.6.1. Unexplored High-Spin, High-Anisotropy Building Units
1.6.2. Toward Switchable Single-Molecule and Single-Chain Magnets
1.6.2.1. Redox Switching
1.6.2.2. Light Switching
1.6.2.3. Temperature Switching
1.6.2.4. Pressure Switching
1.7. Conclusions and Outlook
1.8. Acknowledgments
1.9. References

1.1 Introduction

Nearly two decades ago, researchers discovered that the molecular cluster compound $Mn_{12}O_{12}(O_2CCH_3)_{16}(H_2O)_4$ exhibits slow magnetic relaxation after removal of an applied dc magnetic field, a phenomenon that corresponds to an energy barrier to spin inversion.[1] The structure of this molecule, depicted in Figure 1.1, consists of a central $Mn^{IV}_4O_4$ cubane unit bridged through oxide ligands to an outer disk containing eight Mn^{III} ions. The peripheral Mn^{III} centers feature significant elongation along the axial Mn-O bonds stemming from Jahn-Teller effects. At low temperature, the Mn^{III} and Mn^{IV} ions couple antiferromagnetically, giving rise to an overall spin ground state of $S = 10$. In this ground state, the energies of the 21 M_S levels (M_S = 10, 9, …, -9, -10) are split in the absence of an external magnetic field (see Figure 1.2), owing to a magnetic easy axis within the molecule along the direction of the Jahn-Teller distorted Mn^{III} ions. This zero-field splitting positions the $M_S = \pm 10$ levels (whose magnetic orientations align along the easy axis) lowest in energy and the $M_S = 0$ level (whose magnetic orientation aligns perpendicular to the easy axis) highest in energy. Thus, considering quantum mechanical selection rules, inverting the magnetization from "spin-up" ($M_S = 10$) to "spin-down" ($M_S = -10$) requires traversal of an energy barrier. The height of this spin-reversal barrier can be quantified according to the expression $U = S^2|D|$ (following the Hamiltonian $H = DS_z^2$, where S_z is the component of S along the z direction) for an integer spin or $U = (S^2 - {}^1/_4)|D|$ for a half-integer spin, thus leading to a theoretical barrier of 50 cm^{-1} in the case of the Mn_{12} cluster.[2] Indeed, an experimental relaxation barrier of 42 cm^{-1} has been determined for this molecule through ac susceptibility measurements, where the low experimental value stems from quantum tunneling of the magnetization through the thermal barrier.[3] This remarkable discovery generated much excitement, in large part because such a molecule could potentially find use in applications such as high-density information storage and quantum computing.[4] As a result, a tremendous effort has been undertaken by numerous researchers with the goal of isolating other molecules that demonstrate slow magnetic relaxation, which have come to be known as single-molecule magnets.[5]

Ten years after the discovery of slow magnetic relaxation in molecules, a similar phenomenon was uncovered in the one-dimensional chain compound $Co(hfac)_2(NITPhOMe)$, which exhibits a relaxation barrier of 107 cm^{-1} stemming from

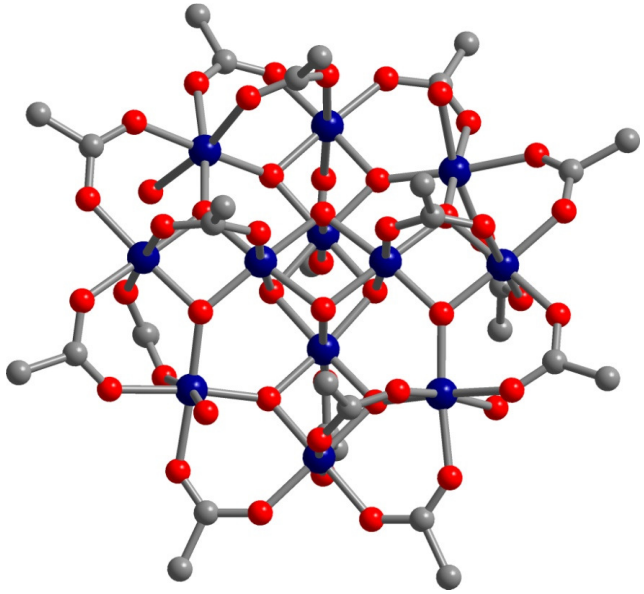


Figure 1.1. Crystal structure of $Mn_{12}O_{12}(O_2CCH_3)_{16}(H_2O)_4$. Dark blue, red, and gray spheres represent Mn, O, and C atoms, respectively; H atoms are omitted for clarity.

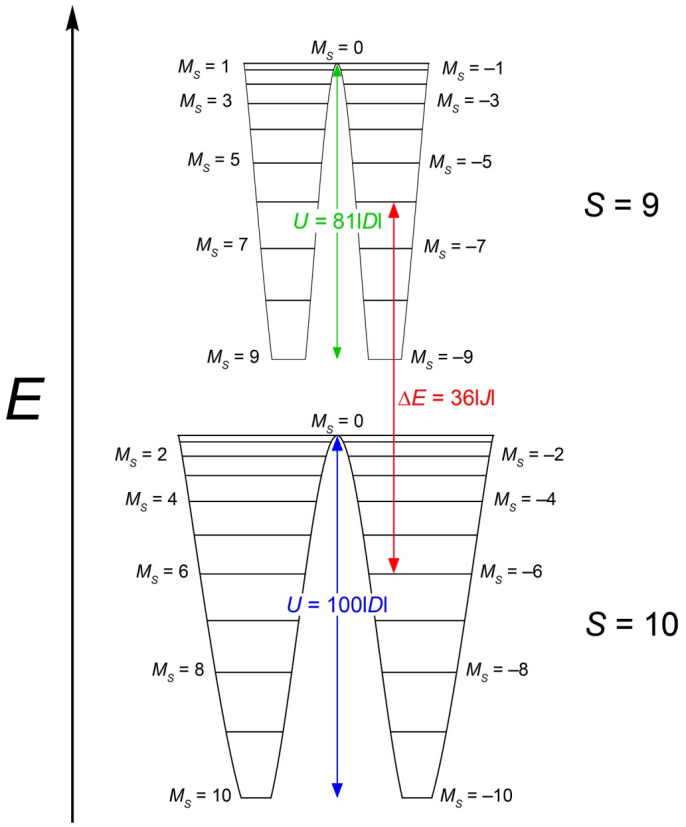


Figure 2.2. Energy splitting of the ground state and first excited state for an $S = 10$ molecule with uniaxial anisotropy.

antiferromagnetic coupling between anisotropic Co^{II} ions (effective $S = {}^1/_2$) and nitroxide radical ligands ($S = {}^1/_2$).[6] This discovered confirmed the theoretical prediction of Glauber over forty years ago that slow magnetization dynamics is possible in one-dimensional systems.[7] Shortly after this breakthrough, slow magnetic relaxation was reported in the one-dimensional solid $[(saltmen)_2(py)_2Mn^{III}{}_2Ni^{II}(pao)_2]^{2+}$, which exhibits a barrier of 50 cm^{-1}.[8] As depicted in Figure 1.3, the structure of the Mn_2Ni compound consists of alternating $[(saltmen)_2Mn_2]^{2+}$ dimers and $Ni(pao)_2(py)_2$ units, where Mn^{III} and Ni^{II} ions are antiferromagnetically coupled through the oximato bridging ligand. A second, much weaker exchange interaction exists between neighboring Mn^{III} ions, which are ferromagnetically coupled through the saltmen ligand. Thus, the interaction along each chain can be modeled as weak ferromagnetic coupling between trinuclear MnNiMn units, each possessing a net spin of $S = 3$. The modular salen-type ligand scaffold present in this chain has enabled the syntheses of many related compounds, thereby providing a comprehensive study into both the static and dynamic properties of these compounds, which have been termed single-chain magnets.[9] Nevertheless, this system has not been extended to encompass transition metal ions other than Mn^{III} and Ni^{II}.

As evident in the foregoing examples, single-chain magnets often demonstrate relaxation barriers considerably higher than those found in single-molecule magnets. This increase stems from to an additional energy component to the overall barrier in one-dimensional systems. Similar to molecules, single-chain magnets face the same anisotropy barrier toward relaxation, given as $\Delta_A = S^2|D|$.[10] In addition, however, single-chain magnets confront a second component to the overall relaxation barrier that stems from short-range magnetic correlation along each individual chain. The magnetic correlation length, ξ, increases exponentially as the temperature is lowered, such that each chain consists of domains of length $L = \xi$.[11] In order to invert a single spin or ensemble of spins within one of these domains, two domain walls must be created, where the correlation energy (Δ_ξ) corresponds the energy required to create each domain wall. Thus, the total relaxation barrier for a single-chain magnet (Δ_τ) may be expressed as $\Delta_\tau = 2\Delta_\xi + \Delta_A$.[12] Importantly, this expression describes the relaxation energy only in a regime where the chain can be considered infinite. As the temperature is lowered, the correlation length grows exponentially, until finally being limited by defects within the solid.[13] In this finite-size regime, the expression of the total relaxation energy reduces to $\Delta_\tau = \Delta_\xi + \Delta_A$, since each end of a finite chain must only create a single domain wall in order to relax its magnetization.[10,11]

Despite the tremendous effort aimed at synthesizing single-molecule and single-chain magnets with higher relaxation barriers, progress toward this goal has been limited. Indeed, the barrier of 42 cm^{-1} measured for the original Mn_{12} cluster remains among the highest for molecules, with the current world record barrier eclipsing this mark by only 25 cm^{-1}.[5f] Similarly, the barrier of 107 cm^{-1} observed for the original Co^{II} solid remains the highest yet reported for a single-chain magnet. Clearly, dramatic increases in relaxation energy must be achieved for these compounds to find use in applications at practical temperatures. The limited progress toward this end has resulted in large part due to the types of molecules and solids being prepared and studied thus far. To date, the vast majority of cases in which slow magnetic relaxation has been observed have featured oxo-bridged manganese clusters and solids.[5] While the axial elongation of the Mn^{III} ion

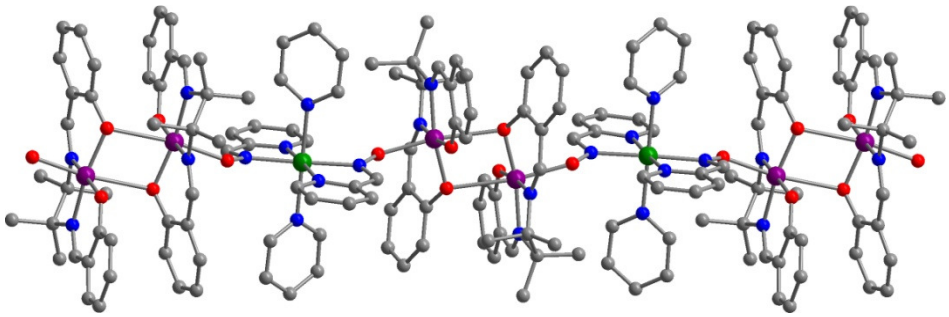


Figure 1.3. Crystal structure of $[(saltmen)_2(py)_2Mn^{III}{}_2Ni^{II}(pao)_2]^{2+}$. Purple, green, red, blue, and gray spheres represent Mn, Ni, O, N, and C atoms, respectively; H atoms are omitted for clarity. Chains are composed of oxo-bridged MnNiMn units.

provides the requisite uniaxial anisotropy for slow dynamics, the use of oxide as a bridging ligand requires that syntheses of these compounds rely largely on serendipity. An oxide ligand can link two to six metal centers in a number of coordination geometries, with M-O-M angles spanning a wide range. As a bridging ligand, cyanide provides an attractive alternative to oxide. Cyanide demonstrates a strong preference to bridge only two metal centers in a near linear geometry, enabling one to both predict and design coordination architectures featuring a wide range of structure types. Additionally, the nature of superexchange coupling (i.e. ferromagnetic vs. antiferromagnetic) through the linear M-CN-M′ linkage can be predicted based on molecular orbital considerations.[14] Indeed, the degree of control over structure and magnetic exchange afforded by the cyanide ligand has resulted over the last eight years in a number of new molecules and chain compounds demonstrating slow magnetic relaxation. Herein, we present a survey of the structures and magnetic properties of known cyano-bridged single-molecule and single-chain magnets, with an emphasis on the role of cyanometalate building units in directing the formation of desired structure types. We extend this discussion to structurally-characterized compounds that have demonstrated magnetic hysteresis at any measurable temperature or have shown frequency-dependent ac susceptibility with or without application of a dc field.

1.2 A Building-Block Approach to Cyano-Bridged Coordination Compounds

1.2.1 The Cyanide Ligand

In comparison to the isoelectronic CO ligand, the CN^- ion is a stronger σ-donor and a weaker π-acceptor.[15] These properties can be attributed in part to its negative charge, the result of which is a greater capacity to stabilize transition metals in high oxidation states. In this sense, metal-cyanide complexes are often discussed in the context of classical coordination chemistry rather than organometallic chemistry. In actuality, the properties of the cyanide ligand are somewhere in between since it exhibits the ability to form stable complexes with both high-valent (pseudohalide character) and low-valent (π-acid character) metals. Although a distributed-charge model is favored for the cyanide anion,[16] terminal coordination to a metal center usually occurs at the carbon end. The

M–C bonding tends to be rather strong, such that the reaction chemistry can be explored without substantial concern regarding displacement of the cyanide ligands. The unusual combination of stability and inducible reactivity intrinsic to metal complexes with terminal cyanide ligands forms the foundation of preparative metal-cyanide chemistry, permitting kinetic rather than thermodynamic control in the synthesis of clusters.

The cyanide ligand exhibits good donor ability at both its carbon and nitrogen termini. Thus, while several binding modes have been observed,[17] the linear bridging mode between just two metal centers is strongly preferred. This feature is central to the structural predictability and tunability of cyano-bridged coordination chemistry. Within this M–CN–M′ fragment, the M–C≡N and M′–N≡C angles can deviate significantly from linearity, although such distortions are usually most pronounced at the N-terminus. The degree of bending is often ascribed to strength of π-backbonding interactions that can impart some sp^2 character to the cyanide ligand, but constraints imposed by the coordination geometry of the metal centers and the steric requirements of other ligands can also have a significant effect. The ambidentate nature of the cyanide ligand is further reflected in the differences in ligand field strengths at the carbon and nitrogen ends. Carbon-bound cyanide is positioned at the strong field end of the spectrochemical series and typically induces a low-spin electronic configuration on the metal, while the weaker-field N-terminus frequently stabilizes the high-spin state. Thermodynamically, the softer carbon end prefers to bond to softer metal centers, which induces a susceptibility to linkage isomerism in certain heterometallic species. This is particularly important in the design of magnetic clusters and solids, as cyanide reorientation can affect the spin state and even coordination geometry of metal ions within the molecule.

1.2.2 Cyanide Bridge-Forming Reactions

The first cyanide bridge-forming reaction was reported in the early eighteenth century, with the accidental discovery of the solid pigment Prussian Blue by the German artist Diesbach.[18] This compound, whose chemical formula is $Fe^{III}_4[Fe^{II}(CN)_6]_3 \cdot zH_2O$, is readily prepared through reaction of ferrocyanide with Fe^{3+} ions in aqueous solution according to Equation 1.1:

$$4\,[Fe^{III}(H_2O)_6]^{3+} + 3\,[Fe^{II}(CN)_6]^{4-} \longrightarrow Fe^{III}_4[Fe^{II}(CN)_6]_3 \cdot zH_2O \qquad (1.1)$$

Here, the nucleophilic nitrogen end of the cyanide ligand displaces the labile H_2O molecule to form an Fe^{II}-CN-Fe^{III} linkage. As this process occurs for all six cyanide ligands at each Fe^{II} center, the overall result is the formation of an extended solid propagating infinitely in three dimensions (see Figure 1.4). Since the discovery of Prussian Blue, this reaction has been generalized to accommodate a wide range of transition metal ions and hexacyanometalate complexes, as shown in Equation 1.2:

$$x\,[M(H_2O)_6]^{y+} + y\,[M'(CN)_6]^{x-} \longrightarrow M_x[M'(CN)_6]_y \cdot zH_2O \qquad (1.2)$$

Indeed, this generalized approach has led to the formation of a myriad of Prussian Blue analogues that exhibit interesting electronic and magnetic properties.[19] Furthermore, the porous structures of these solids have proven utile in applications such as molecule sieves, cation exchange, catalysis, and gas storage.[19b,20]

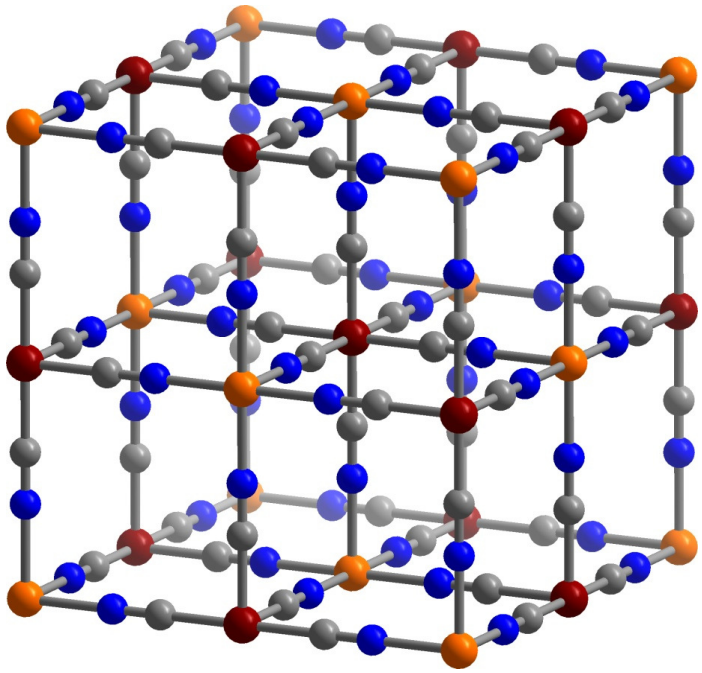


Figure 1.4. Crystal structure of the solid Prussian Blue, $Fe^{III}_4[Fe^{II}(CN)_6]_3$. Maroon, orange, blue, and gray spheres represent Fe^{II}, Fe^{III}, N, and C ions/atoms, respectively; H atoms are omitted for clarity.

In addition to the versatility afforded by Equation 1.2, one can envision a similar approach wherein one or more of the terminal cyanide ligands have been replaced with an inert blocking ligand. This modification can serve to forestall the formation of a three-dimensional solid and instead generate a one- or two-dimensional structure or a discrete molecule. Moreover, this approach can be extended to the other metal ion involved in the reaction, where the labile solvent molecules or leaving groups are replaced by blocking ligands. By varying the denticity and stereochemistry of the blocking ligands on each metal reagent, the cyanide bridge formation can engender a nearly infinite number of low-dimensional compounds featuring countless structure types.

1.2.3 Magnetic Superexchange through a Cyanide Bridge

The linear M–CN–M′ interaction (ca. 5.0 Å) provides an effective pathway for magnetic superexchange coupling within coordination compounds.[14] The nature of nearest-neighbor magnetic interactions is illustrated in Figure 1.5 for two octahedral metal centers connected through a linear cyanide bridge. Antiferromagnetic exchange coupling is expected for unpaired electrons in symmetry-compatible orbitals ($t_{2g} + t_{2g}$ or $e_g + e_g$), which interact through cyanide π and π* orbitals. Here, mixing of the two compatible interacting orbitals leads to a new lower-energy molecular orbital. The two electrons then occupy the new orbital and adopt an antiparallel configuration, as imposed by the Pauli exclusion principle. Conversely, unpaired electron density in orthogonal metal orbitals ($t_{2g} + e_g$) will leak into orthogonal cyanide-based orbitals, such that no

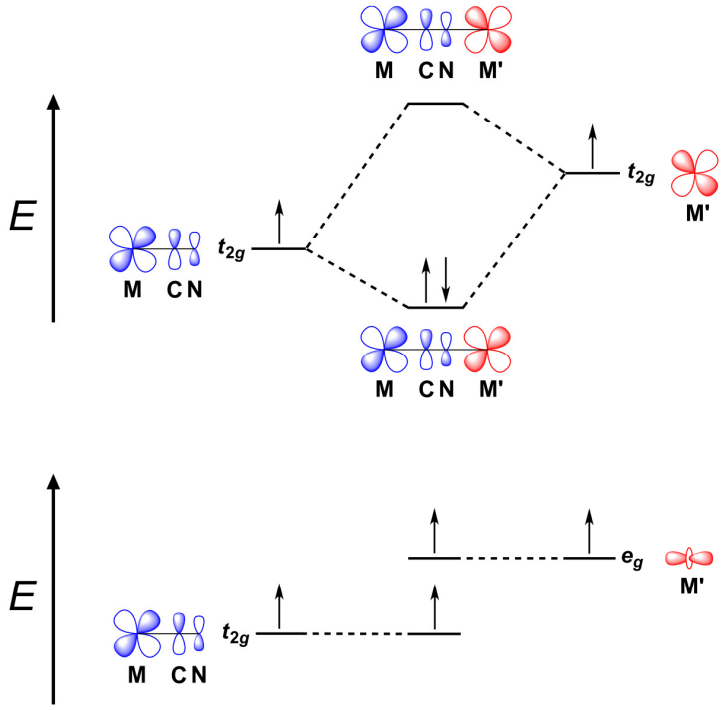


Figure 1.5. Orbital interactions across a bridging cyanide ligand giving rise to magnetic superexchange. Upper: Unpaired electrons in symmetry compatible t_{2g} orbitals interact through cyanide π^* orbitals, resulting in antiferromagnetic coupling based on the Pauli exclusion principle. Lower: Unpaired electrons in symmetry incompatible t_{2g} and e_g orbitals leak over into orthogonal cyanide-based orbitals, resulting in ferromagnetic coupling based on Hund's rules.

orbital mixing occurs. This absence of an interaction enforces ferromagnetic exchange, in accordance with Hund's rules. Notably, the antiferromagnetic interaction is inherently much stronger, as it provides the greatest decrease in total energy, and thus usually dominates the superexchange in a competitive situation.

1.2.4 Mononuclear Metal-Cyanide Building Units

Maximum utilization and further expansion of the diversity associated with cyano-bridged assemblies hinges on our ability to develop and employ cyanometalate building units. In view of the widespread interest in Prussian Blue-type solids,[21] it is not surprising that octahedral $[M(CN)_n]^{x-}$ complexes are among the most common cyanometalate building units (see Figure 1.6). A compilation of structurally-characterized, paramagnetic examples of homoleptic cyanometalate complexes is given in Table 1, illustrating the diversity of such complexes. Indeed, inspection of the Table 1.1 reveals molecules bearing twelve different transition elements, spanning seven coordination geometries and all five spin ground states possible for a transition metal ion. In addition, several of the complexes feature transition metal ions that should exhibit

Table 1.1. Structurally-Characterized Examples of Homoleptic Paramagnetic Mononuclear Cyanometalate Complexes.

complex	geometry[a]	S	ref.	complex	geometry[a]	S	Ref.
$[Ti(CN)_6]^{3-}$	octahedral	$^1/_2$	22	$[Co(CN)_4]^{2-}$	square planar	$^1/_2$	33
$[V(CN)_6]^{4-}$	octahedral	$^3/_2$	23	$[Co(CN)_5]^{3-}$	square pyramidal	$^1/_2$	34
$[V(CN)_7]^{4-}$	pentagonal bipyr.	1	24	$[Mo(CN)_6]^{3-}$	octahedral	$^3/_2$	35
$[Cr(CN)_5]^{3-}$[b]	square pyramidal	2	25	$[Mo(CN)_7]^{4-}$	pentagonal bipyr.	$^1/_2$	36
$[Cr(CN)_6]^{4-}$	octahedral	1	26	$[Mo(CN)_8]^{3-}$	dodecahedral	$^1/_2$	37
$[Cr(CN)_6]^{3-}$	octahedral	$^3/_2$	27	$[Ru(CN)_6]^{3-}$	octahedral	$^1/_2$	38
$[Mn(CN)_4]^{2-}$	tetrahedral	$^5/_2$	28	$[Nb(CN)_8]^{4-}$	dodecahedral	$^1/_2$	39
$[Mn(CN)_6]^{4-}$	octahedral	$^5/_2$	29	$[W(CN)_8]^{3-}$	square antiprismatic	$^1/_2$	40
$[Mn(CN)_6]^{3-}$	octahedral	1	30	$[Re(CN)_7]^{3-}$	pentagonal bipyr.	$^1/_2$	41
$[Mn(CN)_6]^{2-}$	octahedral	$^3/_2$	31	$[Os(CN)_6]^{3-}$	octahedral	$^1/_2$	42
$[Fe(CN)_6]^{3-}$	octahedral	$^1/_2$	32				

[a]In the case where multiple salts have been isolated, the coordination geometry of the potassium-containing salt is provided. [b]Both square pyramidal and distorted trigonal bipyramidal geometries are present in the crystal structure.

strong magnetic anisotropy, stemming from unquenched orbital angular momentum (e. g. $[Fe(CN)_6]^{3-}$),[32] heavy nuclei (e. g. $[Re(CN)_7]^{3-}$),[41] or low molecular symmetry (e. g. $[Mo(CN)_7]^{4-}$).[36] In considering homoleptic cyanometalates in the design of multinuclear assemblies, these complexes are well-suited to occupy the central unit of a molecular cluster, binding through a cyanide ligand one to six $[LM']^{y+}$ units and thus giving rise to dinuclear to heptanuclear assemblies.

As discussed in Section 1.2.2, a method of introducing further versatility in cyano-bridged assemblies involves utilizing cyanometalate complexes of the form $[LM(CN)_n]^{x-}$, where L is an auxiliary ligand that blocks one or more coordination sites (see Figure 1.6). In addition to the proscription of undesirable bridging interactions that lead to the formation of extended materials, judicious selection of the auxiliary ligand(s) provides an element of control in the construction of specific structural architectures. Here, coordination sites not occupied by blocking ligands feature terminal cyanide ligands to be used for bridging interactions, such that the number and relative configuration of these cyanide ligands will direct the overall structure. For instance, a *cis*-dicyanometalate complex can serve as the corner unit of a molecular square, whereas moving to a *fac*-tricyanometalate will lead to a cubic structure. In addition, a *trans*-dicyanometalate is an ideal precursor for directing the formation of a one-dimensional structure. A survey of Table 1.2 demonstrates the vast library of mixed ligand cyanometalate building units. Akin to their homoleptic counterparts, these complexes span a wide range of metal elements, from vanadium to uranium. In addition, molecules bearing one to six terminal cyanide ligands in various coordination geometries can be readily accessed. As for the range of magnetic properties, Table 1.2 reveals the presence

Table 1.2. Selected Structurally-Characterized Examples of Mixed-Ligand Paramagnetic Mononuclear Cyanometalate Complexes.

complex	geometry	S	ref.	complex	geometry	S	ref.	complex	geometry	S	ref.
one cyanide ligand			43	*trans*-(OEOP)Fe(CN)$_2$[t]	octahedral	$^1/_2$	64	*mer*-[(pzcq)Fe(CN)$_3$]$^-$[mm]	octahedral	$^1/_2$	87
[(dmpe)$_2$Cr(CN)Cl]$^+$[a]	O_h	$^3/_2$	43	*trans*-[(bpmb)Fe(CN)$_2$]$^-$[u]	octahedral	$^1/_2$	65	*mer*-[(mpzcq)Fe(CN)$_3$]$^-$[nn]	octahedral	$^1/_2$	88
[(dmpe)$_2$Cr(CN)Br]$^+$	O_h	$^3/_2$	43	[Tp*Co(CN)$_2$]$^-$	SP$_{distorted}$	$^1/_2$	55	*fac*-(Me$_3$tacn)Mo(CN)$_3$	octahedral	$^3/_2$	89
[(dmpe)$_2$Cr(CN)I]$^+$	O_h	$^3/_2$	43	*trans*-[(acac)$_2$Ru(CN)$_2$]$^-$[v]	octahedral	$^1/_2$	66	*fac*-[(triphos)Re(CN)$_3$]$^-$[oo]	octahedral	$^1/_2$	90
(dmpe)$_2$Cr(CN)Cl	O_h	1	43	*trans*-[(salen)$_2$Ru(CN)$_2$]$^-$[w]	octahedral	$^1/_2$	67	[Cp*$_2$U(CN)$_3$]$^{2-}$	C_1	$J = ^{15}/_2$	91
(dmpe)$_2$Cr(CN)I	O_h	1	43	*trans*-[PcRe(CN)$_2$]$^-$	octahedral	1	68	[Cp*$_2$U(CN)$_3$]$^-$	C_{2v}	$J = 6$	91
(TPP)Mn(CN)[b]	SP[c]	2	44	*trans*-[(dppe)$_2$Re(CN)$_2$]	D_{2h}	$^1/_2$	69	**four cyanide ligands**			
[(dppm)$_2$Mn(CN)(CO)]$^+$[d]	C_{2v}	$^1/_2$	45	*trans*-[ReCl$_4$(CN)$_2$]$^{2-}$	octahedral	$^3/_2$	70	[Cr(CN)$_4$(N)(py)]$^{2-}$	octahedral	$^1/_2$	92
[(NS$_3$)Fe(CN)]$^-$[e]	TBP[f]	$^5/_2$	46	*trans*-[(salen)$_2$Os(CN)$_2$]$^-$	octahedral	$^1/_2$	71	[(2,2′-bpy)Cr(CN)$_4$]$^-$	octahedral	$^3/_2$	93
(TPP)Fe(CN)(py)[g]	octahedral	$^1/_2$	43	**three cyanide ligands**				[(amp)Cr(CN)$_4$]$^-$[pp]	octahedral	$^3/_2$	94
[(NS$_3$)Co(CN)]$^-$	TBP	1	47	*fac*-[Tp*V(CN)$_3$]$^-$	octahedral	1	72	[(phen)Cr(CN)$_4$]$^-$[qq]	octahedral	$^3/_2$	94
[(tren)Cu(CN)]$^+$[h]	TBP	$^1/_2$	48	(cyclen)V(CN)$_3$[x]	TBTB[y]	1	73	[Fe(CN)$_4$(NO)]$^{2-}$	SP		95
[(2,2′-bpy)$_2$Cu(CN)]$^+$[i]	TBP$_{distorted}$	$^1/_2$	49	[Cp*Cr(CN)$_3$]$^-$[z]	octahedral	$^3/_2$	74	[(phen)Fe(CN)$_4$]$^-$	octahedral	$^1/_2$	96
[(Me$_6$tren)Cu(CN)]$^+$[j]	TBP	$^1/_2$	50	*fac*-(P$_3$)Cr(CN)$_3$[aa]	octahedral	$^3/_2$	75	[(2,2′-bpy)Fe(CN)$_4$]$^-$	octahedral	$^1/_2$	97
[(tpma)Cu(CN)]$^+$[k]	TBP	$^1/_2$	51	*fac*-(Me$_3$tacn)Cr(CN)$_3$[bb]	octahedral	$^3/_2$	76	[(bpym)Fe(CN)$_4$]$^-$[rr]	octahedral	$^1/_2$	98
[(en)$_2$Cu(CN)]$^+$[l]	TBP	$^1/_2$	52	*fac*-(tach)Cr(CN)$_3$[cc]	octahedral	$^3/_2$	77	[Fe(CN)$_4$(py)$_2$]$^-$	octahedral	$^1/_2$	99
(N$_3$N)Mo(CN)[m]	TBP	1	53	*fac*-[TpCr(CN)$_3$]$^-$[dd]	octahedral	$^3/_2$	78	[Co(CN)$_4$(py)]$^{2-}$	SP	$^1/_2$	100
(dppe)$_2$Mo(CN)Cl[n]	C_{2v}	1	54	*fac*-[TpFe(CN)$_3$]$^-$	octahedral	$^1/_2$	79	**five cyanide ligands**			
two cyanide ligands				*fac*-(dien)Fe(CN)$_3$[ee]	octahedral	$^1/_2$	80	[Fe(CN)$_5$(NH$_3$)]$^{2-}$	octahedral	$^1/_2$	103
[Tp*Cr(CN)$_2$]$^-$[o]	SP$_{distorted}$	2	55	*fac*-(tach)Fe(CN)$_3$	octahedral	$^1/_2$	77	[Fe(CN)$_5$(py)]$^{2-}$	octahedral	$^1/_2$	99,104
trans-[(cyclam)Cr(CN)$_2$]$^+$[p]	octahedral	$^3/_2$	56	*mer*-[(bpca)Fe(CN)$_3$]$^-$[ff]	octahedral	$^1/_2$	81	[Re(CN)$_5$(NO)]$^{2-}$	octahedral	$^1/_2$	105
trans-[(cyclam)Mn(CN)$_2$]$^+$	octahedral	1	57	*mer*-[(pcq)Fe(CN)$_3$]$^-$[gg]	octahedral	$^1/_2$	82	[W(CN)$_5$(CO)$_2$]$^{2-}$	PBP[ss]	$^1/_2$	106
cis-(2,2′-bpy)$_2$Mn(CN)$_2$	octahedral		58	*fac*-[Tp*Fe(CN)$_3$]$^-$	octahedral	$^1/_2$	83	[Cp*$_2$U(CN)$_5$]$^{3-}$	D_{5h}	$J = 6$	91
trans-[PcMn(CN)$_2$]$^-$[q]	octahedral	1	59	*fac*-[(pzTp)Fe(CN)$_3$]$^-$[hh]	octahedral	$^1/_2$	84	[Cp*$_2$U(CN)$_5$]$^{2-}$	D_{5h}	$J = ^7/_2$	91
trans-[PcFe(CN)$_2$]$^-$	octahedral	$^1/_2$	60	*fac*-[(HBInPz$_3$)Fe(CN)$_3$]$^-$[ii]	octahedral	$^1/_2$	85	**six cyanide ligands**			
cis-[(2,2′-bpy)$_2$Fe(CN)$_2$]$^+$	octahedral	$^1/_2$	61	*fac*-[(MeBPz$_3$)Fe(CN)$_3$]$^-$[jj]	octahedral	$^1/_2$	86	[(2,2′-bpy)W(CN)$_6$]$^-$	SAP[tt]	$^1/_2$	107
trans-[(acacen)Fe(CN)$_2$]$^-$[r]	octahedral	$^1/_2$	62	*fac*-[(^{i}BuBPz$_3$)Fe(CN)$_3$]$^-$[kk]	octahedral	$^1/_2$	86				
trans-[(bpb)Fe(CN)$_2$]$^-$[s]	octahedral	$^1/_2$	63	*fac*-[(PhBPz$_3$)Fe(CN)$_3$]$^-$[ll]	octahedral	$^1/_2$	86				

[a]dmpe = 1,2-bis(dimethylphosphino)ethane. [b]TTP^{2-} = (*meso*-tetraphenylporphinato) dianion. [c]SP = square pyramidal. [d]dppm = 1,2-bis(diphenylphospino)methane. [e]NS$_3$ = tris(2-thiolatoethyl)amine. [f]TBP = trigonal bipyramidal. [g]py = pyridine. [h]tren = tris(2-aminoethyl)amine. [i]2,2′-bpy = 2,2′-bipyridine. [j]Me$_6$tren = tris(2-(dimethylamino)ethyl)amine. [k]tmpa = tris(2-pyridylmethyl)amine. [l]en = 1,2-diaminoethane. [m](N$_3$N)$^{3-}$ = [(Me$_3$SiNCH$_2$CH$_2$)$_3$N]$^{3-}$. [n]dppe = 1,2-bis(diphenylphospino)ethane. [o]Tp*$^-$ = hydrotris(3,5-dimethylpyrazol-1-yl)borate. [p]cyclam = 1,4,8,11-tetraazacyclotetradecane. [q]Pc^{2-} = phthalocyanine dianion. [r]acacen^{2-} = *N,N′*-ethylenebis(acetylacetonylideneimino) dianion. [s]bpb^{2-} = 1,2-bis(pyridine-2-carboxamido)benzenate. [t]OEOP = octaethyloxoporphyrinato dianion. [u]bpmb^{2-} = 1,2-bis(pyridine-2-carboxamido)-4-methylbenzene dianion. [v]acac$^-$ = acetylacetonate. [w]salen^{2-} = *N,N′*-ethylenebis(salicylideneaminato) dianion. [x]cyclen = 1,4,7,10-tetraazacyclododecane. [y]TBTB = trigonal base-tetragonal base. [z]Cp*$^-$ = pentamethylcyclopentadiene anion. [aa]P$_3$ = 1,1,1-tris((dimethylphosphino)methyl)ethane. [bb]Me$_3$tacn = *N,N′,N″*-trimethyl-1,4,7-triazacyclononane. [cc]tach = 1,3,5-triaminocyclohexane. [dd]Tp$^-$ = hydrotris(pyrazol-1-yl)borate. [ee]dien = diethylenetriamine. [ff]bpca = *mer*-(bis(2-pyridylcarbonyl)amino) anion. [gg]pcq$^-$ = 8-(pyridine-2-carboxamido)quinoline anion. [hh]pzTp$^-$ = tetra(pyrazol-1-yl)borate. [ii]HBInPz$_3^-$ = hydrotris(indazol-1-yl)borate. [jj]MeBPz$_3^-$ = methyltris(pyrazol-1-yl)borate. [kk] ^{i}BuBPz$_3^-$ = isobutyltris(pyrazol-1-yl)borate. [ll]PhBPz$_3^-$ = phenyltris(pyrazol-1-yl)borate. [mm]pzcq$^-$ = 8-(pyrazine-2-carboxamido)quinoline anion. [nn]mpzcq$^-$ = 8-(5-methylpyrazine-2-carboxamido)quinoline anion. [oo]triphos = 1,1,1-tris((diphenylphosphino)methyl)ethane. [pp]amp = 2-(aminomethyl)pyridine. [qq]phen = 1,10-phenanthroline. [rr]bpym = 2,2′-bipyrimidine. [ss]PBP = pentagonal bipyramidal. [tt]SAP = square antiprismatic.

of ground states from $S = {}^1/_2$ to $J = {}^{15}/_2$. Furthermore, the majority of listed molecules should exhibit significant anisotropy. In fact, the zero-field splitting has even been measured in some cases, such as in the complex $[ReCl_4(CN)_2]^{2-}$.

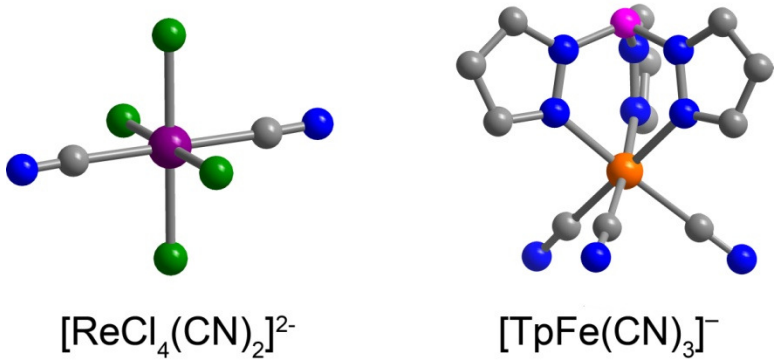
1.3 Raising the Relaxation Barrier by Controlling Magnetic Parameters

Starting with the myriad of available homoleptic and mixed-ligand cyanometalate building units, one can envision a plethora of both molecular and one-dimensional architectures, ranging from dinuclear complexes to giant clusters containing fifteen metal centers. Furthermore, once a topology has been achieved synthetically, the inherent modularity of cyanometalate building units enables access to interchangeable metal sites, where various metal ions can be substituted in order to tune the magnetic properties of the overall assembly. Specifically, as outlined in Section 1.1, the relaxation barrier height in both single-molecule and single-chain magnets depends on three key parameters: spin ground state (S), axial zero-field splitting parameter (D), and superexchange coupling constant (J) (see Figure 1.2). Thus, by judicious selection of building units that exhibit desired parameters, one can systematically vary and increase the relaxation barrier height, while developing and expanding a basic understanding of magnetostructural correlations in cyano-bridged materials.

1.3.1 Spin Ground State (S)

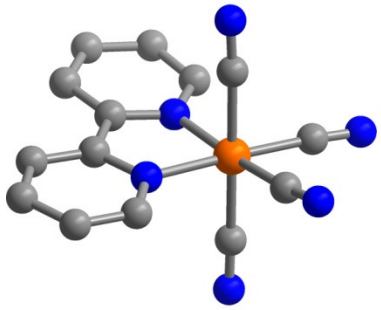
The relaxation barrier in single-molecule and single-chain magnets increases with increasing values of the spin ground state, assuming constant D and J values (see Section 1.1). Thus, one approach to raise this barrier centers on generating high-nuclearity clusters (or repeating units in the case of chains) that contain high-spin ferromagnetically coupled metal centers. The cyanide ligand is uniquely suited to direct the formation of such assemblies, as the predictable linear bridging mode between two metal centers grants control over structure and thus nuclearity. For instance, one can envision an octahedral metal complex in which one face is capped by a tridentate blocking ligand, while the other three coordination sites are ligated by terminal cyanide ligands, acting as the corner unit of a cubic structure. The $S = {}^3/_2$ complex $[TpCr(CN)_3]^-$ (Tp^- = hydrotris(pyrazol-1-yl)borate) provides an example of such a molecule.[78] Here, the spin ground state for a mononuclear tricyanide complex is maximized with a t_{2g}^3 electron configuration. Reaction of this building unit with $[Cu(H_2O)_6]^{2+}$ results in the formation of a face-centered cubic cluster $[Tp_8(H_2O)_6Cu^{II}{}_6Cr^{III}{}_8(CN)_{24}]^{4+}$, with eight $[TpCr(CN)_3]^-$ units at the corners of the cube bridged through cyanide to six Cu^{II} centers situated just above the cube faces (see Figure 1.7). Based on the orbital considerations outlined in Section 1.2.3, ferromagnetic exchange coupling is expected between Cr^{III} and Cu^{II} centers. Indeed, such interactions are evident in the magnetic behavior of the cluster, which demonstrates an $S = 15$ spin ground state at low temperature.

While incorporating combinations of metal ions that promote ferromagnetic interactions provides the most direct route for generating high-spin ground states, antiferromagnetic exchange between metal centers featuring different numbers of unpaired electrons can also accomplish this task. Indeed, the highest spin ground state yet observed for a metal-cyanide cluster belongs to the body-centered, face-capped octahedral clusters $(ROH)_{24}Mn^{II}{}_9M^{V}{}_6(CN)_{48}$ (M = Mo, W, R = Me, Et), whose

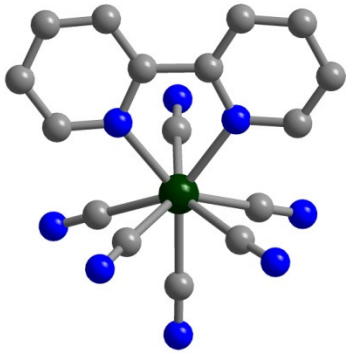


$[ReCl_4(CN)_2]^{2-}$

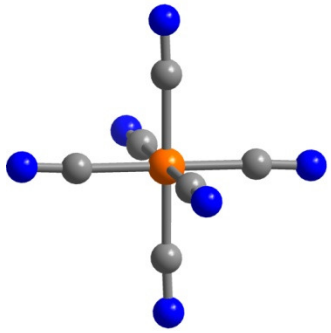
$[TpFe(CN)_3]^-$



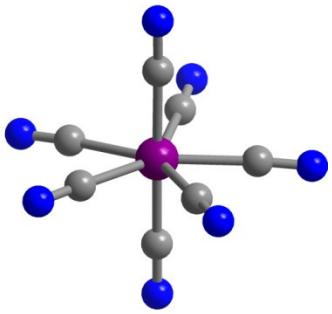
$[(bpy)Fe(CN)_4]^-$



$[(bpy)W(CN)_6]^-$



$[Fe(CN)_6]^{3-}$



$[Re(CN)_7]^{3-}$

Figure 1.6. Crystal structures of selected cyanometalate building units. Purple, dark green, orange, green, blue, and gray spheres represent Re, W, Fe, Cl, N, and C atoms, respectively; H atoms are omitted for clarity.

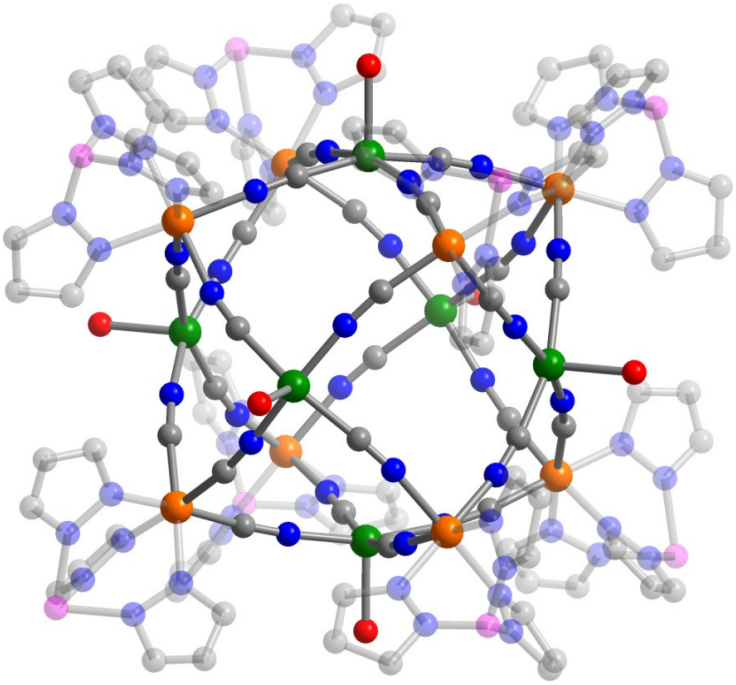


Figure 1.7. Crystal structure of the face-centered cubic cluster $[Tp_8(H_2O)_6Cu^{II}_6Cr^{III}_8(CN)_{24}]^{4+}$. Orange, green, magenta, red, blue, and gray spheres represent Cr, Cu, B, O, N, and C atoms, respectively; H atoms are omitted for clarity. The Tp^- ligands are transparent for better visualization of the cluster core.

formations are templated by six face-capping $[W(CN)_8]^{3-}$ units bridged through cyanide ligands to nine Mn^{II} centers positioned at the center and vertices of the cube (see Figure 1.8).[108,109] Here, the maximum possible disparity of unpaired electrons between two transition metal ions is utilized by the presence of W^V ($S = {}^1/_2$) and high-spin Mn^{II} ions ($S = {}^5/_2$). Moreover, the nine Mn^{II} centers outnumber the six W^V centers, further promoting the generation of a high spin. As expected, magnetic measurements revealed the presence of an $S = {}^{39}/_2$ ground state for each of the clusters.[108,109,110]

1.3.2 Axial Zero-Field Splitting Parameter (*D*)

Despite the markedly high spin ground states displayed by the $(ROH)_{24}Mn^{II}_9M^V_6(CN)_{48}$ clusters, none of the complexes behaves as a single-molecule magnet.[108,109] The absence of slow magnetic relaxation is a direct consequence of a lack of magnetic anisotropy in the molecules. Indeed, establishing an energy barrier to magnetization relaxation requires both a high-spin ground state and a significant negative *D* value. Like generating high-spin ground states, imparting anisotropy into a cluster or solid may be achieved in a controllable fashion through use of cyanometalate building units. While precise predictions of the sign and magnitude of *D* values are much less straightforward than those of spin, the synthetic chemist can utilize several basic principles in designing high-anisotropy building units. First, magnetic anisotropy can arise from a structural distortion or asymmetry in the local coordination environment of a

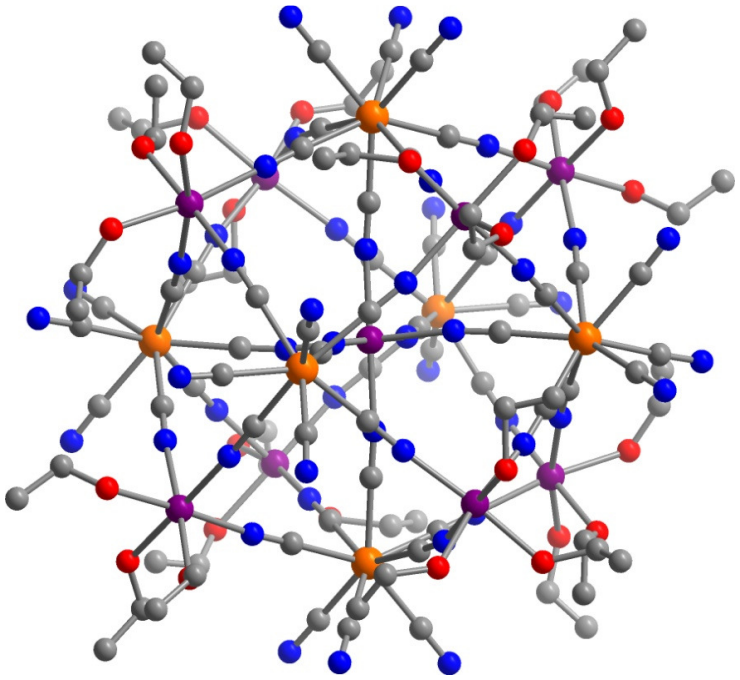


Figure 1.8. Crystal structure of the face-capped, body-centered cluster $(EtOH)_{24}Mn^{II}_{9}W^{V}_{6}(CN)_{48}$. Orange, purple, red, blue, and gray spheres represent W, Mn, O, N, and C atoms, respectively; H atoms are omitted for clarity.

paramagnetic metal center. Since the discovery of single-molecule magnets, this technique has been the most documented method of generating anisotropy, as demonstrated in the utilization of Jahn-Teller elongated high-spin Mn^{III} centers. While the vast majority of this work has centered on oxo-bridged manganese clusters, recent years have seen the appendage of Mn^{III} centers to cyanometalate building units, giving rise to cyano-bridged clusters[111,112,113] and solids[112] exhibiting large D values.

A second method for designing a high-anisotropy building unit centers on selecting a metal ion that features significant spin-orbit coupling. One way to accomplish this is to employ a metal ion possessing an electron configuration that gives rise to unquenched orbital angular momentum. In an octahedral coordination geometry, the low-spin iron(III) ion (t_{2g}^{5}) presents an example of just such a configuration. Indeed, the trigonal bipyramidal complex $[Tp_2(Me_3tacn)_3Cu^{II}_{3}Fe^{III}_{2}(CN)_6]^{4+}$ (Me_3tacn = *N*,*N*′,*N*″-trimethyl-1,4,7-triazacyclononane),[114] derived from the building unit $[TpFe(CN)_3]^{-}$,[79] demonstrates the largest zero-field splitting parameter (D = -5.7 cm^{-1}) yet reported for any multinuclear transition metal cluster. Further illustrating the impact of Fe^{III} in generating this anisotropy, the D value of the related cluster $[(Me_3tacn)_5Cu^{II}_{3}Cr^{III}_{2}(CN)_6]^{6+}$ is too small to be measured by magnetization experiments.[115] Alternatively, spin-orbit coupling can be introduced through use of a relatively heavy metal. For instance, the complex $Cr(acac)_3$ ($acac^{-}$ = acetylacetonate) shows modest zero-field splitting, with a D value of -0.59 cm^{-1}.[116] Substitution of Mo^{III} for the Cr^{III} center, however, results in a more than ten-fold increase to D = -6.3 cm^{-1}.[117] Indeed, this

principle has been exploited in the preparation of the building unit complex $[ReCl_4(CN)_2]^{2-}$,[70] which demonstrates the largest zero-field splitting parameter (D = -14.4 cm^{-1}) yet reported for a metal-cyanide complex.

In addition to the single-ion anisotropy imparted to a cluster or solid from the building unit, the overall shape of the structure governs how the anisotropy axes of the constituent metal ions sum together. Generally, highly-symmetric assemblies tend to align these axes such that the overall anisotropy is minimized. For instance, the $(ROH)_{24}Mn^{II}_9M^{V}_6(CN)_{48}$ (M = Mo, W) clusters described above each contain six Mo^{V} or W^{V} ions, which possess strong spin-orbit coupling and thus magnetic anisotropy owing to their relatively heavy nuclei. Nevertheless, neither molecule demonstrates any significant magnetic anisotropy. This lack of anisotropy stems from the relative orientations of the M^{V} ions, which occupy the points of an octahedron. In this geometry, the easy magnetic axes oppose one another and thus cancel the single-ion anisotropy terms. Moreover, this effect is apparent in two related $Cu^{II}_mFe^{III}_n$ clusters. The face-centered cubic cluster $[Tp_8(H_2O)_6Cu^{II}_6Fe^{III}_8(CN)_{24}]^{4+}$, with O_h point symmetry, possesses a zero-field splitting parameter of D = -0.16 cm^{-1}.[118] Upon reduction of the symmetry to D_{3h}, as found in the trigonal bipyramidal cluster $[Tp_2(Me_3tacn)_3Cu^{II}_3Fe^{III}_2(CN)_6]^{4+}$,[114] this value increases drastically to D = -5.7 cm^{-1} (see Figure 1.9). In view of such dramatic variations in anisotropy, an ideal candidate for a single-molecule magnet would possess both a high-spin ground state and significant magnetic anisotropy.

1.3.3 Superexchange Interaction (J)

As outlined in Section 1.2.3, the ability to predict the nature of magnetic superexchange coupling through a bridging cyanide ligand between metal centers renders the cyanide ligand an ideal linker for constructing preconceived structural architectures. In addition, exploiting this ligand to aid in raising relaxation barriers in single-molecule and single-chain magnets demands the maximization of exchange strength. In multinuclear molecules, the energy separation between the spin ground state and excited states is directly proportional to the magnitude of magnetic exchange (J) (see Figure 1.2). Thus, in order for a single-molecule magnet to function at high temperature, the entire M_S manifold of the ground state must lie cleanly below the first excited state. An even more pronounced effect is found in single-chain magnets, where the magnitude of the relaxation barrier increases directly as a function of J. For a single-chain magnet comprised of a repeating paramagnetic unit with spin S, the relaxation barrier can be expressed as $\Delta_\tau = 2\Delta_\xi + \Delta_A$ in the infinite size regime. Within the Ising limit, where $|D/J| > {}^4/_3$, the correlation energy and anisotropy energy are related to the magnetic parameters as $\Delta_\xi = 4|J|S^2$ and $\Delta_A = |D|S^2$.[12] As such, the overall relaxation barrier can be written in terms of the magnetic parameters as $\Delta_\tau = S^2|8J + D|$. Thus, increasing the strength of coupling will enhance the relaxation barrier at the same rate as will increasing D.

The strength of the magnetic exchange interaction (quantified by the exchange Hamiltonian $\hat{H} = -2J\hat{S}_1\cdot\hat{S}_2$ for two metal centers) is correlated to the degree of overlap between metal- and cyanide-based orbitals. Thus, the exchange constant should be greatest for metal-cyanide systems involving the diffuse d orbitals of second- or third-row transition metals. This principle is exemplified in the cyano-bridged clusters $[(Me_3tacn)_2(cyclam)Ni^{II}M^{III}_2(CN)_6]^{2+}$ (cyclam = 1,4,8,11-tetraazacyclotetradecane) and

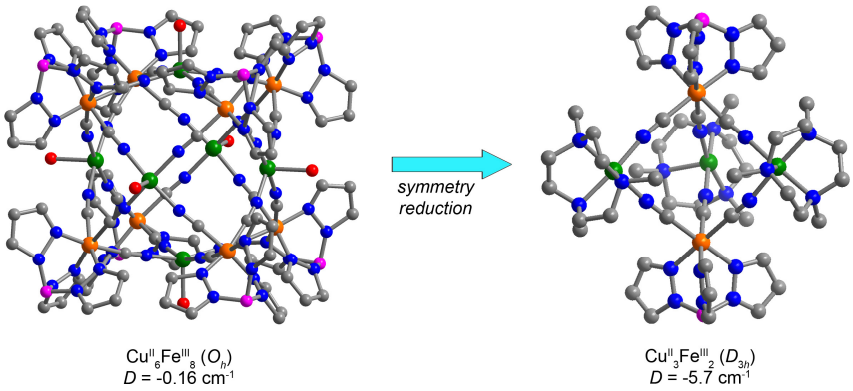


Figure 1.9. The influence of cluster symmetry on magnetic anisotropy, as seen in the increase in zero-field splitting magnitude in moving from the face-centered cubic cluster $[Tp_8(H_2O)_6Cu^{II}_6Fe^{III}_8(CN)_{24}]^{4+}$ to the trigonal bipyramidal cluster $[Tp_2(Me_3tacn)_3Ni^{II}_3Fe^{III}_2(CN)_6]^{4+}$. Orange, green, magenta, red, blue, and gray spheres within the crystal structures represent Fe, Cu, B, O, N, and C atoms, respectively; H atoms are omitted for clarity.

$[(Me_3tacn)_6Mn^{III}M^{III}_6(CN)_{18}]^{2+}$ (M = Cr, Mo), where the Mo congeners feature significant increases in coupling strength (J = 17.0-17.6 and -6.7 cm^{-1}, respectively)[119] relative the chromium analogues (J = 10.9 and -3.0 cm^{-1}).[120] Additionally, the largest value of J yet reported for superexchange through cyanide belongs to the S = 0 dinuclear complex $[Mo_2(CN)_{11}]^{5-}$, which boasts an exchange parameter of J = -113 cm^{-1}.[35] Alternatively, incorporation of an axially-elongated Cu^{II} ion into a M-CN-Cu^{II} linkage, with the cyanide bridge lying in the basal plane, has been shown to enhance the magnitude of exchange.[19f,121] This effect arises from the presence of a d^9 electron configuration with local C_{4v} symmetry. The coordination environment of the Cu^{II} center serves to lower the energy of the d_z^2 orbital relative to the $d_{x^2-y^2}$ orbital, thereby localizing the unpaired electron along the Cu-N_{CN} bond, in the direction of magnetic exchange. Similarly, incorporation of a cyanide linkage along the z^2 orbital of a Cu^{II} ion trigonal bipyramidal coordination leads to strict orthogonality of the z^2 orbital and the π^* orbital of the cyanide ligand, thus engendering strong ferromagnetic exchange. Indeed, one of the strongest magnetic exchange interactions for first-row transition metal-cyanide compounds has been reported for the dinuclear species $[Cu_2(tren)_2(CN)]^{3+}$ (tren = tris(2-aminoethyl)amine, J = -88 cm^{-1}).[123] Comparison with related $[Cu_2(L)_4(CN)]^{3+}$ (L = 2,2′-bipyridine, J = -9.4 cm^{-1}; L = 1,10-phenanthroline, J = -29 cm^{-1}) complexes, where the z^2 orbitals lie perpendicular to the cyanide bridge, demonstrates the dramatic effects of orbital compatibility on the magnetic exchange parameter.

1.4 Cyano-Bridged Single-Molecule Magnets

1.4.1 Trinuclear Clusters

1.4.1.1 Linear M_2M' Clusters

One of the simplest structure types to consider when designing a single-molecule magnet is a trinuclear M_2M' cluster, where a cyanometalate complex occupies the central position and is appended by two peripheral metal complexes. Ideally, the central unit of such a cluster would consist of a cyanometalate complex featuring two axial cyanide ligands, with the equatorial plane passivated by an inert blocking ligand (L′) to prevent the formation of extending bonding networks. Along these lines, the metal center within the outer unit should bear only one coordination site accessible to the nitrogen end of cyanide, with a polydentate blocking ligand (L) capping the other sites. This type of structure can be attained through a general assembly reaction depicted in Equation 1.3:

$$2\ [LM(solv)]^{x+} + \textit{trans}\text{-}[L'M'(CN)_2]^{y-} \longrightarrow [LM(\mu\text{-}NC)M'L'(\mu\text{-}CN)ML]^{2x-y} \qquad (1.3)$$

An inspection of Table 1.2 reveals a number of reported cyanometalate complexes that feature two axial cyanide ligands, containing Mn^{III}, Fe^{III}, Ru^{III}, $Re^{II/III/IV}$, and Os^{III} centers. Further emphasizing the potential of these building units, their constituent metal ions should all possess anisotropic spin ground states by virtue of significant spin-orbit coupling. Surprisingly, though, none of these complexes have been incorporated into single-molecule magnets. In fact, no complex of the form *trans*-$[LM(CN)_2]^{x-}$ has been employed in the formation of a single-molecule magnet. Rather, the only examples of trinuclear single-molecule magnets incorporating a complex featuring axial cyanide ligands are $[(5\text{-Brsalen})_2(H_2O)_2Mn^{III}{}_2M^{III}(CN)_6]^-$[123] (5-Brsalen^{2-} = *N*,*N*′-ethylenebis(5-bromosalicylideneiminato) dianion, M = Cr, Fe) and $[(salmen)_2(MeOH)_2Mn^{III}{}_2Fe^{III}(CN)_6]^-$ (salmen^{2-} = *rac*-*N*,*N*′-(1-methylethylene)bis(salicylideneiminato) dianion) (see Table 1.3),[112] all constructed from the homoleptic cyanometalate complexes $[M(CN)_6]^{3-}$ (M = Cr, Fe (see Figure 1.6)). The structure of these complexes consists of a central $[M(CN)_6]^{3-}$ unit bridged through two axial cyanide ligands to two $[LMn(solv)]^+$ units (see Figure 1.10). In these clusters, variable-temperature dc susceptibility data clearly demonstrated the presence of antiferromagnetic and ferromagnetic coupling between Cr^{III} and Mn^{III} centers and Fe^{III} and Mn^{III} centers, respectively, giving rise to spin ground states of $S = {}^5/_2$ and $S = {}^9/_2$. Slow magnetic relaxation in $[(5\text{-Brsalen})_2(H_2O)_2Mn^{III}{}_2M^{III}(CN)_6]^-$ was evidenced by frequency-dependent peaks in the variable-temperature out-of-phase ac magnetic susceptibility (χ_M''). From the χ_M'' data, a relaxation time (τ) was extracted for each peak through the expression $\tau = 1/2\pi\nu$, where ν is the switching frequency of the ac field. For a single-molecule magnet, the temperature dependence of the relaxation time should follow an Arrhenius (or thermally-activated) behavior, where τ is enhanced exponentially as temperature is decreased. Thus, a plot of $\ln(\tau)$ vs. $1/T$ should be linear, with the slope corresponding to the spin-reversal barrier, U_{eff}. Indeed, plots of $\ln(\tau)$ vs. $1/T$ for the clusters were found to be linear, and the corresponding fits gave effective spin-reversal barriers of U_{eff} = 16 (Cr) and 25 (Fe) cm^{-1}. Importantly, however, the magnitudes of the observed χ_M'' peaks represent only a small fraction of the total susceptibility, with the maximum of the most intense peak failing to reach χ_M'' = 0.1 $cm^3 \cdot K/mol$. This suggests

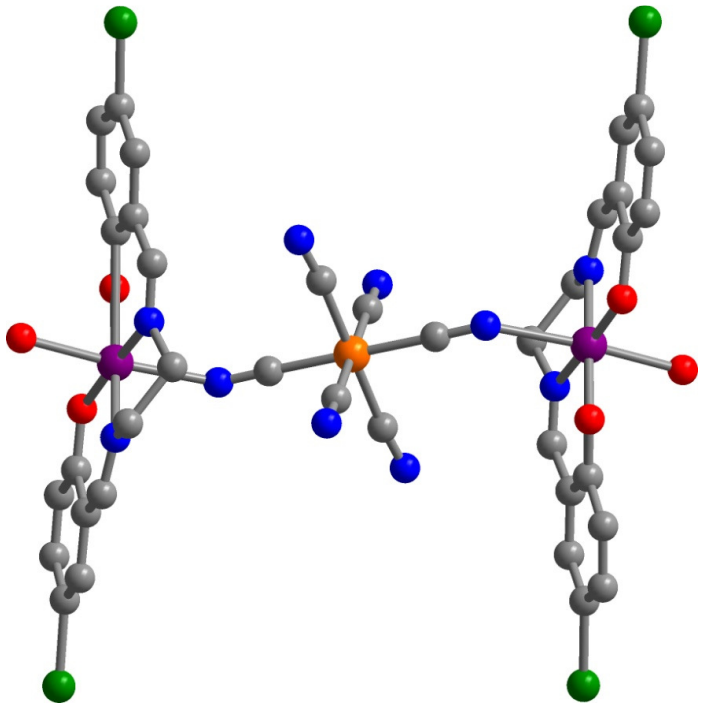


Figure 1.10. Crystal structure of the linear trinuclear cluster $[(5\text{-Brsalen})_2(H_2O)_2Mn^{III}{}_2Fe^{III}(CN)_6]^-$. Orange, purple, green, red, blue, and gray spheres represent Fe, Mn, Cl, O, N, and C atoms, respectively; H atoms are omitted for clarity.

the observed signals in χ_M'' may not originate from the major component of the magnetic sample.

The magnetic behavior of the $(5\text{-Brsalen})_2Mn_2Fe$ cluster was later reexamined by another research group, who observed no signal in χ_M'' at temperatures down to 1.8 K and frequencies up to 1500 Hz. The authors hypothesized that the original peaks may have arisen from sample impurity or crystalline defects, which would explain their low magnitude relative to the total susceptibility. Nevertheless, this report described the magnetic behavior of the related compound $[(salmen)_2(MeOH)_2Mn^{III}{}_2Fe^{III}(CN)_6]^-$,[112,124] which demonstrates unambiguous single-molecule magnet behavior. As shown in the bottom panel of Figure 1.11, the plot of χ_M'' vs. T for this cluster displays a series of peaks that shift to lower temperature with decreasing frequency, indicative of slow magnetic relaxation. This slow dynamics can also be observed in the field-dependence of the magnetization at very low temperatures. Indeed, variable-field magnetization measurements performed on a single crystal, with the molecular magnetic easy axis oriented parallel to the applied field direction, showed hysteresis effects below 1.1 K (see Figure 1.11, middle). Two important observations can be made from the hysteresis loops. First, the coercive field becomes larger with decreasing temperature, as less thermal energy is available to randomize the magnetization, until becoming temperature-independent below 0.5 K. This suggests the presence of a dominant non-thermal process below 0.5 K. Second, the hysteresis loop obtained at 0.04 K features two steps, one

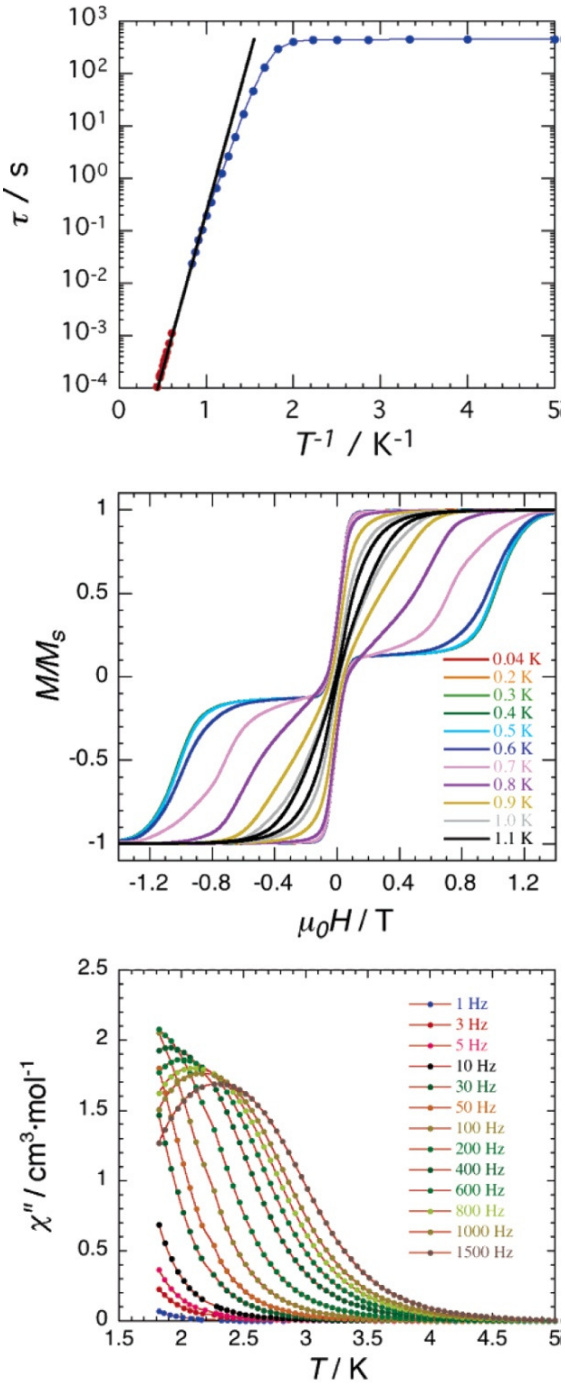


Figure 1.11. Lower: Variable-temperature out-of-phase ac magnetic susceptibility data for $[(salmen)_2(MeOH)_2Mn^{III}{}_2Fe^{III}(CN)_6]^-$. Middle: Reduced magnetization plot for Mn_2Fe cluster, showing quantum tunneling at low temperature. Upper: Arrhenius plot of relaxation time for Mn_2Fe cluster, showing thermally-activated regime at high temperature and pure quantum tunneling regime at low temperature. Taken from ref. 112.

appearing near zero field and the other at ca. 1 T. These steps were attributed to quantum tunneling of the magnetization between $M_S = \pm^9/_2$ and $M_S = +^9/_2$ and $-^7/_2$, respectively. The magnitude of field required to bring the $M_S = +^9/_2$ and $-^7/_2$ levels into resonance provides the energy separation between the levels, corresponding to a zero-field splitting parameter of $D = -0.90$ cm^{-1}, in good agreement with a value of $D = 0.848$ cm^{-1} obtained from fitting the reduced magnetization data. In order to quantify the spin-reversal barrier in the cluster, relaxation times were extracted from the χ_M'' data, as described above, in addition to direct dc measurements of the magnetization decay upon removal of an applied field. An Arrhenius plot, constructed from both methods of determining relaxation times, is shown in the top panel of Figure 1.11. Here, the high-temperature region of the plot clearly shows a thermally-activated relaxation process, with a linear fit to the data giving $U_{eff} = 9.7$ cm^{-1}. This barrier falls well short of the theoretical barrier $U = 17$ cm^{-1}, based on $S = ^9/_2$ and $D = -0.87$ cm^{-1} (mean value for both experiments), owing to the presence of thermally-assisted quantum tunneling. Indeed, as the temperature is lowered, the relaxation time deviates from a thermally-activated process, reaching temperature independence below 0.5 K, in accordance with the hysteresis loops collected below this temperature.

1.4.1.1 A Bent MM'_2 Cluster

A parallel synthetic strategy for targeting trinuclear cyano-bridged clusters involves the use of two cyanometalate complexes as the peripheral units, flanking a central metal ion. Such a reaction proceeds according to Equation 1.4:

$$[LM(solv)_2]^{x+} + 2\,[L'M'(CN)]^{y-} \longrightarrow [L'M'(\mu\text{-}CN)ML(\mu\text{-}NC)M'L']^{x-2y} \qquad (1.4)$$

This route involves a building unit of the form LM(CN), where all but one coordination sites are sequestered by a polydentate capping ligand (see Table 1.2). Despite the potential utility of this approach, no single-molecule magnet to date has been derived from a monocyanide building unit. The only example of a trinuclear single-molecule magnet incorporating peripheral cyanometalate units is the bent cluster $(pzTp)_2(bpy)_2Ni^{II}_2Fe^{III}(CN)_6$,[84] ($pzTp^-$ = tetra(pyrazol-1-yl)borate, bpy = 2,2′-bipyridine) assembled in the one-pot reaction of $[(pzTp)Fe(CN)_3]^-$, $Ni(SO_3CF_3)_2$, and 2,2′-bipyridine. The structure of this cluster consists of a central Ni^{II} ion residing in an octahedral coordination environment, with four sites occupied by bpy ligands and two sites coordinated in a cis configuration to the nitrogen ends of cyanide ligands from $[(pzTp)Fe(CN)_3]^-$ units (see Figure 1.12, upper). Variable-temperature dc magnetic susceptibility data revealed the presence of ferromagnetic coupling between the Fe^{III} and Ni^{II} centers, as evidenced by a monotonic rise in the plot of $\chi_M T$ vs. T with decreasing temperature (see Figure 1.12, lower). The presence of ferromagnetic coupling, expected for a superexchange interaction between Fe^{III} (t_{2g}^5) and Ni^{II} ($t_{2g}^6e_g^2$) based on orbital considerations, leads to a spin ground state of $S = 2$ at low temperature. A fit to the $\chi_M T$ data provided a coupling constant of $J = +4.9$ cm^{-1}. In addition, variable-temperature ac susceptibility measurements indicated the presence of slow magnetic relaxation, with an effective energy barrier of $U_{eff} = 8.3$ cm^{-1}. Notably, the characteristic frequency of the relaxation process is shown to decrease upon application of a small dc field to the ac

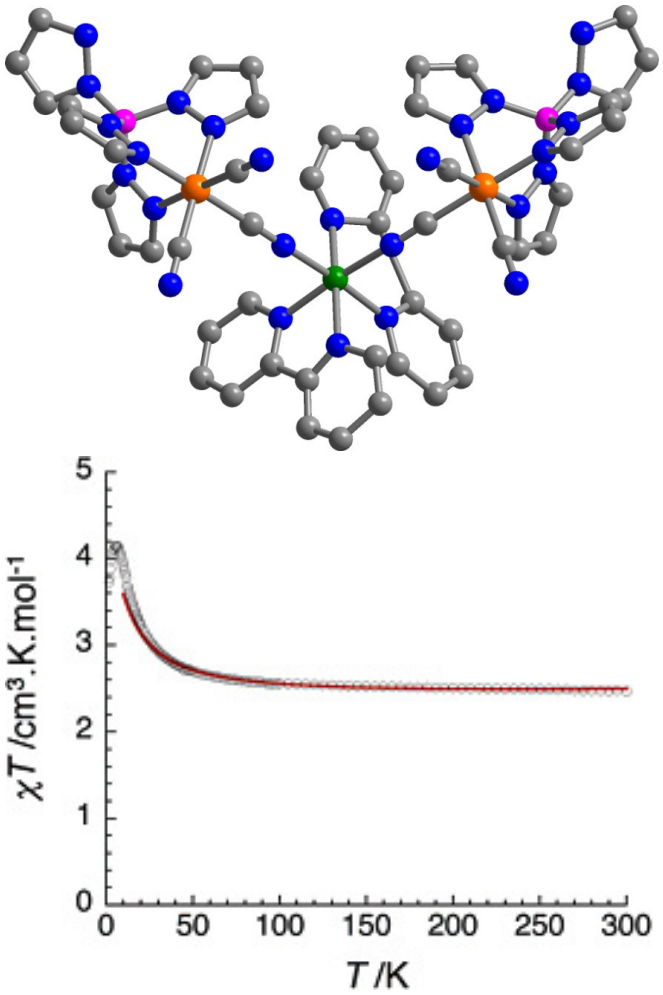


Figure 1.12. Upper: Crystal structure of the bent trinuclear cluster $(pzTp)_2(bpy)_2Ni^{II}_2Fe^{III}(CN)_6$. Orange, purple, green, red, blue, and gray spheres represent Fe, Mn, Cl, O, N, and C atoms, respectively; H atoms are omitted for clarity. Lower: Variable-temperature dc magnetic susceptibility data for the Ni_2Fe cluster. The red line represents a fit to the data, giving $J = +4.9(1)$ cm^{-1}. Taken from ref. 84.

measurement. This dependence arises from tunneling processes shortcutting the thermal barrier at zero-field, similar to the above Mn_2Fe example.

The dearth of trinuclear single-molecule magnets in the literature stems in large part from the limitations on building up a high-spin ground state for low-nuclearity complexes. For instance, assuming a low-spin cyanometalate building unit, the highest ground state achievable for coupling between three transition metal ions is $S = {}^{13}/_2$, which would arise from ferromagnetic coupling between $[Cr(CN)_6]^{3-}$ and two high-spin Mn^{II} centers. Based on orbital symmetry, this metal combination is very unlikely to engender a ferromagnetic interaction. Indeed, no reported trinuclear cyano-bridged cluster has eclipsed the $S = {}^9/_2$ ground state present in the foregoing examples. Furthermore, the

enormous anisotropy sometimes associated with mononuclear complexes often drops off precipitously upon introduction of exchange interactions with a second metal. Additionally, the magnitude of anisotropy does not necessarily undergo a significant further decrease with increasing nuclearity. Thus, the fact that trinuclear clusters generally do not exhibit significantly stronger anisotropy relative to their higher-nuclearity counterparts, in conjunction with their inability to accrue a large spin, leads to difficulty in designing cyano-bridged single-molecule magnets incorporating only three metal centers.

1.4.2 Tetranuclear Clusters

1.4.2.1 An Arch-Like $M_2M'_2$ Cluster

While the formation of linear clusters bearing three metal centers is relatively straightforward, extension of the linear topology to larger aggregates is extremely rare. In fact, only one example of a tetranuclear cyano-bridged cluster with a linear arrangement of metal ions has been structurally characterized to date.[113] A noteworthy synthetic challenge here is that the formation of such compounds requires either a stepwise assembly process or the reaction of two bifunctional reagents. Nevertheless, the sole report on the preparation of a linear, tetranuclear molecule described the arch-like cluster $(bpmb)_2(Clsalpn)_2Mn^{III}{}_2Fe^{III}{}_2(CN)_4$ ($bpmb^{2-}$ = 1,2-bis(pyridine-2-carboxamido)-4-methylbenzene dianion, $Clsalpn^{2-}$ = *N*,*N*′-bis(5-chlorosalicylidene)-1,3-diaminopropano dianion), formed in the reaction of $[(bpmb)Fe(CN)_2]^-$ with $[(Clsalpn)Mn]^+$.[113] The structure of this unique cluster consists of alternating $[(bpmb)Fe(CN)_2]^-$ and $[(Clsalpn)Mn]^+$ units (see Figure 1.13), where each Fe^{III} center resides in an octahedral coordination environment, with $bpmb^{2-}$ ligands occupying the equatorial plane and cyanide ligands binding the axial sites. One Fe^{III} center is bridged through two cyanide ligands to Mn^{III} ions, while the other, positioned on the end of the cluster, features one bridging and one terminal cyanide ligand. Similarly, each Mn^{III} center features octahedral geometry, with the equatorial plane being formed by a $Clsalpn^{2-}$ ligand. The inner Mn^{III} ion is bound in the axial positions to two nitrogen ends of bridging cyanides, while the outer Mn^{III} is bound by the nitrogen end of one bridging cyanide ligand and one water molecule that caps off further cluster aggregation.

Variable-temperature dc magnetic susceptibility measurements on the Mn_2Fe_2 cluster demonstrated the presence of ferromagnetic coupling between Mn^{III} (S = 2) and Fe^{III} (S = $^1/_2$) centers, resulting in a spin ground state of S = 5 at low temperature. Additionally, fits to magnetization data revealed the presence of zero-field splitting, with D = -0.42 cm^{-1}. In accordance with these findings, variable-temperature ac susceptibility measurements showed the onset of frequency-dependent peaks down to 1.8 K at frequencies up to 9999 Hz, thus establishing the cluster as a single-molecule magnet.

1.4.2.2 An $M'M_2M'$ Cluster

While the arch-like Mn_2Fe_2 cluster features an alternating Mn^{III}-Fe^{III} structure, use of a dimeric complex $[(Rsalen)_2Mn_2(H_2O)_2]^{2+}$ ($salen^{2-}$ = *N*,*N*′-ethylenebis(salicylideneaminato) dianion) as a starting material can lead to a tetranuclear cluster with the intact dimer serving as a central unit and cyanometalate groups occupying the periphery. Indeed, reaction of $[L_2Mn_2(H_2O)_2]^{2+}$ (L^{2-} = *N*,*N*′-

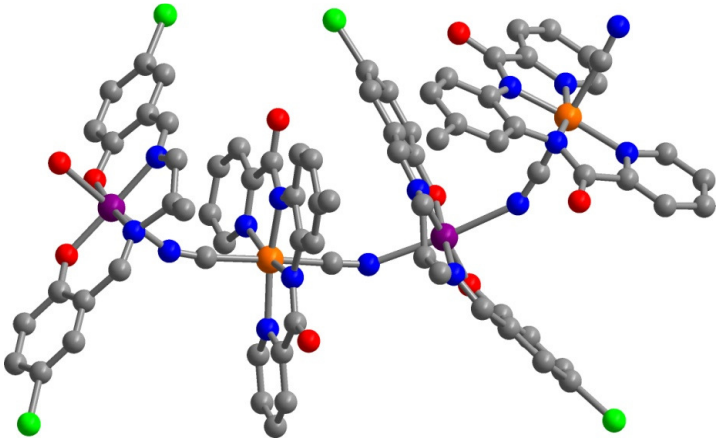


Figure 1.13. Crystal structure of the arch-like tetranuclear cluster $(bpmb)_2(Clsalpn)_2Mn^{III}{}_2Fe^{III}{}_2(CN)_4$. Orange, purple, green, red, blue, and gray spheres represent Fe, Mn, Cl, O, N, and C atoms, respectively; H atoms are omitted for clarity.

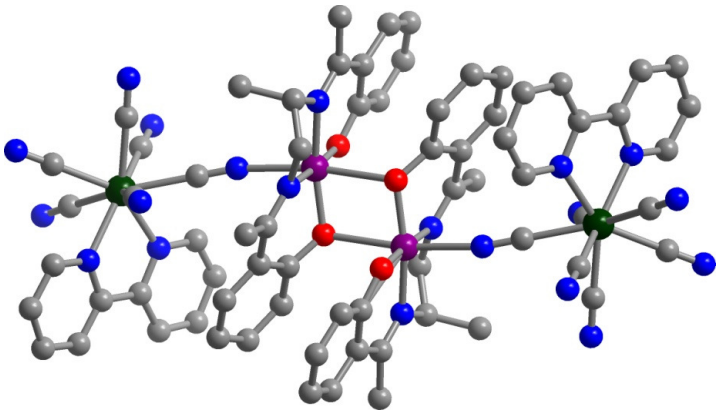


Figure 1.14. Crystal structure of the tetranuclear cluster $(bpy)_2L_2Mn^{III}{}_2W^{V}{}_2(CN)_{12}$. Dark green, purple, red, blue, and gray spheres represent W, Mn, O, N, and C atoms, respectively; H atoms are omitted for clarity.

propylenebis(2-hydroxyacetophenylideneaminato) dianion) with $[W(bpy)(CN)_6]^-$ (see Figure 1.6) leads to the formation of just such a complex, $(bpy)_2L_2Mn^{III}{}_2W^{V}{}_2(CN)_{12}$.[125] During the reaction, the coordinated water molecule on each Mn^{III} center is displaced by the nitrogen end of one cyanide from each $[W(bpy)(CN)_6]^-$ unit, while the other five cyanide ligands remain terminal (see Figure 1.14).

Variable-temperature dc susceptibility measurements revealed that both the $W^V\cdots Mn^{III}$ and $Mn^{III}\cdots Mn^{III}$ interactions are ferromagnetic in nature, however both interactions were found to be quite weak, with fits to the $\chi_M T$ vs. T data affording coupling constants of $J_{W\cdots Mn} = +0.83$ cm^{-1} and $J_{Mn\cdots Mn} = +0.95$ cm^{-1}. The ferromagnetic exchange leads to an overall ground state at low temperature of $S = 5$, arising from $S_{Mn} = 2$ and $S_W = {}^1/_2$. Due to the low magnitude of the coupling, however, the spin ground state

is not well isolated from excited states, which led to complications in interpreting magnetization data and thus an inability to extract *D*. Nevertheless, the presence of both elongated Mn^{III} ions and heavy W^{V} centers generates magnetic anisotropy in the cluster, leading to frequency-dependent peaks in the plot of χ_M'' vs. *T*. An Arrhenius fit of the corresponding relaxation times gave a barrier of U_{eff} = 22 cm^{-1}. Notably, the attempt frequency obtained from the Arrhenius fit was found to be $\tau_0 = 5.1 \times 10^{-12}$ s, three orders of magnitude smaller than what is usually observed for single-molecule magnets. This low value may result from the lack of data points in the Arrhenius plot, which includes only three maxima in χ_M''. Since the τ_0 parameter dramatically affects the magnitude of U_{eff}, this barrier must be regarded with some caution.

1.4.2.3 A T-Shaped M_3M' Cluster

Starting with a homoleptic hexacyanometalate complex, one can envision appending to it anywhere between one and six metal complexes, depending on reaction stoichiometry, steric effects, and electronic effects. In certain solvents, the cluster possessing a neutral charge can be thermodynamically favored. Indeed, the assembly reaction between $[Fe(CN)_6]^{3-}$ and $[(salen)Mn(H_2O)]^{+}$ in a mixture of methanol and ethanol generates the tetranuclear cluster $(salen)_3(EtOH)_3Mn^{III}_3Fe^{III}(CN)_6$ as the major product (see Figure 1.15).[127] Here, the central $[Fe(CN)_6]^{3-}$ unit bears three terminal cyanide ligands and three bridging cyanide ligands in a meridional configuration. The bridging cyanide ligands connect the Fe^{III} ion to three $[(salen)Mn(EtOH)]^{+}$ units, where each Mn^{III} ion is bound equatorially by a $salen^{2-}$ ligand with an ethanol molecule occupying the remaining axial coordination site. Notably, the structure of the Mn_3Fe cluster features three distinctly different Mn-N-C bond angles, with mean angles of 148.9(2)°, 161.9(2)°, and 170.7(2)°. The two angles closest to linearity belong to two Mn-N-C linkages oriented trans to one another, with the most bent angle corresponding to the middle Mn-N-C linkage. Such bending likely results from steric conflicts between the bulky $[(salen)Mn(EtOH)]^{+}$ units.

The plot of $\chi_M T$ vs. *T* for the Mn_3Fe cluster shows a downturn with decreasing temperature, which appears at first glance to denote antiferromagnetic coupling between Mn^{III} and Fe^{III} centers. However, owing to the stark differences in Mn-N-C angles present in the cluster, describing the magnetic behavior could not be accomplished in such a simple manner. Indeed, modeling the $\chi_M T$ data required the use of multiple *J* parameters. Here, the exchange parameters corresponding to the two less bent Mn-N-C angles were constrained to be equivalent ($J_1 = J_3$), while the one corresponding to the most bent angle was allowed to vary (J_2). This approach led to a fit that provided exchange constants of $J_1 = J_3$ = -2.8 cm^{-1} and J_2 = +3.3 cm^{-1}. The system can then be considered as possessing a ground state of $S = {}^3/_2$, arising from antiferromagnetic coupling between two Mn^{III} centers (each $S = 2$) and an $S = {}^5/_2$ central unit arising from ferromagnetic coupling between one Mn^{III} ion and the $S = {}^1/_2$ Fe^{III} center. As evident in the above examples, both distorted Mn^{III} and low-spin Fe^{III} ions generate magnetic anisotropy. As such, a plot of χ_M'' vs. *T* obtained for the Mn_3Fe cluster shows the onset of slow magnetic relaxation at low temperature. Notably, this is the lowest spin ground state ($S = {}^3/_2$) for which slow magnetic relaxation has been observed.

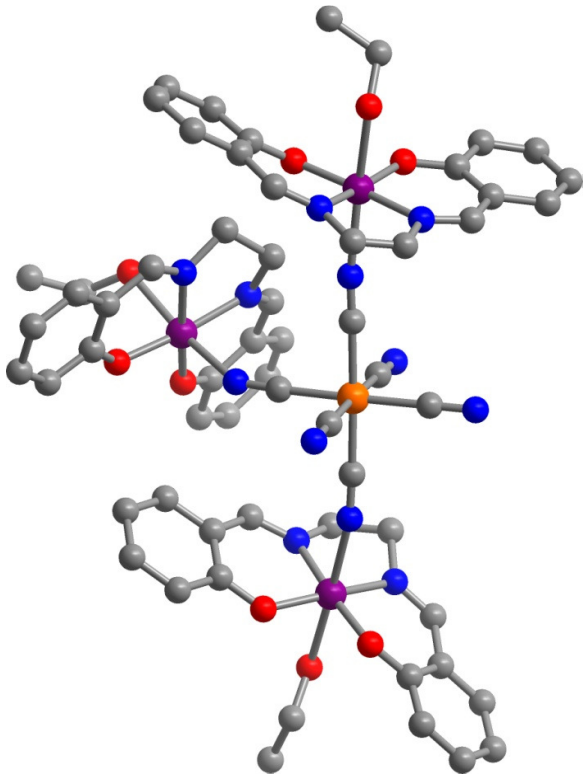


Figure 1.15. Crystal structure of the T-shaped tetranuclear cluster $(salen)_3(EtOH)_3Mn^{III}{}_3Fe^{III}(CN)_6$. Orange, purple, red, blue, and gray spheres represent Fe, Mn, O, N, and C atoms, respectively; H atoms are omitted for clarity.

1.4.2.4 Square $M_2M'_2$ Clusters

As described in Section 1.4.2.1, tetranuclear clusters often take the form of an enclosed square-like $M_2M'_2$ architecture. This type of cluster may be synthesized through a self-assembly reaction according to Equation 1.5:

$$2\,[LM(solv)_2]^{x+} + 2\,\textit{cis}\text{-}[L'M'(CN)_2]^{y-} \longrightarrow [L_2'L_2M_2M'_2(\mu\text{-}CN)_4]^{2(x-y)} \qquad (1.5)$$

Here, an ideal cyanometalate building unit consists of a metal ion featuring two terminal cyanide ligands orientated cis to one another, with the other coordination sites bound by a blocking ligand (see Table 1.2). Two of these units can then act as two opposite corners of the square, with the other two corners comprised of metal centers bearing the nitrogen ends of the cyanide ligands.

Slow magnetic relaxation was realized for a cyano-bridged square in 2005 in the clusters $[Tp^*{}_2(DMF)_8M^{II}{}_2Fe^{III}{}_2(CN)_6]^{2+}$ (Tp^{*-} = hydrotris(3,5-dimethylpyrazol-1-yl)borate, M = Co, Ni).[128] These molecules were assembled from reaction of the anisotropic, $S = {}^1/_2$ complex $[Tp^*Fe(CN)_3]^-$ with $M(SO_3CF_3)_2$. The structure of each square, as depicted in Figure 1.16, consists of two $[Tp^*Fe(CN)_3]^-$ units occupying

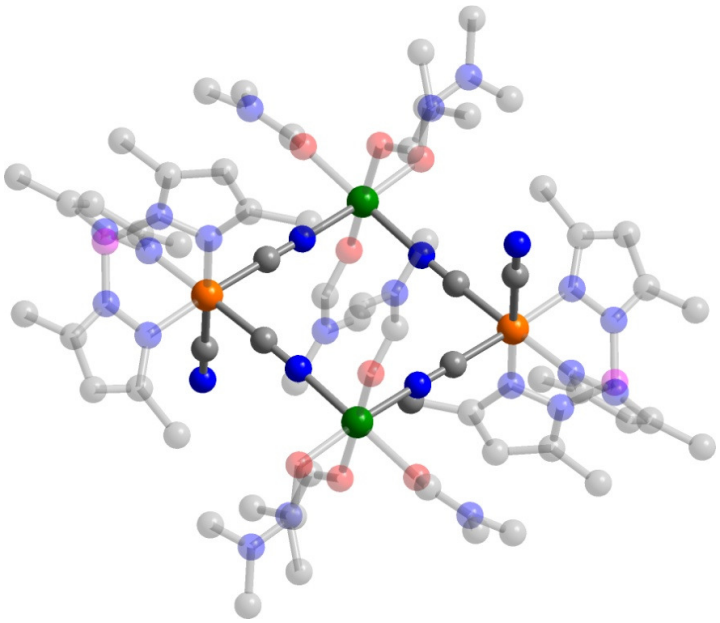


Figure 1.16. Crystal structure of the square tetranuclear cluster $[Tp^*_2(DMF)_8Ni^{II}_2Fe^{III}_2(CN)_6]^{2+}$. Orange, green, magenta, red, blue, and gray spheres represent Fe, Ni, O, N, and C atoms, respectively; H atoms are omitted for clarity. The Tp^{*-} ligands are transparent for better visualization of the cluster core.

opposite corners, bridged through cyanide to M^{II} centers residing at the remaining two corners. The coordination environment of each Fe^{III} center approximates an octahedron, with a face being blocked by a Tp^{*-} ligand, two bridging cis cyanide ligands, and one terminal cyanide ligand. Likewise, the M^{II} ion resides in an octahedral coordination geometry, with two cis sites ligated to bridging cyanide ligands and the other four bound by DMF ligands. The two terminal cyanide ligands in each cluster project out of the M_2Fe_2 plane in opposite directions relative to one another.

Variable-temperature dc susceptibility measurements on the M_2Fe_2 clusters revealed the presence of antiferromagnetic interactions between Co^{II} ($t_{2g}^4e_g^2$) and Fe^{III} (t_{2g}^5) centers, and ferromagnetic interactions between Ni^{II} ($t_{2g}^6e_g^2$) and Fe^{III} centers, as expected based on orbital considerations, giving rise to ground states of S = 2 and 3, respectively. Fits to these plots provided exchange constants of J = -10 (Co) and +5.3 (Ni) cm^{-1}. Additionally, low-temperature magnetization measurements for the two compounds demonstrated strong uniaxial anisotropy, with fits to the data giving zero-field splitting parameters of D = -3.04 (Co) and -3.98 (Ni) cm^{-1} (see Figure 1.17). Consistent with the presence of an anisotropy energy barrier, variable-temperature ac susceptibility measurements showed signals for both complexes that shift to higher temperature with increasing frequency. However, a peak maximum can only be observed for the Ni congener, and this maximum is only present above 1.8 K at 997 Hz, thus effective spin-reversal barriers have not been evaluated.

In search of magneto-structural correlations for the Ni_2Fe_2 square topology, a related cluster of the form $[Tp^*_2(bpy)_4Ni^{II}_2Fe^{III}_2(CN)_6]^{2+}$ was prepared by adding 2,2′-

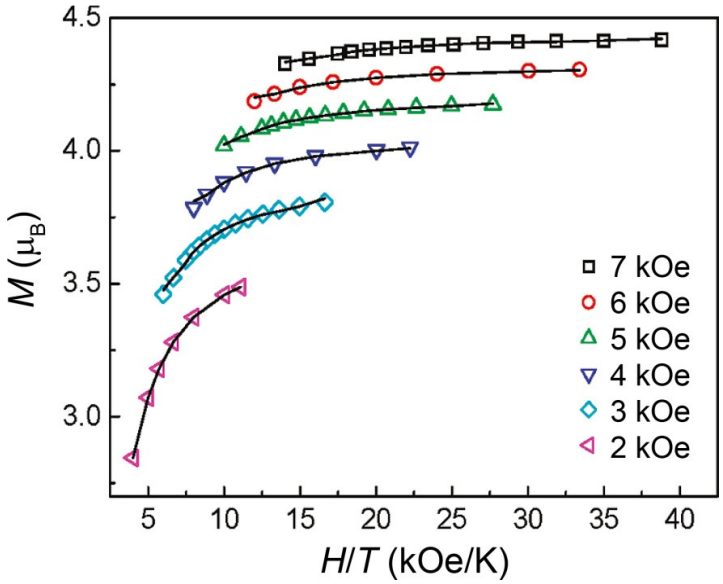


Figure 1.17. Low-temperature magnetization data for the square cluster $[Tp_2L^{S1}{}_8Ni^{II}{}_2Fe^{III}{}_2(CN)_6]^{2+}$. Solid lines represent fits to the data, giving D = -2.85 cm^{-1}. Modified from ref. 129.

bipyridine to a solution containing the $(DMF)_8Ni_2Fe_2$ cluster.[128] The structure of this complex appears very similar to that of the precursor cluster, with the exception that it features significantly more bent Ni-N-C angles (167.1(4)°, compared to 176.9(4)° in the precursor cluster), arising from steric conflicts between Tp* and bpy ligands. This bending results in a distortion of the $Ni_2Fe_2(CN)_4$ core from planarity. Nevertheless, this structural distortion does not lead to a significant change in the magnetic properties, with a fit to the $\chi_M T$ data gave J = +6.5(2) cm^{-1}. The peaks in the plot of χ_M'' vs. T do shift to slightly higher temperature, however, enabling access to relaxation times at various frequencies and thus providing a spin-reversal barrier of U_{eff} = 14 cm^{-1}.

Recent work has led to the formation of two new Ni_2Fe_2 square clusters of formulae $[Tp_2L^{S1}{}_8Ni^{II}{}_2Fe^{III}{}_2(CN)_6]^{2+}$ (L^{S1} = 4,5-[1′,4′]dithiino[2′,3′-*b*]quinoxaline-2-bis(2-pyridyl)methylene-1,3-dithiole) and $[(^{i}BuTp)_2L^{S3}{}_8Ni^{II}{}_2Fe^{III}{}_2(CN)_6]^{2+}$ ($^{i}BuTp^{-}$ = 2-methylpropyltris(pyrazol-1-yl)borate, L^{S3} = dimethyl 2-(di(pyridin-2-yl)methylene)-1,3-dithiole-4,5-dicarboxylate).[129] Here, dithiole ligands were employed as blocking ligands on the Ni^{II} ions, as molecules featuring such ligands have been implicated in applications such as molecular conductors. The structures of these clusters resemble the squares discussed above. Each Ni^{II} ion resides in distorted octahedral coordination environment, bound to two bridging cyanide ligands and two bidentate blocking ligands.

Variable-temperature dc susceptibility measurements conducted on the two clusters revealed the expected presence of ferromagnetic coupling to give rise to S = 3 ground states. Fits to the data gave coupling constants of J = +4.3 and +4.2 cm^{-1} for the Tp- and ^{i}BuTp-substituted clusters, respectively. In addition, fits to plots of reduced magnetization showed uniaxial zero-field splitting, with D = -2.85 and -3.04 cm^{-1}, respectively. Consistent with these observations, plots of χ_M'' vs. T constructed for the two complexes showed frequency-dependent peaks. Finally, Arrhenius fits to the

relaxation times extracted from these plots afforded spin-reversal barriers of U_{eff} = 6.0 and 9.4 cm^{-1}, respectively.

1.4.3 Pentanuclear Clusters

1.4.3.1 Star-Like M_4M' Clusters

Inspection of Table 1.1 reveals dozens of paramagnetic homoleptic cyanometalate complexes. These complexes are particularly well-suited to act as building units for generating high-spin, high-nuclearity magnetic clusters, as each terminal cyanide ligand is capable of displacing a labile ligand on a secondary metal complex, thereby generating multiple M-CN-M′ linkages. Moreover, the range of available metals within this set of building units enables fine-tuning of magnetic parameters, such as *S*, *D*, and *J*. This simple type of assembly reaction proceeds as shown in Equation 1.6:

$$m\,[\mathrm{LM\,(solv)}]^{x+} + [\mathrm{M'(CN)}_n]^{y-} \longrightarrow [\mathrm{L}_m\mathrm{M}_m\mathrm{M'(CN)}_n]^{mx-y} \qquad (1.6)$$

As described in Section 1.2.4, this type of reaction can produce structures of various nuclearity, depending on reaction conditions and the electronic and steric effects of the building units. This general synthetic route has led to the formation of many high-nuclearity M_nM' (n = 4-6) clusters over the years.[130,131,132] Despite this effort, until recently no clusters of this type demonstrated slow magnetic relaxation. This is in large part due to the lack of magnetic anisotropy associated with the clusters. For instance, the common building unit $[Cr(CN)_6]^{3-}$ features an isotropic spin ground state, such that clusters assembled around this complex are very unlikely to function as single-molecule magnets. Moreover, many of these clusters possess M_6M'-type structures, thus the O_h symmetry of the molecule promotes cancellation of the anisotropy axes. Nevertheless, recent work has uncovered a series of M_4M' clusters derived from the complex $[Re(CN)_7]^{3-}$.[5d,133] This building unit features a highly anisotropic $^2E_1''$ electronic ground state, owing to the low-symmetry pentagonal bipyramidal coordination and spin-orbit coupling associated with rhenium (see Figure 1.6). Indeed, the anisotropy of the $S = {}^1/_2$ spin ground state was confirmed through EPR measurements, which give $g_\parallel = 3.66$ and $g_\perp = 1.59$.[41] Reaction of $[Re(CN)_7]^{3-}$ with four equivalents of $[(PY5Me_2)Mn(MeCN)]^{2+}$ ($PY5Me_2$ is the pentadentate blocking ligand 2,6-bis(1,1-bis(2-pyridyl)ethyl)pyridine) at -40 °C affords the cluster $[(PY5Me_2)_4Mn_4Re(CN)_7]^{5+}$.[5d] Notably, this reaction and subsequent crystallization must be carried out at low temperature in order to forestall a spontaneous, solvent-assisted reduction of Re^{IV} ($S = {}^1/_2$) to Re^{III} ($S = 0$) within the cluster. The structure of the Mn_4Re cluster consists of a central $[Re(CN)_7]^{3-}$ unit, connected through cyanide bridges to four $[(PY5Me_2)Mn]^{2+}$ moieties (see Figure 1.18). The four Mn^{II} centers constitute a distorted square arrangement, with two units bound by axial cyanide ligands and two bound by non-neighboring equatorial cyanide ligands.

Variable-temperature dc susceptibility data collected for the Mn_4Re cluster revealed the presence of ferromagnetic intracluster coupling between high-spin Mn^{II} ($S = {}^5/_2$) and low-spin D_{5h} Re^{IV} ($S = {}^1/_2$) centers, giving rise to an $S = {}^{21}/_2$ ground state. A fit to the $\chi_M T$ data gave a coupling constant of J = +2.3 cm^{-1}. As expected for a cluster incorporating a highly anisotropic $[Re(CN)_7]^{3-}$ unit, magnetization measurements showed a zero-field splitting parameter of D = -0.44 cm^{-1}. Indeed, the presence of an anisotropic *S*

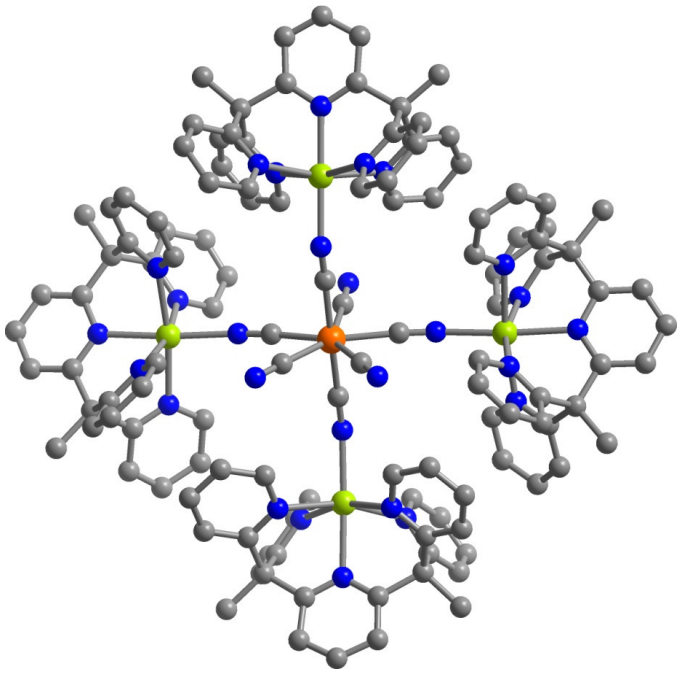


Figure 1.18. Crystal structure of the pentanuclear cluster $[(PY5Me_2)_4Mn^{II}_4Re^{IV}(CN)_7]^{4+}$. Orange, lime, blue, and gray spheres represent Re, Mn, N, and C atoms, respectively; H atoms are omitted for clarity.

= $^{21}/_2$ ground state is evident in the temperature dependence of the out-of-phase magnetic susceptibility, which shows a series of frequency-dependent peaks (see Figure 1.19). An Arrhenius fit to the relaxation times extracted from this plot gives a spin-reversal barrier of U_{eff} = 33 cm^{-1}, the highest yet observed for a cyano-bridged single-molecule magnet. The presence of such a large barrier emphasizes the utility of a building block approach in designing magnetic clusters, as it directly resulted from a predesigned, directed structure featuring a high-anisotropy metal ion coupled to multiple high-spin metal centers.

The proclivity toward spontaneous reduction of the Re^{IV} ion in the Mn_4Re cluster stems from the transfer of electron density from the Re^{IV} center toward the pendant $[(PY5Me_2)Mn]^{2+}$ groups during cluster formation, thereby destabilizing the +4 oxidation state. One solution to this problem is to replace the Mn^{II} ion with a more electron-rich metal ion in order to lessen the destabilization of the Re^{IV} ion. Indeed, the analogous cluster $[(PY5Me_2)_4Ni_4Re(CN)_7]^{5+}$ is stable toward reduction at room temperature.[133] Here, some spin is sacrificed in moving from Mn^{II} ($S = {}^5/_2$) to Ni^{II} (S = 1). As expected for superexchange between this metal combination, the magnetic susceptibility indicate ferromagnetic coupling (J = +4.4 cm^{-1}) and a resulting $S = {}^9/_2$ ground state at low temperature. The presence of a central $[Re(CN)_7]^{3-}$ unit imparts significant anisotropy to the cluster, as evidenced by a fit to the reduced magnetization data giving a zero-field splitting parameter of D = -0.93 cm^{-1}. Indeed, ac susceptibility measurements revealed single-molecule magnet behavior, with a spin-reversal barrier of U_{eff} = 17 cm^{-1}.

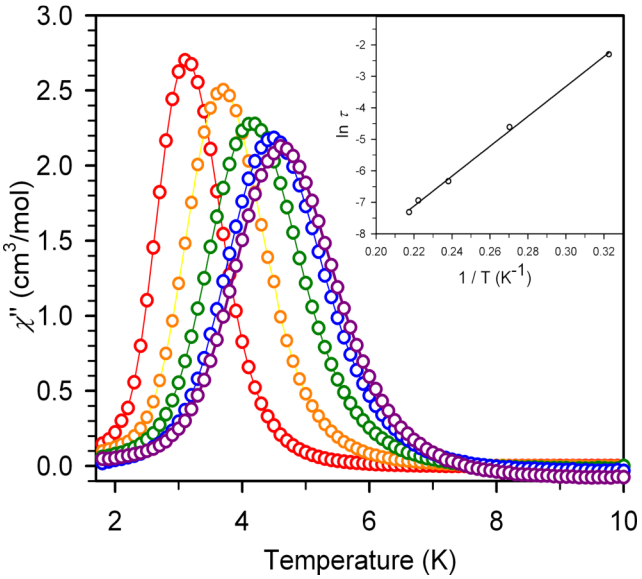


Figure 1.19. Variable-temperature out-of-phase ac magnetic susceptibility for $[(PY5Me_2)_4Mn^{II}_4Re^{IV}(CN)_7]^{4+}$, collected at switching frequencies of 1 (red), 10 (orange), 500 (green), 1030 (blue), and 1488 (purple) Hz. Inset: Arrhenius plot affording U_{eff} = 33 cm^{-1}. Taken from ref. 5d.

1.4.3.2 Trigonal Bipyramidal $M_3M'_2$ Clusters

Along with the four-point star clusters, trigonal bipyramidal $M_3M'_2$ clusters have received the most attention of the pentanuclear complexes. Such molecules are readily accessed through the general assembly reaction shown in Equation 1.7:

$$3\ [LM(solv)_2]^{x+} + 2\ [(\textit{fac}\text{-}L')M'(CN)_3]^{y-} \longrightarrow [L_2'L_3M_3M'_2(\mu\text{-}CN)_6]^{3x-2y} \quad (1.7)$$

Here, the coordination environment of the cyanometalate building unit features three terminal cyanide ligands and a face-capping ligand. Similarly, the secondary metal complex features a blocking ligand that leaves two sites available for coordination by bridging cyanide ligands. We note that such a reaction could also entail the use of a cis-dicyanometalate complex and with a metal complex featuring three accessible coordination sites, however the former combination lends itself to a more extensive library of building units. The first instance of single-molecule magnet behavior in a trigonal bipyramidal complex was reported for the cluster $(tmphen)_6Mn^{II}_3Mn^{III}_2(CN)_{12}$ (tmphen = 3,4,7,8-tetramethyl-1,10-phenanthroline), generated through the assembly reaction of $[Mn(CN)_6]^{3-}$ and $(tmphen)_2Mn(NO_3)_2$.[134] As depicted in Figure 1.20, the structure of this molecule consists of a trigonal bipyramid with the axial positions of the bipyramid occupied by $[Mn(CN)_6]^{3-}$ units, each of which is bridged through three cyanide ligands to $[(tmphen)_2Mn]^{2+}$ units situated at the corners of the trigonal plane.

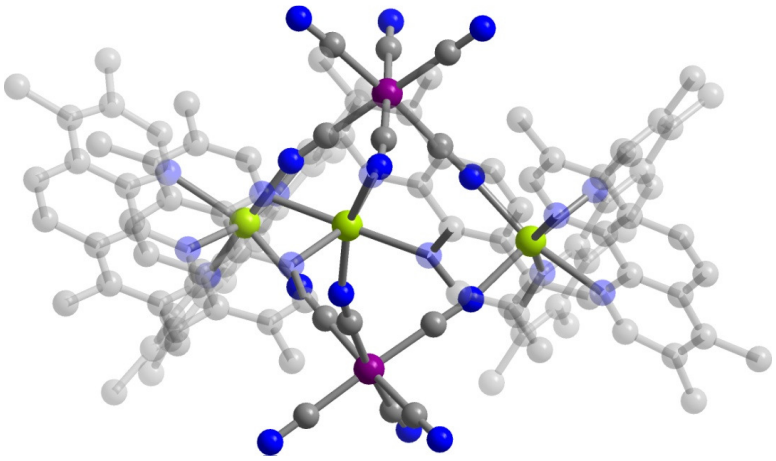


Figure 1.20. Crystal structure of the pentanuclear cluster $(tmphen)_6Mn^{II}_3Mn^{III}_2(CN)_{12}$. Purple, lime, blue, and gray spheres represent Mn^{III}, Mn^{II}, N, and C ions/atoms, respectively; H atoms are omitted for clarity.

Variable-temperature dc susceptibility data collected for the $Mn^{II}_3Mn^{III}_2$ cluster revealed the presence of antiferromagnetic coupling, as expected between low-spin Mn^{III} (t_{2g}^4) and high-spin Mn^{II} ($t_{2g}^3e_g^2$) ions. These data, in conjunction with variable-temperature magnetization data obtained at various fields, confirmed the expected ground state of $S = {}^{11}/_2$. In addition, a fit to the magnetization data provided a zero-field splitting parameter of $D = -0.348$ cm^{-1}. Consistent the presence of uniaxial anisotropy and high-spin ground state, a plot of χ_M'' vs. T showed the onset of slow magnetic relaxation at temperatures down to 1.8 K and frequencies up to 1000 Hz.

Two examples of single-molecule magnets exhibiting the trigonal bipyramidal topology have incorporated the anisotropic complex $[TpFe(CN)_3]^-$, whose substituted variants have been employed in the formation of several other single-molecule magnets, as described above (see Figure 1.6). Reaction of $[TpFe(CN)_3]^-$ with $[(Me_3tacn)Cu(H_2O)_2]^{2+}$ yields the cluster complex $[Tp_2(Me_3tacn)_3Cu^{II}_3Fe^{III}_2(CN)_6]^{4+}$, whose structure consists of a trigonal bipyramidal core comprised of two opposing $[TpFe(CN)_3]^-$ units connected through a trigonal plane composed of three $[(Me_3tacn)Cu]^{2+}$ units, where each Cu^{II} ion resides in a square pyramidal geometry (see Figure 1.9, right).[114]

Variable-temperature dc susceptibility measurements on the Cu_3Fe_2 cluster confirmed the presence of the expected ferromagnetic coupling between low-spin Fe^{III} (t_{2g}^5) and Cu^{II} ($e^4b_2^2b_1^2a_1^1$) centers, giving rise to an $S = {}^5/_2$ ground state at low temperature. Remarkably, magnetization measurements revealed a zero-field splitting parameter of $D = -5.7$ cm^{-1} for this cluster, stemming from a combination of anisotropic low-spin Fe^{III} ions and a low core symmetry of D_{3h}. Indeed, the same combination of metal ions within a cubic Cu_6Fe_8 cluster, with a core symmetry of O_h, leads to a dramatic reduction in the zero-field splitting parameter of $D = -0.16$ cm^{-1}. Despite the relatively small spin ground state of the cluster, the presence of such strong anisotropy leads to significant single-molecule magnet behavior, with ac susceptibility measurements giving

a spin-reversal barrier of U_{eff} = 16 cm^{-1}. While this barrier falls into the top 20% of those yet observed for cyano-bridged complexes, it nonetheless falls well short of the predicted value of U = 34 cm^{-1}, which suggests the presence of significant quantum tunneling effects. This may stem in part from the low spin ground state of the cluster, as tunneling rate increasing with decreasing spin.

The observation of such a large zero-field splitting in the Cu_3Fe_2 cluster highlights the promise of similar architectures, where the Cu^{II} ion has been replaced by a higher-spin metal ion, as single-molecule magnets. This possibility led to the formation of the related cluster $[Tp_2(cyclen)_3Ni^{II}_3Fe^{III}_2(CN)_6]^{4+}$ (cyclen = 1,4,7,10-tetraazacyclododecane), which features ferromagnetic exchange between Fe^{III} and S = 1 Ni^{II} centers and a resulting S = 4 ground state.[113] Unfortunately, this increase in spin relative to the Cu_3Fe_2 cluster is partially offset by a decrease in the zero-field splitting parameter to D = -2.6 cm^{-1}.[135] Thus, the overall barrier was found to decrease, with the plot of χ_M'' vs. T showing only the onset of slow relaxation at 1.8 K and 1488 Hz. As in the case of the Cu_3Fe_2 cluster, tunneling appears to be a facile process here, as S and D values predict a barrier of 42 cm^{-1}. While this metal substitution did not lead to the desired increase in barrier, further substitution using high-spin metal ions such as Mn^{II} may ultimately lead to realization of higher barriers within this topology.

1.4.4 Hexanuclear Clusters

1.4.4.1 An Extended Square $M_4M'_2$ Cluster

In cyano-bridged cluster chemistry, hexanuclear clusters are rare.[131,136] In fact, only one example of a hexanuclear cyano-bridged single-molecule magnet has appeared in the literature.[137] This complex, $(tptz)_4(MeOH)_4(DMF)_2(NO_3)_2Mn^{II}_4W^{V}_2(CN)_{16}$ (tptz = 2,4,6-tris(2-pyridyl)-1,3,5-triazine), can be described as an extended molecular square, where the core square consists of $[W(CN)_8]^{3-}$ units at opposing corners, bridged through cyanide to $[(tptz)Mn(MeOH)(DMF)]^{2+}$ units positioned at the other two corners (See Figure 1.21). At each W^V center, in addition to the two cyanides connected to the Mn^{II} ions within the square, a third bridging cyanide connects to a pendant $[(tptz)Mn(MeOH)(NO_3)]^+$ unit.

Variable-temperature dc susceptibility data collected for the Mn_4W_2 cluster revealed the presence of antiferromagnetic coupling, as expected between high-spin Mn^{II} and W^V ions, with a fit to the $\chi_M T$ data giving J = -6.1 cm^{-1}. These data, in conjunction with a fit of the variable-field magnetization data to the Brillouin function, confirm the anticipated S = 9 ground state. A variable-temperature ac susceptibility measurement showed no signal in χ_M'' in the absence of an applied field. However, upon conducting the measurement under an applied dc field of 1000 Oe, a set of frequency-dependent peaks appeared, corresponding to a spin-reversal barrier of U_{eff} = 6.1 cm^{-1}. Furthermore, upon increasing the magnitude of the dc field, the peaks shifted to higher temperatures and thus demonstrated higher relaxation barriers. A linear fit to the plot of variable-field relaxation barriers was extrapolated to H = 0, giving a zero-field barrier of U_{eff} = 1.6 cm^{-1}. The field dependence of the relaxation was ascribed to a quenching of the thermally-activated relaxation by a fast relaxation process, possibly quantum tunneling of the magnetization, at zero-applied field. If tunneling is responsible for a shortcutting of the relaxation barrier at zero-field due to near-degeneracy of the $\pm M_S$ levels, then application

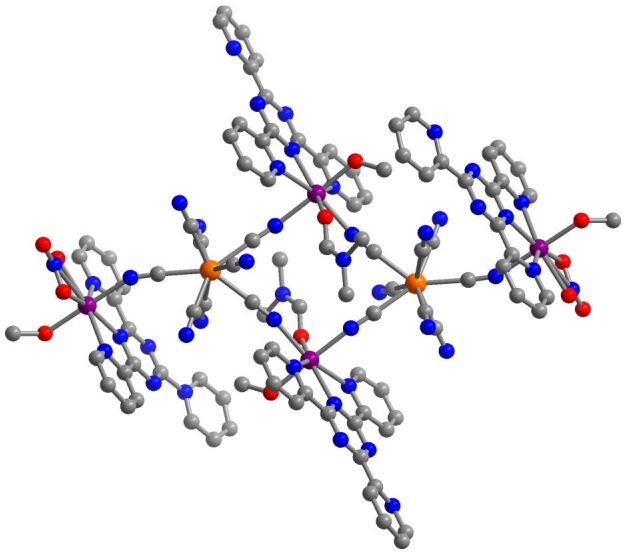


Figure 1.21. Crystal structure of the hexanuclear cluster $(tptz)_4(CH_3OH)_4(DMF)_2(NO_3)_2Mn^{II}_4W^{V}_2(CN)_{16}$. Orange, purple, red, blue, and gray spheres represent W, Mn, N, and C atoms, respectively; H atoms are omitted for clarity.

of a dc field will remove that degeneracy, thereby diminishing the tunneling and slowing the magnetic relaxation.

1.4.5 Heptanuclear Clusters

1.4.5.1 A Trigonal Prismatic MM'_6 Cluster

The tremendous effort directed toward constructing clusters from homoleptic hexacyanometalate building units has resulted in the generation of numerous clusters of the form $[L_6M_6M'(CN)_6]$, where each terminal cyanide ligand from the precursor complex now acts as a bridge.[132] Despite the large number of molecules of this type, however, to date no structurally-characterized example of an M_6M' cluster has been shown to exhibit slow magnetic relaxation.[138] The absence of single-molecule magnets from this class likely stems from a number of factors, such as high molecular symmetry, single-ion magnetic isotropy of the constituent metal complexes, and weak exchange coupling arising from the bent M-CN-M′ linkages necessary to accommodate six pendant metal complexes. Indeed, only two examples of heptanuclear cyano-bridged single-molecule magnets have been observed, with both instances involving clusters with molecule symmetry lower than O_h. The first example of such behavior in a cyano-bridged molecule was observed in the trigonal prismatic complex $[(Me_3tacn)_6MnMo_6(CN)_{18}]^{2+}$.[139] The structure of this cluster, depicted in Figure 1.22, consists of a central Mn^{II} ion, coordinated to the nitrogen ends of six bridging cyanide ligands to $(Me_3tacn)Mo(CN)_3$ units. The two parallel trigonal faces arising from the six Mo^{III} ions approximate a trigonal prism, with the faces twisted about the 3-fold axis 22.6° away from the fully eclipsed position.

Variable-temperature dc susceptibility data collected for the $MnMo_6$ cluster demonstrated the presence of antiferromagnetic coupling, as expected for an interaction

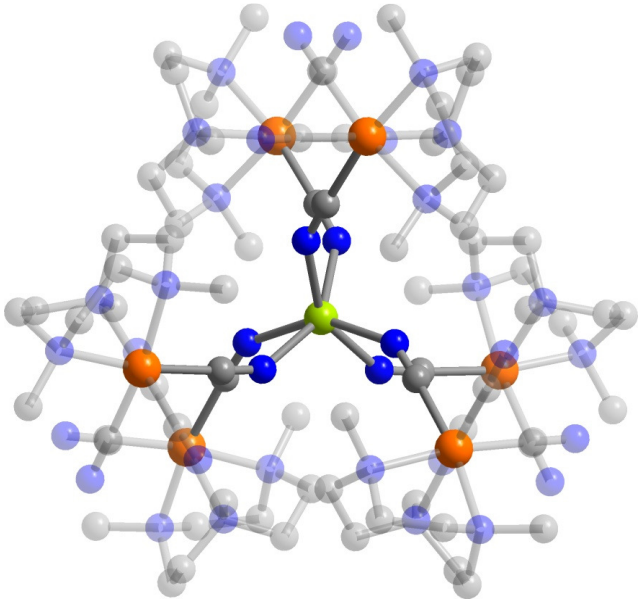


Figure 22. Crystal structure of the heptanuclear cluster $[(Me_3tacn)_6Mn^{II}Mo^{III}_6(CN)_{18}]^{2+}$, viewed along the D_3 axis. Orange, lime, red, blue, and gray spheres represent Mo, Mn, N, and C atoms, respectively; H atoms are omitted for clarity.

between a high-spin Mn^{II} ion ($t_{2g}^3e_g^2$) Mo^{III} ions (t_{2g}^3), giving rise to a spin ground state at low temperature of $S = {}^{13}/_2$. Notably, the exchange constant of J = -6.7 cm^{-1}, obtained from a fit of the $\chi_M T$ vs. T data, represents a greater than two-fold increase over the analogous $MnCr_6$ cluster.[140] This substantial boost is a direct result of the radial extension of the d orbitals in traversing the periodic table from Cr^{III} down to Mo^{III}. Additionally, a fit to the low-temperature magnetization data for the $MnMo_6$ cluster provided a zero-field splitting parameter of D = -0.33 cm^{-1}. This anisotropy likely arises from a combination of spin-orbit coupling within the Mo^{III} ions and an overall molecular shape approximating D_3 symmetry. Indeed, the presence of magnetic anisotropy and a large spin ground state is echoed by the χ_M'' vs. T data, which show frequency-dependent peaks corresponding to an effective spin-reversal barrier of U_{eff} = 10 cm^{-1}.

1.4.5.2 A C_3-Symmetric M_6M' Cluster

Another strategy to introduce anisotropy and slow magnetic relaxation into a heptanuclear cluster involves the perturbation of an M_6M' arrangement from O_h symmetry through use of a trinucleating blocking ligand, which can serve to contract each M_3 face of the octahedron. Indeed, the success of this method was demonstrated in the cluster $[(talen^{tBu_2})_2Mn^{III}_6Cr^{III}(CN)_6]^{3+}$ ($talen^{tBu\ 6-}$ = 2,4,6-tris(1-(2-salicylaldimino-2-methylpropylimino)-ethyl)-1,3,5-trihydroxybenzene hexanion).[141] The structure of this molecule consists of a central Cr^{III} ion bridged through cyanide to six peripheral Mn^{III} centers (see Figure 1.23). Each Mn^{III} ion resides in a square pyramidal coordination environment, with the bridging cyanide binding the apical site one of three N_2O_2 pockets of the $talen^{tBu_2\ 6-}$ ligand occupying the equatorial plane. Importantly, one $talen^{tBu_2\ 6-}$

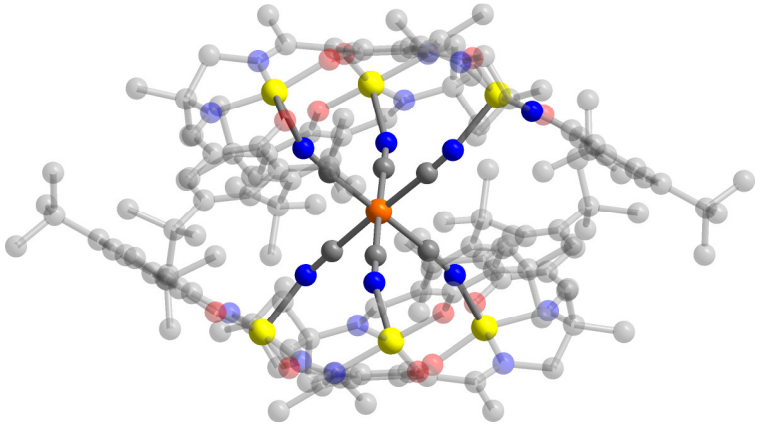


Figure 1.23. Crystal structure of the heptanuclear cluster $[(\text{talen}^{t\text{Bu}2})_2\text{Mn}^{\text{III}}_6\text{Cr}^{\text{III}}(\text{CN})_6]^{3+}$. Orange, yellow, red, blue, and gray spheres represent Mo, Mn, N, and C atoms, respectively; H atoms and weakly-coordinated solvent molecules are omitted for clarity.

ligand, which has been described as a triple salen unit, encapsulates each Mn^{III}_3 face of the cluster. The presence of this trinucleating ligand distorts the Mn-Cr-Mn angles and leads to an overall molecular symmetry of C_{3v}.

Variable-temperature dc susceptibility data collected for the Mn_6Cr cluster indicate the presence of antiferromagnetic coupling between Mn^{III} and Cr^{III} centers, giving rise to an overall $S = {}^{21}/_2$ ground state. Fits to the provided an exchange constant of J = -5.0 cm^{-1}. Additionally, the fit indicated the presence of an additional antiferromagnetic interaction, J' = -1.03 cm^{-1}, between intrafacial Mn^{III} ions. Ac susceptibility measurements showed a set of frequency-dependent peaks in the plot of χ_{M}'' vs. T, with a corresponding spin-reversal barrier of U_{eff} = 18 cm^{-1}. In addition, the variable-field magnetization data showed hysteresis below 1.5 K. Indeed, the presence of slow magnetic relaxation in this cluster demonstrates the utility in decreasing molecular symmetry from O_h to C_{3v}.

1.4.6 Higher-Nuclearity Clusters

1.4.6.1 Simple Cubic $\text{M}_4\text{M}'_4$ Clusters

As discussed in Section 1.4.2.4, a cyanometalate complex featuring two terminal cyanide ligands in a cis configuration acts as an ideal building unit for a molecule square, where each cyanometalate unit occupies a corner of the square. Along these lines, one can envision the employment of a *fac*-tricyanometalate complex as the precursor for a molecule cube. Additionally, the secondary metal complex also bears only three facially oriented sites accessible to the nitrogen end of a cyanide ligand. An assembly reaction of this type proceeds according to the reaction depicted in Equation 1.8:

$$4\,[(\textit{fac}\text{-L})\text{M}(\text{solv})_3]^{x+} + 4\,[(\textit{fac}\text{-L}')\text{M}'(\text{CN})_3]^{y-} \longrightarrow [\text{L}'_4\text{L}_4\text{M}_4\text{M}'_4(\mu\text{-CN})_{12}]^{4(x-y)} \quad (1.8)$$

This synthetic strategy has found use in the assembly of numerous cyano-bridged cubic clusters,[142] and its utility in generating a single-molecule magnet was first demonstrated

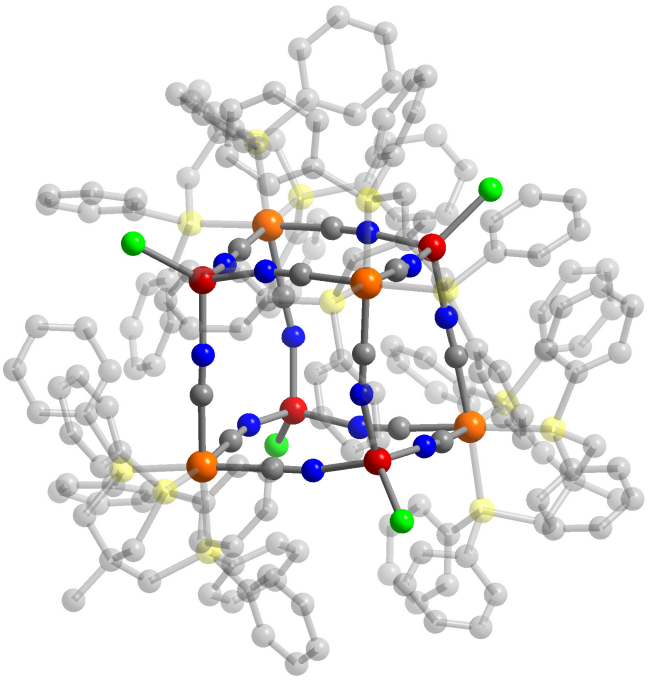


Figure 1.24. Crystal structure of the octanuclear cubic cluster $(triphos)_4Cl_4Mn^{II}{}_4Re^{II}{}_4(CN)_{12}$. Orange, dark red, green, yellow, blue, and gray spheres represent Re, Mn, Cl, P, N, and C atoms, respectively; H atoms are omitted for clarity. Triphos ligands are transparent for better visualization of the cluster core.

in 2004 with the complex $(triphos)_4Cl_4Mn^{II}{}_4Re^{II}{}_4(CN)_{12}$ (triphos = 1,1,1-tris(diphenylphosphinomethyl)ethane), prepared through reaction of the $S = {}^1/_2$ anisotropic building unit $[(triphos)Re(CN)_3]^-$ with $MnCl_2$.[143] The structure of the Mn_4Re_4 cluster takes the form of a distorted cube, where alternating corners of the cube are composed of $[(triphos)Re(CN)_3]^-$ units bridged through cyanide to $[MnCl]^+$ units at the remaining corners (see Figure 1.24). While the coordination environment of each Re^{II} ion approximates the usual octahedral geometry associated with the corner unit of a molecular cube, each Mn^{II} ion is situated in a distorted tetrahedral environment, bound by three nitrogen ends of bridging cyanide ligands and one terminal chloride ligand. Further emphasizing the degree of structural distortion within the cluster, the twelve Mn-N-C angles are all crystallographically unique, with angles ranging from 161.8(8)-165.5(9)°. Finally, a slight compression of one of the C_3 axes along the body diagonal of the cube is evident, further reducing the molecular symmetry.

Variable-temperature dc susceptibility measurements collected for the Mn_4Re_4 cluster revealed the presence of antiferromagnetic coupling, as expected between low-spin Re^{II} ($t_{2g}{}^5$) and high-spin Mn^{II} ($t_{2g}{}^3e_g{}^2$) ions, giving rise at low temperature to a ground state of $S = 8$. Attempts to fit the low-temperature magnetization measurements to quantify the zero-field splitting of the cluster were unsuccessful, likely a result of low-lying spin states. Nevertheless, ac susceptibility measurements showed the onset of a frequency-dependent signal at low temperature in the plot of χ_M'' vs. T. In order to

quantify this event, high-frequency measurements were performed (5-25 kHz) in order to access peak maxima. From these maxima, relaxation times were extracted, and the corresponding Arrhenius fit gave a spin-reversal barrier of U_{eff} = 8.8 cm^{-1}. To further probe the slow relaxation dynamics of the Mn_4Re_4 cluster, variable-field magnetization data were collected at temperatures down to 0.04 K on a single crystal with its easy magnetic axis aligned parallel to the applied field.[144] The measurements revealed hysteresis loops below 4 K, which were found to become temperature-independent below 0.2 K while remaining highly dependent on field sweep rate down to 0.04 K. Consistent with the temperature independence of the hysteresis below 0.2 K, the hysteresis loops feature a step at H = 0 corresponding to a fast relaxation process such as quantum tunneling.

Following the work with the Mn_4Re_4 complex, a series of Ni_4Fe_4 cubic clusters were prepared from the complex $[(pzTp)Fe(CN)_3]^-$. Reaction of this precursor with $Ni(SO_3CF_3)_2$ and a substituted pyrazolate (pz)-based ligand ^nL (n = 1 = 2,2,2-tris(pyrazol-1-yl)ethanol, n = 2 = $(pz)_3C(CH_2)_6SAc$, n = 3 = $(pz)_3C(CH_2)_{10}SAc$) afforded the compounds $[(pzTp)_4{}^nL_4Ni^{II}{}_4Fe^{III}{}_4(CN)_{12}]^{4+}$.[145,146] The structure of these clusters consists of a simple cube where four $[(pzTp)Fe(CN)_3]^-$ units reside at alternating corners and are bridged through cyanide ligands to four $[^nLNi]^{2+}$ units positioned at the other corners (see Figure 1.25). The coordination environments of both the Fe^{III} and Ni^{II} centers approximate octahedra.

Variable-temperature dc susceptibility measurements collected for the Ni_4Fe_4 clusters confirmed the expected ferromagnetic exchange between low-spin Fe^{III} ($t_{2g}{}^5$) and Ni^{II} ($t_{2g}{}^6e_g{}^2$) centers, leading to a spin ground state at low temperature of S = 6. In addition, low-temperature magnetization measurements demonstrated the presence of magnetic anisotropy, likely arising from the unquenched orbital angular momentum of the Fe^{III} centers, providing zero-field splitting parameters of D = -0.33, -0.35, and -0.33 cm^{-1} for n = 1-3, respectively. Despite the presence of considerable anisotropy and an S = 6 ground state, the plot of χ_M'' vs. T obtained for the $^1L_4Ni_4Fe_4$ cluster in the absence of an applied dc field shows only a weak frequency-independent peak. Upon application of a small applied dc field, however, the plot of χ_M'' vs. ν demonstrates the presence of two frequency-dependent relaxation modes. The source of these independent modes remains unknown. The plots of χ_M'' vs. T obtained for the $^nL_4Ni_4Fe_4$ (n = 2, 3) clusters show the onset of frequency-dependent peaks at temperatures down to 1.8 K and frequencies up to 1500 Hz.

Shortly after the accounts of the foregoing examples of Ni_4Fe_4 cubic clusters, another research group reported the formation and magnetic behavior of the related cluster $Tp_8Ni^{II}{}_4Fe^{III}{}_4(CN)_{12}$, derived from the complex $[TpFe(CN)_3]^-$.[147] The structure of this cluster is analogous to that of the others, with the exception that here both Fe^{III} and Ni^{II} ions are bound by unsubstituted Tp^- ligands. This ligand difference results in an overall neutral charge of the cluster. Magnetic measurements showed intracluster ferromagnetic coupling and a zero-field splitting parameter at low temperature of D = -0.27 cm^{-1}. In addition, the plot of χ_M'' vs. T shows the onset of slow magnetic relaxation at low temperature.

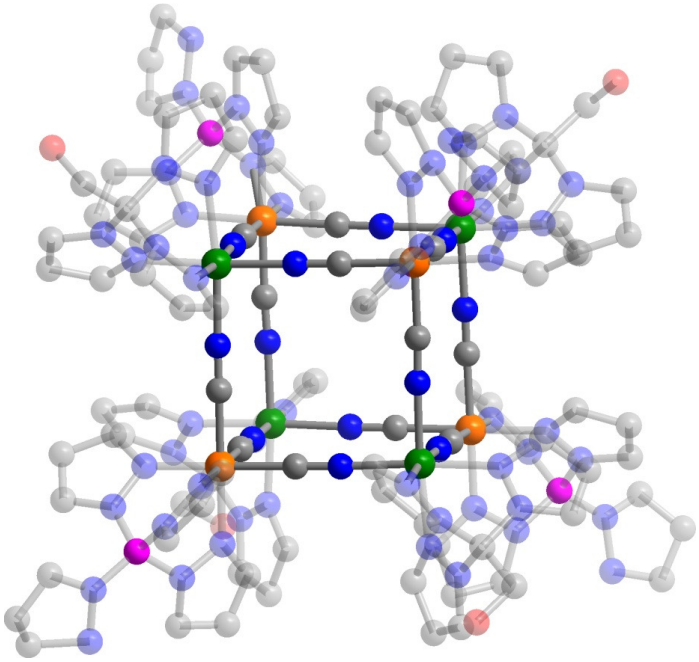


Figure 1.25. Crystal structure of the octanuclear cubic cluster $[(pzTp)_4L_4Ni^{II}_4Fe^{III}_4(CN)_{12}]^{4+}$. Orange, green, magenta, red, blue, and gray spheres represent Fe, Ni, B, O, N, and C atoms, respectively; H atoms are omitted for clarity. Blocking ligands are transparent for better visualization of the cubic core.

1.4.6.2 Face-Centered Cubic $M_6M'_8$ Clusters

As an extension of the $[(fac\text{-}L)M(CN)_3]^{n-}$ precursor methodology, reactions similar to those outlined in Equation 1.8 can be carried out in which only one of the metal reagents is capped with a blocking ligand, according to Equation 1.9:

$$6\,[M(solv)_6]^{x+} + 8\,[(fac\text{-}L')M'(CN)_3]^{y-} \longrightarrow [L'_8M_6M'_8(\mu\text{-}CN)_{24}]^{6x-8y} \qquad (1.9)$$

Such reactions permit cluster growth to propagate beyond the M_8 cage motif. Indeed, reaction of the complex $[TpFe(CN)_3]^-$ with $[Cu(H_2O)_6]^{2+}$ affords the face-centered cubic cluster $[Tp_8(H_2O)_6Cu^{II}_6Fe^{III}_8(CN)_{24}]^{4+}$.[148] The structure of this cluster features a cubic arrangement of eight $[TpFe(CN)_3]^-$ units, connected through cyanide bridges to six Cu^{II} ions, each one situated slightly above the center of each cube face (see Figure 1.9, left). Each Cu^{II} resides in a square pyramidal coordination environment, with four nitrogen-bound cyanide ligands constituting the basal plane and a water molecule bound in the apical position.

Variable-temperature dc susceptibility measurements conducted on the Cu_6Fe_8 cluster revealed the presence of ferromagnetic coupling, as expected for exchange between low-spin Fe^{III} (t_{2g}^5) and square-pyramidal Cu^{II} ($e^4b_2^2b_1^2a_1^1$) centers. These data, along with low-temperature magnetization measurements, confirmed the presence of an $S = 7$ ground state with a coupling constant of $J = +15$ cm^{-1}. The relatively large value of J likely arises from a combination of nearly linear Cu-N-C angles, with a mean angle of

174.8(6)°, along with the positioning of those linkages within the basal plane of the Cu^{II} square pyramid. In addition, the low-temperature magnetization data were fit to give a zero-field splitting parameter of D = -0.16 cm^{-1}. Notably, the analogous Cu_6Cr_8 cluster was found to exhibit no measureable zero-field splitting.[78] This contrasting behavior in the two molecules clearly demonstrates the utility in employing the octahedral Fe^{III} ion, which possesses unquenched orbital angular momentum, over the isotropic Cr^{III} ion, to generate magnetic anisotropy. In line with this discovery of uniaxial magnetic anisotropy within the Cu_6Fe_8 cluster, variable-temperature ac susceptibility measurements revealed the onset of slow magnetic relaxation down to 1.8 K at frequencies up to 1488 Hz.

1.4.6.3 An Extended Trigonal Bipyramidal $M_7M'_2$ Cluster

In addition to the trigonal bipyramidal clusters outlined in Section 1.4.3.2, one can envision use of hexacyanometalate complexes as precursors to be incorporated into the axial positions of the bipyramid. Then, during cluster formation, each $[M(CN)_6]^{x-}$ unit will have three remaining terminal cyanide ligands with which to bind another metal ion.[149] Caution must be taken when using this strategy, however, as the presence of the additional terminal cyanide ligands can result in the formation of undesired extended solids. Nevertheless, reaction of $[Cr(CN)_6]^{3-}$ with (^{i}Prtacn)$NiCl_2$ (^{i}Prtacn = 1,4,7-tris-isopropyl-1,4,7-triazacyclononane) was shown to afford the cluster $[(^i\text{Prtacn})_7Cl_4Ni^{II}_7Cr^{III}_2(CN)_{12}]^{4+}$.[150] The structure of this molecule consists of a central trigonal bipyramid core, with $[Cr(CN)_6]^{3-}$ units in the axial positions bridged through cyanide ligands to $[(^i\text{Prtacn})Ni]^{2+}$ units situated within the trigonal plane (see Figure 1.26). In addition to this Ni_3Cr_2 core, however, two of the three remaining cyanide ligands from each Cr^{III} center bridge two additional pendant $[(^i\text{Prtacn})NiCl]^+$ units. The coordination environment of the core Ni^{II} ions approximates a square pyramid, with two nitrogen-bound bridging cyanide ligands and a tridentate ^{i}Prtacn ligand, while that of the pendant Ni^{II} centers more closely resembles a trigonal pyramidal geometry, with one nitrogen-bound bridging cyanide, one terminal chloride ligand, and a tridentate ^{i}Prtacn ligand comprising the coordination sphere.

Variable-temperature dc susceptibility measurements conducted on the Ni_7Cr_2 cluster showed the presence of ferromagnetic coupling, as expected between Cr^{III} (t_{2g}^3) and Ni^{II} ($t_{2g}^6e_g^2$) ions. However, the maximum in $\chi_M T$ fails to reach even 17 cm^3·mol/K, far below the value of 55 cm^3·mol/K expected for an S = 10 ground state stemming from ferromagnetic coupling between two Cr^{III} and seven Ni^{II} centers. In addition, variable-field magnetization measurements showed a saturation of the magnetization at M = 13.3 μ_B, well below the value of M = 20 μ_B expected for an S = 10 ground state. These unexpected observations in the magnetic behavior led to the conclusion that the Ni^{II} ions constituting the trigonal plane are actually diamagnetic. Thus, the overall molecule can best be described as two isolated $S = {}^7/_2$ Ni_2Cr units. Indeed, this assignment is consistent with the difference in geometry for the two contrasting coordination environments of the Ni^{II} centers.

With the foregoing magnetic analysis in mind, the low-temperature magnetization data were fit to give a zero-field splitting parameter of D = -0.67 cm^{-1}. The source of this anisotropy was not discussed in the report. However, given the absence of any metal ions within the cluster that possess unquenched orbital angular momentum, this anisotropy

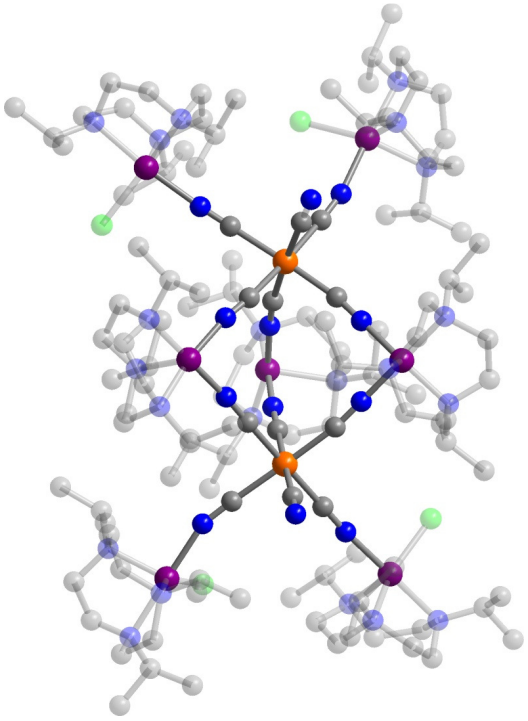


Figure 1.26. Crystal structure of the extended trigonal bipyramidal cluster $[(^{i}\text{Prtacn})_7\text{Cl}_4\text{Ni}^{\text{II}}_7\text{Cr}^{\text{III}}_2(\text{CN})_{12}]^{4+}$. Orange, purple, green, blue, and gray spheres represent Cr, Ni, Cl, N, and C atoms, respectively; H atoms are omitted for clarity. ^{i}Prtacn and Cl^- ligands are transparent for better visualization of the cluster core.

may arise from the structurally distorted Ni^{II} ions. To probe the relaxation dynamics of the cluster, variable-field magnetization measurements were carried out at low temperature on a single crystal with its easy magnetic easy axis oriented parallel to the applied field. This experiment revealed the presence of a hysteresis loop at 0.04 K that was highly dependent on field sweep rate. In addition, a sharp step in the loop was observed at zero-field. These observations suggest the presence of quantum tunneling in the cluster.

1.4.6.4 A Wheel-Like $M_6M'_6$ Cluster

The synthesis of high-nuclearity ring-type complexes is often thwarted by the propensity for growth to propagate and form one-dimensional solids. The largest cyano-bridged molecule of this type is the elliptical wheel-like cluster $(\text{salen})_6(\text{bpmb})_6\text{Mn}^{\text{III}}_6\text{Fe}^{\text{III}}_6(\text{CN})_{12}$, incorporating the building unit $[\text{Fe}(\text{bpmb})(\text{CN})_2]^-$.[113,151] This remarkable molecule is very closely related to the arch-like cluster $(\text{bpmb})_2(\text{Clsalpn})_2\text{Mn}^{\text{III}}_2\text{Fe}^{\text{III}}_2(\text{CN})_4$ (see Section 1.4.2.3), as the two were prepared in an analogous manner. The structure of this cluster consists of alternating $[\text{Fe}(\text{bpmb})(\text{CN})_2]^-$ and $[(\text{salen})\text{Mn}]^+$ units, linked together in a wheel-like topology (see Figure 1.27). Notably, the Mn-N-C angles deviate significantly from linearity (140.8(4)–163.3(5)°), thereby allowing the formation of a wheel rather than a one-dimensional

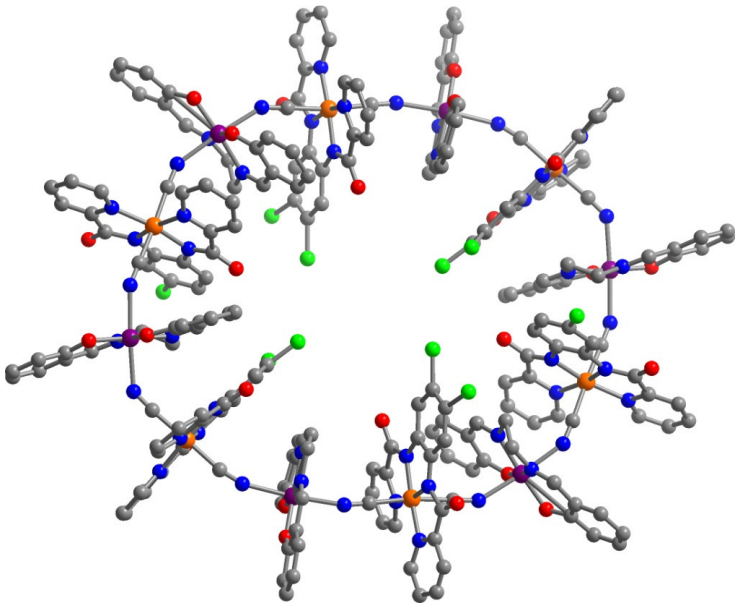


Figure 27. Crystal structure of the dodecanuclear cluster $(bpmb)_6(salen)_6Mn^{III}{}_6Fe^{III}{}_6(CN)_{12}$. Orange, purple, green, red, blue, and gray spheres represent Fe, Mn, Cl, O, N, and C atoms, respectively; H atoms are omitted for clarity.

solid. Indeed, substitution of $[Fe(bpb)(CN)_2]^-$ for $[Fe(bpmb)(CN)_2]^-$ (bpb^{2-} = 1,2-bis(pyridine-2-carboxamido)benzene dianion) results in just such a one-dimensional structure, featuring less bent Mn-N-C angles ranging from 151.8(3)° to 158.6(3)°.

Variable-temperature dc susceptibility measurements conducted on the Mn_6Fe_6 cluster revealed the presence of ferromagnetic coupling between high-spin Mn^{III} ($t_{2g}{}^3e_g{}^1$) and low-spin Fe^{III} ($t_{2g}{}^5$) ions, giving rise to a spin ground state of S = 15. While fitting of the low-temperature magnetization data was complicated by low-lying excited spin states, an approximate zero-field splitting parameter of -0.1 cm^{-1} was provided. In addition, magnetization decay experiments conducted in the temperature 0.04–1 K provided a means through which to directly measure the magnetization relaxation, and the resulting data gave an effective spin-reversal barrier of U_{eff} = 5.8 cm^{-1}.

1.4.6.5 Centered, Face-Capped Octahedral $M_9M'_6$ Clusters

Assembly reactions involving $[M'^{V}(CN)_8]^{3-}$ building units (see Table 1.1) and M^{2+} ions have led to several clusters of the formula $[(ROH)_9M^{II}{}_9M'^{V}{}_6(CN)_{48}]$, according to Equation 1.10:[108,109,152]

$$9\,[M(ROH)_6]^{2+} + 6\,[M'(CN)_8]^{3-} \longrightarrow (ROH)_{24}M^{II}{}_9M'^{V}{}_6(CN)_{48} \qquad (1.10)$$

Despite the O_h symmetry of these clusters, several of them have been shown to behave as single-molecule magnets. The first instance of such behavior was reported in 2005 for the molecules $(MeOH)_{24}Co^{II}{}_9M^{V}{}_6(CN)_{48}$ (M = Mo, W), prepared according to Equation 1.10.[153] The structure of these clusters consists of nine Co^{II} ions arranged in a body-

centered cubic geometry with a $[M^{V}(CN)_8]^{3-}$ unit positioned above each of the six cube faces (see Figure 1.8). The dodecahedral geometry of each $[M^{V}(CN)_8]^{3-}$ unit enables its coordination via cyanide bridges to four facial Co^{II} ions and one Co^{II} ion residing in the center of the cube. The remaining terminal cyanide ligands protrude from the $Co_9M_6(CN)_{30}$ core, which is also capped by three MeOH ligands bound to each corner octahedral Co^{II} unit.

Variable-temperature dc susceptibility data collected for the Mn_9M_6 clusters provided ambiguous information regarding the nature of coupling between Mn^{II} and M^{V} centers. The maximum in $\chi_M T$ occurs closer to that expected for antiferromagnetic coupling than ferromagnetic coupling, however the dip in $\chi_M T$ generally associated with the former type of coupling is not evident. Nevertheless, variable-field magnetization data unambiguously demonstrated the presence of an $S = {}^{21}/_2$ spin ground state, arising from antiferromagnetic coupling between high-spin Mn^{II} ($t_{2g}^3e_g^2$) and M^{V} (t_{2g}^1) centers. While variable-temperature magnetization data collected at multiple applied dc fields revealed the presence of non-superimposable isofield lines, indicative of magnetic anisotropy, no quantitative analysis of the zero-field splitting was performed. However, a recent DFT study on the anisotropy of the two clusters calculated parameters of D = -0.32 (Mo) and -0.36 (W) cm^{-1}.[154] These signs of D are in congruence with plots of χ_M'' vs. T obtained for both clusters, which reveal frequency-dependent signals indicative of slow magnetic relaxation.[153] While the Mo congener only demonstrates the onset of peaks, actual peak maxima were observed for its W counterpart. For the latter, a spin-reversal barrier of U_{eff} = 19 cm^{-1} was obtained from the corresponding Arrhenius fit.

As the Co_9M_6 clusters demonstrate slow magnetic relaxation despite the presence of O_h symmetry, one strategy to increase the relaxation barriers is to reduce the overall molecular symmetry of the molecules. Toward this end, the clusters $(MeOH)_{24}Co^{II}{}_9M^{V}{}_5Re^{V}(CN)_{48}$ were prepared, where one $[M(CN)_8]^{3-}$ unit in each cluster has been replaced by an $S = 0$ $[Re(CN)_8]^{3-}$ unit.[155] This substitution reduces the overall point symmetry of the cluster from O_h to C_{4v}. In the case of the Co_9Mo_5Re cluster, this symmetry reduction did not have a significant effect on the relaxation behavior in comparison to that of the unsubstituted analogue. In the case of the Co_9W_5Re, a dramatic difference was observed upon comparison of the χ_M'' vs. T plots obtained for the unsubstituted and substituted clusters. While the data obtained for the Co_9W_6 cluster showed clear peak maxima, only a rise in χ_M'' was evident for the Co_9W_5Re cluster at low temperature. Thus, lowering the core symmetry of the cluster resulted in a lowering of the spin-reversal barrier rather than the expected raising.

One potential drawback to handling these octahedral $M_9M'_6$ clusters is their propensity to lose coordinated MeOH molecules, giving rise to cluster decomposition and long-range magnetic interactions. To overcome this obstacle, a related molecule of formula $(bpy)_8(H_2O)_8Ni^{II}{}_9W^{V}{}_6(CN)_{48}$ was prepared, where the three MeOH molecules on each M center has been replaced by one H_2O molecule and a bpy ligand.[156] Indeed, these substitutions resulted in a more robust assembly that is stable in air.

Variable-temperature dc susceptibility measurements conducted on the Ni_9W_6 cluster revealed the presence of ferromagnetic coupling, as expected for exchange between Ni^{II} ($t_{2g}^6e_g^2$) and W^{V} (t_{2g}^1) centers, giving rise to an $S = 12$ ground state at low temperature. In addition, variable-temperature ac susceptibility data collected at

Table 1.3. Examples of Cyano-Bridged Single-Molecule Magnets.

complex	S	D (cm^{-1})	U_{eff} (cm^{-1})[a]	ref.
$[(PY5Me_2)_4Mn^{II}{}_4Re^{IV}(CN)_7]^{5+}$ [b]	$^{21}/_2$	-0.44	33	5d
$(bpy)_8(H_2O)_8Ni^{II}{}_9W^{V}{}_6(CN)_{48}$ [c]	12		33[d]	156
$[(5\text{-}Brsalen)_2(H_2O)_2Mn^{III}{}_2Fe^{III}(CN)_6]^{-}$ [e,f]	$^{9}/_2$		25	123
$(bpy)_2L_2Mn^{III}{}_2W^{V}{}_2(CN)_{12}$ [g]	5		22[h]	125
$(MeOH)_{24}Co^{II}{}_9W^{V}{}_6(CN)_{48}$	$^{21}/_2$		19	153
$[(talen^{tBu}{}_2)_2Mn^{III}{}_6Cr(CN)_6]^{3+}$ [i]	$^{21}/_2$		18	141
$[(PY5Me_2)_4Ni^{II}{}_4Re^{IV}(CN)_7]^{5+}$	$^{9}/_2$	-0.93	17	133
$[Tp_2(Me_3tacn)_3Cu^{II}{}_3Fe^{III}{}_2(CN)_6]^{4+}$ [j,k]	$^{5}/_2$	-5.7	16	114
$[(5\text{-}Brsalen)_2(H_2O)_2Mn^{III}{}_2Cr^{III}(CN)_6]^{-}$ [f]	$^{5}/_2$		16	123
$[Tp^*{}_2(bpy)_4Ni^{II}{}_2Fe^{III}{}_2(CN)_6]^{2+}$ [l]	3		14	128
$[(Me_3tacn)_6Mn^{II}Mo^{III}{}_6(CN)_{18}]^{2+}$	$^{13}/_2$	-0.33	10	139
$[(salmen)_2(MeOH)_2Mn^{III}{}_2Fe^{III}(CN)_6]^{-}$ [m]	$^{9}/_2$	-0.85	9.7[n]	112
$[(^{i}BuTp)_2L^{S3}{}_8Ni^{II}{}_2Fe^{III}{}_2(CN)_6]^{2+}$ [o,p]	3	-3.04	9.4	129
$(triphos)_4Cl_4Mn^{II}{}_4Re^{II}{}_4(CN)_{12}$ [q]	8		8.8	143,144
$(pzTp)_2(bpy)_2Ni^{II}Fe^{III}{}_2(CN)_6$ [r]	2		8.3	84
$[Tp_2L^{S1}{}_8Ni^{II}{}_2Fe^{III}{}_2(CN)_6]^{2+}$ [s]	3	-2.85	6.0	129
$(bpmb)_6(salen)_6Mn^{III}{}_6Fe^{III}{}_6(CN)_{12}$ [t,u]	15	-0.1	5.8[v]	113,151
$(tptz)_4(MeOH)_4(DMF)_2(NO_3)_2Mn^{II}{}_4W^{V}{}_2(CN)_{16}$ [w]	9		1.6[x]	137
$[Tp_2(cyclen)_3Ni^{II}{}_3Fe^{III}{}_2(CN)_6]^{4+}$ [y]	4	-2.6		115
$[Tp^*{}_2(DMF)_8Ni^{II}{}_2Fe^{III}{}_2(CN)_6]^{2+}$	3	-3.98		127
$[Tp^*{}_2(DMF)_8Co^{II}{}_2Fe^{III}{}_2(CN)_6]^{2+}$	2	-3.04		127
$(tmphen)_6Mn^{II}{}_3Mn^{III}{}_2(CN)_{12}$ [z]	$^{11}/_2$	-0.348		134
$Tp_8Ni^{II}{}_4Fe^{III}{}_4(CN)_{12}$	6	-0.27		147
$[(PY5Me_2)_4Cu^{II}{}_4Re^{IV}(CN)_7]^{5+}$	$^{5}/_2$	-1.49		133
$[(pzTp)_4(tpm(CH_2OH))_4Ni^{II}{}_4Fe^{III}{}_4(CN)_{12}]^{4+}$ [aa]	6	-0.23		145
$(pzTp)_8(L1)_2Ni^{II}{}_4Fe^{III}{}_4(CN)_{12}$ [bb]	6	-0.24		146
$(pzTp)_8(L2)_2Ni^{II}{}_4Fe^{III}{}_4(CN)_{12}$ [cc]	6	-0.23		146
$[(^{i}Prtacn)_7Cl_4Ni^{II}{}_7Cr^{III}{}_2(CN)_{12}]^{4+}$ [dd,ee]	$^{7}/_2$	-0.67		150
$[Tp_8(H_2O)_6Cu^{II}{}_6Fe^{III}{}_8(CN)_{24}]^{4+}$	7	-0.16		148
$(bpmb)_2(Clsalpn)_2Mn^{III}{}_2Fe^{III}{}_2(CN)_4$ [ff]	5	-0.42		113
$(tmphen)_6(MeOH)_6(H_2O)_6Ni^{II}{}_9W^{V}{}_6(CN)_{48}$	12	-0.039		157
$(MeOH)_{24}Co^{II}{}_9W^{V}{}_5Re^{V}(CN)_{48}$	11			155
$(MeOH)_{24}Co^{II}{}_9Mo^{V}{}_5Re^{V}(CN)_{48}$	11			155
$(MeOH)_{24}Co^{II}{}_9Mo^{V}{}_6(CN)_{48}$	$^{21}/_2$			153
$(salen)_3(EtOH)_3Mn^{III}{}_3Fe^{III}(CN)_6$	$^{3}/_2$			126

[a]Unless otherwise noted, this value was obtained through ac susceptibility measurements. [b]$PY5Me_2$ = 2,6-bis(1,1-bis(2-pyridyl)ethyl)pyridine. [c]bpy = 2,2′-bipyridine. [d]This value is associated with an unusually small attempt frequency ($\tau_0 = 1.5 \times 10^{-13}$ s) and should be regarded with caution. [e]5-$Brsalen^{2-}$ = *N*,*N*′-ethylenebis(5-bromosalicylideneiminato) dianion. [f]The observed slow relaxation likely originates from sample impurities, rather than from the cluster, as described in the text. [g]L^{2-} = *N*,*N*′-propylenebis(2-hydroxyacetophenylideneaminato) dianion. [h]This value is associated with an unusually small attempt frequency ($\tau_0 = 5.1 \times 10^{-12}$ s) and should be regarded with caution. [i]$talen^{tBu\ 6-}$ = 2,4,6-tris(1-(2-salicylaldimino-2-methylpropylimino)-ethyl)-1,3,5-trihydroxybenzene hexanion. [j]Tp^{-} = hydrotris(pyrazol-1-yl)borate. [k]Me_3tacn = *N*,*N*′,*N*″-trimethyl-1,4,7-triazacyclononane. [l]Tp^{*-} = hydrotris(3,5-dimethylpyrazol-1-yl)borate. [m]$salmen^{2-}$ = *rac*-*N*,*N*′-(1-methylethylene)bis(salicylideneiminato) dianion. [n]This value was obtained from dc magnetization decay and ac susceptibility measurements. [o]$^{i}BuTp^{-}$ = 2-methylpropyltris(pyrazol-1-yl)borate. [p]L^{S3} = dimethyl 2-[di(pyridin-2-yl)methylene]-1,3-dithiole-4,5-dicarboxylate. [q]triphos = 1,1,1-tris(diphenylphosphinomethyl)ethane. [r]$pzTp^{-}$ = tetra(pyrazol-1-yl)borate. [s]L^{S1} = 4,5-[1′,4′]dithiino[2′,3′-b]quinoxaline-2-bis(2-pyridyl)-methylene-1,3-dithiole. [t]$bpmb^{2-}$ = 1,2-bis(pyridine-2-carboxamido)-4-methylbenzene dianion. [u]$salen^{2-}$ = N,N′-ethylenebis(salicylideneaminato) dianion. [v]This value was obtained from dc magnetization decay measurements. [w]tptz = 2,4,6-tris(2-pyridyl)-1,3,5-triazine. [x]This value was obtained from extrapolation of values obtained from data collected under applied dc fields. [y]cyclen = 1,4,7,10-tetraazacyclododecane. [z]tmphen = 3,4,7,8-tetramethyl-1,10-phenanthroline. [aa]$tpm(CH_2OH)$ = 2,2,2-tris(pyrazol-1-yl)ethanol. [bb]L1 = tris(pyrazol-1-yl)-$C(CH_2)_6SAc$. [cc]L1 = tris(pyrazol-1-yl)-$C(CH_2)_{10}SAc$. [dd]$^{i}Prtacn$ = 1,4,7-tris-isopropyl-1,4,7-triazacyclononane. [ee]This cluster is comprised of two $S = {}^{7}/_2$ Ni_2Cr subunits connected through diamagnetic $Ni_3(CN)_6$ units. [ff]$Clsalpn^{2-}$ = *N*,*N*′-bis(5-chlorosalicylidene)-1,3-diaminopropano dianion.

frequencies up to 7000 Hz revealed a set of frequency-dependent peaks. An Arrhenius fit to the resulting relaxation times provided a spin-reversal barrier of U_{eff} = 33 cm^{-1}. While this value shares the record barrier for cyano-bridged single-molecule magnets with the Mn_4Re cluster described in Section 1.4.3.1, its large magnitude arises due to the closeness of the peaks rather than their corresponding temperatures. Indeed, this close proximity of the peaks is quantified in the attempt frequency, which was found to be τ_0 = 1.5×10^{-13} s in this case, four orders of magnitude lower than what is generally observed in single-molecule magnets. Thus, this relaxation barrier must be considered with some caution.

1.5 Cyano-Bridged Single-Chain Magnets

1.5.1 Chain Compounds Incorporating $[M(CN)_n]^{x-}$ Units

Section 1.4.1.1 provided a description of the use of hexacyanometalate complexes ($[M(CN)_6]^{3-}$) in binding two other molecules of the form LM′ (where L is a blocking ligand) in a trans configuration to afford linear trinuclear clusters. To prevent growth along the M′MM′ direction, M′ must attain coordinative saturation upon binding the nitrogen end of one cyanide ligand. If coordination sites remain open, the cluster can then propagate infinitely and form a one-dimensional solid. While this effect is undesired and actively circumvented in cluster chemistry, it can be utilized in efforts to design single-chain magnets. Indeed, the preparation of one such one-dimensional cyano-bridged coordination solid that demonstrates slow dynamics of its magnetization harnessed this approach. While reaction of $[(salmen)Mn(H_2O)]^+$ with $[Fe(CN)_6]^{3-}$ afforded the trinuclear cluster $[(salmen)_2(MeOH)_2Mn^{III}{}_2Fe^{III}(CN)_6]^-$, substitution of $[(5\text{-}MeOsalen)Mn(H_2O)]^+$ (5-MeOsalen^{2-} = *N,N*′-ethylenebis(5-methoxysalicylideneiminato) dianion) into the reaction scheme generated a solid containing the chain $[(5\text{-}MeOsalen)_2Mn^{III}{}_2Fe^{III}(CN)_6]^-$.[112] In contrast to the cluster, where each Mn^{III} center features an axially coordinated H_2O molecule, each Mn^{III} center in the solid is bound through two bridging oxide ligands from the 5-MeOsalen^{2-} to another Mn^{III} center, thereby forming the chain (see Figure 1.28). Thus, the overall topology of the chain consists of repeating $[(5\text{-}MeOsalen)_2Mn^{III}{}_2Fe^{III}(CN)_6]^-$ units, connected via $[(5\text{-}MeOsalen)_2Mn_2]^{2+}$ dimeric units. The absence of a H_2O molecule coordinated to Mn^{III} ion in the solid, in contrast to the cluster, likely results from crystal packing differences brought about by ligand variation.

In order to appropriately describe the static magnetic interactions in the Mn_2Fe solid, two intrachain magnetic exchange pathways were considered. First, the cyanide bridge between Fe^{III} and Mn^{III} centers was expected to mediate coupling between the two paramagnetic centers. In addition, the oxide ligands connecting the two Mn^{III} centers should provide a second exchange pathway, and this interaction was expected to be much weaker than the former. With this in mind, the system was treated as a trinuclear Mn_2Fe molecule with relatively weak intermolecular Mn-O-Mn interactions. The dc susceptibility data were modeled accordingly, where the Van Vleck equation, which describes the magnetic susceptibility of a discrete molecule, was applied with the addition of a mean-field approximation to account for the interactions between trinuclear Mn_2Fe units. This approach reproduced the experimental data well down to below 10 K, affording coupling parameters of $J_{Mn\text{-}Fe}$ = +4.5 cm^{-1} and $J_{Mn\text{-}Mn}$ = +0.097 cm^{-1} (see Table

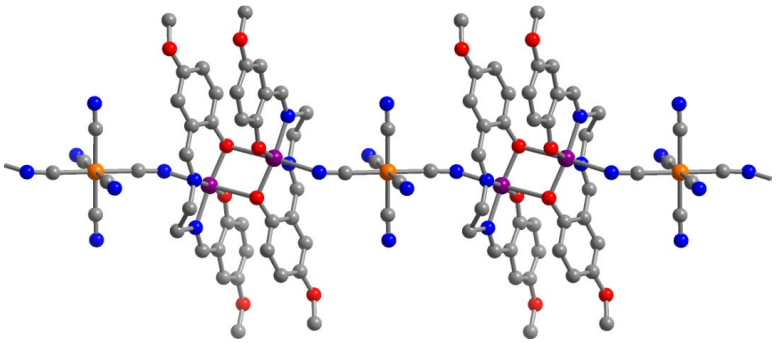


Figure 1.28. Crystal structure of the one-dimensional solid $(Et_4N)[(MeOsalen)_2Mn^{III}{}_2Fe^{III}(CN)_6$. Orange, purple, red, blue, and gray spheres represent Fe, Mn, O, N, and C atoms, respectively; H atoms are omitted for clarity.

1.4). Since $J_{Mn\text{-}Fe} >> J_{Mn\text{-}Mn}$, the interactions along the chain can best be described as weak ferromagnetic coupling between repeating units of $S = {}^9/_2$ ($S_{Mn} = 2$, $S_{Fe} = {}^1/_2$).

In addition to obtaining coupling strengths between metal centers, a quantitative determination of the magnetic anisotropy was sought. One method of extracting this information involves monitoring the magnetization as a function of applied field to ascertain the magnitude of field necessary to attain complete saturation of the magnetization. Then, this magnetization value can be directly correlated to the zero-field splitting parameter. This type of measurement is best applied to a single crystal of the sample, with its easy magnetic axis oriented perpendicular to the applied field. The magnetization should increase linearly along the isotropic direction of the hard plane, and thus this orientation should increase the ease of identifying the exact point of saturation. Toward this end, variable-field magnetization data were collected for an oriented single crystal of Mn_2Fe solid up to 10 T. Indeed, the plot of M vs. H clearly shows a linear increase in magnetization with increasing field until ultimately reaching saturation (see Figure 1.29, upper). Extrapolation of the linear region of the curve to the saturation provided the anisotropy field, $H_a = 6.3$ T. Finally, the expression $2|D|S^2 = g\mu_B S H_a$ was used to give a zero-field splitting parameter for the repeating Mn_2Fe unit of $D = -0.65$ cm^{-1}. Importantly, having determined both parameters J and D, the Ising nature of the solid could be assessed. As discussed in Section 1.3.3, an analytical expression describing the relaxation barrier in a single-chain magnet in terms of S, J, and D only applies to systems within the Ising limit, where $|D/J| > {}^4/_3$. In this case, $|D/J| = 6.7$, thus the relaxation barrier for the Mn_2Fe solid could be calculated according the expression $\Delta_\tau = S^2|8J + D|$.

To ascertain the single-chain magnet behavior in the Mn_2Fe solid, variable-field magnetization data were collected along the easy magnetic axis of the single crystal. Indeed, at temperatures below 1.4 K, the plot of M vs. H shows hysteresis loops, thus demonstrating magnet-like behavior in the solid. To investigate the slow magnetization dynamics, variable-frequency ac susceptibility data were collected for the Mn_2Fe solid at various temperatures. In corroboration with the magnet-like behavior observed in the magnetization experiments, plots of χ_M' vs. ν and χ_M'' vs. ν show strong frequency dependence of the susceptibility (see Figure 1.30, upper). These plots were fit to a

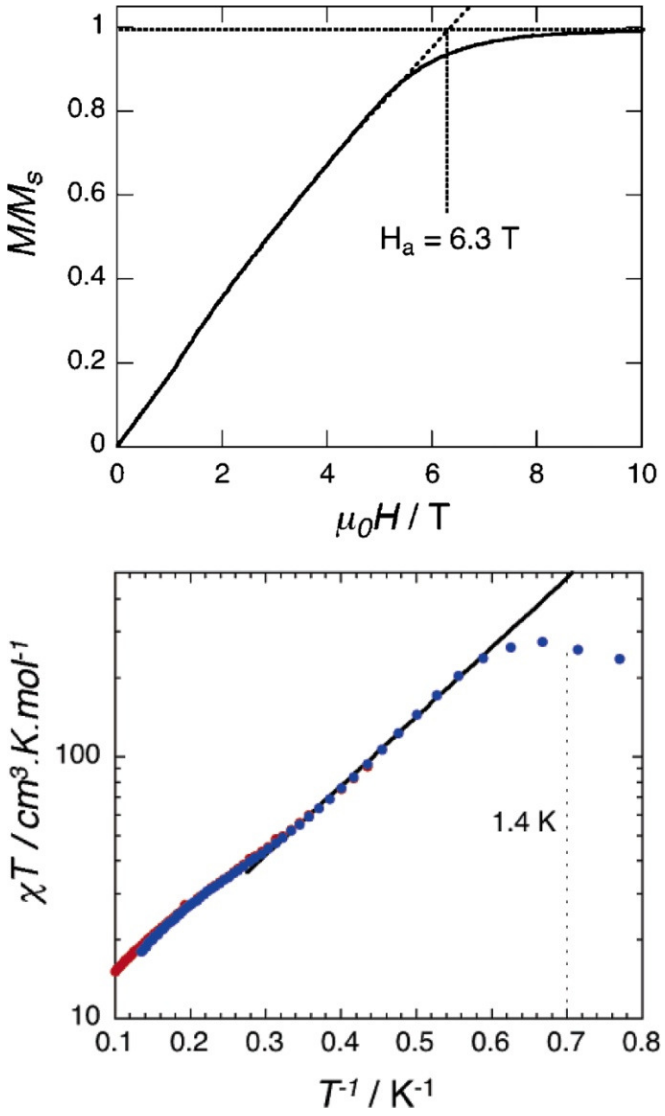


Figure 1.29. Upper: Normalized variable-field magnetization data for the solid $(Et_4N)[(MeOsalen)_2Mn^{III}{}_2Fe^{III}(CN)_6$, collected on a single crystal oriented perpendicular to the applied field. Lower: Semilog plot of χT vs. T for the MnFe solid. Red and blue circles correspond to data obtained from ac and dc measurements, respectively. The solid line represents a fit to the linear region, giving $\Delta_\xi = 4.2$ cm^{-1}. Taken from ref. 112.

generalized Debye model to obtain relaxation times at the various temperatures. In addition, in order to procure relaxation times at very low temperatures, magnetization decay measurements were conducted down to 0.8 K. An Arrhenius plot of relaxation time was then constructed, including times from both ac and dc experiments. As shown in the lower panel of Figure 1.30, the resulting plot features two distinct linear regions that intersect at 1.4 K. Linear fits to the two regions gave relaxation barriers of $\Delta_{\tau 1} = 22$ cm^{-1} and $\Delta_{\tau 2} = 17$ cm^{-1}. The presence of two barriers was attributed to two size regimes within the solid. As described in Section 1.1, at low temperatures, the magnetic correlation length saturates due to crystalline defects within the solid, and the infinite chain becomes finite. In this infinite-size regime, the total energy needed to invert the magnetization is given as $\Delta_\tau = 2\Delta_\xi + \Delta_A$, whereas this expression reduces $\Delta_\tau = \Delta_\xi + \Delta_A$ in the finite-size regime where the reversal of the magnetization becomes more probable from the ends of the finite chains. Thus, if ac susceptibility data are collected within a temperature range spanning both size regimes, two distinct relaxation barriers should be observed, with the intersection of the lines corresponding to the crossover temperature, T^*.

To further investigate the crossover to a finite-size regime in the Mn_2Fe solid, the temperature dependence of the susceptibility was reevaluated. For a classical one-dimensional system, $\chi_M T$ is directly proportional to the correlation length in zero applied field. Specifically, for an Ising-like system, the correlation length, and thus $\chi_M T$, increases exponentially with decreasing temperature, according to Equation 1.11:

$$\chi_M T/C \approx \exp(\Delta_\xi/k_B T) \tag{1.11}$$

where C is the effective Curie constant, Δ_ξ is the correlation energy, and k_B is the Boltzmann constant. From this expression, a plot of $\ln(\chi_M T)$ vs. $1/T$ should display a linear region, with the line of best fit exhibiting a slope corresponding to the correlation energy. Indeed, in the case of the Mn_2Fe solid, the plot of $\ln(\chi_M T)$ vs. $1/T$ features a linear region that saturates at ca. 1.4 K (see Figure 1.29, lower). A fit to the linear region provided a value for the correlation energy of $\Delta_\xi = 4.2$ cm^{-1}. Having established that the solid behaves within the Ising limit, the correlation energy could be equated with the coupling constant between $S = {}^9/_2$ units (J) according to expression $\Delta_\xi = 4JS^2$, giving $J = +0.26$ cm^{-1}, close to the value of $J = +0.097$ cm^{-1} obtained from the mean field approximation. Inserting this value into the expressions $\Delta_{\tau 1} = S^2|8J + D|$ and $\Delta_{\tau 2} = S^2|4J + D|$ provided theoretical values for the relaxation barrier in the infinite- and finite-size regimes of $\Delta_{\tau 1} = 22$ cm^{-1} and $\Delta_{\tau 2} = 18$ cm^{-1}, respectively, in excellent agreement with the experimental values.

1.5.2 Chain Compounds Incorporating $[LM(CN)_2]^{x-}$ Units

In selecting a building unit for directing the formation of a single-chain magnet, an ideal structure consists of a metal complex bearing two terminal cyanide ligands oriented trans to one another, as outlined in the context of trinuclear cluster precursors in Section 1.4.1.1. This type of complex can be reacted with another metal species to generate a simple linear chain that features an alternating MM′ composition, as generalized in Equation 1.3. Despite the diverse selection of dicyanometalate building units (see Table 1.2), only recently was such a molecule incorporated into a single-chain

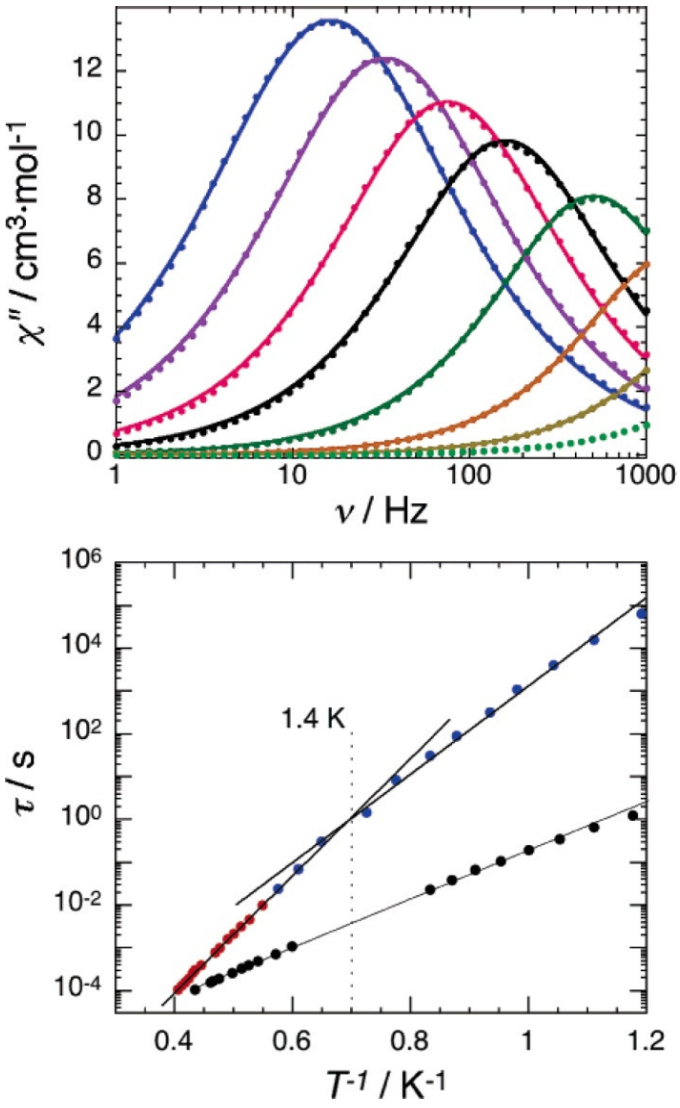


Figure 1.30. Upper: Variable-frequency out-of-phase ac magnetic susceptibility data for the solid $(Et_4N)[(MeOsalen)_2Mn^{III}{}_2Fe^{III}(CN)_6$, collected between 1.82 and 2.9 K. The solid lines represent fits obtained using a generalized Debye model. Lower: Arrhenius plot of the relaxation time, obtained for the Mn_2Fe solid using ac (red) and dc (blue) measurements to give $\Delta_{\tau 1}$ = 22 cm^{-1} and $\Delta_{\tau 2}$ = 17 cm^{-1}, in comparsion with plot obtained for the cluster $[(salmen)_2(MeOH)_2Mn^{III}{}_2Fe^{III}(CN)_6]^-$ (black circles; see Section 4.1.1) with U_{eff} = 9.7 cm^{-1}. Taken from ref. 112.

magnet.[70] This precursor complex, $[ReCl_4(CN)_2]^{2-}$, features a central Re^{IV} ion that resides in an octahedral coordination environment (see Figure 1.6). The Re^{IV} center binds four chloride ligands in the equatorial plane and two cyanide ligands in the axial coordination sites. The complex features a spin ground state of $S = {}^3/_2$, and magnetization measurements revealed the presence of strong uniaxial magnetic anisotropy, with $D = -14.4$ cm^{-1}. Indeed, the immense magnitude of the zero-field splitting parameter, which stems from spin-orbit coupling associated with the third-row transition metal, is the largest yet reported for a metal-cyanide complex.

Reaction of $[ReCl_4(CN)_2]^{2-}$ with simple solvated divalent metal salts $[M(DMF)_6]^{2+}$ (M = Mn, Fe, Co, Ni) leads to the formation of the isostructural series of one-dimensional solids of formulae $(DMF)_4Mn^{II}Re^{IV}Cl_4(CN)_2$ (M = Mn, Fe, Co, Ni).[70] The structure of these solids consists of one-dimensional chains, wherein each chain is composed of alternating $[ReCl_4(CN)_2]^{2-}$ and $[M(DMF)_4]^{2+}$ units connected via bridging cyanide ligands (see Figure 1.31, upper). The coordination environment of each M^{II} center approximates an octahedron, with the equatorial sites bound by DMF ligands and the axial sites bound by the nitrogen ends of two bridging cyanide ligands. Notably, the M-N-C angles deviate significantly from linearity, with mean angles ranging from 155.8(1)° (M = Mn) to 159.4(1)° (M = Co).[160]

Variable-temperature dc susceptibility measurements on the MRe solids revealed the presence of intrachain antiferromagnetic coupling in the Mn analogue and ferromagnetic coupling in the other three solids, giving rise to repeating spin units of $S = 1$ (Mn), ${}^7/_2$ (Fe), 3 (Co), and ${}^5/_2$ (Ni). Fits to plots of $\chi_M T$ vs. T gave coupling constants of -5.4 (Mn), +4.8 (Fe), +2.4 (Co), and +3.7 (Ni) cm^{-1}. In addition, plots of $\ln(\chi_M' T)$ vs. $1/T$ constructed for the solids show linear regions, allowing the extraction of correlation energies of Δ_ξ = 19 (Mn), 28 (Fe), 8.5 (Co), and 8.8 (Ni) cm^{-1}. As outlined in Section 1.5.1, the correlation energy of a chain within the Ising limit is related to the coupling strength through the expression $\Delta_\xi = 4JS_1S_2$. Thus, having obtained values for J and Δ_ξ from independent experimental methods, the Ising nature of the chains could be evaluated. For instance, considering the value of J obtained for the Mn analogue from fitting the $\chi_M T$ vs. T data, $4|JS_1S_2| = 81$ cm^{-1}, more than four times the experimental value of Δ_ξ. Likewise, comparisons of $4|JS_1S_2|$ and Δ_ξ for the other solids indicate strong disagreement between values. These disagreements demonstrate that the compounds do not fall within the Ising limit with sharp domain walls and instead possess the broad domain walls expected when the anisotropy energy is not sufficiently larger than the exchange energy. In this regime, no analytic expression exists that relates Δ_ξ to J and S. In addition, the $\ln(\chi_M' T)$ vs. $1/T$ plots show maxima at low temperatures corresponding to crossover temperatures of T^* = 6.5 (Mn), 14 (Fe), 5.9 (Co), and 6.7 (Ni) K. Finally, variable-field magnetization measurements conducted down to 1.8 K showed hysteresis loops for only the Fe congener, which demonstrates strong magnet-like behavior with a coercive field of H_C = 1.0 T at a sweep rate of 150 Oe/min (see Figure 1.31, lower).

To probe the relaxation dynamics in the MRe solids, the ac susceptibility was monitored as a function of both temperature and frequency. The variable-temperature and variable-frequency measurements for all solids showed peaks in χ_M' and χ_M'' that exhibit strong frequency dependence, indicating the presence of slow relaxation along the chains. Indeed, linear fits to Arrhenius plots of the relaxation times derived from these

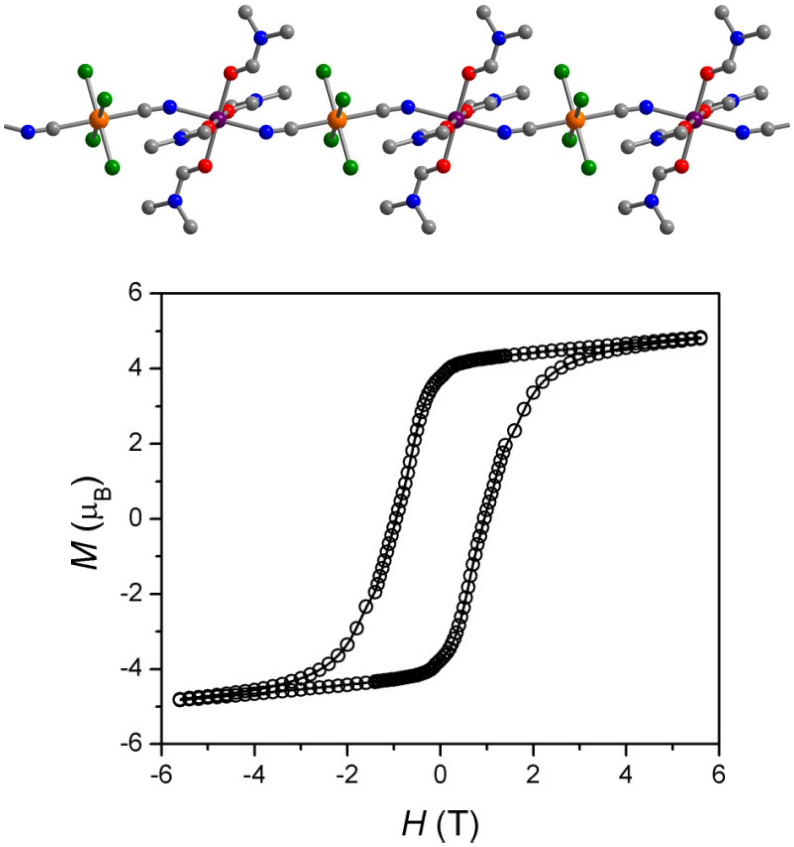


Figure 1.31. Upper: Crystal structure of the one-dimensional solid $(DMF)_4Fe^{II}Re^{IV}Cl_4(CN)_2$. Orange, purple, green, red, blue, and gray spheres represent Re, Fe, Cl, O, N, and C atoms, respectively; H atoms are omitted for clarity. Lower: Variable-field magnetization data for the FeRe solid, collected at 1.8 K with a sweep rate of 150 Oe/min. This plot gives H_C = 1.0 T and M_R = 3.77 μ_B. Taken from ref. 70.

experiments gave relaxation barriers of Δ_τ = 31 (Mn), 56 (Fe), 17 (Co), and 20 (Ni) cm^{-1}. Notably, these barriers correspond to the finite-size regime, as the ac measurements were conducted below the crossover temperatures obtained from $\ln(\chi_M T)$ data.

1.5.3 Chain Compounds Incorporating $[LM(CN)_3]^{n-}$ Units

In addition to their utility in the formation of clusters, tricyanometalate complexes of the form $[(fac\text{-}L)M(CN)_3]^{x-}$ have found use as building units for single-chain magnets. Indeed, the versatile $S = {}^1/_2$ precursor $[TpFe(CN)_3]^-$, which has been incorporated into several single-molecule magnets, has been employed as the backbone in the compounds $Tp_2LCu^{II}Fe^{III}{}_2(CN)_6$ (L = MeOH,[161] DMF[162]). These compounds exhibit a structure that has been described as a double zig-zag chain (see Figure 1.32). Here, each $[TpFe(CN)_3]^-$ unit is bridged through two of its cyanide ligands to a Cu^{II} ion, while the third cyanide remains terminal. Each Cu^{II} ion resides in a distorted square pyramidal geometry. In the

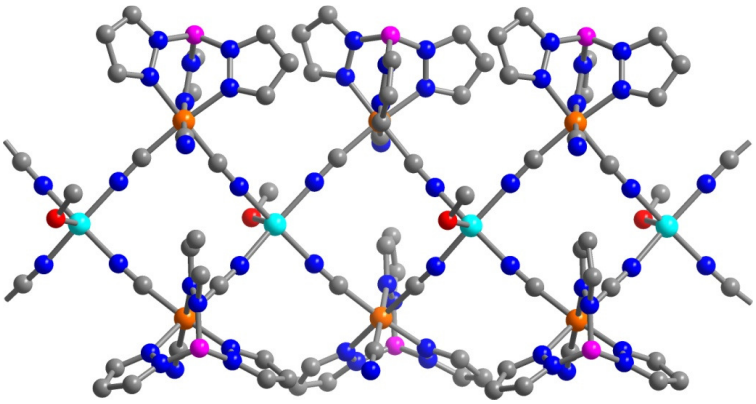


Figure 1.32. Crystal structure of the one-dimensional solid $Tp_2(CH_3OH)Cu^{II}Fe^{III}{}_2(CN)_6$. Orange, cyan, magenta, red, blue, and gray spheres represent Fe, Cu, B, O, N, and C atoms, respectively; H atoms are omitted for clarity.

basal plane, two cis coordination sites are bound by the nitrogen ends of cyanide ligands originating from two separate and adjacent $[TpFe(CN)_3]^-$ units, while the other two sites are bound to cyanide ligands of a second pair of $[TpFe(CN)_3]^-$ units. Finally, each Cu^{II} ion features a coordinated MeOH or DMF molecule in the apical position. Notably, the mean Cu-N-C angles differ somewhat for the two compounds, with mean angles of 174.1(3)° and 171.1(3)° for the MeOH- and DMF-bound chains, respectively.

Variable-temperature dc susceptibility data collected for the $CuFe_2$ compounds revealed the presence of ferromagnetic intrachain coupling, as expected between low-spin Fe^{III} ($t_{2g}{}^5$) and square-pyramidal Cu^{II} ($e^4b_2{}^2b_1{}^2a_1{}^1$) centers. In order to obtain a fit to these data, each compound was treated as a repeating trinuclear unit. Here, each trinuclear unit consists of a central Cu^{II} ion bound through cyanide to two trans Fe^{III} centers. Two distinct coupling constants arise from this approximation, where J_1 corresponds to the interaction within the trinuclear unit and J_2 between trinuclear units. This treatment gave exchange parameters of $J_1 = +16$ cm^{-1} and $J_2 = +6.2$ cm^{-1} for the MeOH-bound chain and $J_1 = +7.5$ cm^{-1} and $J_2 = +4.9$ cm^{-1} for the DMF-bound chain. The considerable increase in coupling strength for the MeOH-bound chain in contrast to the DMF-bound chain likely arises in large part due to the less bent Cu-N-C angles for the MeOH-bound chain. As the relaxation barrier for a single-chain magnet is directly correlated with the strength of coupling, this difference indicates that the MeOH-bound chain should exhibit a higher barrier, assuming similar D values for the two chains. Indeed, while no hysteresis was observed in the plot of M vs. H for the DMF-bound solid down to 1.8 K, the plot obtained for the MeOH-bound solid revealed a hysteresis loop at 1.8 K with a coercive field of $H_C = 120$ Oe.

To further probe the single-chain magnet behavior in the $CuFe_2$ compounds, variable-temperature ac susceptibility data were collected at multiple temperatures. The resulting plots of χ_M'' vs. T indeed show frequency-dependent peaks, with Arrhenius fits to the relaxation times yielding relaxation barriers of $\Delta_\tau = 78$ cm^{-1} for the MeOH-bound chain and 28 cm^{-1} for the DMF-bound chain. The significant difference in barriers is

likely a direct result of the disparate J values and thus demonstrates the critical role M-N-C angles can play in the relaxation barriers of single-chain magnets.

A reaction similar to those described above that lead to a double zig-zag chain topology, with the exception that here the metal complex allowed to react with $[TpFe(CN)_3]^-$ also features a blocking ligand, can lead to a different chain structure type. Indeed, reaction of $[TpFe(CN)_3]^-$ with $[(dpt)Ni(H_2O)_2]^{2+}$ (dpt = dipropylenetriamine) generates the compound $Tp_2(dpt)Ni^{II}Fe^{III}{}_2(CN)_6$.[163] The structure of this compound features chains that can be considered as extended zig-zag chains. The core chain consists of $[TpFe(CN)_3]^-$, each bridged through one cyanide to a $[(dpt)Ni]^{2+}$ unit. Each Ni^{II} center resides in an approximate octahedral geometry, where three coordination sites are bound by a dpt ligand in a meridional configuration. Another two sites bind the nitrogen ends of two cyanides from separate $[TpFe(CN)_3]^-$ units in a cis configuration, thus forming the zig-zag chain. In addition, the sixth coordination site is bound by the nitrogen end of another pendant $[TpFe(CN)_3]^-$ unit not associated with the core zig-zag structure.

Variable-temperature dc susceptibility data confirmed the expected ferromagnetic coupling between low-spin Fe^{III} ($t_{2g}{}^5$) and Ni^{II} ($t_{2g}{}^6e_g{}^2$) centers, giving rise to a repeating unit of with $S = 2$. These data were fit to provide an average coupling constant for the two types of cyanide bridges of $J = +5.3$ cm^{-1}. Below 8 K, the susceptibility becomes strongly field-dependent. For instance, under an applied field of 400 Oe, χ_M exhibits a maximum at 4 K and subsequent downturn with decreasing temperature. This maximum in χ_M then shifts to lower temperature with increasing field, until finally disappearing at fields of 700 Oe and above. This field dependence of χ_M is indicative of metamagnetic behavior, involving a magnetic phase transition from an ordered antiferromagnetic ground state (H < 700 Oe) to a paramagnetic ground state ($H \geq 700$ Oe), known as metamagnetic behavior.

Variable-temperature ac susceptibility data collected for the $NiFe_2$ in the absence of an applied dc field showed a peak at 4.5 K in χ_M' and no signal in χ_M'' at temperatures down to 1.9 K and frequencies up to 1000 Hz, consistent with antiferromagnetic ordering with $T_N = 4.5$ K. In stark contrast, measuring the ac susceptibility in the presence of an applied dc field of 800 Oe, where the magnetic energy overcomes the long-range ordering, led to the appearance of a frequency-dependent signal in χ_M''. This result demonstrates the occurrence of field-quenching of magnetic ordering to enable slow magnetic relaxation. However, it should be noted that single-chain magnet behavior can indeed be observed within an ordered phase, as was recently demonstrated in the compounds $[Mn_2(5\text{-MeOsaltmen})_2(H_2O)_2](PF_6)_2$[164] (5-MeOsaltmen^{2-} = *N,N′*-(1,1,2,2-tetramethylethylene)bis(5-methoxysalicylideneiminate) and $[(3,5\text{-}Cl_2\text{saltmen})(phen)Mn^{III}Ni^{II}(pao)_2]PF_6$[165] (3,5-$Cl_2$saltmen^{2-} = *N,N′*-(1,1,2,2-tetramethylethylene)bis(3,5-dichlorosalicylideneiminate).

1.5.4 Chain Compounds Incorporating $[LM(CN)_4]^{x-}$ Units

In cyano-bridged single-chain magnet research, the most heavily utilized type of building unit has been complexes of the form $[LFe(CN)_4]^-$ (L = bpy (see Figure 1.6), phen, bpym = 2,2′-bipyrimidine).[96-98,166] Here, a central $S = {}^1/_2$ Fe^{III} center is situated in an octahedral coordination environment, with two sites capped by a bidentate ligand and the other four bound by terminal cyanide ligands. Indeed, the complexes $[LFe(CN)_4]^-$ (L

= bpy, phen) were shown to direct the formation of the first single-chain magnets to exhibit the double zig-zag chain topology.[167] Reaction of $[(bpy)Fe(CN)_4]^-$ with $[Co(H_2O)_6]^{2+}$ in water leads to the formation of the compound $(bpy)_2(H_2O)_2Co^{II}Fe^{III}_2(CN)_8$.[168] This compound contains chains that exhibit the double zig-zag topology described in Section 1.5.3 for the $CuFe_2$ chain compound (see Figure 1.33, upper). Here, each $[(bpy)Fe(CN)_4]^-$ unit is bridged through two of its cyanide ligands to a Co^{II} ion, while the other two cyanides remain terminal. Each Co^{II} ion resides in a distorted octahedral geometry. In the basal plane, two cis coordination sites are bound by the nitrogen ends of cyanide ligands originating from two separate and adjacent $[(bpy)Fe(CN)_4]^-$ units, while the other two sites are bound to cyanide ligands of a second pair of $[TpFe(CN)_3]^-$ units. Each Co^{II} ion is coordinated by two H_2O molecules in the axial positions. Additionally, the chains feature relatively bent Fe-CN-Co linkages, with a mean Co-N-C angle of 167.6(1)°. Finally, the structure consists of two independent chains that feature Co-O bonds that are canted ±31° from the crystallographic *b*-axis (see Figure 1.34, upper).

Variable-temperature dc susceptibility data revealed the presence of expected ferromagnetic coupling between low-spin Fe^{III} (t_{2g}^5) and high-spin Co^{II} ($t_{2g}^5e_g^2$) centers, giving rise to a repeating unit of with $S = {}^5/_2$. To assess the magnetic anisotropy of the compounds, variable-temperature magnetization data were recorded for an oriented single crystal. Surprisingly, the magnetization remained weak and constant when the field was applied along the *a*-axis, the direction of the chain. In contrast, the magnetization along the *b*- and *c*-axes was found to rise with decreasing temperature, with the value along the *b*-axis reaching a maximum nearly twice the magnitude of that along the *c*-axis. To further explore this anisotropy, a measurement was conducted in which a magnetic field was applied along the *a*-axis at 5 K, and the magnetization was measured as the crystal was rotated in the *bc*-plane. Here again, a maximum value was observed along the *b*-axis, and a minimum occurred at a 59° from the *b*-axis (see Figure 1.34, lower). These results led to the conclusion each of the two distinct chains exhibits an easy magnetic axis along the Co-O bond (perpendicular to the chain direction). Thus, a measurement of a crystal containing both chains will show a maximum at an angle where the sum of the two Co-O vectors is maximized. In addition, the minimum value at 59° from the *b*-axis corresponds to an axis perpendicular to one of the Co-O bonds.

The considerable magnetic anisotropy evident in the $CoFe_2$ solid leads to single-chain magnet behavior at low temperature. Indeed, variable-field magnetization measurements obtained along the *b*-axis showed hysteresis loops below 8 K, with a coercive field of 1000 Oe at 2 K employing a field sweep rate of 20 Oe/s. Additionally, a plot of χ_M'' vs. *T* displays a series of frequency-dependent peaks. An Arrhenius fit to the corresponding relaxation times gave a relaxation barrier of 99 cm^{-1}.

Upon performing the above reaction in a 90:10 mixture of acetonitrile and water, the compound $(bpy)_2(H_2O)Co^{II}Fe^{III}_2(CN)_8$ ($CoFe_2$-2) is obtained.[169] The structure of this compound is similar to that observed for $(bpy)_2(H_2O)_2Co^{II}Fe^{III}_2(CN)_8$ ($CoFe_2$-1), except one of the axial H_2O molecules present in $CoFe_2$-1 has been replaced with the nitrogen end of a cyanide ligand from a $[(bpy)Fe(CN)_4]^-$ unit. This third bridging cyanide ligand is oriented cis to the other two. Thus, the structure of $CoFe_2$-2 can be considered a "doubled" analogue of $CoFe_2$-1.

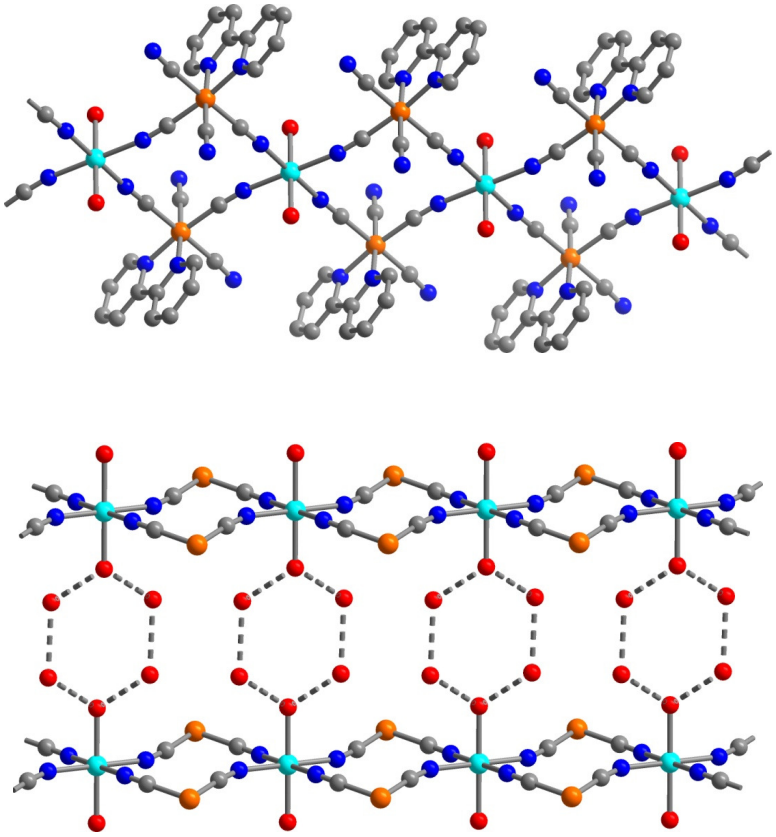


Figure 1.33. Upper: Crystal structure of the one-dimensional solid $(bpy)_2(H_2O)_2Co^{II}Fe^{III}_2(CN)_8$. Orange, cyan, red, blue, and gray spheres represent Fe, Co, B, O, N, and C atoms, respectively; H atoms are omitted for clarity. Lower: Crystal structure of $(bpym)_2(H_2O)_2Co^{II}Fe^{III}_2(CN)_8$, highlighting interchain $(H_2O)_6$–mediated connections. Terminal cyanide and bpy ligands have been omitted for clarity.

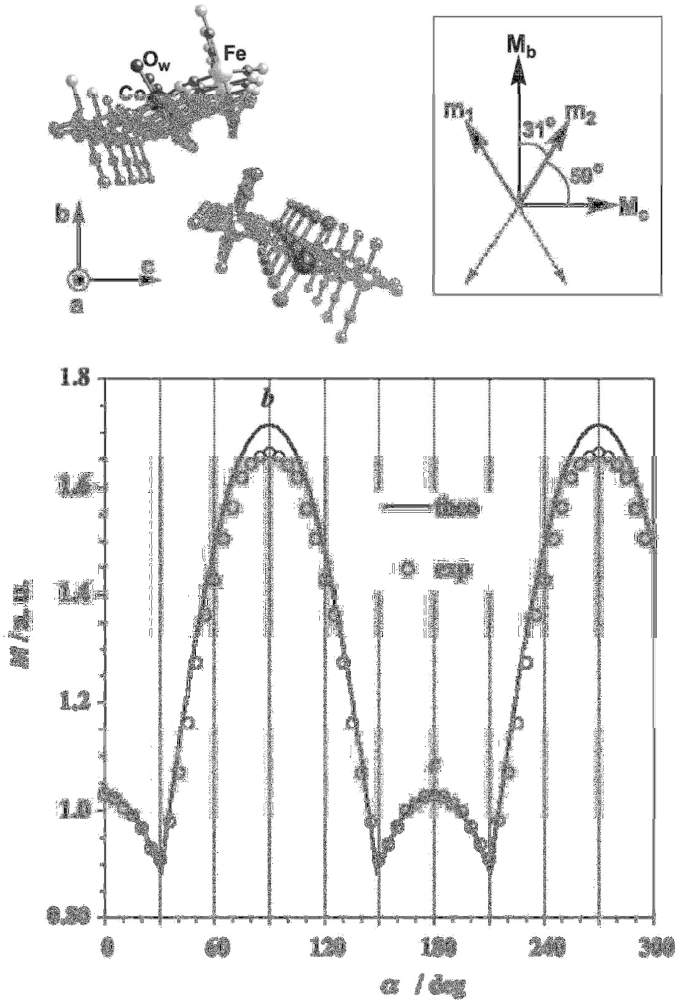


Figure 1.34. Upper: View of two chains in $(bpy)_2(H_2O)_2Co^{II}Fe^{III}{}_2(CN)_8$ down the *a*-axis, highlighting the magnetic easy axes along Co-O bond. Lower: Magnetization as a function of rotation angle in the *bc*-plane at 5 K under an applied dc field of 5000 Oe. Experimental data are shown as circles. Taken from ref. 9d.

Monitoring the variable-temperature dc susceptibility of $CoFe_2$-2 at a variety of applied fields demonstrated a field-dependent maximum in χ_M that disappears for fields greater than 600 Oe. This metamagnetic behavior, is similar to that described in Section 1.5.3 for the compound $Tp_2LCu^{II}Fe^{III}_2(CN)_6$. Along those lines, the variable-temperature ac susceptibility data were collected under an applied dc field of 800 Oe. The resulting plot of χ_M'' shows the presence of weakly frequency-dependent peaks corresponding to a relaxation barrier of 106 cm^{-1}. This value must be considered with caution, however, as the corresponding attempt frequency ($\tau_0 = 1.5 \times 10^{-17}$ s) is three to four orders of magnitude lower than what is normally observed in single-chain magnets.

Substitution of bpym for bpy in $[LFe(CN)_4]^-$ leads to a chain compound exhibiting quite different magnetic properties. Reaction of $[(bpym)Fe(CN)_4]^-$ with $[Co(H_2O)_6]^{2+}$ results in the formation of the compound $(bpym)_2(H_2O)_2Co^{II}Fe^{III}_2(CN)_8$.[170] The structure of this compound consists of chains nearly identical to those observed in $CoFe_2$-1. Notably, the Co-N-C linkage is significantly more bent in this chain than in $CoFe_2$-1, with a mean angle of 159.9°. In this structure, each Co^{II}-bound axial H_2O molecule serves as the 1- or 6-position of a hexameric network of hydrogen-bonded H_2O molecules. Thus, the overall structure of this compound can be seen as two-dimensional sheets lying in the *ab*-plane that are comprised of $(H_2O)_6$-connected $(bpym)_2CoFe_2$ chains (see Figure 1.33, lower).

Similar to the other $CoFe_2$ chains, the $(bpym)CoFe_2$ chain features ferromagnetic coupling between Fe^{III} and Co^{II} centers. In addition, single-molecule magnet behavior was confirmed through variable-field magnetization measurements, which showed hysteretic behavior at 2.0 K with a coercive field of H_C = 250 Oe. Furthermore, an Arrhenius plot of relaxation time, as obtained from ac susceptibility and dc magnetization decay experiments, shows two linear regions, corresponding to infinite- and finite-size regimes. Linear fits to these regions gave relaxation barriers of $\Delta_{\tau 1}$ = 43 cm^{-1} and $\Delta_{\tau 2}$ = 26 cm^{-1}. It is somewhat surprising to see the dramatic reduction in barrier relative to $CoFe_2$-1, considering their similar structures. This difference likely stems in large part from the difference in Co-N-C angles (167.6° for bpy vs. 159.9° for bpym), where the less bent angle should give rise to stronger coupling and thus a higher barrier. Indeed, this hypothesis is in line with the differing relaxation behavior observed in $Tp_2LCu^{II}Fe^{III}_2(CN)_6$ (L = MeOH, DMF) and further emphasizes the importance in targeting linear M-CN-M′ linkages when designing one-dimensional structures.

1.5.4 Chain Compounds Incorporating $[LM(CN)_6]^{x-}$ Units

In Section 1.4.2.2, the utility of the anisotropic $S = {}^1/_2$ complex $[(bpy)W(CN)_6]^-$ as a building unit for single-molecule magnets was discussed within the context of the cluster $(bpy)_2L_2Mn^{III}_2W^V_2(CN)_{12}$. In addition, this precursor complex has been shown to direct the formation a single-chain magnet. Reaction of $[(bpy)W(CN)_6]^-$ with $[(L3)Mn(H_2O)]^+$ ($L3^{2-}$ = *N*,*N*′-ethylenebis(1′-hydroxy-2′-acetonaphthylideneiminato) dianion) leads to assembly of the one-dimensional solid $(bpy)(L3)Mn^{III}W^V(CN)_6$.[173] The structure of this compound features chains composed of alternating $[(bpy)W(CN)_6]^-$ and $[(L3)Mn]^+$ units. Each W^V center resides in a square antiprismatic coordination environment and is bridged through two opposing cyanide ligands to Mn^{III} ions (see Figure 1.35). Accordingly, the coordination environment of the Mn^{III} ion approximates a

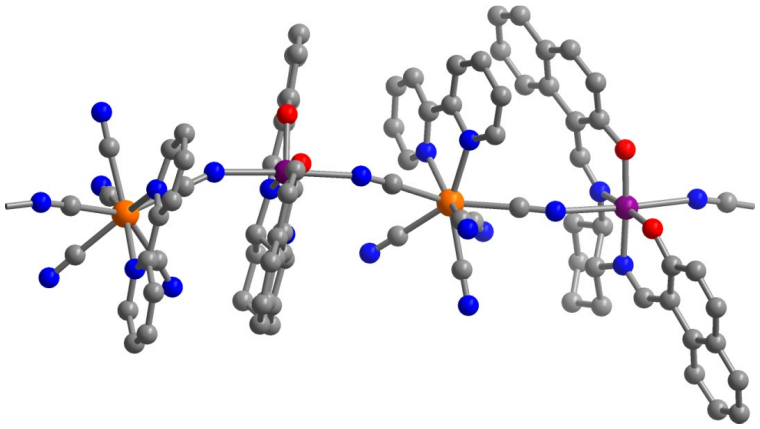


Figure 1.35. Crystal structure of the one-dimensional solid (bpy)(L2)$Mn^{III}W^{V}(CN)_6$. Orange, purple, red, blue, and gray spheres represent W, Mn, O, N, and C atoms, respectively; H atoms are omitted for clarity.

distorted octahedron, with L3 occupying the equatorial plane the nitrogen ends of two bridging cyanide ligands binding the axial positions with elongated Mn-N bonds.

Variable-temperature dc susceptibility data for the MnW compound revealed the presence of antiferromagnetic coupling between metal centers, giving rise to a net repeating unit of $S = {}^3/_2$. Fitting the $\chi_M T$ data provided a coupling constant of J = -5.9 cm^{-1}. Additionally, a plot of $\ln(\chi_M T)$ vs. $1/T$ showed a linear region of slope Δ_ξ = 2.5 cm^{-1}, confirming the one-dimensionality of the chain. To probe the possibility of single-chain magnet behavior, variable-temperature ac susceptibility data were collected at multiple frequencies. Indeed, the resulting plot of χ_M'' vs. T showed a set of frequency-dependent peaks, corresponding to a relaxation barrier of 18 cm^{-1}.

1.6 Future Directions in Cyano-Bridged Single-Molecule and Single-Chain Magnets

1.6.1 Unexplored High-Spin, High-Anisotropy Building Units

Despite the structural and magnetic diversity observed in the more than 40 single-molecule and single-chain magnets surveyed above, those compounds have incorporated less than 15 of the nearly 90 building units enumerated in Tables 1.1 and 1.2. Reasons for such a marked underutilization likely include factors such as synthetic difficulty and complex stability. However, a number of these potential building units were originally synthesized and studied for purposes totally unrelated to magnetism, and thus some may remain largely unknown. One building unit that has already seen considerable success in two- and three-dimensional magnetic solids is the pentagonal bipyramidal complex $[Mo(CN)_7]^{4-}$.[36] Structurally similar to its Re^{IV} counterpart, this molecule features a highly-anisotropic g value associated with its $^2E_1''$ ground state.[36b,175] Accordingly, $[Mo(CN)_7]^{4-}$ has been incorporated into three-dimensional M_2Mo (M = V,[176] Mn[177]) and $Ni_{1.7}Mo$[178] solids and a two-dimensional Mn_3Mo_2,[179] all of which exhibit highly anisotropic ground states that give rise to high ordering temperatures. Indeed, incorporation of this complex into a molecular or one-dimensional solid should have a similar effect and lead to a high relaxation barrier.

Table 1.4. Examples of Cyano-Bridged Single-Chain Magnets.

complex	S^a	J (cm^{-1})^b	Δ_τ (cm^{-1})
$(bpy)_2(H_2O)Co^{II}Fe^{III}{}_2(CN)_8$	$^5/_2$		106[c,d]
$(bpy)_2(H_2O)_2Co^{II}Fe^{III}{}_2(CN)_8$[e]	$^5/_2$		99
$Tp_2(MeOH)Cu^{II}Fe^{III}{}_2(CN)_6$	$^3/_2$	+16,+6.2[f]	78
$(DMF)_4Fe^{II}Re^{IV}Cl_4(CN)_2$	$^7/_2$	+4.8	56
$(bpym)_2(H_2O)_2Co^{II}Fe^{III}{}_2(CN)_8$[g]	$^5/_2$		43,26[h]
$(bpy)_2Cu^{II}Fe^{III}{}_2(CN)_8$	$^3/_2$		35[c]
$(DMF)_4Mn^{II}Re^{IV}Cl_4(CN)_2$	1	+5.4	31
$Tp_2(DMF)Cu^{II}Fe^{III}{}_2(CN)_6$	$^3/_2$	+7.5,+4.9[f]	28
$[(5\text{-MeOsalen})_2Mn^{III}{}_2Fe^{III}(CN)_6]^-$[i]	$^9/_2$	+4.5,+0.097[j]	22,17[h]
$(DMF)_4Ni^{II}Re^{IV}Cl_4(CN)_2$	$^5/_2$	+3.7	20
$(bpy)(L3)Mn^{III}W^{V}(CN)_6$[k]	$^3/_2$	-5.9	18
$(DMF)_4Co^{II}Re^{IV}Cl_4(CN)_2$	3	+2.4	17
$(L4)_2Cu^{II}{}_2Dy^{III}Mo^{V}(CN)_8$[l]	1[m]	-4,+5.9,+7.7,-4.2[n]	13
$Tp_2(dpt)Ni^{II}Fe^{III}{}_2(CN)_6$[o]	2	+5.7	
$(phen)_2(H_2O)_2Ni^{II}Fe^{III}{}_2(CN)_8$	2		
$(bpy)_2(H_2O)_2Cu^{II}Fe^{III}{}_2(CN)_8$	$^3/_2$		
$(bpy)(L5)Mn^{III}W^{V}(CN)_6$[p]	$^3/_2$	-4.7	
$[(5\text{-Clsalen})_2(H_2O)Mn^{III}{}_2Mo^{V}(CN)_8]^-$[q]	$^7/_2$	-2.0, -0.22[r]	
$[(5\text{-Brsalen})_2(H_2O)Mn^{III}{}_2W^{V}(CN)_8]^-$	$^7/_2$	-4.8, -0.50[r]	

[a] S denotes the spin of the repeating unit. [b] These values are based on fits to $\chi_M T$ vs. T data considering a $-2J$ Hamiltonian. [c] This value was obtained from ac measurements conducted under an applied dc field. [d] This value is associated with an unusually small attempt frequency ($\tau_0 = 1.5 \times 10^{-17}$ s) and should be considered with caution. [e] Similar behavior was observed for the isostructural compound $(phen)_2(H_2O)_2Co^{II}Fe^{III}{}_2(CN)_8$. [f] These values correspond to coupling within and between repeating $CuFe_2$ units, respectively. [g] bpym = 2,2′-bipyrimidine. [h] These values correspond to relaxation barriers in the infinite- and finite-size regimes, respectively. [i] 5-MeOsalen^{2-} = *N*,*N*′-ethylenebis(5-methoxysalicylideneiminato) dianion. [j] These values correspond to coupling within and between repeating Mn_2Fe units, respectively. [k] L3^{2-} = *N*,*N*′-ethylenebis(1′-hydroxy-2′-acetonaphthylideneiminato) dianion. [l] L4^{2-} = *N*,*N*′-propylenebis(3-methoxysalicylideneiminato) dianion. [m] This value assumes an effective $S = {}^1/_2$ ground state for the Dy^{III} ion. [n] These values correspond to $J_{Mo\text{-}Cu1}$, $J_{Mo\text{-}Cu2}$, $J_{Dy\text{-}Cu}$, and $J_{Dy\text{-}Mo}$, respectively. [o] dpt = dipropylenetriamine. [p] L5^{2-} = *N*,*N*′-ethylenebis(2-hydroxynaphthalene-1-carbaldehydeneiminato) dianion. [q] 5-Clsalen^{2-} = *N*,*N*′-ethylenebis(5-chlorosalicylideneiminato) dianion. [r] These values correspond to coupling within and between repeating Mn_2W units, respectively.

Incorporation of complexes that contain f-elements offers another route to pursue single-molecule and single-chain magnets. The immense spin-orbit coupling associated with these metals relative to transition metals could give rise to large relaxation barriers.[180] Indeed, f-elements have already been incorporated into non-cyanide-containing multinuclear single-molecule[181] and single-chain magnets,[182] as well as mononuclear

single-molecule magnets.[183] Within the f-element block of the periodic table, uranium provides an ideal target for incorporation into exchange-coupled assemblies, as the radial extension of the 5f-orbitals relative to the 4f-orbitals provides the overlap with bridging ligand orbitals necessary for significant exchange interactions with other metal centers.[184] In addition, compared to the other actinide elements, uranium-238 exhibits low levels of radioactivity, thereby minimizing the difficulty associated with its handling. Indeed, inspection of Table 1.2 shows four uranium cyanometalate complexes, bearing three or five cyanide ligands and ranging in uranium oxidation state from 3+ to 5+. These compounds could potentially be employed as the central unit of a cluster, wherein one to five cyanide ligands bridge to pendant transition metal units. In addition, appendage of two metal centers, each featuring two open coordination sites, could lead to the formation of a zig-zag chain structure.

1.6.2 Toward Switchable Single-Molecule and Single-Chain Magnets

1.6.2.1 Redox Switching

While raising relaxation barriers in single-molecule and single-chain magnets represents the most pressing challenge in upcoming years, several research groups have begun focusing efforts on the goal of imparting secondary function to these compounds. Specifically, the ability to reversibly "switch" on or off a single-molecule or single-chain magnet could find use in practical applications, as such a function would provide a third dimension of information storage in addition to the directions of magnetization. One possible method of introducing this switching effect would make use of electrochemistry. For instance, the Re^{IV} ion located in the Mn_4Re cluster outlined in Section 1.4.3.1 undergoes a spontaneous one-electron reduction to a diamagnetic Re^{III} configuration.[5d]5d Accordingly, cyclic voltammetry performed on the cluster show a reversible wave corresponding to the $Re^{III/IV}$ couple. In addition, spontaneous reduction of a central cyanometalate unit to a diamagnetic state upon appendage of peripheral metal units has been observed in a number of complexes. Such a process is generally not further investigated, as it eliminates any substantial magnetic exchange between metal centers within the cluster. As such, the electrochemistry of many of these complexes remains unexplored. The discovery of reversible redox processes in these species could lead to further investigation of the phenomenona in single-molecule transistors and other molecule devices.

1.6.2.2 Photomagnetic Switching

Light represents another physical switch that could be employed to "turn on" single-molecule magnet behavior. Here, absorption of a photon by a compound in its electronic ground state can result in an excitation to metastable excited state, generally through an intermediate excited state. The compound is considered to be photomagnetic if the magnetization of the ground state is different than that of the metastable state.[185] The bulk of research directed toward effecting photomagnetic processes has centered on using light to induce a charge-transfer. Cyano-bridged materials have provided an excellent framework upon which to accomplish and comprehensively study photo-induced charge-transfer, as demonstrated in a number of CoFe Prussian Blue analogues

where irradiation of light at low temperature has been shown to induce a transition from diamagnetic $Fe^{II}Co^{III}(t_{2g}^6, t_{2g}^6)$ phase to an ordered $Fe^{III}Co^{II}$ ($t_{2g}^5, t_{2g}^5e_g^2$) phase.[186]

The CoFe Prussian Blue analogue work was recently extended to a molecular system with a photomagnetic study of the cluster $[(pzTp)_4(tpmCH_2OH)_4Co_4Fe_4(CN)_{12}]^{4+}$, structurally analogous to the Ni_4Fe_4 cluster described in Section 1.4.6.1 (see Figure 1.36, upper).[187] Here, X-ray diffraction analysis of a single crystal revealed the presence of a high-spin Co^{II} and low-spin Fe^{III} centers at 260 K, in contrast to low-spin Co^{III} and Fe^{II} centers at 90 K (when cooled at a rate of 1 K/min), indicating the presence of a thermally-induced electron-transfer between Co and Fe ions. However, upon rapid cooling of the crystal in the absence of light, the paramagnetic $Co^{II}Fe^{III}$ state was shown to be preserved at 90 K. To probe this phenomenon further, variable-temperature dc magnetic susceptibility data were collected for the cluster. At 300 K, the plot of $\chi_M T$ vs. T clearly demonstrates the presence of isolated Co^{II} and Fe^{III} ions. Upon slowly cooling the sample, the data plummet toward $\chi_M T = 0$ below 265 K, corresponding to an electron transfer from Co to Fe and thus a diamagnetic $Co^{III}Fe^{II}$ ground state. In accordance with the structural measurements, rapidly cooling the magnetic sample led to preservation of the high-spin state down to 16 K. This metastability of the high-spin state was attributed to the structural change that accompanies the electron transfer and thus suggested the possibility that a $Co^{III}Fe^{II} \rightarrow Co^{II}Fe^{III}$ electron transfer could be initiated at low temperature and trapped for some finite period of time. Indeed, irradiation of the diamagnetic state at 30 K for 20 h led to a boost in $\chi_M T$ to a value corresponding to complete conversion to the high-spin state. Remarkably, upon ceasing the irradiation, the paramagnetic state exhibits a relaxation time at 120 K of ca. 10 years.

Upon photo-induction of the paramagnetic $Co^{II}Fe^{III}$ state at low temperature, the expected exchange coupling between Co^{II} and Fe^{III} centers, in conjunction with the magnetic anisotropy associated with both types of ion, suggests the possibility of slow magnetic relaxation of in the metastable state. Unfortunately, this system undergoes a magnetic phase transition to a three-dimensional antiferromagnetic ground state at 16 K, likely due to intermolecular interactions between clusters. Thus, any potential single-molecule magnet behavior, which would almost certainly be detectable well below this critical temperature, would be eliminated due to the magnetic ordering. Nevertheless, this result offers the possibility of targeting similar photomagnetic behavior in molecular Prussian Blue analogues where magnetic ordering is not a factor. In such species, a photo-induced excitation from a diamagnetic state to a metastable paramagnetic state featuring anisotropic metal ions may lead to a photoswitchable single-molecule magnet.

Similar photomagnetic behavior has also been observed in three-dimensional solids[188] and molecules[189] incorporating the complex $[Mo(CN)_8]^{3-/4-}$, as exemplified in the heptanuclear star-like cluster $[(tren)_6Cu^{II}{}_6Mo^{IV}(CN)_8]^{8+}$ (tren = tris(2-aminoethyl)amine).[189b] The structure of this molecule consists of a central Mo^{IV} ion, residing in a dodecahedral coordination environment, connected through six cyanide ligands to six $[(tren)Cu]^{2+}$ units (see Figure 1.37). Each Cu^{II} ion is positioned in trigonal bipyramidal geometry, bound by the nitrogen end of a cyanide ligand in an axial position. The plot of $\chi_M T$ vs. T obtained for the Cu_6Mo cluster shows a nearly constant value of $\chi_M T = 2.5$ $cm^3 \cdot mol/K$ from 300 K down to 20 K, consistent with the presence of six isolated $S = {}^1/_2$ Cu^{II} ions bridged through cyanide to an $S = 0$ dodecahedral Mo^{IV} center.

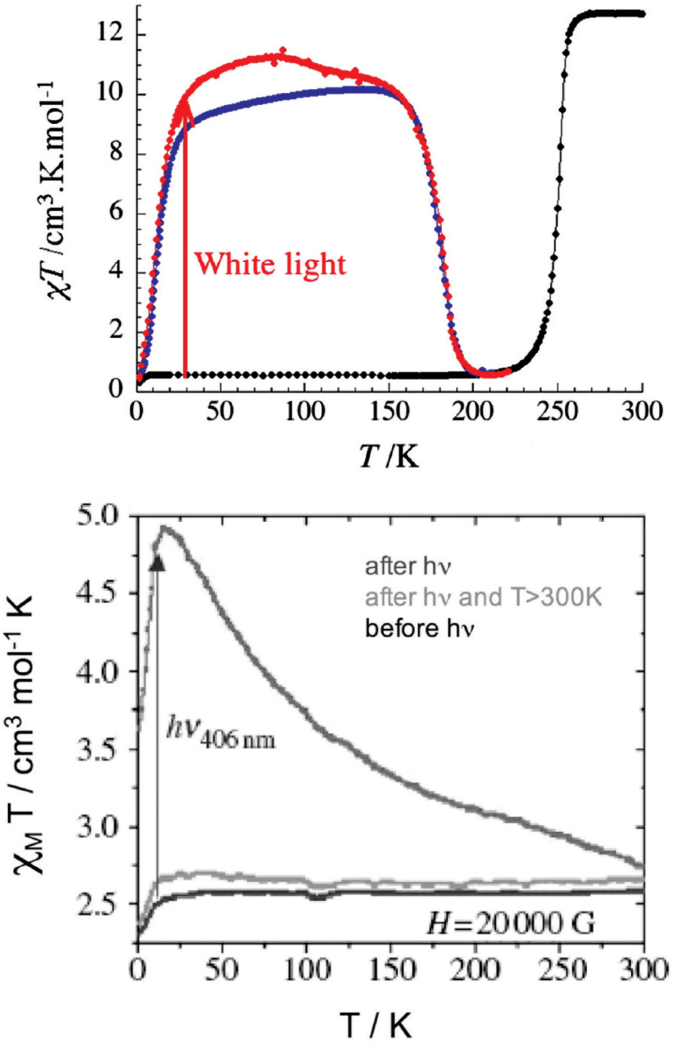


Figure 1.36. Upper: Variable-temperature magnetic susceptibility data for $[(pzTp)_4(tpmCH_2OH)_4Co_4Fe_4(CN)_{12}]^{4+}$ obtained during slow (black) and rapid (blue) cooling, and after irradiation (red). Bottom: Variable-temperature magnetic susceptibility data for $[(tren)_6Cu_6Mo(CN)_8]^{8+}$, under various conditions. Taken from ref. 187.

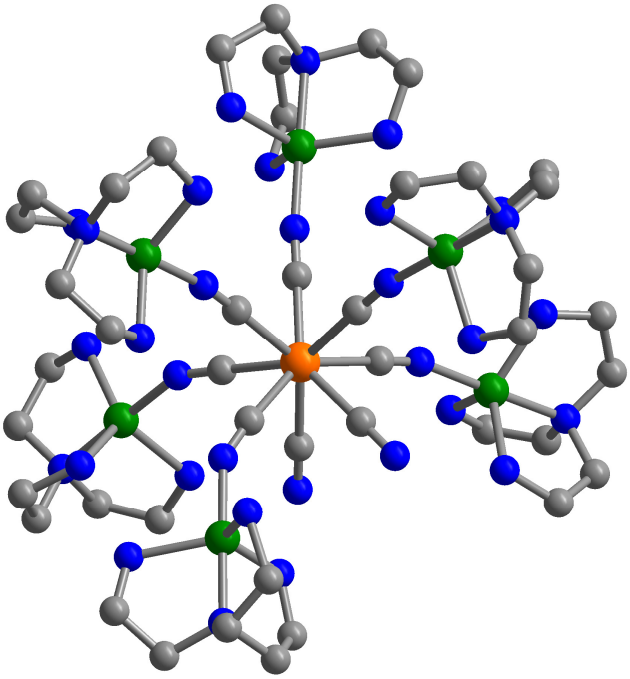


Figure 1.37. Crystal structure of the cluster $[(tren)_6Cu_6Mo(CN)_8]^{8+}$. Orange, green, blue, and gray spheres represent Mo, Cu, N, and C atoms, respectively; H atoms are omitted for clarity.

Below 20 K, $\chi_M T$ begins a decline with decreasing temperature, suggesting the presence of antiferromagnetic coupling between neighboring cluster molecules. Upon irradiation of the sample with blue light at 10 K for 10 h, the data climb to a value of $\chi_M T$ = 4.8 cm^3·mol/K. Subsequent warming of the sample in the dark resulted in an initial increase in $\chi_M T$ to 5 cm^3·mol/K, followed by a gradual decrease until the value of $\chi_M T$ reaches the value before irradiation at ca. 300 K. Moreover, repeating this cool-irradiate-warm cycle gave an identical dataset, demonstrating the reversibility of the process (see Figure 1.36, lower).

To better characterize the photomagnetic response of the Cu_6Mo cluster, variable-field magnetization data were collected at 5 K both before and after irradiation. As expected, the data before irradiation correspond to six isolated $S = {}^1/_2$ Cu^{II} ions. In sharp contrast, the data rise to a value of M = 5 μ_B at 5 T, consistent with 75% of the sample being converted to a molecule with an S = 3 ground state. In addition, the calculated Brillouin function for this proposed scenario is in good agreement with the data. Indeed, such a ground state corresponds to a cluster of metal ion composition $Cu^ICu^{II}{}_6Mo^V$, where an electron has transferred from the Mo center to a peripheral Cu ion, giving rise to ferromagnetic coupling between five $S = {}^1/_2$ Cu^{II} ions and an $S = {}^1/_2$ Mo^V ion. While ac susceptibility studies showed that this cluster does not undergo slow magnetic relaxation at low temperature, substitution of the constituent metals ions could lead to such behavior. For instance, one could envision replacement of the central $[Mo(CN)_8]^{3-/4-}$ unit with other redox-active cyanometalates, such as $[M(CN)_6]^{3-/4-}$ (M = Fe, Ru, Os), $[Re(CN)_7]^{3-/4-}$, or $[W(CN)_8]^{3-/4-}$. Alternatively, the peripheral metal ion sites to be varied

to incorporate other high-spin centers, such as $Cr^{II/III}$ or $Mn^{I/II}$. Indeed, such metal substitutions in photomagnetic complexes remain scarce in the literature.[190] In addition, the tren blocking ligand could be replaced with a ligand that leaves multiple coordination sites open, thereby providing the foundation for one-dimensional solid formation.

1.6.2.3 Thermal Switching

As the relaxation barriers in single-molecule and single-chain magnets continue to climb, the large thermal window in which slow relaxation can be observed will lend itself to the development of thermally-induced switching of the behavior on and off. Moreover, while simply increasing thermal energy beyond the relaxation barrier of the compound ceases any slow relaxation, good methods to *activate* this behavior by increasing temperature do not currently exist. One convenient method that could be employed to effect this process is spin crossover, a transition of a metal ion from a high-spin to low-spin electron configuration, or vice versa, as a function of temperature.[191] For instance, one can envision a cluster consisting of a central paramagnetic cyanometalate bridged through cyanide ligands to pendant low-spin Fe^{II} centers with spin $S = 0$. Magnetically, this system would behave as a simple paramagnet with a spin ground state corresponding to that of the central metal ion. Upon increasing the temperature, however, the low-spin Fe^{II} ions can undergo spin crossover, each being converted to the high-spin $S = 2$ configuration. After this transition, the paramagnetic Fe^{II} ions will magnetically couple to the central metal ion, giving rise to a high-spin ground state of the cluster and possibly a single-molecule magnet. Likewise, an alternating chain where one position is occupied by a spin crossover metal could engender a single-chain magnet.

While a single-molecule or single-chain magnet exhibiting spin crossover has not been realized, recent work has uncovered a number of high-spin cyano-bridged clusters[192] and extended solids[193] that do indeed demonstrate this phenomenon. The bulk of molecular work has been focused on trigonal bipyramidal clusters, as exemplified with the complexes $(tmphen)_6Fe^{II}{}_3M^{III}{}_2(CN)_{12}$ (M = Fe, Co).[192e] Here, X-ray diffraction and Mössbauer analyses revealed that the three equatorial Fe^{II} centers adopt a high-spin configuration at high temperature and a low-spin configuration at low temperature.[194] In accordance with these findings, plots of $\chi_M T$ vs. T constructed for the two clusters show a dramatic variation of the data with temperature. Below 100 K, the values of $\chi_M T$ correspond to the equatorial Fe^{II} centers being low-spin and nearly all low-spin for the Fe and Co congeners, respectively. As temperature is increased, however, $\chi_M T$ rises considerably, as the Fe^{II} centers adopt a high-spin configuration. Indeed, at 375 K, data for both compounds are still rising.

Spin crossover has also recently been observed in the one-dimensional cyano-bridged solid $(3CNpy)_4Fe^{II}Cu^{I}{}_2(CN)_4$ (3CNpy = 3-cyanopyridine).[195] This solid features chains that are structurally reminiscent of the double zig-zag topology described in Section 1.5. Each Fe^{II} ion resides in a distorted octahedral coordination environment, bound by four equatorial nitrogen ends of cyanide and two axial 3CNpy ligands. The coordination environment of each Cu^{I} ion approximates a trigonal plane, with two coordination sites bound by bridging cyanide ligands and the other bound by a 3CNpy ligand. Single-crystal X-ray structures obtained at different temperatures revealed the presence of Fe-N bond distances corresponding to low-spin Fe^{II} at 130 K and high-spin

Fe^{II} at 293 K. Additionally, variable-temperature dc susceptibility and calorimetric measurements indicated a complete conversion from high-spin to low-spin Fe^{II} occurring at ca. 172 K. Unfortunately, the presence of diamagnetic Cu^{I} ions precludes any significant magnetic exchange interactions along the chain. However, substitution of paramagnetic metal centers into similar chain topologies could lead to magnetic exchange and possibly single-chain magnet behavior, while preserving the spin crossover phenomenon. Moreover, extending the spin crossover behavior observed in Prussian Blue analogues to their molecular counterparts could lead to single-molecule magnets.

1.6.2.4 Pressure Switching

Modulating the amount of pressure exerted on a compound can also reversibly alter the compound's magnetic properties. One method for introducing pressure-dependent magnetic properties into cyano-bridged compounds centers on linkage isomerism of a bridging cyanide ligand (i.e. M-CN-M′ → M-NC-M′). Indeed, such an isomerism was shown to induce spin crossover in the Prussian Blue analogue $K_{0.4}Fe_4[Cr(CN)_6]_{2.8}\cdot 16H_2O$.[196] At ambient pressure, magnetic measurements revealed ferromagnetic ordering in the solid with a critical temperature of T_C = 18.5 K and a magnetization saturation of M_{sat} = 18 μ_B. Upon application of 1200 MPa pressure, the ordering parameters decreased to T_C = 18.5 K and M_{sat} = 10 μ_B. Removal of the applied pressure resulted in a complete return to the original ambient pressure magnetic behavior. Variable-pressure Raman spectroscopy, along with X-ray absorption spectroscopy and magnetic circular dichroism measurements, indicated that the applied pressure induces a reorientation of the cyanide ligands, such that the Fe^{II} centers become carbon-bound to the bridging cyanide ligands. This reorientation was attributed to a smaller unit cell for the isomerized product, which becomes thermodynamically favored as pressure is increased. This claim was supported by the observation of a thermally-activated linkage isomerism shown to convert $Fe_3[Cr(CN)_6]_2$ to $Cr_4[Fe(CN)_6]_3$, which caused a contraction from 10.67 Å to 10.45 Å in the *a*-axis of the unit cell. Importantly, the stronger ligand field imposed by the carbon end of cyanide relative to the nitrogen end causes the Fe^{II} ions to adopt a low-spin S = 0 configuration. The presence of diamagnetic Fe^{II} centers leads to a reduction in total magnetic moment and thus a decrease in ordering temperature and magnetization saturation. Extending this type of behavior to molecular or one-dimensional systems could lead to pressure-switchable single-molecule or single-chain magnets. Indeed, a number of cyano-bridged clusters have already been shown to exhibit cyanide linkage isomerism.[78,115,192f,197]

1.6 Conclusions and Outlook

The foregoing discussion demonstrates the effectiveness of a directed approach to constructing single-molecule and single-chain magnets from mononuclear cyanometalate building units. The vast library of precursor complexes, spanning nearly the entire transition metal set of the periodic table and bearing a myriad of ligand platforms, has resulted in the assembly of countless coordination clusters and one-dimensional solids. Importantly, the realization of these compounds has not relied on serendipitous reaction pathways, rather it has resulted directly from the structural and magnetic predictability inherent to the cyanide ligand. Indeed, owing to judicious selection of metal ions for

incorporation into predesigned structure types, many of the resulting architectures have been shown to demonstrate energy barriers to magnetization relaxation. While these barriers continue to climb, as does the wealth of knowledge surrounding single-molecule and single-chain magnets, many building units remain unutilized for such applications. It is our hope that the forthcoming years will see incorporation of new building units and the realization of materials with switchable magnetic properties, ultimately leading to new cyano-bridged single-molecule and single-chain magnets that exhibit relaxation barriers accessible to practical applications.

1.7 Acknowledgments

This research was funded by NSF grants No. ECS-0210426 and CHE-0617063. We thank Tyco Electronics for providing T.D.H. with a predoctoral fellowship.

1.8 References and Notes

(1) (a) Caneschi, A.; Gatteschi, D.; Sessoli, R.; Barra, A. L.; Brunel, L. C.; Guillot, M. *J. Am.Chem. Soc.* **1991**, *113*, 5873. (b) Sessoli, R.; Tsai, H.-L.; Schake, A. R.; Wang, S.; Vincent, J. B.; Folting, K.; Gatteschi, D.; Christou, G.; Hendrickson, D. N. *J. Am. Chem. Soc.* **1993**, *115*, 1804. (c) Sessoli, R.; Gatteschi, D.; Caneschi, A.; Novak, M. A. *Nature* **1993**, *365*, 141.

(2) A wavenumber as a unit of energy is related to the Kelvin through the following expression: $E(\mathrm{cm}^{-1})/k_B = E(\mathrm{K})$, where k_B is the Boltzmann constant, such that 1 cm^{-1} = 1.44 K.

(3) (a) Friedman, J. R.; Sarachik, M. P.; Tejada, J.; Ziolo, R. *Phys. Rev. Lett.* **1996**, *76*, 3830. (b) Thomas, L.; Lionti, F.; Ballou, R.; Gatteschi, D.; Sessoli, R.; Barbara, B. *Nature* **1996**, *383*, 145. (c) Sangregorio, C.; Ohm, T.; Paulsen, C.; Sessoli, R.; Gatteschi, D. *Phys. Rev. Lett.* **1997**, *78*, 4646. (d) Gatteschi, D.; Sessoli, R. *Angew. Chem., Int. Ed.* **2003**, *42*, 268 and references therein.

(4) (a) Garanin, D. A.; Chudnovsky, E. M. *Phys. Rev. B* **1997**, *56*, 11102. (b) Leuenberger, M. N.; Loss, D. *Nature* **2001**, *410*, 789. (c) Heersche, H. B.; de Groot, Z.; Folk, J. A.; van der Zant, H. S. J.; Romeike, C.; Wegewijs, M. R.; Zobbi, L.; Barreca, D.; Tondello, E.; Cornia, A. *Phys. Rev. Lett.* **2006**, *96*, 206801. (d) Jo, M.-H.; Grose, J. E.; Liang, W.; Baheti, K.; Deshmukh, M. M.; Sokol, J. J.; Rumberger, E. M.; Hendrickson, D. N.; Long, J. R.; Park, H.; Ralph, D. C. *Nano Lett.* **2006**, *6*, 2014.

(5) (a) Long, J. R. Molecular Cluster Magnets. In Chemistry of Nanostructured Materials; Yang, P., Ed.; World Scientific: Hong Kong, 2003; pp 291-315 and references therein. (b) Gatteschi D.; Sessoli R.; Villain J. *Molecular Nanomagnets*, Oxford University Press: New York, 2006 and references therein. (c) Milios, C. J.; Vinslava, A.; Wernsdorfer, W.; Moggach, S.; Parsons, S.; Perlepes, S. P.; Christou, G.; Brechin, E. K. *J. Am. Chem. Soc.* **2007**, *129*, 2754. (d) Freedman, D. E.; Jenkins, D. M.; Iavarone, A. T.; Long, J. R. *J. Am. Chem. Soc.* **2008**, *130*, 2884. (e) Yoshihara, D.; Karasawa, S.; Koga, N. *J. Am. Chem. Soc.* **2008**, *130*, 10460.

(6) Caneschi, A.; Gatteschi, D.; Lalioti, N.; Sangregorio, C.; Sessoli, R.; Venturi, G.; Vindigni, A.; Rettori, A.; Pini, M. G.; Novak, M. A. *Angew. Chem., Int. Ed.* **2001**, *40*, 1760.
(7) Glauber, R. J. *J. Math. Phys.* **1963**, *4*, 294.
(8) Clérac, R.; Miyasaka, H.; Yamashita, M.; Coulon, C. *J. Am. Chem. Soc.* **2002**, *124*, 12837.
(9) (a) Miyasaka, H.; Clérac, R.; Mizushima, K.; Sugiura, K.; Yamashita, M.; Wernsdorfer, W.; Coulon, C. *Inorg. Chem.* **2003**, *42*, 8203. (b) Saitoh, A.; Miyasaka, H.; Yamashita, M.; Clérac, R. *J. Mater. Chem.* **2007**, *17*, 2002. (c) Miyasaka, H.; Saitoh, A.; Yamashita, M.; Clérac, R. *Dalton Trans.* **2008**, 2422. (d) Miyasaka, H.; Julve, M.; Yamashita, M.; Clérac, R. *Inorg. Chem.* **2009**, *48*, 3420 and references therein.
(10) Coulon, C.; Clérac, R.; Lecren, L.; Wernsdorfer, W.; Miyasaka, H. *Phys. Rev. B* **2004**, *69*, 132408.
(11) Loveluck, J. M.; Lovesey, S. W.; Aubry, S. *J. Phys. C: Solid State Phys.* **1975**, *8*, 3841.
(12) (a) Coulon, C.; Miyasaka, H.; Clérac, R. *Struct. Bonding (Berlin)* **2006**, *122*, 163. (b) Bogani, L.; Vindigni, A.; Sessoli, R.; Gatteschi, D. *J. Mater. Chem.* **2008**, *18*, 4750.
(13) (a) Imry, Y.; Montano, P. A.; Hone, D. *Phys. Rev. B* **1975**, *12*, 253. (b) Leal de Silva, J. K.; Moreira, A. G.; Soares, M. S.; Sá Barreto, F. C. *Phys. Rev. B* **1995**, *52*, 4527. (c) Luscombe, J. H.; Luban, M.; Reynolds, J. P. *Phys. Rev. E* **1996**, *53*, 5852.
(14) (a) Entley, W. R.; Trentway, C. R.; Girolami, G. S. *Mol. Cryst. Liq. Cryst.* **1995**, *273*, 153. (b) Weihe, H.; Güdel, H. U. *Comments Inorg. Chem.* **2000**, *22*, 75.
(15) Fielder, S. S.; Osborne, M. C.; Lever, A. B. P.; Pietro, W. J. *J. Am. Chem. Soc.* **1995**, *117*, 6990.
(16) Ladd, M. F. C. *J. Chem. Soc., Dalton Trans.* **1977**, 220.
(17) Golub, A. M.; Köhler, H. K. H.; Skopenko, V. V. In *Chemistry of Pseudohalides;* Clark, R. J. H.; Ed.; Elsevier: New York, NY, 1986; pp 77.
(18) (a) Anonymous. *Misc. Berlinensia Incrementum Scientarium (Berlin)* **1710**, *1*, 377. (b) Woodward, J. *Phil. Trans*. **1724**, *33*, 15. (c) Brown, J. *Phil. Trans.* **1724**, *33*, 19.
(19) (a) Shriver, D. F.; Shriver, S. A.; Anderson, S. E. *Inorg. Chem.* **1965**, *4*, 725. (b) Dunbar, K. R.; Heintz, R. A. *Prog. Inorg. Chem.* **1997**, *45*, 283 and references therein. (c) Ferlay, S.; Mallah, T.; Ouahes, R.; Veillet, P.; Verdaguer, M. *Nature* **1995**, *378*, 701. (d) Entley, W. R.; Girolami, G. S. *Science* **1995**, *268*, 397. (e) Holmes, S. M.; Girolami, G. S. *J. Am. Chem. Soc.* **1999**, *121*, 5593. (e) Verdaguer, M.; Girolami, G. In *Magnetism: Molecules to Materials V;* Miller, J. S.; Drillon, M.; Eds.; Wiley-VCH: Weinheim, 2005; pp 283. (f) Shatruk, M.; Avendano, C.; Dunbar, K. in *Progress in Inorganic Chemistry*, ed. K. D. Karlin, John Wiley & Sons, Amsterdam, 2009, vol. 56, pp. 155 and references therein.
(20) (a) Seifer, G. B. *Russ. J. Inorg. Chem.* **1959**, *4*, 841. (b) Loos-Neskovic, C.; Fedoroff, M.; Garnier, E. *Talanta* **1989**, *36*, 749. (c) Kuyper, J.; Boxhoorn, G. *J.*

Catal. **1987**, *105*, 163. (d) Kaye, S. S.; Choi, H. J.; Long, J. R. *J. Am. Chem. Soc.* **2008**, *130*, 16921.

(21) Ludi, A.; Güdel, H. U. *Struct. Bond.* **1973**, *14*, 1. (b) Itaya, K.; Uchida, I.; Neff, V. D. *Acc. Chem. Res.* **1986**, *19*, 162. (c) Lefebvre, J.; Leznoff, D. B. In *Macromolecules Containing Metal and Metal-Like Elements;* Abd-El-Aziz, A. S.; Carraher, C. E.; Pittman, C. U.; Sheats, J. E.; Zeldin, M.; Eds.; Wiley: Hoboken, NJ, 2005; Vol. 5, pp 155. (d) Ohba, M.; Ōkawa, H. *Coord. Chem. Rev.* **2000**, *198*, 313. (e) Pilkington, M.; Decurtins, S. In *Comprehensive Coordination Chemistry II;* Fujita, M.; Powell, A.; Creutz, C.; Eds.; Pergamon: Oxford, UK, 2004; Vol. 7, 177.

(22) Entley, W. R.; Treadway, C. R.; Wilson, S. R.; Girolami, G. S. *J. Am. Chem. Soc.* **1997**, *119*, 6251.

(23) Jagner, S. *Acta Chem. Scand.* **1975**, *A29*, 255.

(24) (a) Fried, J.; Sih, J. C.; Lin, C. H.; Dalven, P. *J. Am. Chem. Soc.* **1972**, *94*, 4345. (b) Levenson, R A.; Towns, R. L. R. *Inorg. Chem.* **1974**, *13*, 105.

(25) Nelson, K. J.; Giles, I. D.; Shum, W. W.; Arif, A. M.; Miller, J. S. *Angew. Chem. Int. Ed.* **2005**, *44*, 3129.

(26) (a) Ljungstrom, E. *Acta Chem. Scand.* **1977**, *A31*, 104. (b) Eaton, J. P.; Nicholls, D. *Transit. Met. Chem.* **1981**, *6*, 203.

(27) (a) Gottfried, C.; Nagelschmidt, J. G. *Z. Krist.* **1930**, *73*, 357. (b) Chowdury, M. R. *Acta Chem. Scand.* **1974**, *28*, 623.

(28) Buschmann, W. E.; Arif, A. M.; Miller, J. S. *Angew. Chem. Int. Ed.* **1998**, *37*, 781.

(29) (a) Meyer, J. *Z. Anorg. Allg. Chem.* **1913**, *81*, 385. (b) Tullberg, A.; Vannerberg, N. G. *Acta Chem. Scand.* **1974**, *28*, 551.

(30) (a) Lower, J. A.; Fernelius, W. C. *Inorg. Synth.* **1946**, *2*, 213. (b) Vannerberg, N. G. *Acta Chem. Scand.* **1970**, *24*, 2335. (c) Gupta, M. P.; Milledge, H. J.; McCarthy, A. E. *Acta Crystallogr., Sect. B: Struct. Sci.* **1974**, *B30*, 656. (d) Buschmann, W. E.; Liable-Sands, L.; Rheingold, A. R.; Miller, J. S. *Inorg. Chim. Acta* **1999**, *284*, 175.

(31) Buschmann, W. E.; Vazquez, C.; Ward, M. D.; Jones, N. C.; Miller, J. S. *Chem. Commun.* **1997**, 409.

(32) (a) Figgis, B. N.; Skelton, B. W.; White, A. H. *Aust. J. Chem.* **1978**, *31*, 1195. (b) Katila, T.; Leskelä, M.; Niinistö, L.; Riski, K. J.; Valkonen, J.; Ylä-Jääski, J. *J. Solid State Chem.* **1980**, *35*, 341. (c) Iijima, S.; Mizutani, F.; Watanabe, M.; Sato, M. *J. Radioanal. Nucl. Chem.* **2003**, *255*, 503.

(33) (a) Carter, S. J.; Foxman, B. M.; Stuhl, J. S. *J. Am. Chem. Soc.* **1984**, *106*, 4265. (b) Meier, I. K.; Pearlstein, R. M.; Ramprasad, D.; Pez, G. *Inorg. Chem.* **1997**, *36*, 1707.

(34) Brown, L. D.; Raymond, K. N. *Inorg. Chem.* **1975**, *14*, 2590.

(35) Beauvais, L. G.; Long, J. R. *J. Am. Chem. Soc.* **2002**, *124*, 2110.

(36) (a) Young, R. C. *J. Am. Chem. Soc.* **1932**, *54*, 1402. (b) Hursthouse, M. B.; Malik, K. M. A.; Soares, A. M.; Gibson, J. F.; Griffith, W. P. *Inorg. Chim. Acta* **1980**, *45*, L81.

(37) (a) Corden, B. J.; Cunningham, J. A.; Eisenberg, R. *Inorg. Chem.* **1970**, *9*, 356. (b) Basson, S. S.; Leipoldt, J. G.; Bok, L. D. C.; van Vollenhoven, J. S.; Cilliers, P. J. *Acta Crystallogr. Sect. B: Struct. Sci.* **1980**, *B36*, 1765.
(38) (a) Eller, S.; Fischer, R. D. *Inorg. Chem.* **1990**, *29*, 1289. (b) Bendix, J.; Steenberg, P.; Søtofte, I. *Inorg. Chem.* **2003**, *42*, 4510.
(39) Laing, M.; Gafner, G.; Griffith, W. P.; Kiernan, P. M. *Inorg. Chim. Acta* **1979**, *33*, L119.
(40) Bok, L. D. C.; Leipoldt, J. G.; Basson, S. S. *Acta Crystallogr. Sect. B: Struct. Sci.* **1970**, *B26*, 684.
(41) Bennett, M. V.; Long, J. R. *J. Am. Chem. Soc.* **2003**, *125*, 2394.
(42) (a) Alexander, J. J.; Gray, H. B. *J. Am. Chem. Soc.* **1968**, *90*, 4260. (b) Albores, P.; Slep, L. C.; Baraldo, L. M.; Baggio, R.; Garland, M. T.; Rentschler, E. *Inorg. Chem.* **2006**, *45*, 2361.
(43) Karunadasa, H. I.; Arquero, K. D.; Berben, L. A.; Long, J. R., *Inorg. Chem.* **2010**, Article ASAP.
(44) Scheidt, W. R.; Lee, Y. J.; Luangdilok, W.; Haller, K. J.; Anzai, K.; Hatano, K. *Inorg. Chem.* **1983**, *22*, 1516.
(45) Carriedo, G. A.; Connelly, N. G.; Perez-Carreno, E.; Orpen, A. G.; Rieger, A. L.; Rieger, P. H.; Riera, V.; Rosair, G. M. *J. Chem. Soc., Dalton Trans.* **1993**, 3103.
(46) Davies, S. C.; Hughes, D. L.; Richards, R. L.; Sanders, J. R. *J. Chem. Soc., Dalton Trans.* **2002**, 1442.
(47) Davies, S. C.; Durrant, M. C.; Hughes, D. L.; Richards, R. L.; Sanders, J. R. *J. Chem. Soc., Dalton Trans.* **2000**, 4694.
(48) Duggan, D. M.; Hendrickson, D. N. *Inorg. Chem.* **1974**, *13*, 1911.
(49) Tyagi, S.; Hathaway, B. J. J. *Chem. Soc., Dalton Trans.* **1983**, 199.
(50) (a) Lee, S. C.; Scott, M. J.; Kauffmann, K.; Münck, E.; Holm, R. H. *J. Am. Chem. Soc.* **1994**, *116*, 401. (b) Scott, M. J.; Lee, S. C.; Holm, R. H. *Inorg. Chem.* **1994**, *33*, 4651.
(51) Corsi, D. M.; Murthy, N. N.; Young, Jr., V. G.; Karlin, K. D. *Inorg. Chem.* **1999**, *38*, 848.
(52) Brau, M. F.; Pfitzner, A. *Naturforsch., B.: Chem. Sci.* **2006**, *61*, 775.
(53) Greco, G. E.; O'Donoghue, M. B.; Seidel, S. W.; Davis, W. M.; Schrock, R. R. *Organometallics* **2000**, *19*, 1132.
(54) Hills, A.; Hughes, D. L.; Macdonald, C. J.; Mohammed, M. Y.; Pickett, C. J. *J. Chem. Soc., Dalton Trans.* **1991**, 121.
(55) Li, D.; Ruschman, C.; Parkin, S.; Clérac, R.; Holmes, S. M. *Chem. Commun.* **2006**, 4036.
(56) (a) Kane-Maguire, N. A. P. *Inorg. Chim. Acta* **1983**, *76*, L123. (b) Hemmings, A. M.; Lisgarten, J. N.; Palmer, R. A.; Gazi, D. M. *Acta Crystallogr., Sect. C* **1990**, *C46*, 205.
(57) (a) Daugherty, P. A.; Glerup, J.; Goodson, P. A.; Hodgson, D. J.; Michelsen, K. *Acta Chem. Scand.* **1991**, *45*, 244. (b) Mossin, S.; Sørensen, H. O.; Weihe, H. *Acta Crystallogr., Sect. C* **2002**, *C58*, m204.
(58) Smith, J. A.; Galán-Mascarós, J.-R.; Clérac, R.; Sun, J.-S.; Ouyang, X.; Dunbar, K. R. *Polyhedron* **2001**, *20*, 1727.

(59) Matsuda, M.; Yamaura, J.-I.; Tajima, H.; Inabe, T. *Chem. Lett.* **2005**, *34*, 1524.
(60) (a) Kalz, W.; Homborg, H.; Küppers, H.; Kennedy, B. J.; Murray, K. S. *Z. Naturforsch., B.: Chem. Sci.* **1984**, *39*, 1478. (b) Küppers, H.; Kalz, W.; Homborg, H. *Acta Crystallogr., Sect. C* **1985**, *C41*, 1420.
(61) (a) Agarwala, B. V.; Ramanathan, K. V.; Khetrapal, C. L. *J. Coord. Chem.* **1985**, *14*, t33. (b) Lu, T.-H.; Kao, H.-Y.; Wu, D. I.; Kong, K. C.; Cheng, C. H. *Acta Crystallogr., Sect. C* **1988**, *C44*, 1184.
(62) Wang, X.; Pennington, W. T.; Ankers, D. L.; Fanning, J. C. *Polyhedron* **1992**, *11*, 2253.
(63) (a) Ray, M.; Mukherjee, R.; Richardson, J. F.; Buchanan, R. M. *J. Chem. Soc., Dalton Trans.* **1993**, 2451. (b) Dutta, S. K.; Beckmann, U.; Bill, E.; Weyhermüller, T.; Wieghardt, K. *Inorg. Chem.* **2000**, *39*, 3355.
(64) Balch, A. L.; Noll, B. C.; Safari, N. *Inorg.Chem.* **1993**, *32*, 2901.
(65) Ni, Z.-H.; Kou, H.-Z.; Zhang, L.-F.; Ge, C.; Cui, A.-L.; Wang, R.-J.; Li, Y.; Sato, O. *Angew. Chem., Int. Ed.* **2005**, *44*, 7742.
(66) Yeung,W. F.; Lau, P. H.; Lau, T. C.; Wei, H. Y.; Sun, H. L.; Gao, S.; Chen, Z. D.; Wong, W. T. *Inorg. Chem.* **2005**, *44*, 6579.
(67) Yeung, W. F.; Man, W. L.; Wong, W. T.; Lau, T. C.; Gao, S. *Angew. Chem., Int. Ed.* **2001**, *40*, 3031.
(68) Goldner, M.; Homborg, H. *Z. Anorg. Allg. Chem.* **2000**, *626*, 1803.
(69) Fernanda, M.; Carvalho, N. N.; Galvão, A. M.; Pombeiro, A. J. L. *J. Chem. Soc., Dalton Trans.* **2000**, 3393.
(70) Harris, T. D.; Bennett, M. V.; Clérac, R.; Long, J. R. *J. Am. Chem. Soc*. **2010**, *132*, 3980.
(71) Guo, J.-F.; Yeung, W.-F.; Lau, P.-H.; Wang, X.-T.; Gao, S.;Wong, W.-T.; Chui, S. S.-Y.; Che, C.-M.; Wong, W.-Y.; Lau, T.-C. *Inorg. Chem.* **2010**, *49*, 1607.
(72) Li, D.; Parkin, S.; Wang, G.; Yee, G. T.; Holmes, S. M. *Inorg. Chem.* **2006**, *45*, 2773.
(73) Lee, I. S.; Long, J. R. *Dalton Trans.* **2004**, 3434.
(74) Mattamana, S. P.; Poli, R. *Organometallics* **1997**, *16*, 2427.
(75) Suzuki, T.; Kashiwabara, K.; Usami, T.; Imamura, T.; Kiki, M.; Fujita, J.; Kaizaki, S. *Bull. Chem. Soc. Jpn.* **2001**, *74*, 1055.
(76) Berseth, P. A.; Sokol, J. J.; Shores, M. P.; Heinrich, J. L.; Long, J. R. *J. Am. Chem. Soc.* **2000**, *122*, 9655.
(77) Yang, J. Y.; Shores, M. P.; Sokol, J. J.; Long, J. R. *Inorg. Chem.* **2003**, *42*, 1403.
(78) Harris, T. D.; Long, J. R. *Chem. Commun.* **2007**, 1360.
(79) (a) Lescouëzec, R.; Vaissermann, J.; Lloret, F.; Julve, M.; Verdaguer, M. *Inorg. Chem.* **2002**,*41*, 5943. (b) Kim, J.; Han, S.; Cho, I.-K.; Choi, K. Y.; Heu, M. Yoon, S.; Suh, B. J.*Polyhedron* **2004**, *23*, 1333.
(80) Goto, M.; Koga, N.; Ohse, Y.; Kudoh, Y.; Kukihara, M.; Okuno, Y.; Kurosaki, H. *Inorg. Chem.* **2004**, *43*, 5120.
(81) Lescouëzec, R.; Vaissermann, J.; Toma, L. M.; Carrasco, R.; Lloret, F.; Julve, M. *Inorg. Chem.* **2004**, *43*, 2234.
(82) Ni, Z. H.; Kou, H.-Z.; Zhang, L.-F.; Ni, W.-W.; Jiang, Y.-B.; Cui, A.-L.; Ribas, J.; Sato, O. *Inorg. Chem.* **2005**, *44*, 9631.

(83) Li, D.; Parkin, S.; Wang, G.; Yee, G. T.; Holmes, S. M. *Inorg. Chem.* **2006**, *45*, 1951.
(84) Li, D.; Clérac, R.; Parkin, S.; Wang, G.; Yee, G. T.; Holmes, S. M. *Inorg. Chem.* **2006**, *45*, 5251.
(85) Gu, Z.-G.; Liu, W.; Yang, Q.-F.; Zhou, X.-H.; Zuo, J. L.; You, X.-Z. *Inorg. Chem.* **2007**, *46*, 3236.
(86) Wang, C.-F.; Liu, W.; Song, Y.; Zhou, X.-H.; Zuo, J.-L.; You, X.-Z. *Eur. J. Inorg. Chem.* **2008**, 717.
(87) Kim, J. I.; Yoo, H. S.; Koh, E. K.; Kim, H. C.; Hong, C. S. *Inorg. Chem.* **2007**, *46*, 8481.
(88) Kim, J. I.; Yoo, H. S.; Koh, E. K.; Hong, C. S. *Inorg. Chem.* **2007**, *46*, 10461.
(89) Shores, M. P.; Sokol, J. J.; Long, J. R. *J. Am. Chem. Soc.* **2002**, *124*, 2279.
(90) Schelter, E. J.; Bera, J. K.; Bacsa, J.; Galán-Mascarós, J. R.; Dunbar, K. R. *Inorg. Chem.* **2003**, *42*, 4256.
(91) Maynadié, J.; Barros, N.; Berthet, J.-C.; Thuéry, P.; Maron, L.; Ephritikhine, M. *Angew. Chem., Int. Ed.* **2007**, *46*, 2010.
(92) Bendix, J.; Meyer, K.; Weyhermuller, T.; Bill, E.; Metzler-Nolte, N.; Wieghardt, K. *Inorg. Chem.* **1998**, *37*, 1767.
(93) Toma, L.; Lescouëzec, R.; Vaissermann, J.; Delgado, F. S.; Ruiz-Pérez, C.; Carrasco, R.; Cano, J.; Lloret, F.; Julve, M. *Chem.−Eur. J.* **2004**, *10*, 6130.
(94) Toma, L.; Lescouëzec, R.; Vaissermann, J.; Herson, P.; Marvaud, V.; Lloret, F.; Julve, M. *New J. Chem.* **2005**, *29*, 210.
(95) Kopf, J.; Schmidt, J. *Z. Naturforsch., B.: Chem. Sci.* **1977**, *32*, 275.
(96) Lescouezec, R.; Lloret, F.; Julve, M.; Vaissermann, J.; Verdaguer, M.; Llusar, R.; Uriel, S. *Inorg. Chem.* **2001**, *40*, 2065.
(97) Lescouëzec, R.; Lloret, F.; Julve, M.; Vaissermann, J.; Verdaguer, M. *Inorg. Chem.* **2002**, *41*, 818.
(98) Toma, L. M.; Lescouëzec, R.; Pasan, J.; Ruiz-Pérez, C.; Vaissermann, J.; Cano, J.; Carrasco, R.; Wernsdorfer, W.; Lloret, F.; Julve, M. *J. Am. Chem. Soc.* **2006**, *128*, 4842.
(99) Chiarella, G. M.; Melgarejo, D. Y.; Koch, S. A. *J. Am. Chem. Soc.* **2006**, *128*, 1416.
(100) Meier, I. K.; Pearlstein, R. M.; Ramprasad, D.; Pez, G. P. *Inorg.Chem.* **1997**, *36*, 1707.
(101) (a) Griffith, W. P.; Lewis, J.; Wilkinson, G. *J. Chem. Soc.* **1959**, 872. (b) Enemark, J. H.; Quinby, M. S.; Reed, L. L.; Steuck, M. J.; Walthers, K. K. *Inorg. Chem.* **1970**, *9*, 2397.
(102) (a) Manchot, W.; Merry, E.; Woringer, P. *Ber. Dtsch. Chem. Ges.* **1913**, *45*, 2869. (b) Lanfranconi, A. H.; Alvarez, A. G.; Castellano, E. E. *Acta Crystallogr., Sect. B* **1973**, *29*, 1733.
(103) (a) Brauer, G. Handbuch der Preparativen Anorganische Chemie **1962**, *2*, 1318. (b) Tullberg, A.; Vannerberg, N. G. *Acta Chem. Scand.* **1972**, *26*, 3382.
(104) Parise, A. R.; Piro, O. E.; Castellano, E. E.; Olabe, J. A. *Inorg. Chim. Acta* **2001**, *319*, 199.

(105) (a) Bhattacharyya, R.; Roy, P. S. *Trans. Met. Chem.* **1984**, *9*, 280. (b) Chowdhury, S. R.; Dinda, S.; Chakraborty, S.; Simonnet, C.; Mukherjee, A. K.; Okamoto, K.-I.; Bhattacharyya, R. *Inorg. Chem. Commun.* **2005**, *8*, 61.
(106) Karunadasa, H. I.; Long. J. R. *Angew. Chem. Int. Ed.* **2009**, *48*, 738.
(107) (a) Szklarzewicz, J. *Inorg. Chim. Acta* **1993**, *205*, 85. (b) Stawski, T.; Szklarzewicz, J.; Lewinski, K. *Transition Met. Chem.* **2006**, *31*, 353.
(108) Zhong, Z. J.; Seino, H.; Mizobe, Y.; Hidai, M.; Fujishima, A.; Ohkoshi, S.-I.; Hashimoto, K. *J. Am. Chem. Soc.* **2000**, *122*, 2952.
(109) Larionova, J.; Gross, M.; Pilkington, M.; Andres, H.; Stoeckli-Evans, H.; Güdel, H. U.; Decurtins, S. *Angew. Chem. Int. Ed.* **2000**, *39*, 1605.
(110) Ruiz, E.; Rajaraman, G.; Alvarez, S.; Gillon, B.; Stride, J.; Clérac, R.; Larionova, J.; Decurtins, S. *Angew. Chem., Int. Ed.*, **2005**, *44*, 2711.
(111) Choi, H. J.; Sokol, J. J.; Long, J. R. *J. Phys. Chem. Solids* **2004**, *65*, 839.
(112) Ferbinteanu, M.; Miyasaka, H.; Wernsdorfer, W.; Nakata, K.; Sugiura, K.; Yamashita, M.; Coulon, C.; Clérac, R. *J. Am. Chem. Soc.* **2005**, 127, 3090.
(113) Ni, Z.-H.; Zhang, L.-F.; Tangoulis, V.; Wernsdorfer, W.; Cui, A.-L.; Sato, O.; Kou, H.-Z. *Inorg. Chem.* **2007**, *46*, 6029.
(114) Wang, C.-F; Zuo, J.-L.; Bartlett, B. M.; Song, Y.; Long, J. R.; You, X.-Z. *J. Am. Chem. Soc.* **2006**, *128*, 7162.
(115) Bartlett, B. M.; Harris, T. D.; DeGroot, M. W.; Long, J. R. *Z. Anorg. Allg. Chem.* **2007**, 2380.
(116) (a) Singer, L. S. *J. Chem. Phys.* **1955**, *23*, 379. (b) Elbers, G.; Remme, S.; Lehmann, G. *Inorg. Chem.* **1986**, *25*, 896.
(117) (a) Gregson, A. K.; Anker, M. *Aust. J. Chem.* **1979**, *32*, 503. (b) Averill, B. A.; Orme-Johnson, W. H. *Inorg. Chem.* **1980**, *19*, 1702.
(118) Wang, S.; Zou, J.-L.; Zhou, H.-C.; Choi, H. J.; Ke, Y.; Long, J. R.; You, X.-Z. *Angew. Chem., Int. Ed.* **2004**, *43*, 5940.
(119) Shores, M. P.; Sokol, J. J.; Long, J. R. *J. Am. Chem. Soc.* **2002**, *122*, 2279.
(120) Berseth, P. A.; Sokol, J. J.; Shores, M. P.; Heinrich, J. L.; Long, J. R. *J. Am. Chem. Soc.* **2000**, *122*, 9655.
(121) (a) Rodríguez-Fortea, A.; Alemany, P.; Alvarez, S.; Ruiz, E.; Scuiller, A.; Decroix, C.; Marvaud, V.; Vaissermann, J.; Verdaguer, M.; Rosenman, I.; Julve, M. *Inorg. Chem.* **2001**, *40*, 5868. (b) Marvaud, V.; Decroix, C.; Scuiller, A.; Guyard-Duhayon, C.; Vaissermann, J.; Gonnet, F.; Verdaguer, M. *Chem.–Eur. J.* **2003**, *9*, 1678. (c) Harris, T. D.; Clérac, R. Long, J. R., *submitted.*
(122) Bieksza, D. S.; Hendrickson, D. N. *Inorg. Chem.* **1977**, *16*, 924.
(123) Choi, H. J.; Sokol, J. J.; Long, J. R. *Inorg. Chem.* **2004**, *43*, 1606.
(124) Miyasaka, H.; Ieda, H.; Matsumoto, N.; Re, N.; Crescenzi, R.; Floriani, C. *Inorg. Chem.* **1998**, *37*, 25.
(125) Yoon, J. H.; Lim, J. H.; Kim, H. C.; Hong, C. S. *Inorg. Chem.* **2006**, *45*, 9613.
(126) Miyasaka, H.; Takahashi, H.; Madanbashi, T.; Sugiura, K.; Clérac, R.; Nojiri, H. *Inorg. Chem.* **2005**, *44*, 5969.
(127) Li, D.; Parkin, S.; Wang, G.; Yee, G. T.; Prosvirin, A. V.; Holmes, S. M. *Inorg. Chem.* **2005**, *44*, 4903.

(128) Li, D.; Clérac, R.; Wang, G.; Yee, G. T.; Holmes, S. M. *Eur. J. Inorg. Chem.* **2007**, 1341.
(129) Peng, Y.-H.; Meng, Y.-F.; Hu, L.; Li, Q.-X.; Li, Y.-Z.; Zuo, J.-L.; You, X.-Z. *Inorg. Chem.* **2010**, *49*, 1905.
(130) (a) Meyer, F.; Winter, R. F.; Kaifer, E. *Inorg. Chem.* **2001**, *40*, 4597. (b) Flay, M.-L.; Vahrenkamp, H. *Eur. J. Inorg. Chem.* **2003**, 1719. (c) Si, S.-F.; Tang, J.-K.; Liu, Z.-Q.; Liao, D.-Z.; Jiang, Z.-H.; Yan, S.-P.; Cheng, P. *Inorg. Chem. Commun.* **2003**, *6*, 1109. (d) Hong, C. S.; You, Y. S. *Inorg. Chim. Acta* **2004**, *357*, 3271. (e) Gu, J.-Z.; Kou, H.-Z.; Lu, T.-B.; Tan, M.-Y. *Inorg. Chim. Acta* **2006**, *359*, 2015.
(131) (a) Fritz, M.; Rieger, D.; Bär, E.; Beck, G.; Fuchs, J.; Holzmann, G.; Fehlhammer, W. P. *Inorg. Chim. Acta* **1992**, *198-200*, 513. (b) Marvaud, V.; Decroix, C.; Scuiller, A.; Tuyèras, F.; Guyard-Duhayon, C.; Vaissermann, J.; Marrot, J.; Gonnet, F.; Verdaguer, M. *Chem. Eur. J.* **2003**, *9*, 1692.
(132) (a) Parker, R. J.; Hockless, D. C. R.; Moubaraki, B.; Murray, K. S.; Spiccia, L. *Chem. Commun.* **1996**, 2789. (b) Gembický, M.; Boča, R.; Renz, F. *Inorg. Chem. Commun.* **2000**, *3*, 662. (c) Rogez, G.; Parsons, S.; Paulsen, C.; Villar, V.; Mallah, T. *Inorg. Chem.* **2001**, *40*, 3836. (d) Shen, X.; Li, B.; Zou, J.; Hu, H.; Xu, Z. *J. Mol. Struct.* **2003**, *657*, 325. (e) Marvaud, V.; Decroix, C.; Scuiller, A.; Guyard-Duhayon, C.; Vaissermann, J.; Gonnet, F.; Verdaguer, M. *Chem. Eur. J.* **2003**, *9*, 1677. (f) López, J. P.; Heinemann, F. W.; Grohmann, A. *Z. Anorg. Allg. Chem.* **2003**, *629*, 2449.
(133) Zadrozny, J. M.; Freedman, D. E.; Jenkins, D. M.; Iavarone, A. T.; Harte, E.; Mathonière, C.; Clérac, R.; Long, J. R., *submitted*.
(134) (a) Berlinguette, C. P.; Vaughn, D.; Cañada-Vilalta, C.; Galán-Mascarós, J. R.; Dunbar, K. R. *Angew. Chem., Int. Ed.* **2003**, *42*, 1523. (b) Palii, A. V.; Ostrovsky, S. M.; Klokishner, S. I.; Tsukerblat, B. S.; Berlinguette, C. P.; Dunbar, K. R.; Galán-Mascarós, J. R. *J. Am. Chem. Soc.* **2004**, *126*, 16860.
(135) The best fit gave D = +2.6 cm^{-1}, however the presence of slow magnetic relaxation indicates that the value is actually negative.
(136) (a) Zhao, Y.; Hong, M.; Su, W.; Cao, R.; Zhou, Z.; Chan, A. S. C. *Dalton Trans.* **2000**, 1685. (b) Sieklucka, B.; Szklarzewicz, J.; Kemp, T. J.; Errington, W. *Inorg. Chem.* **2000**, *39*, 5156. (c) Contakes, S. M.; Rauchfuss, T. B. *Angew. Chem. Int. Ed.* **2000**, *39*, 1984. (d) Kim, J.; Han, S.; Pokhodnya, K. I.; Migliori, J. M.; Miller, J. S. *Inorg. Chem.* **2005**, *44*, 6983.
(137) Zhao, H.; Shatruk, M.; Prosvirin, A. V.; Dunbar, K. R. *Chem. Eur. J.* **2007**, *13*, 6573.
(138) Slow magnetic relaxation has been reported for the cluster $[(tetren)_6Ni_6Cr(CN)_6]^{9+}$, however the crystal structure of this compound has not been reported. (a) Mallah, T.; Auberger, C.; Verdaguer, M.; and Veillet, P. *Chem. Commun.* **1995**, 61. (b) Mallah, T; Marvilliers, A; Miller, J. S.; Drillon, M. **2001**, Magnetism: Molecules to Materials II. Wiley, Weinheim. (c) Rebilly, J.-N.; Mallah, T. *Struct. Bonding (Berlin)* **2006**, *122*, 163.
(139) Sokol, J. J.; Hee, A. G.; Long, J. R. *J. Am. Chem. Soc.* **2002**, *124*, 7656.

(140) Heinrich, J. L.; Sokol, J. J.; Hee, A. G.; Long, J. R. *J. Solid State Chem.* **2001**, *159*, 293.
(141) Glaser, T.; Heidemeier, M.; Weyhermüller, T.; Hoffmann, R.-D.; Rupp, H.; Müller, P. *Angew. Chem., Int. Ed.* **2006**, *45*, 6033.
(142) (a) Heinrich, J. L.; Berseth, P. A.; Long, J. R. *Chem. Commun.* **1998**, 1231. (b) Klausmeyer, K. K.; Rauchfuss, T. B.; Wilson, S. R. *Angew. Chem. Int. Ed.* **1998**, *37*, 1694. (c) Klausmeyer, K. K.; Wilson, S. R.; Rauchfuss, T. B. *J. Am. Chem. Soc.* **1999**, *121*, 2705. (d) Yang, J. Y.; Shores, M. P.; Sokol, J. J.; Long, J. R. *Inorg. Chem.* **2003**, *42*, 1403. (e) Kuhlman, M. L.; Rauchfuss, T. B. *Inorg. Chem.* **2004**, *43*, 430. (f) Ramesh, M.; Rauchfuss, T. B. *J. Organomet. Chem.* **2004**, *689*, 1425. (g) Schelter, E. J.; Prosvirin, A. V.; Reiff, W. M.; Dunbar, K. R. *Angew. Chem. Int. Ed.* **2004**, *43*, 4912.
(143) Schelter, E. J.; Prosvirin, A. V.; Dunbar, K. R. *J. Am. Chem. Soc.* **2004**, *126*, 15004.
(144) Schelter, E. J.; Karadas, F.; Avendano, C.; Prosvirin, A. V.; Wernsdorfer, W.; Dunbar, K. R. *J. Am. Chem. Soc.* **2007**, *129*, 8139.
(145) Li, D.; Parkin, S.; Wang, G.; Yee, G. T.; Clérac, R.; Wernsdorfer, W.; Holmes, S. M. *J. Am. Chem. Soc.* **2006**, *128*, 4214.
(146) Li, D.; Parkin, S.; Clérac, R.; Holmes, S. M. *Inorg. Chem.* **2006**, *45*, 7569.
(147) Kim, J.; Han, S.; Lim, J. M.; Choi, K.-Y.; Nojiri, H.; Suh, B. J. *Inorg. Chim. Acta* **2007**, *360*, 2647.
(148) Wang, S.; Zou, J.-L.; Zhou, H.-C.; Choi, H. J.; Ke, Y.; Long, J. R.; You, X.-Z. *Angew. Chem., Int. Ed.* **2004**, *43*, 5940.
(149) Berlinguette, C. P.; Dunbar, K. R. *Chem. Commun.* **2005**, 2451.
(150) Rebilly, J.-N.; Catala, L.; Rivière, E.; Guillot, R.; Wernsdorfer, W.; Mallah, T. *Chem. Commun.* **2006**, 735.
(151) Ni, Z.-H.; Kou, H.-Z.; Zhang, L.-F.; Ge, C.; Cui, A.-L.; Wang, R.-J.; Li, Y.; Sato, O. *Angew. Chem., Int. Ed.* **2005**, *44*, 7742.
(152) Bonadio, F.; Gross, M.; Stoeckli-Evans, H.; Decurtins, S. *Inorg. Chem.* **2002**, *41*, 5891.
(153) Song, Y.; Zhang, P.; Ren, X.-M.; Shen, X.-F.; Li, Y.-Z.; You, X.-Z. *J. Am. Chem. Soc.* **2005**, *127*, 3708.
(154) Zhang, Y.-Q.; Luo, C. L. *Inorg. Chem.* **2009**, *48*, 10486.
(155) Freedman, D. E.; Bennett, M. V.; Long, J. R. *Dalton Trans.* **2006**, 2829.
(156) Lim, J. H.; Yoon, J. H.; Kim, H. C.; Hong, C. S. *Angew. Chem., Int. Ed.* **2006**, *45*, 7424.
(157) Hilfiger, M. G.; Zhao, H.; Prosvirin, A.; Wernsdorfer, W.; Dunbar, K. R. *Dalton Trans.* **2009**, 5155.
(158) Visinescu, D.; Madalan, A. M.; Andruh, M.; Duhayon, C.; Sutter, J.-P.; Ungur, L.; Van den Heuvel, W.; Chibotaru, L. F. *Chem.−Eur. J.* **2009**, *15*, 11808.
(159) Yoo, H. S.; Ko, H. H.; Ryu, D. W.; Lee, J. W.; Yoon, J. H.; Lee, W. R.; Kim, H. C.; Koh, E. K.; Hong, C. S. *Inorg. Chem.* **2009**, *48*, 5617.
(160) The structure of the Ni congener was confirmed through powder X-ray diffraction, thus bond angles are not available.

(161) Wang, S.; Zuo, J.-L.; Gao, S.; Song, Y.; Zhou, H.-C.; Zhang, Y.-Z.; You, X.-Z. *J. Am. Chem. Soc.* **2004**, *126*, 8900.
(162) Wen, H.-R.; Wang, C. F.; Song, Y.; Gao, S.; Zuo, J.-L.; You, X.-Z. *Inorg. Chem.* **2006**, *45*, 8942.
(163) Costa, V.; Lescouëzec, R.; Vaissermann, J.; Herson, P.; Journaux, Y.; Araujo, M. H.; Clemente-Juan, J. M.; Lloret, F.; Julve, M. *Inorg. Chim. Acta* **2008**, *361*, 3912.
(164) Coulon, C.; Clérac, R.; Wernsdorfer, W.; Colin, T.; Miyasaka, H. *Phys. Rev. Lett.* **2009**, *102*, 167204.
(165) Miyasaka, H.; Takayama, K.; Saitoh, A.; Furukawa, S.; Yamashita, M.; Clérac, R. **2010**, *16*, 3656.
(166) Lescouëzec, R.; Toma, L. M.; Vaissermann, J.; Verdaguer, M.; Delgado, F. S.; Ruiz-Pérez, C.; Lloret, F.; Julve, M. *Coord. Chem. Rev.* **2005**, *249*, 2691.
(167) Lescouëzec, R.; Vaissermann, J.; Ruiz-Pérez, C.; Lloret, F.; Carrasco, R.; Julve, M.; Verdaguer, M.; Dromzée, Y.; Gatteschi, D.; Wernsdorfer, W. *Angew. Chem., Int. Ed.* **2003**, *42*, 1483.
(168) We will focus on the bpy-containing compound, but the phen-containing analogue was reported to show similar magnetic behavior.**Error! Bookmark not defined.**
(169) Toma, L. M.; Lescouëzec, R.; Lloret, F.; Julve, M.; Vaissermann, J.; Verdaguer, M. *Chem. Commun.* **2003**, 1850.
(170) Toma, L. M.; Lescouëzec, R.; Pasán, J.; Ruiz-Pérez, C.; Vaissermann, J.; Cano, J.; Carrasco, R.; Wernsdorfer, W.; Lloret, F.; Julve, M. *J. Am. Chem. Soc.* **2006**, *128*, 4842.
(171) Toma, L. M.; Delgado, F. S.; Ruiz-Pérez, C.; Carrasco, R.; Cano, J.; Lloret, F.; Julve, M. *Dalton. Trans.* **2004**, 2836.
(172) Toma, L. M.; Lescouëzec, R.; Uriel, S.; Llusar, R.; Ruiz-Pérez, C.; Vaissermann, J.; Lloret, F.; Julve, M. *Dalton. Trans.* **2007**, 3690.
(173) Choi, S. W.; Kwak, H. Y.; Yoon, J. H.; Kim, H. C.; Koh, E. K; Hong, C. S. *Inorg. Chem.* **2008**, *47*, 10214.
(174) Choi, S. W.; Ryu, D. W.; Lee, J. W.; Yoon, J. H.; Kim, H. C.; Lee, H.; Cho, B. K.; Hong, C. S. *Inorg. Chem.* **2009**, *48*, 9066.
(175) Rossman, G. R.; Tsay, F. D.; Gray, H. B. *Inorg. Chem.* **1973**, *12*, 824.
(176) Tomono, K.; Tsunobuchi, Y.; Nakabayashi, K.; Ohkoshi, S. *Inorg. Chem.* **2010**, *49*, 1298.
(177) (a) Larionova, J.; Sanchiz, J.; Golhen, S.; Ouahab, L.; Kahn, O. *Chem. Commun.* **1998**, 953. (b) Larionova, J.; Clérac, R.; Sanchiz, J.; Kahn, O.; Golhen, S.; Ouahab, L. *J. Am. Chem. Soc.* **1998**, *120*, 13088. (c) Larionova, J.; Kahn, O.; Golhen, S.; Ouahab, L.; Clérac, R. *Inorg. Chem.* **1999**, *38*, 3621.
(178) Tomono, K.; Tsunobuchi, Y.; Nakabayashi, K.; Kosaka, W.; Matsuda, T.; Ohkoshi, S. *Chem. Lett.* **2009**, *38*, 810.
(179) Larionova, J.; Kahn, O.; Golhen, S.; Ouahab, L.; Clérac, R. *J. Am. Chem. Soc.* **1999**, *121*, 3349.
(180) (a) Wybourne, B. G. *Spectroscopic Properties of Rare Earths*; Wiley: New York, 1965. (b) Siddall, T. H. *Theory and Applications of Molecular Paramagnetism*; Wiley: New York, 1976. (c) Kanellakopulos, B. In *Organometallics of the f-*

Elements; Marks, T. J.; Fischer, R. D.; Eds.; NATO Advanced Study Institutes Series; D. Reidel: Dordrecht, Netherlands, 1978. (d) Orchard, A. F. *Magnetochemistry*; Oxford University Press Inc: New York, 2003. (e) Edelstein, N. M.; Lander, G. H. In *The Chemistry of the Actinide and Transactinide Elements*, 3rd ed; Morss, L. R.; Edelstein, N. M.; Fuger, J.; Eds; Springer: Dordrecht, Netherlands, 2006; Vol 4, p 2225. (f) Rinehart, J. D.; Harris, T. D.; Kozimor, S. A.; Bartlett, B. M.; Long. J. R. *Inorg. Chem.* **2009**, *48*, 3382.

(181) (a) Osa, S.; Kido, T.; Matsumoto, N.; Re, N.; Pochaba, A.; Mrozinski, J. *J. Am. Chem. Soc.* **2004**, *126*, 420. (b) Mishra, A.; Wernsdorfer, W.; Abboud, K. A.; Christou, G. *J. Am. Chem. Soc.* **2004**, *126*, 15648. (c) Zaleski, C. M.; Depperman, E. C.; Kampf, J. W.; Kirk, M. L.; Pecoraro, V. L. *Angew. Chem., Int. Ed.* **2004**, *43*, 3912. (d) Mishra, A.; Wernsdorfer, W.; Parsons, S.; Christou, G.; Brechin, E. K. *Chem. Commun.* **2005**, 2086. (e) Mori, F.; Nyui, T.; Ishida, T.; Nogami, T.; Choi, K.-Y.; Nojiri, H. *J. Am. Chem. Soc.* **2006**, *128*, 1440. (f) Tang, J.; Hewitt, I.; Madhu, N. T.; Chastanet, G.; Wernsdorfer, W.; Anson, C. E.; Benelli, C.; Sessoli, R.; Powell, A. K. *Angew. Chem., Int. Ed.* **2006**, *45*, 1729. (g) Ferbinteanu, M.; Kajiwara, T.; Choi, K.-y.; Nojiri, H.; Nakamoto, A.; Kojima, N.; Cimpoesu, F.; Fujimura, Y.; Takaishi, S.; Yamashita, M. *J. Am. Chem. Soc.* **2006**, *128*, 9008. (h) Tangoulis, V.; Figuerola, A. *Chem. Phys.* **2007**, *340*, 293. (i) Chandrasekhar, V.; Pandian, B. M.; Boomishankar, R.; Steiner, A.; Vittal, J. J.; Houri, A.; Clérac, R. *Inorg. Chem.* **2008**, *47*, 4918. (j) Lin, P.-H.; Burchell, T. J.; Clérac, R.; Murugesu, M. *Angew. Chem., Int. Ed.* **2008**, *47*, 8848. (k) Mereacre, V.; Ako, A. M.; Clérac, R.; Wernsdorfer, W.; Hewitt, I. J.; Anson, C. E.; Powell, A. K. *Chem. Eur. J.* **2008**, *14*, 3577. (l) Gamer, M. T.; Lan, Y.; Roesky, P. W.; Powell, A. K.; Clérac, R. *Inorg. Chem.* **2008**, *47*, 6581. (m) Hussain, B.; Savard, D.; Burchell, T. J.; Wernsdorfer, W.; Murugesu, M. *Chem. Commun.* **2009**, *9*, 1100. (n) Ako, A. M.; Mereacre, V.; Clérac, R.; Wernsdorfer, W.; Hewitt, I. J.; Anson, C. E.; Powell, A. K. *Chem. Commun.* **2009**, *5*, 544. (o) Abbas, G.; Lan, Y.; Mereacre, V.; Wernsdorfer, W.; Clérac, R.; Buth, G.; Sougrati, M. T.; Grandjean, F.; Long, G. J.; Anson, C. E.; Powell, A. K. *Inorg. Chem.* **2009**, *48*, 9345. (p) Lin, P.-H.; Burchell, T. J.; Ungur, L.; Chibotaru, L. F.; Wernsdorfer, W.; Murugesu, M. *Angew. Chem., Int. Ed.* **2009**, *48*, 9489.

(182) (a) Bogani, L.; Sangregorio, C.; Sessoli, R.; Gatteschi, D. *Angew. Chem., Int. Ed.* **2005**, *44*, 5817. (b) Bernot, K.; Bogani, L.; Caneschi, A.; Gatteschi, D.; Sessoli, R. *J. Am. Chem. Soc.* 2006, 128, 7947. (c) Bernot, K.; Bogani, L.; Sessoli, R.; Gatteschi, D. *Inorg. Chim. Acta* **2007**, *360*, 3807. (d) Huang, Y.-G.; Wang, X.-T.; Jiang, F.-L.; Gao, S.; Wu, M.-Y.; Gao, Q.; Wei, W.; Hong, M.-C. *Chem.–Eur. J.* **2008**, *14*, 10340. (e) Bernot, K.; Luzon, J.; Caneschi, A.; Gatteschi, D.; Sessoli, R.; Bogani, L.; Vindigni, A.; Rettori, A.; Pini, M. G. *Phys. Rev. B* **2009**, *79*, 134419.

(183) (a) Ishikawa, N.; Sugita, M.; Ishikawa, T.; Koshihara, S.-y.; Kaizu, Y. *J. Am. Chem. Soc.* **2003**, *125*, 8694. (b) Ishikawa, N.; Sugita, M.; Ishikawa, T.; Koshihara, S.; Kaizu, Y. *J. Phys. Chem. B* **2004**, *108*, 11265. (c) Ishikawa, N.; Mizuno, Y.; Takamatsu, S.; Ishikawa, T.; Koshihara, S. *Inorg. Chem.* **2008**, *47*, 10217. (d) AlDamen, M. A.; Clemente-Juan, J. M.; Coronado, E.; Marti-Gastaldo,

C.; Gaita-Arino, A. *J. Am. Chem. Soc.* **2008**, *130*, 8874. (e) AlDamen, M. A.; Cardona-Serra, S.; Clemente-Juan, J. M.; Coronado, E.; Gaita-Arino, A.; Marti-Gastaldo, C.; Luis, F.; Montero, O. *Inorg. Chem.* **2009**, *48*, 3467. (f) Rinehart, J. D.; Long, J. R. *J. Am. Chem. Soc.* **2009**, *131*, 12558.

(184) (a) Crosswhite, H. M.; Crosswhite, H.; Carnall, W. T.; Paszek, A. P. *J. Chem. Phys.* **1980**, *72*, 5103. (b) Costes, J.-P.; Dahan, F.; Dupuis, A.; Laurent, J.-P. *Chem. Eur. J.* **1998**, *4*, 1616. (c) Kahn, M. L.; Mathonière, C.; Kahn, O. *Inorg. Chem.* **1999**, *38*, 3692. (d) Benelli, C.; Gatteschi, D. *Chem. Rev.* **2002**, *102*, 2369 and references therein. (e) Gaunt, A. J.; Reilly, S. D.; Enriquez, A. E.; Scott, B. L.; Ibers, J. A.; Sekar, P.; Ingram, K. I. M.; Kaltsoyannis, N.; Neu, M. P. *Inorg. Chem.* **2008**, *47*, 29.

(185) Bleuzen, A.; Marvaud, V.; Mathonière, C.; Sieklucka, B.; Verdaguer, M. *Inorg. Chem.* **2009**, *48*, 3453.

(186) (a) Sato, O.; Iyoda, T.; Fujishima, A.; Hashimoto, K. *Science* **1996**, *272*, 704. (b) Sato, O.; Einaga, Y.; Fujishima, A.; Hashimoto, K. *Inorg. Chem.* **1999**, *38*, 4405. (c) Shimamoto, N.; Ohkoshi, S.; Sato, O.; Hashimoto, K. *Inorg. Chem.* **2002**, *41*, 678. (d) Bleuzen, A.; Lomenech, C.; Escax, V.; Villain, F.; Varret, F.; Cartier dit Moulin, C.; Verdaguer, M. *J. Am. Chem. Soc.* **2000**, *122*, 6648. (e) Escax, V.; Bleuzen, A.; Cartier dit Moulin, C.; Villain, F.; Goujon, A.; Varret, F.; Verdaguer, M. *J. Am. Chem. Soc.* **2001**, *123*, 12536. (f) Gawali-Salunke, S.; Varret, F.; Maurin, I.; Enachescu, C.; Malarova, M.; Boukheddaden, K.; Codjovi, E.; Tokoro, H.; Ohkoshi, S.; Hashimoto, K. *J. Phys. Chem. B* **2005**, *109*, 8251. (g) Varret, F.; Boukheddaden, K.; Codjovi, E.; Maurin, I.; Tokoro, H.; Ohkoshi, S.; Hashimoto, K. *Polyhedron* **2005**, *24*, 2857.

(187) Li, D.; Clérac, R.; Roubeau, O.; Harté, E.; Mathonière, C.; Le Bris, R.; Holmes, S. M. *J. Am. Chem. Soc.* **2008**, *130*, 252.

(188) (a) MacKnight, F.; Haight, G. P. *Inorg. Chem.* **1973**, *12*, 3007. (b) Ohkoshi, S.; Machida, N.; Zhong, Z. J.; Hashimoto, K. *Synth. Met.* **2001**, *122*, 523. (c) Rombaut, G.; Verelst, M.; Golhen, S.; Ouahab, L.; Mathonière, C.; Kahn, O. *Inorg. Chem.* **2001**, *40*, 1151. (d) Ohkoshi, S.; Machida, N.; Abe, Y.; Zhong, Z. J.; Hashimoto, K. *Chem. Lett.* **2001**, 312. (e) Sato, O. *J. Photochem. Photobiol., C* **2004**, *5*, 203 and references therein. (f) Hozumi, T.; Hashimoto, H.; Ohkoshi, S. *J. Am. Chem. Soc.* **2005**, *127*, 3864. (g) Ohkoshi, S.; Tokoro, H.; Hozumi, T.; Zhang, Y.; Hashimoto, K.; Mathonière, C.; Bord, I.; Rombaut, G.; Verelst, M.; Cartier dit Moulin, C.; Villain, F. *J. Am. Chem. Soc.* **2006**, *128*, 270.

(189) (a) Rombaut, G.; Verelst, M.; Golhen, S.; Ouahab, L.; Mathionière, C.; Kahn, O. *Inorg. Chem.* **2001**, *40*, 1151. (b) Herrera, J.-M.; Marvaud, V.; Verdaguer, M.; Marrot, J.; Kalisz, M.; Mathonière, C. *Angew. Chem., Int. Ed.* **2004**, *43*, 5468. (c) Herrera, J. M.; Bachschmidt, A.; Villain, F.; Bleuzen, A.; Marvaud, V.;Wernsdorfer, W.; Verdaguer, M. *Phil. Trans. R. Soc. A* **2008**, *366*, 127. (d) Long, J.; Chamoreau, L.-M.; Mathonière, C.; Marvaud, V. *Inorg. Chem.* **2009**, *48*, 22. (e) Arrio, M.-A.; Long, J.;Cartier dit Moulin, C.; Bachschmidt, A.; Marvaud, V.; Rogalev, A.; Mathonière, C.; Wilhelm, F.; Sainctavit, P. *J. Phys. Chem. C* **2010**, *114*, 593.

(190) (a) Li, G.; Akitsu, T.; Sato, O.; Einaga, Y. *J. Am. Chem. Soc.* **2003**, *125*, 12396. (b) Mathoniere, C.; Podgajny, R.; Guionneau, P.; Labrugere, C.; Sieklucka, B. *Chem. Mater.* **2005**, *17*, 442.

(191) Gütlich, P.; Goodwin, H. A.; Eds. Spin Crossover in Transition Metal Compounds. *Topics in Current Chemistry*; Springer: New York, 2004; Vols. *233*, *234*, and *235*.

(192) (a) Herchel, R.; Boca, R.; Gembicky, M.; Kozisek, J.; Renz, F. *Inorg. Chem.* **2004**, *43*, 4103. (b) Berlinguette, C. P.; Dragulescu-Andrasi, A.; Sieber, A.; Galan-Mascaros, J. R.; Güdel, H.-U.; Achim, C.; Dunbar, K. R. *J. Am. Chem. Soc.* **2004**, *126*, 6222. (c) Nihei, M.; Ui, M.;Yokota, M.; Han, L.; Maeda, A.; Kishida, H.; Okamoto, H.; Oshio, H. *Angew. Chem., Int. Ed.* **2005**, *44*, 6484. (d) Berlinguette, C. P.; Dragulescu-Andrasi, A.; Sieber, A.; Güdel, H. U.; Achim, C.; Dunbar, K. R. *J. Am. Chem. Soc.* **2005**, *127*, 6766. (e) Shatruk, M.; Dragulescu Andrasi, A.; Chambers, K. E.; Stoian, S. A.; Bominaar, E. L.; Achim, C.; Dunbar, K. R. *J. Am. Chem. Soc.* **2007**, *129*, 6104.

(193) (a) Kitazawa, T.; Gomi, Y.; Takahashi, M.; Takeda, M.; Enemoto, A.; Miyazaki, T.; Enoki, T. *J. Mater. Chem.* **1996**, *6*, 119. (b) Kosaka, W.; Nomura, K.; Hashimoto, K.; Ohkoshi S. *J. Am. Chem. Soc.* **2005**, *127*, 8590. (c) Kosaka, W.; Tokoro, H.; Matsuda, T.; Hashimoto, K.; Ohkoshi, S. *J. Phys. Chem. C* **2009**, *113*, 15751. (e) Agustí, G.; Muñoz, M. C.; Gaspar, A. B.; Real, J. A. *Inorg. Chem.* **2009**, *48*, 3371 and references therein.

(194) Fits to the Mössbauer data indicated that 10% of the equatorial Fe^{II} centers retain a high-spin configuration below 150 K.

(195) Galet, A.; Muñoz, M. C.; Real, J. A. *Inorg. Chem.* **2006**, *45*, 4583.

(196) (a) Coronado, E.; Giménez-López, M. C.; Levchenko, G.; Romero, F. M.; García-Baonza, V.; Milner, A.; Paz-Pasternak, M. *J. Am. Chem. Soc.* **2005**, *127*, 4580 (b) Coronado, E.; Giménez-López, M. C.; Korzeniak, T.; Levchenko, G.; Romero, F. M.; Segura, A.; García-Baonza, V.; Cezar, J. C.; de Groot, F. M. F.; Milner, A.; Paz-Pasternak, M. *J. Am. Chem. Soc.* **2008**, *130*, 15519.

(197) (a) Shatruk, M.; Chambers, K. E.; Prosvirin, A. V.; Dunbar, K. R. *Inorg. Chem.* **2007**, *46*, 5155. (b) Avendano, C.; Karadas, F.; Hilfiger, M.; Shatruk, M.; Dunbar, K. R. *Inorg. Chem.* **2010**, *49*, 583.

Chapter 2: Linkage Isomerism In a Face-Centered Cubic $Cu_6Cr_8(CN)_{24}$ Cluster With an $S = 15$ Ground State

2.1 Introduction

Over the past twenty years, certain transition metal clusters have been found to exhibit magnetic bistability, owing to the presence of a high-spin ground state (S) with negative uniaxial magnetic anisotropy (D).[1] Although much of the work in this area has focused on oxo-bridged clusters,[1,2] the use of cyanide as a bridging ligand has also attracted considerable attention.[3] Here, controlled assembly can sometimes be achieved through a bottom-up approach, in which ligand-capped cyanometalates are employed as building units. For example, the complex $(Me_3tacn)Cr(CN)_3$ (Me_3tacn = *N*,*N*′,*N*″-trimethyl-1,4,7-triazacyclononane) was shown to react with $[Ni(H_2O)_6]^{2+}$ in boiling water to generate the face-centered cubic cluster $[(Me_3tacn)_8Cr_8Ni_6(CN)_{24}]^{12+}$.[4] During formation of the cluster, a thermally-induced cyanide linkage isomerism occurs, wherein the bridging cyanide ligands reorient such that the carbon ends bind the Ni^{II} centers instead of the Cr^{III} centers. The stronger ligand field then induces a change in the coordination geometry of the Ni^{II} centers from octahedral to square planar, thereby rendering them diamagnetic. By performing the reaction in methanol at −40 °C, a metastable precursor species could be isolated that retained high-spin Ni^{II} and exhibited magnetic properties suggestive of an $S = 18$ ground state.[4] Unfortunately, the high charge of this species, tentatively formulated as $[(Me_3tacn)_8(H_2O)_{12}Ni_6Cr_8(CN)_{24}]^{12+}$, prohibited its crystallization at low temperature. Recent work has exposed a means of reducing the charge of such clusters through use of the compact, monoanionic ligand hydrotris(pyrazol-1-yl)borate (Tp^-). The complex $[TpFe(CN)_3]^-$, which had previously been employed in the synthesis of several cyano-bridged clusters,[5,6] was found to react with $[Cu(H_2O)_6]^{2+}$ to yield the face-centered cubic cluster $[Tp_8(H_2O)_6Cu_6Fe_8(CN)_{24}]^{4+}$.[7] This species possesses an $S = 7$ ground state, arising from ferromagnetic exchange coupling between the low-spin Fe^{III} centers ($S = {}^1/_2$) and the square pyramidal Cu^{II} centers ($S = {}^1/_2$). While it does not display signs of linkage isomerism, the cluster does, by virtue of its lower charge, provide a high-spin building unit with improved solubility and terminal water ligands that can potentially be substituted. Herein, we report the synthesis of an analogous face-centered cubic cluster, $[Tp_8(H_2O)_6Cu_6Cr_8(CN)_{24}]^{4+}$, which displays a higher spin ground state of $S = 15$ and, unexpectedly, undergoes a partial cyanide linkage isomerism.

2.2 Experimental Section

General Considerations. The compounds KTp[8] and $CrCl_3(THF)_3$[9] were prepared following literature procedures. The compounds NaCN and $Cu(ClO_4)_2{\cdot}6H_2O$ were purchased from Aldrich and used as received. ***Caution!*** Although we have experienced no problems while working with them, perchlorate salts are potentially explosive and should be handled with care and only in small quantities.

$(Bu_4N)[TpCrCl_3]\cdot 2H_2O$. This compound was prepared via a modified literature procedure.[10] Under a dinitrogen atmosphere, a colorless solution of KTp (1.8 g, 7.1 mmol) in 20 mL of acetonitrile was added dropwise via cannula to a stirred purple solution of $CrCl_3(THF)_3$ (2.7 g, 7.1 mmol) in 30 mL of acetonitrile, resulting in a green slurry. After the slurry had stirred for 20 min, Bu_4NCl (2.0 g, 7.2 mmol) was added, and the stirring was continued for 2 h. The reaction mixture was then filtered in air through Celite. The green filtrate was reduced to dryness *in vacuo*, and then sonicated under 20 mL of water to solidify the oily residue. The green solid was washed with successive aliquots of water (2 × 10 mL) and Et_2O (3 × 10 mL), and dried *in vacuo* for 6 h to yield 3.0 g (65%) of product. Anal. Calcd for $C_{28}H_{50}BCrN_{10}O_2$: C, 46.22; H, 7.70; N, 15.10. Found: C, 45.85; H, 7.68; N, 15.64.

$(Bu_4N)[TpCr(CN)_3]$ (1). Under a dinitrogen atmosphere, a green solution of (Bu_4N)-$[TpCrCl_3]\cdot 2H_2O$ (0.507 g, 0.781 mmol) in 8 mL of DMF was added to solid NaCN (0.298 g, 6.08 mmol) to give a green mixture. The mixture was stirred and heated at 150 °C for 3 days. During this period, the color of the reaction mixture changed from green to orange to yellow. The reaction mixture was reduced in volume to ca. 1 mL by heating at 70 °C under reduced pressure. In air, 40 mL of Et_2O was added to the slurry to give a yellow precipitate. The solid was collected via filtration, and 5 mL of water was added to the yellow filtrate. With stirring, Bu_4NCl (0.241 g, 0.867 mmol) was added to the mixture, resulting in the precipitation of additional yellow solid. The solid was collected by filtration, washed with successive aliquots of water (2 × 5 mL) and Et_2O (3 × 15 mL), and dried *in vacuo* at 50 °C for 12 h to yield 0.307 g (67%) of product. Absorption spectrum (CH_3CN): λ_{max}/nm 420 (ε/L mol^{-1} cm^{-1} 73). IR (ATR): ν_{max}/cm^{-1} 2114 (CN) and 2512 (BH). ES-MS$^-$ (CH_3CN): *m/z* 343 ($[TpCr(CN)_3]^-$). μ_{eff} = 3.64 μ_B at 300 K. Anal. Calcd for $C_{28}H_{46}BCrN_{10}$: C, 57.45; H, 7.87; N, 23.94. Found: C, 57.31; H, 7.91; N, 23.86. X-ray analysis for **1**·3H_2O ($C_{28}H_{52}BCrN_{10}O_3$, fw = 639.61) at T = 150 K: space group P–1, a = 11.193(2), b = 11.258(2), c = 16.323(3) Å, α = 76.275(3), β = 87.493(3), γ = 60.506(3) deg, V = 1732.8(6) Å^3, Z = 2, μ = 0.372 mm^{-1}, 6336 unique reflections, 9825 total reflections, R_{int} = 0.0187, R_1 = 0.0622, wR_2 = 0.1821.

$[Tp_8(H_2O)_6Cu_6Cr_8(CN)_{24}](ClO_4)_4\cdot 7H_2O\cdot 13THF$ (2). Solid $Cu(ClO_4)_2\cdot 6H_2O$ (84 mg, 0.23 mmol) was added to a stirred yellow solution of **1** (94 mg, 0.16 mmol) in 6 mL of a 2:1 (v/v) mixture of acetonitrile and ethanol, resulting in the immediate formation of a green solution. After stirring for 5 min, the solution was filtered. Diffusion of THF vapor into the filtrate at room temperature afforded 67 mg (71%) of product as orange block-shaped crystals. IR (ATR): ν_{max}/cm^{-1} 2123 and 2167 (CN) and 2528 (BH). Anal. Calcd for $C_{148}H_{210}B_8Cl_4Cr_8Cu_6$-$N_{72}O_{42}$: C, 37.86; H, 4.51; N, 21.48. Found: C, 37.88; H, 4.49; N, 21.65. X-ray analysis for **2** ($C_{148}H_{210}B_8Cl_4Cr_8Cu_6N_{72}O_{42}$, fw = 4695.40) at T = 160 K: space group F–43c, a = 34.994(1) Å, V = 42853(15) Å^3, Z = 8, μ = 1.103 mm^{-1}, 3678 unique reflections, 56,940 total reflections, R_{int} = 0.0731, R_1 = 0.0646, wR_2 = 0.2248.

$[Tp_8(H_2O)_6Cu_6Cr_8(CN)_{24}](ClO_4)_4\cdot 15H_2O\cdot 13THF$ (3): Solid $Cu(ClO_4)_2\cdot 6H_2O$ (82 mg, 0.22 mmol) was added to a stirred yellow solution of **1** (100 mg, 0.17 mmol) in 6 mL of a 2:1 (v/v) mixture of acetonitrile and ethanol chilled in an ice bath, resulting in the immediate formation of a green solution. After stirring for 5 min, the solution was filtered. Diffusion of THF vapor into the filtrate at 0 °C afforded 87 mg (84%) of **3** as

green cube-shaped crystals. IR (ATR): ν_{max}/cm^{-1} 2183 (CN) and 2521 (BH). Anal. Calcd for $C_{148}H_{236}B_8Cl_4Cr_8Cu_6N_{72}O_{50}$: C, 36.73; H, 4.71; N, 20.84. Found: C, 36.59; H, 4.55; N, 20.89. X-ray analysis for **3** at T = 156 K: space group $P4/m$, a = 25.183(3), c = 32.984(3) Å, V = 20917(6) Å^3, Z = 4.

Magnetic Measurements. Magnetic data were collected using a Quantum Design MPMS-XL SQUID magnetometer. DC susceptibility data were collected at temperatures ranging from 5 to 300 K at fields of 500, 1000, and 5000 Oe. Magnetization data were collected at 2, 5 and 8 K, with applied fields ranging from 0 to 5 T. All data were corrected for diamagnetic contributions employing both a background subtraction and Pascal's constants. Samples were restrained with petroleum jelly to prevent torquing of the crystallites.

2.3. Results and Discussion

The complex $[TpCr(CN)_3]^-$ could not be obtained cleanly using procedures analogous to any of those employed in preparing $[TpFe(CN)_3]^-$,[5,11] but rather required utilization of pure $[TpCrCl_3]^-$ as a precursor. Treatment of $(Bu_4N)[TpCrCl_3]$ with excess NaCN in hot DMF for 3 days afforded $(Bu_4N)[TpCr(CN)_3]$ (**1**). Diffusion of Et_2O vapor into a wet acetonitrile solution of **1** gave yellow block-shaped crystals of **1**·3H_2O suitable for X-ray analysis. The resulting crystal structure, depicted in Figure 2.1, features the expected octahedral coordination geometry for Cr^{III}, with a mean Cr–C distance of 2.072(4) Å and a mean C–Cr–C angle of 90.1(1)°. A magnetic susceptibility measurement gave μ_{eff} = 3.64 μ_B at 300 K, confirming an $S = {}^3/_2$ spin state. We note that this is only the second complex of the type $[TpM(CN)_3]^{n-}$. Although two closely related species, $[Tp^*M(CN)_3]^-$ (Tp^{*-} = hydrotris(3,5-dimethylpyrazol-1-yl)borate; M = V, Fe), have also been reported,[12] these have not yet been shown to generate face-centered cubic clusters.

Reaction of **1** with $[Cu(H_2O)_6]^{2+}$ in a mixture of acetonitrile and methanol, followed by crystallization via THF vapor diffusion at room temperature, produces orange cube-shaped crystals of $[Tp_8(H_2O)_6Cu_6Cr_8(CN)_{24}](ClO_4)_4$·7$H_2O$·13THF (**2**). The structure of the $[Tp_8(H_2O)_6Cu_6Cr_8(CN)_{24}]^{4+}$ clusters in **2** features a cubic arrangement of eight Tp^--capped Cr^{III} ions connected via cyanide bridges to six Cu^{II} ions, one situated slightly above the center of each cube face (see Figure 2.2). Each Cu^{II} experiences square pyramidal coordination, with four cyanide ligands constituting the basal plane and a water molecule bound in the apical position. Most notably, two *trans* cyanide ligands have reoriented, such that they bind the Cu^{II} through carbon instead of nitrogen. Consequently, four Cr^{III} centers arranged in a tetrahedron have switched from bearing carbon-bound cyanide ligands to having nitrogen-bound cyanide ligands, thereby lowering the idealized cluster symmetry from O_h to T_d. This linkage isomerism follows a thermodynamic rationale, as the softer carbon end of cyanide prefers the softer Cu^{II} center over the harder Cr^{III} center. Although a number of instances of such cyanide linkage isomerism have been reported, particularly for Prussian blue-type solids,[13] to our knowledge, this represents the first example of a molecule that undergoes a partial isomerism.

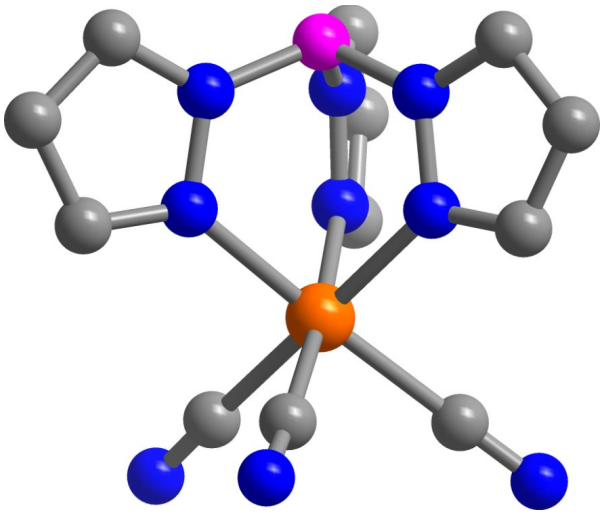


Figure 2.1. Structure of $[TpCr(CN)_3]^-$, as observed in **1**·$3H_2O$. Orange, pink, gray, and blue ellipsoids represent Cr, B, C, and N atoms, respectively; H atoms are omitted for clarity. Selected mean interatomic distances (Å) and angles (deg): Cr–C 2.072(4), Cr–N 2.056(3), C≡N 1.154(5), N–Cr–N 86.4(1), C–Cr–C 90.1(1), Cr–C≡N 177.0(4).

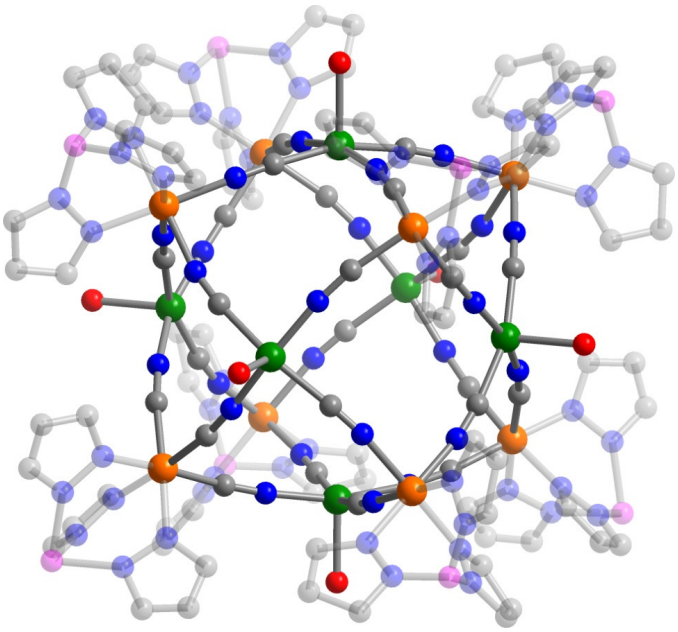


Figure 2.2. Structure of the half-isomerized face-centered cubic cluster $[Tp_8(H_2O)_6Cu_6Cr_8(CN)_{24}]^{4+}$, as observed in 2. Orange, green, purple, gray, blue, and red spheres represent Cr, Cu, B, C, N, and O atoms, respectively; H atoms are omitted for clarity. The Tp^- ligands are drawn transparently for better visualization of the core structure. The molecule resides on a T symmetry site within the crystal.

Evidence for cyanide ligand reorientation in **2** stems from both structural and spectroscopic analyses. The asymmetric unit in the crystal structure of **2** consists of two M–CN–M′ linkages, which model the data significantly better as one Cr–CN–Cu linkage and one Cr–NC–Cu linkage. For example**,** refining the structure with both cyanide linkages as Cr–CN–Cu leads to residual factors of R_1 = 6.66% and wR_2 = 23.08%, and thermal parameters for C and N of 0.031 Å^2 and 0.046 Å^2, respectively. However, reorientation of one cyanide ligand results in R_1 = 6.46% and wR_2 = 22.48%, and gives C and N thermal parameters of 0.038 Å^2 and 0.043 Å^2. Moreover, the difference between the mean Cu–C and Cu–N distances of 1.99(1) and 2.07(2) Å, respectively, is consistent with this assignment. Further support for the presence of a half-isomerized cluster arises from the infrared spectrum of **2**, which displays two distinct ν_{CN} stretches at 2123 and 2167 cm^{-1}. These are assigned to the Cr–NC–Cu and Cr–CN–Cu linkages, respectively.
In an effort to forestall the linkage isomerism and isolate the kinetically-favored isomer of the cluster, the reaction of **1** with $[Cu(H_2O)_6]^{2+}$ was carried out at 0 °C. Diffusion of THF vapor into the ensuing chilled solution afforded green cube-shaped crystals of $[Tp_8(H_2O)_6Cu_6Cr_8(CN)_{24}](ClO_4)_4{\cdot}15H_2O{\cdot}13THF$ (**3**). X-ray analysis confirmed the presence of the usual face-centered cubic cluster geometry; however, a complete structural refinement could not be performed owing to the combined effects of crystal desolvation and four-fold twinning. Consistent with an O_h-symmetry cluster isomer featuring only Cr–CN–Cu linkages, the infrared spectrum of **3** displays a single ν_{CN} stretch at 2183 cm^{-1}.

Over time, samples of **3** gradually change color from green to orange and eventually to red. The infrared spectra associated with these color changes, as induced by heating a solid sample at 80 °C, are shown in the left panel of Figure 2.3. After 1 h, the original peak has shifted slightly and a new peak has appeared at lower energy to yield a spectrum matching that of half-isomerized compound **2**. Further isomerization is significantly slower, with complete loss of the original peak only occurring after 30 h of heating. The resulting red solid is insoluble in water and common organic solvents, and low-temperature magnetic susceptibility measurements indicate the absence of magnetic exchange coupling. We hypothesize that further isomerization of cyanide ligands destabilizes the square pyramidal coordination of the Cu^{II} centers, leading to disintegration of the cluster. Indeed, we could find no reliable crystal structures containing Cu^{II} centers with four carbon-bound cyanide ligands.

In an attempt to elucidate the kinetics of the linkage isomerism, time-resolved UV-vis absorption spectra were collected for a solution of **3** (see Figure 2.3, right). Here, the color changes are similar, but the isomerization occurs much more rapidly at room temperature. Over the course of an hour, the solution color changes from green to orange, as the peak at 420 nm decreases in intensity and the peak at 657 nm shifts to higher energy. Upon further standing for up to 24 h, the solution gradually turns red and a red precipitate forms. The observed spectral changes do not occur as a linear function of time. Moreover, the initial spectra lack clean isosbestic points, suggesting that the isomerization does not proceed through a simple two-step process, with each step involving the simultaneous reorientation of twelve cyanide ligands. Instead, it likely proceeds through a complex series of intermediates, with the half-isomerized product isolated in **2** representing a local minimum along the reaction coordinate.

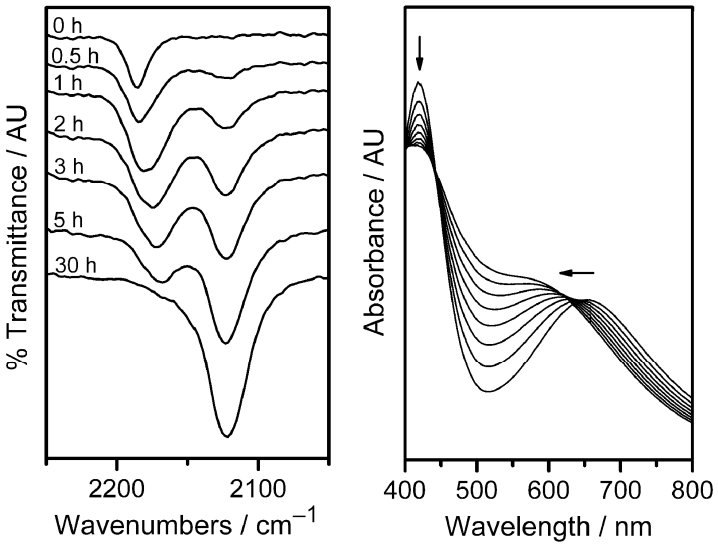


Figure 2.3. Left: Time-resolved infrared spectra for a pulverized sample of 3 heated at 80 °C. Right: UV-visible spectra collected at 10-minute intervals for a room-temperature solution of **3** in a 2:1 mixture of acetonitrile and ethanol. Arrows indicate the direction of peak shifts with time.

Variable-temperature magnetic susceptibility measurements were performed on **2** and **3** to probe the magnetic coupling within the isomeric clusters (see Figure 2.4). At 285 K, **3** exhibits $\chi_M T$ = 19.13 cm^3·K/mol, which is slightly higher than the value of 17.25 cm^3·K/mol expected for eight Cr^{III} centers ($S = {}^3/_2$) and six Cu^{II} centers ($S = {}^1/_2$) assuming g = 2.00 and no exchange coupling. As the temperature decreases, $\chi_M T$ rises, attaining a maximum of 108.5 cm^3·K/mol at 16 K. This behavior indicates the presence of ferromagnetic exchange coupling, as expected for cyanide bridges between octahedral Cr^{III} ($t_{2g}{}^3$) and square pyramidal Cu^{II} (b_{1g}) centers.[14] The maximum for $\chi_M T$ is close to the 120 cm^3·K/mol expected for an S = 15 ground state with g = 2.00. The downturn in the data below 18 K is attributed to Zeeman splitting of the M_S levels in the presence of an applied magnetic field, as evidenced by the calculated behavior for an S = 15 state in a 5000 Oe field (solid line in Fig 3). The magnetic data for **2** follow a similar trend, reaching a maximum of 107.8 cm^3·K/mol at 18 K. Notably, the two data sets do not superimpose, with the $\chi_M T$ data for **2** rising more rapidly as the temperature decreases. This indicates that the ferromagnetic coupling is somewhat stronger in the half-isomerized cluster of **2** than in the unisomerized cluster of **3**. Unfortunately, the large number of spins associated with the cluster precludes a quantitative determination of the magnitude of the coupling.

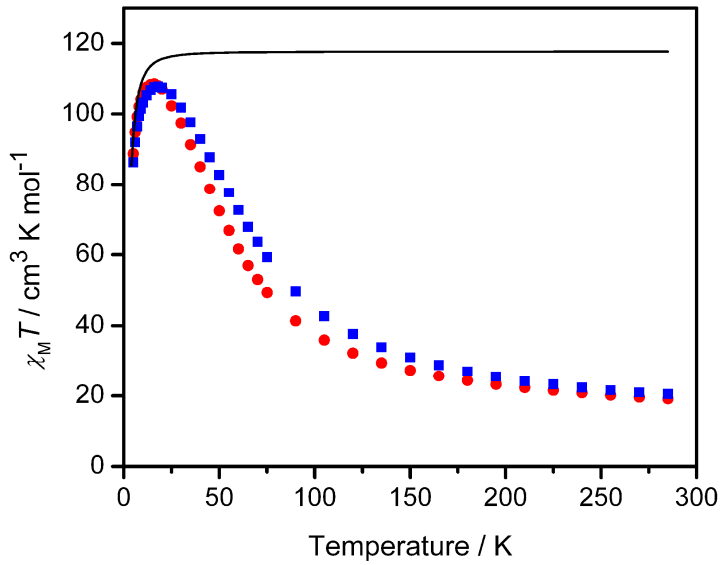


Figure 2.4. Temperature dependence of $\chi_M T$ for **2** (squares) and **3** (circles), as measured in an applied field of 5000 Oe. The solid line indicates the values calculated for population of only an S = 15 state with g = 2.00 and inclusion of the Zeeman splitting.

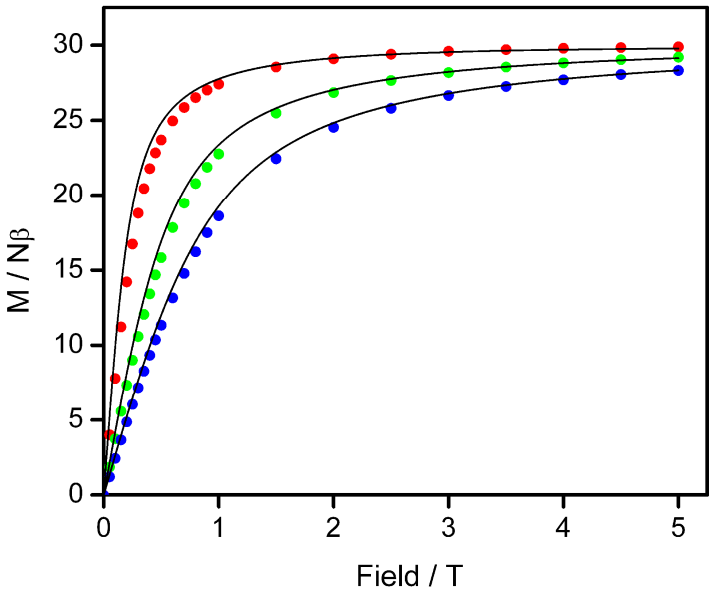


Figure 2.5. Magnetization data for **3** collected at 2 (circles), 5 (squares), and 8 K (triangles). The solid lines represent the simulated Brillouin function for an S = 15 molecule with g = 1.99.

Low-temperature magnetization data collected for **2** and **3** confirm the high-spin ground states (see Figure 2.5). In each case, the observed data at 2, 5, and 8 K closely agree with the calculated Brillouin functions, indicating the presence of a well-isolated S = 15 ground state with negligible zero-field splitting. To our knowledge, this is the second highest ground state spin yet observed in a metal-cyanide cluster, behind the $S = {}^{39}/_{2}$ ground states of the centered, face-capped octahedral clusters $(ROH)_{24}Mn_9M_6(CN)_{48}$ (M = Mo, W; R = Me, Et).[15] Consistent with the apparent lack of magnetic anisotropy, no out-of-phase signal was observed for either sample in ac magnetic susceptibility measurements performed at temperatures as low as 1.8 K with switching frequencies of up to 1500 Hz.

2.4. Conclusions and Outlook

The foregoing results demonstrate the utility of the new $S = {}^{3}/_{2}$ complex $[TpCr(CN)_3]^-$ in generating face-centered cubic clusters with high-spin ground states. These clusters are soluble in a variety of common solvents, and future efforts will focus on their use as building units via substitution of the outer water ligands. Additional experiments will be directed toward substituting heterometals at either the corner or face-centering metal sites as a mean of enhancing anisotropy and generating single-molecule magnets.

2.5 Acknowledgments

We thank Tyco Electronics for providing T.D.H. with a predoctoral fellowship.

2.6 References

(1) (a) Sessoli, R.; Tsai, H. L.; Schake, A. R.; Wang, S.; Vincent, J. B.; Folting, K.; Gatteschi, D.; Christou, G.; Hendrickson, D. N. *J. Am. Chem. Soc.* **1993**, *115*, 1804. (b) Sessoli, R.; Gatteschi, D.; Caneschi, A.; Novak, M. A. *Nature* **1993**, *365*, 141.

(2) (a) Castro, S. L.; Sun, Z. M.; Grant, C. M.; Bollinger, J. C.; Hendrickson, D. N.; Christou, G. *J. Am. Chem. Soc.* **1998**, *120*, 2365. (b) Barra, A. L.; Caneschi, A.; Cornia, A.; Fabrizi de Biani, F.; Gatteschi, D.; Sangregorio, C.; Sessoli R.; Sorace, L. *J. Am. Chem. Soc*. **1999**, *121*, 5302. (c) Oshio, H.; Hoshino, N.; Ito, T.; Nakano, M. *J. Am. Chem. Soc.* **2004**, *126*, 8805. (d) Maheswaran, S.; Chastanet, G.; Teat, S. J.; Mallah, T.; Sessoli, R.; Wernsdorfer, W.; Winpenny, R. E. P. *Angew. Chem., Int. Ed.* **2005**, *44*, 5044.

(3) (a) Scuiller, A.; Mallah, T.; Verdaguer, M.; Nivorozkhin, A.; Tholence, J. L.; Veillet, P. *New J. Chem.* **1996**, *20*, 1. (b) Van Langenberg, K.; Batten, S. R.; Berry, K. J.; Hockless, D. C. R.; Moubaraki, B.; Murray, K. S. *Inorg. Chem.* **1997**, *36*, 5006. (c) Sokol, J. J.; Hee, A. G.; Long, J. R. *J. Am. Chem. Soc.* **2002**, *124*, 7656l. (d) Berlinguette, C. P.; Vaughn, D.; Cañada-Vilalta, C.; Galán-Mascarós, J. R.; Dunbar, K. R. *Angew. Chem., Int. Ed.*, **2003**, *42*, 1523. (e) Schelter, E. J.; Prosvirin, A. V.; Dunbar, K. R. *J. Am. Chem. Soc.* **2004**, *126*, 15004. (f) Beltran, L. M. C.; Long, J. R. *Acc. Chem. Res.* **2005**, *38*, 325. (g) Song, Y.; Zhang, P.; Ren, X.-M.; Shen, X.-F.; Li, Y.-Z.; You, X.-Z. *J. Am. Chem. Soc.* **2005**, *127*, 3708. (h) Li, D.; Parkin, S.; Wang, G.; Yee, G. T.; Clérac, R.;

Wernsdorfer, W.; Holmes, S. M. *J. Am. Chem. Soc.* **2006**, *128*, 4214. (i) Wang, C.-F.; Zuo, J.-L.; Bartlett, B. M.; Song, Y.; Long, J. R.; You, X.-Z. *J. Am. Chem. Soc.* **2006**, *128*, 7162. (j) Glaser, T.; Heidemeier, M.; Weyhermüller, T.; Hoffmann, R.-D.; Rupp, H.; Müller, P. *Angew. Chem., Int. Ed.* **2006**, *45*, 6033.

(4) Berseth, P. A.; Sokol, J. J.; Shores, M. P.; Heinrich, J. L.; Long, J. R. *J. Am. Chem. Soc.* **2000**, *122*, 9655.

(5) (a) Lescoueezec, R.; Vaissermann, J.; Lloret, F.; Julve M.; Verdaguer, M. *Inorg. Chem.* **2002**, *41*, 5943. (b) Kim, J.; Han, S.; Cho, I.-K.; Choi, K. Y.; Heu, M.; Yoon, S.; Suh, B. J. *Polyhedron* **2004**, *23*, 1333.

(6) Wang, S.; Zuo, J.-L.; Zhou, H.-C.; Song, Y.; Gao, S. You, X.-Z. *Eur. J. Inorg. Chem.* **2004**, *18*, 3681.

(7) Wang, C.-F.; Zuo, J.-L.; Zhou, H.-C.; Choi, H. J.; Ke, Y.; Long, J. R.; You, X.-Z. *Angew. Chem., Int. Ed.* **2004**, *43*, 5940.

(8) Trofimenko, S. *Inorg. Synth.* **1970**, *12*, 99.

(9) Shamir, J. *Inorg. Chim. Acta* **1989**, *156*, 163.

(10) Rojas, R.; Valderrama, M.; Wu, G. *Inorg. Chem. Commun.* **2004**, *7*, 1295.

(11) Wang, S.; Zuo, J.-L.; Gao, S.; Song, Y.; Zhou, H.-C.; Zhang, Y.-Z.; You, X.-Z. *J. Am. Chem. Soc.* **2004**, *126*, 8900.

(12) (a) Li, D.; Parkin, S.; Wang, G.; Yee, G.; Holmes, S. M. *Inorg. Chem.* **2006**, *45*, 1951. (b) Li, D.; Parkin, S.; Wang, G.; Yee, G.; Holmes, S. M. *Inorg. Chem.* **2006**, *45*, 2773.

(13) (a) Shriver, D. F.; Shriver, S. A.; Anderson, S. E. *Inorg. Chem.* **1965**, *4*, 725. (b) Brown, D. B.; Shriver, D. F.; Schwartz, L. H. *Inorg. Chem.* **1968**, *7*, 77. (c) Brown, D. B.; Shriver, D. F. *Inorg. Chem.* **1969**, *8*, 37. (d) House, Jr., J. E.; Bailar, Jr., J. C. *Inorg. Chem.* **1969**, *8*, 672. (e) Reguera, E.; Bertrán, J. F.; Nuñez, L. *Polyhedron* **1994**, *13*, 1619. (f) Martínez-Garcia, R.; Knobel, M.; Reguera, E. *J. Phys. Chem. B.* **2006**, *110*, 7296.

(14) (a) Entley, W. R.; Trentway, C. R.; Girolami, G. S. *Mol. Cryst. Liq. Cryst.* **1995**, *273*, 153. (b) Weihe H.; Güdel, H. U. *Comments Inorg. Chem.* **2000**, *22*, 75.

(15) (a) Zhong, Z. J.; Seino, H.; Mizobe, Y.; Hidai, M.; Fujishima, A.; Ohkoashi, S.; Hashimoto, K. *J. Am. Chem. Soc.* **2000**, *122*, 2952. (b) Ruiz, E.; Rajaraman, G.; Alvarez, S.; Gillon, B.; Stride, J.; Clérac, R.; Larionova, J.; Decurtins, S. *Angew. Chem., Int. Ed.* **2005**, *44*, 2711. (c) Freedman, D. E.; Bennett, M. V.; Long, J. R. *Dalton Trans.* **2006**, 2829.

Chapter 3: Survey of Uranium-Containing Molecules Exhibiting Magnetic Exchange

3.1 Introduction

Interest in the magnetic properties of actinide-containing compounds stems from their unique characteristics relative to transition metal- and lanthanide-containing magnetic materials. In many ways, these characteristics can be seen as a blending of the typical magnetic behavior associated with lanthanide compounds, such as spin-orbit coupling and relativistic effects, with that observed in transition metal compounds, such as strong magnetic superexchange. While the magnetic properties of actinide-containing complexes are of interest on a fundamental level, they can also potentially be exploited in producing discrete molecules that exhibit slow magnetic relaxation.[1] Such molecules are known as single-molecule magnets, and their unusual behavior arises from the influence of a negative axial magnetic anisotropy, D, on a high-spin ground state, S. The resulting relaxation barrier of $U = S^2|D|$ for integer S values (or $U = (S^2 - {}^1/_4)|D|$ for half-integer S values) is at most 60 cm^{-1} for known transition metal clusters.[1d] The possibility of increasing this barrier height, and perhaps opening the way for potential applications,[1c,2] provides impetus for the development of new approaches to generating single-molecule magnets.

Transition metals have served extremely well for generating discrete clusters, wherein strong magnetic coupling between many metal centers gives rise to concerted behavior with a large total spin quantum number, S.[3] However, owing to their large single-ion anisotropies, some of the systems exhibiting the largest axial zero-field splitting parameters instead contain lanthanide ions.[4] Indeed, the anisotropy associated with lanthanide ions such as Tb^{3+} and Dy^{3+} has led to manifestations of slow magnetic relaxation, even in molecules containing just one metal center.[5] Despite such large single-ion anisotropy contributions, it is difficult to envision high-nuclearity lanthanide clusters with concerted spin behavior because the 4f valence orbitals typically lack the radial extension necessary to have significant overlap with bridging ligand orbitals.[6] This orbital overlap is requisite for magnetic superexchange through a diamagnetic bridging ligand. In contrast, the greater radial extension of the 5f valence orbitals of actinides can potentially provide increased overlap with bridging ligand orbitals, thereby enhancing the concerted magnetic behavior between bridged metal centers within a single cluster unit.[5a,7]

In this review, we survey recent developments in the synthesis and characterization of molecular systems in which actinide ions potentially engage in magnetic exchange interactions. Thus far, efforts have focused exclusively on species incorporating uranium, since this actinide element offers a minimal radioactivity (in depleted form) with accessible oxidation states allowing for zero, one, two, or three unpaired electrons. Researchers have confronted the intricacies of the magnetic exchange in a number of interesting ways, often with the goal of identifying and, to the extent possible, quantifying ferro- or antiferromagnetic exchange coupling. Understanding these exchange interactions is not only essential to development of models for the basic

electronic structure of the 5f elements, but also may represent the key to producing the first actinide-based single-molecule magnets.

3.2 A Diuranium Complex

The first observation of magnetic exchange coupling in an actinide-containing molecule was reported nearly 20 years ago for the binuclear, 1,4-diimidobenzene-bridged complex $[(MeC_5H_4)_3U]_2(\mu\text{-}1,4\text{-}N_2C_6H_4)$.[8] The presence of coupling between the two U^V centers within this molecule became evident upon a comparison of its variable-temperature magnetic susceptibility to that of structurally similar compounds. The geometric isomer $[(MeC_5H_4)_3U]_2(\mu\text{-}1,3\text{-}N_2C_6H_4)$, for instance, displays essentially constant magnetic susceptibility (χ_M) with decreasing temperature from 300 K down to ca. 150 K, at which point it begins to rise monotonically as the temperature is decreased to 5 K. This behavior, typical of an isolated $5f^1$ center, is essentially the sum of that observed for two $(MeC_5H_4)_3U(NPh)$ complexes and indicates the lack of any magnetic exchange between the two U^V centers.[8,9] In contrast, the magnetic susceptibility data obtained for $[(MeC_5H_4)_3U]_2(\mu\text{-}1,4\text{-}N_2C_6H_4)$ display similar behavior down to ca. 75 K but then exhibit a downturn at lower temperatures, indicative of antiferromagnetic coupling (see Figure 3.1).

In an attempt to obtain a quantitative determination of the coupling in $[(MeC_5H_4)_3U]_2(\mu\text{-}1,4\text{-}N_2C_6H_4)$, the experimental χ_M vs. T data were compared to calculated susceptibilities. The magnetic interaction between the U^V centers was modeled by employing the following Ising Hamiltonian for an isolated dinuclear complex:

$$\hat{H} = -2J(\hat{S}_{z1} \cdot \hat{S}_{z2}) + g_{\parallel}\mu_B \hat{H}_z \cdot (\hat{S}_{z1} + \hat{S}_{z2}) \qquad (1)$$

here $\hat{S}_{zn}$ is the effective spin operator for each $S = {}^1/_2$ U^V ion (the z direction is defined as along the U···U axis), J is the exchange constant, $g_{\parallel}$ is the Landé g factor, μ_B is the Bohr magneton, and $\hat{H}_z$ is the magnetic field vector. Note that this Hamiltonian does not account for deviations in the magnetic susceptibility resulting from depopulation of the uranium Stark sublevels with decreasing temperature but rather it assumes such deviations arise solely from exchange between two $S = {}^1/_2$ ions. This assumption was made based on an analysis of the electron paramagnetic resonance (EPR) spectrum, which suggested that only the lowest Stark sublevel is populated at low temperature. The $J = {}^5/_2$ ground state for a U^V center is split by the ligand field into three Stark sublevels, two corresponding to $\mu = \pm{}^1/_2$ and one corresponding to $\mu = \pm{}^3/_2$, where μ is the crystal quantum number.[10] Considering EPR selection rules, a spectrum is expected for a sublevel with crystal quantum number $\mu = \pm{}^1/_2$, while no spectrum is expected for a sublevel with crystal quantum number $\mu = \pm{}^3/_2$. The uncoupled dinuclear complex, $[(MeC_5H_4)_3U]_2(\mu\text{-}1,3\text{-}N_2C_6H_4)$, gave no EPR spectrum at 4 K, suggesting population of only the lowest-energy Stark sublevel, $\mu = \pm{}^3/_2$. Thus, the drop in the magnetic susceptibility of $[(MeC_5H_4)_3U]_2(\mu\text{-}1,4\text{-}N_2C_6H_4)$, at least at such very low temperatures, can be attributed to magnetic exchange rather than the usual effects of the Stark sublevel depopulation. Figure 3.1 shows the resulting calculated and experimental susceptibility data. The differences between the two experimental data sets were attributed to sample impurity and, as such, the calculated data were modeled with varying amounts of paramagnetic impurity. On the basis of these parameters, the best fit was obtained with an exchange constant of $J = -19$ cm^{-1} and an estimated paramagnetic impurity of 1 mol %.

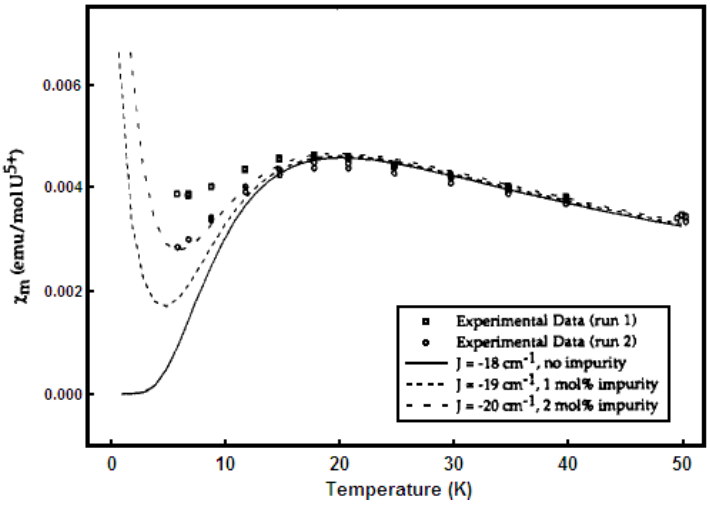


Figure 3.1. Experimental (symbols) versus calculated (lines) molar magnetic susceptibility for $[(MeC_5H_4)_3U]_2(\mu\text{-}1,4\text{-}N_2C_6H_4)$. Each calculated curve is modeled with a different amount of the paramagnetic impurity, $(MeC_5H_4)_3U(THF)$. Taken from Ref 8.

3.3. Other Multiuranium Systems

Although our focus is on actinide-containing molecules for which the occurrence of magnetic coupling has been directly probed, there are a number of intriguing multiuranium systems wherein magnetic exchange is likely but has not been rigorously investigated. For example, attempts to produce clusters that might feature uranium–uranium bonds led to a number of simple diuranium alkoxides, including $[U_2(O_2CMe_3)_9]^{0/1-}$,[11] and the chloro-bridged species $[(C_6Me_6)_2U_2Cl_7]^-$.[12] On the basis of the assumption that nitrogenous ligands promote bridging in actinides,[13] a number of di-, tri-, and tetranuclear uranium amide species were synthesized, including the dinuclear complex $[U(\eta\text{-}C_8H_8)]_2[\mu\text{-}\eta^4\text{:}\eta^4\text{-}HN(CH_2)_3N(CH_2)_2N(CH_2)_3NH]$, which contains the shortest U···U separation yet observed in a molecule.[14] Diuranium systems featuring an arene bridge, such as $[(Mes(^tBu)N)_2U]_2(\mu\text{-}\eta^6\text{:}\eta^6\text{-}C_7H_8)$ and $[(Cp^*)_2U]_2(\mu\text{-}\eta^6\text{:}\eta^6\text{-}C_6H_6)$,[15] and the pyrazolate-bridged dimer $[U(Me_2Pz)_4]_2$ (Me_2Pz^- = 3,5-dimethylpyrazolate),[16] also present the strong possibility of magnetic exchange coupling.

While the foregoing examples constitute only a fraction of the molecular uranium clusters that might exhibit magnetic exchange coupling, they do serve to give an idea of how much synthetic work has already been accomplished in the area. In addition, symmetric dinuclear complexes such as these would serve well in testing general electronic structure models attempting to account for the influence of exchange coupling on the magnetic behavior of actinide ions. Given the current lack of reliable models, a significant step toward probing the presence of exchange coupling in such species would be the development of synthetic methods for preparing mixed-actinide analogues, wherein one of the two actinide centers is rendered diamagnetic. Here, the replacement of

one of the U^{IV} centers with a Th^{IV} center, or one of the U^{III} centers with an Ac^{III} center,[17] would enable a subtraction approach of the type elaborated below to be applied in providing a qualitative assessment of the exchange coupling.

Another type of uranium-containing molecule that offers promise in the area of molecular magnetism is the high-nuclearity uranium oxo cluster. While most oxo-bridged uranium complexes are di- or trinuclear species,[18] it was recently shown that hydrolysis of $UI_3(THF)_4$ in the presence of water and other ligands can result in higher-nuclearity clusters.[19] The largest of these is the discrete dodecanuclear species $U_{12}(\mu_3\text{-}O)_{12}(\mu_3\text{-}OH)_8I_2(\mu_2\text{-}O_3SCF_3)_{16}(CH_3CN)_8$, which contains a double-decker square-antiprism $U_{12}O_{12}(OH)_8$ core.[19d] This type of cluster, while well beyond the scope of current techniques for analyzing magnetic exchange coupling, may offer prospects for observation of the SMM behavior in uranium systems. Indeed, such clusters could potentially combine the desirable properties of large spin and single-ion anisotropy with the high coupling strength of the oxo bridge.

3.4. A Uranium–Lanthanide System

Recently, evidence of exchange coupling was reported for the bent trinuclear 4f–5f cluster $Cp^*_2U[(NC(CH_2C_6H_5)tpy)YbCp^*_2]_2$ (UYb_2; tpy = terpyridyl).[20] The structure of this species features a central $[Cp^*_2U^{IV}]^{2+}$ unit connected through $NC(CH_2C_6H_5)$tpy bridges to two $[Cp^*_2Yb]^{x+}$ (x = 0 or 1) moieties, as shown in Figure 3.2. The cyclic voltammetry and electronic absorption spectra of the UYb_2 cluster suggest the presence of both $Cp^*_2Yb^{II}$tpy and $Cp^*_2Yb^{III}$tpy$^{\bullet}$ species at room temperature.[21] The variable-temperature magnetic susceptibility data obtained for the cluster are plotted in Figure 3.3. Here, $\chi_M T$ follows a gradual downward trend from 350 K to ca. 25 K, followed by a precipitous drop at lower temperatures, which can be understood largely in terms of the orbital angular momentum quenching discussed above for $5f^1$ systems. However, the gradual decline in $\chi_M T$ from its room temperature value is characteristic of multielectron f-element-containing complexes and is generally attributed to thermal depopulation of the Stark sublevels.[10] However, the behavior observed here is further complicated by the presence of both diamagnetic Yb^{II} and paramagnetic Yb^{III} ions, in addition to an unpaired electron residing on the terpyridine fragment.

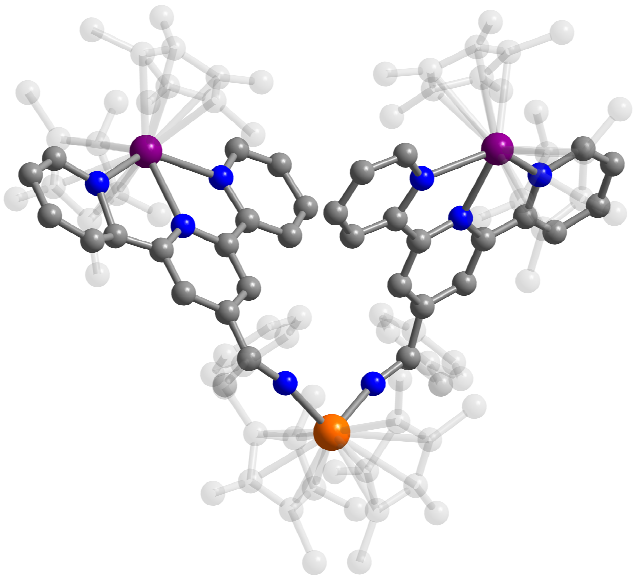


Figure 3.2. Structure of $Cp^*_2U[(NC(CH_2C_6H_5)tpy)YbCp^*_2]_2$.[20] Orange, purple, blue, and gray spheres represent U, Yb, N, and C atoms, respectively; H atoms are omitted for clarity. The Cp* ligands and benzyl groups are drawn transparently for better visualization of the core structure.

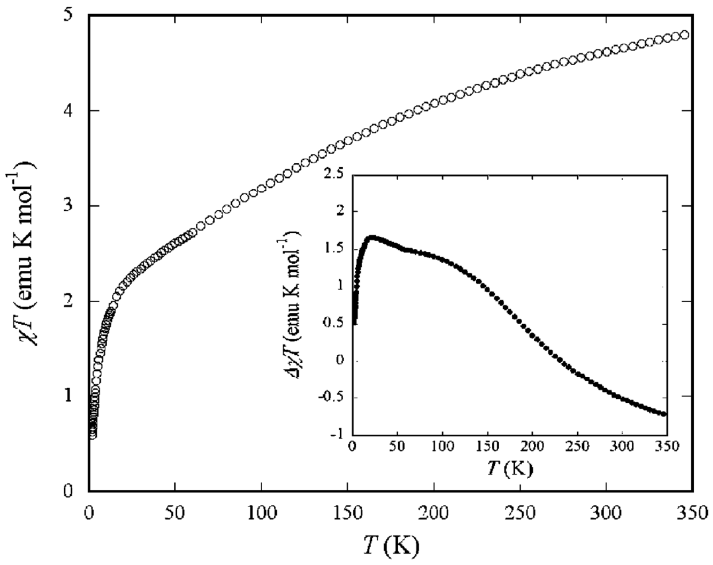


Figure 3.3. Variable-temperature magnetic susceptibility data for $Cp^*_2U[(NC(CH_2C_6H_5)tpy)YbCp^*_2]_2$. Inset: Variable-temperature magnetic susceptibility data obtained upon subtracting data obtained for $Cp^*_2U(NC(CH_2C_6H_5)tpy)_2$ and $Cp^*_2Th[(NC(CH_2C_6H_5)$-$tpy)YbCp^*_2]_2$ from the UYb_2 data. Taken from Ref 20.

In an attempt to deconvolute the magnetic data and extract information regarding potential exchange interactions between the U^{IV} and Yb^{III} centers, a stepwise series of subtractions was performed on the UYb_2 data. First, $\chi_M T$ data collected for the precursor complex $Cp^*_2U(NC(CH_2C_6H_5)tpy)_2$ were subtracted from the UYb_2 data to remove any orbital contribution from the U^{IV} ion to the overall magnetism. Then, to eliminate the magnetic contribution from Yb^{III}, $\chi_M T$ data collected for $Cp^*_2Th[(NC(CH_2C_6H_5)tpy)YbCp^*_2]_2$ ($ThYb_2$) were subtracted. The result of these subtractions, shown as $\Delta\chi_M T$ in the inset of Figure 3.3, is a data set that follows a monotonic increase with decreasing temperature from 350 K to ca. 15 K and then drops precipitously at lower temperatures. The rise in $\Delta\chi_M T$ is interpreted as evidence of exchange coupling within the cluster, although the specific nature of the coupling is unclear because the U^{IV} and Yb^{III} ions and the terpyridine radical represent three distinct paramagnetic centers. The curvature of the data above 60 K is attributed to electronic differences between the UYb_2 and $ThYb_2$ clusters, as evidenced in cyclic voltammetry, where the redox peaks for the two clusters are shifted relative to one another. Furthermore, the authors note that the negative values for $\Delta\chi_M T$ represent an overcorrection during the subtraction process. Thus, while qualitative interpretation of $\Delta\chi_M T$ vs. T suggests the presence of magnetic coupling, the complexity of this system may prohibit a quantitative analysis.

The magnetic properties of an analogous trinuclear species, $Cp^*_6U_3(NC(CH_2C_6H_5)tpy)_2$, in which U^{III} replaces both of the Yb centers, exhibit a similar trend where $\chi_M T$ decreases with decreasing temperature.[22] However, the complications encountered in the data analysis of the UYb_2 species, along with the lack of diamagnetic analogues to the $U^{IV}U^{III}_2$ cluster, have thus far made it impossible to deconvolute the many factors contributing to the magnetic susceptibility and isolate evidence of magnetic exchange coupling.

3.5 Uranium–Transition Metal Systems

To date, the most comprehensively studied class of actinide-containing molecules exhibiting magnetic exchange interactions is a series of trinuclear uranium–transition metal assemblies synthesized by Ephritikhine and coworkers. These clusters have the form $UL^i_2M_2(py)_n$ (M = Cu, Zn; py = pyridine), where L^i is one of a series of nine Schiff-base bridging ligands, each with a modified diimino hydrocarbon backbone (see Figure 3.4).[23] The structure of each cluster consists of a central U^{IV} ion coordinated linearly to two M^{II} ions through orthogonal $(L^i)^{4-}$ bridges, as represented in Figure 3.5. The U^{IV} center resides in a dodecahedral coordination environment, encapsulated by eight O donor atoms. Each M^{II} center is coordinated to two N atoms and two O atoms of the Schiff base in a distorted square-planar geometry and is bound by zero, one, or two pyridine molecules, depending on the bridging ligand. Importantly, the coordination environment around the U^{IV} center remains invariant with changes in the bridging ligand and number of transition metal-coordinated pyridine molecules, suggesting that differences in the magnetic behavior across the series are not due to alterations in the ligand field of the uranium ion.

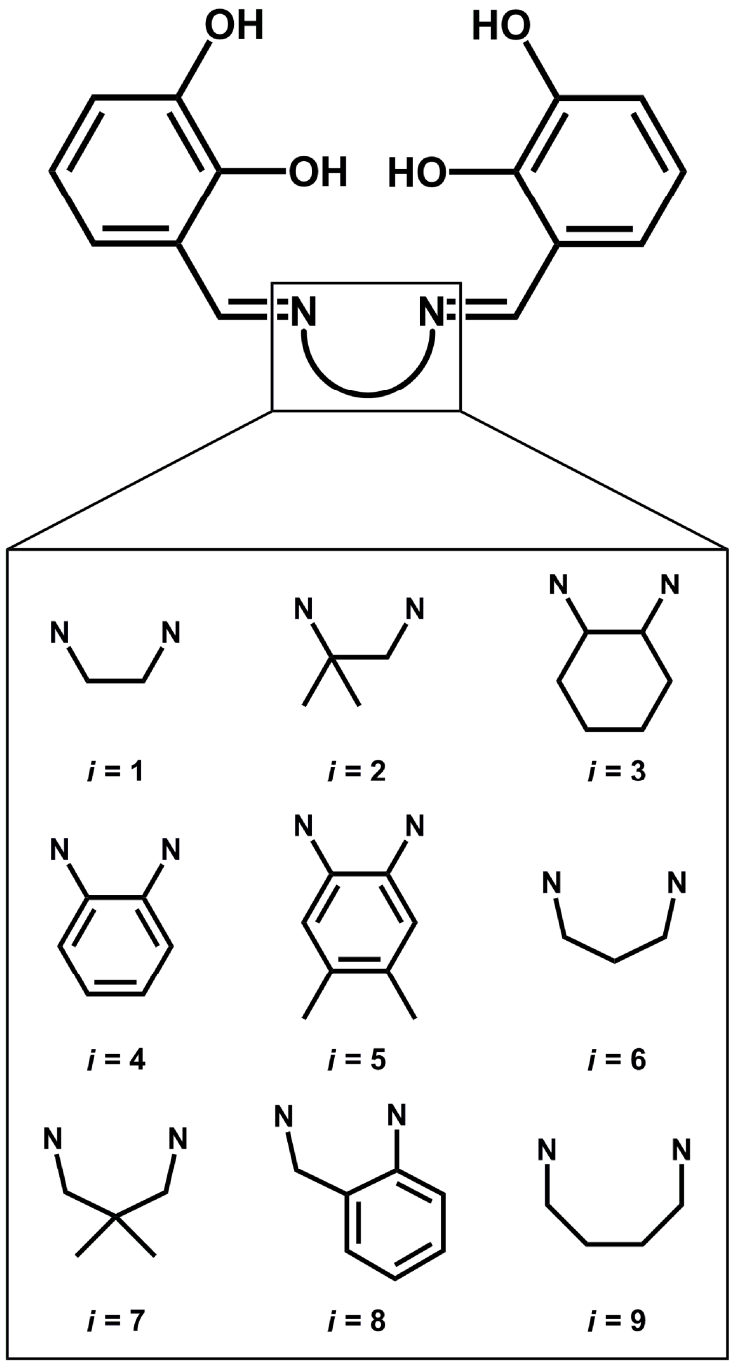


Figure 3.4. Schematic representation of the ligand precursors H_4L^i. Note the two-carbon backbone for i = 1-5, three-carbon backbone for i = 6-8, and four-carbon backbone for i = 9.

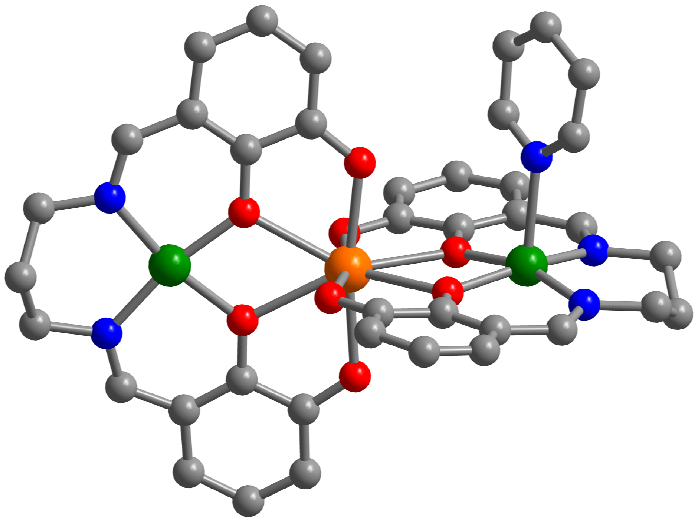


Figure 3.5. Structure of $UL^{6}{}_{2}Cu_{2}(py)$. Orange, green, red, blue and gray spheres represent U, Cu, O, N, and C atoms, respectively; H atoms are omitted for clarity.

The isolation of isostructural copper and zinc analogues of the $UL^{i}{}_{2}M_{2}(py)_{n}$ clusters enabled the use of a subtraction method similar to the one described above, thereby providing a route through which to investigate the magnetic interaction between the U^{IV} and Cu^{II} ions without contamination by single-ion effects of U^{IV}. Variable-temperature magnetic susceptibility data for $UL^{7}{}_{2}M_{2}(py)$ (M = Cu, Zn) are shown at the top of Figure 3.6. For the UZn_{2} cluster, $\chi_{M}T$ remains essentially constant at 0.8 $cm^{3}\cdot K/mol$ as the temperature is lowered from 300 to 100 K and then drops precipitously at lower temperatures, tending toward zero at 2 K. This drop, typical of U^{IV} complexes with a $5f^{2}$ valence electron configuration, can be attributed to the depopulation of the Stark sublevels and subsequent quenching of the total angular momentum, as described above. The $\chi_{M}T$ data for the UCu_{2} cluster exhibit a similar trend, holding constant at 1.7 $cm^{3}\cdot K/mol$ down to 100 K before dropping to 0.8 $cm^{3}\cdot K/mol$ at 2 K, close to the value of 0.75 $cm^{3}\cdot K/mol$ expected for two noninteracting $S = {}^{1}/_{2}$ Cu^{II} centers with $g = 2.00$. Subtraction of the UZn_{2} data from the UCu_{2} data (see Figure 3.6, lower) removes any contribution from the U^{IV} ion, leaving only the spin contribution of the two Cu^{II} ions together with any vestiges of magnetic exchange coupling. Indeed, the product of the subtracted data sets displays a monotonic rise with decreasing temperature, reaching a maximum at $\Delta\chi_{M}T = 0.95$ $cm^{3}\cdot K/mol$. This increase in $\chi_{M}T$ is attributed to a ferromagnetic exchange interaction between the U^{IV} and Cu^{II} centers. Although the subtracted data led to the qualitative determination of the sign of the exchange constant ($J > 0$ for ferromagnetic coupling), no attempts to quantify the magnitude of the interaction have been put forth.

While ferromagnetic coupling is observed for $UL^{7}{}_{2}Cu_{2}(py)$, the nature of the exchange appears highly dependent on the identity of the bridging Schiff base and/or number of pyridine molecules coordinated to the copper center, as found upon a

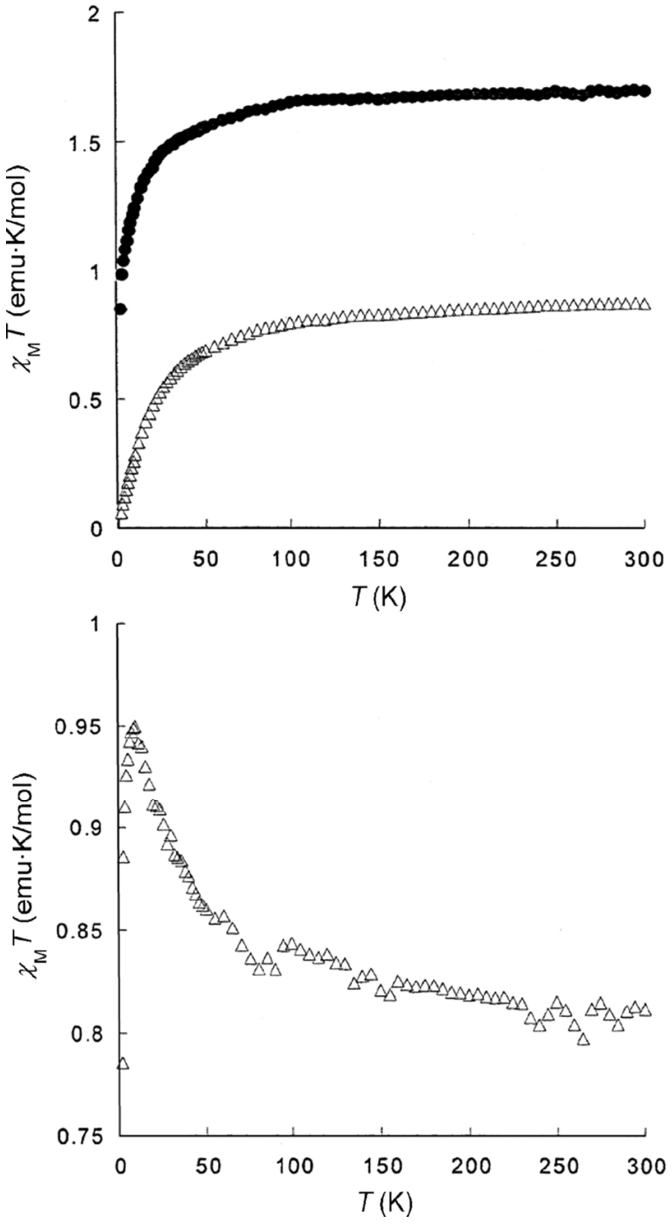


Figure 3.6. Upper: Variable-temperature magnetic susceptibility data for $UL^7{}_2Cu_2(py)$ (filled circles) and $UL^7{}_2Zn_2(py)$ (open triangles) clusters. Lower: Variable-temperature magnetic susceptibility data ($\Delta\chi_M T$) obtained upon subtracting the UZn_2 data from the UCu_2 data. Adapted from Ref 23b.

comparison of the entire series of UM_2 clusters. For i = 6, 8, and 9, behavior similar to that of $UL^7{}_2Cu_2(py)$ was observed, indicative of ferromagnetic coupling. In contrast, for i = 1–5, $\Delta\chi_M T$ turns down below 100 K, indicating an antiferromagnetic exchange interaction. The shift from antiferromagnetic to ferromagnetic coupling occurs as the backbone of the Schiff base increases from two C atoms (i = 1–5) to three (i = 6–8) or four C atoms (i = 9). This phenomenon is attributed to an increase in the Cu···U distance, which is associated with a lengthening in the diimino chain. It should be noted, however, that the observation of an increased metal separation is based on the structural characterization of only four UCu_2 clusters (i = 2, 6, 7, and 9), for which the average Cu···U distances are 3.538, 3.661, 3.641, and 3.647 Å, respectively. In addition, the magnetic behavior may be affected by other exchange pathways, as evidenced by a downturn in $\chi_M T$ below 15 K observed in the analogous $ThL^i{}_2Cu_2$ clusters (i = 1 and 2) and deviation of the magnetization data for $UL^i{}_2Cu_2$ (i = 1–5) at 2 K from the Brillouin function. This weak effect is attributed to a long-range intramolecular Cu···Cu interaction and may play an important role in influencing the overall magnetism. In explaining this behavior, the authors note that similar magnetostructural correlations have been documented in gadolinium–transition metal species, where exchange interactions were found to vary with factors such as Cu···Gd distances and dihedral angles between O–Cu–O and O–Gd–O planes.[24]

Analogous trinuclear clusters of the form $UL^7{}_2M_2(py)_2$ (M = Co, Ni, Zn) were prepared to probe the effect of the transition metal on the overall magnetic properties of the cluster.[23a,b,d] Application of the subtraction method to these systems gave $\Delta\chi_M T$ vs. T plots that show behavior suggestive of antiferromagnetic coupling between the central U^{IV} ion and the paramagnetic transition metal ions, in contrast to the ferromagnetic coupling exhibited by the UCu_2 cluster. However, as the authors note, spin–orbit effects associated with high-spin Co^{II} centers may complicate the interpretation of the magnetic data for the UCo_2 cluster. Similarly, the downturn in the data for the UNi_2 cluster could potentially be attributed to zero-field splitting associated with the S = 1 Ni^{II} centers.

In addition to superexchange interactions, there has been a recent report suggesting that magnetic coupling may occur through direct metal–metal orbital overlap in the mixed-valence linear trinuclear cluster $[UFe^{II}Fe^{III}(C_5H_4NSi(^tBu)Me_2)_4]^+$.[25] This intriguing molecule, prepared through the one-electron oxidation of $UFe^{II}{}_2(C_5H_4NSi(^tBu)Me_2)_4$, exhibits a structure consisting of a central U^{IV} ion coordinated to two 1,1′-bis(amido)ferrocenyl derivatives (see Figure 3.7). Coordination of U^{IV} to the rigid ferrocenylamido moieties enforces U···Fe distances of 2.9556(5) and 2.9686(5) Å.

Variable-temperature magnetic moment measurements show very different behavior for the $UFe^{II}{}_2$ and $UFe^{II}Fe^{III}$ clusters (see Figure 3.8). In the case of the former species, with decreasing temperature, μ_{eff} follows the monotonic drop typical for a U^{IV} center with a $5f^2$ valence electron configuration. In contrast, for the $UFe^{II}Fe^{III}$ cluster, as the temperature is decreased from 300 K, μ_{eff} begins to rise immediately, following a seemingly linear trend before turning over below 20 K. The authors note that the observed behavior is indicative of a magnetic interaction between U^{IV} and Fe^{III} centers. Indeed, the result is without precedent because the spin–orbit coupling and ligand-field effects associated with a paramagnetic uranium center usually give rise to a steady

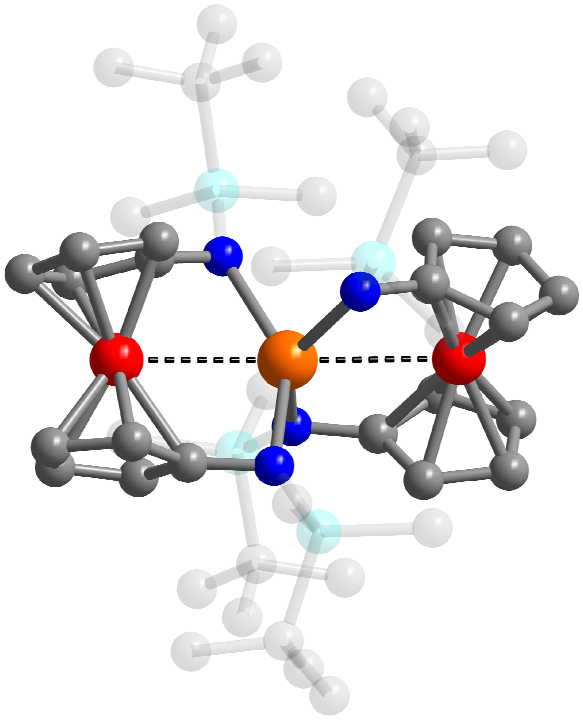


Figure 3.7. Structure of $[UFe^{II}Fe^{III}(C_5H_4NSi(^tBu)Me_2)_4]^+$.[27] Orange, red, blue, cyan, and gray spheres represent U, Fe, N, Si, and C atoms, respectively; H atoms are omitted for clarity. The $(^tBu)Me_2Si$ groups are drawn transparently for better visualization of the metal coordination environments.

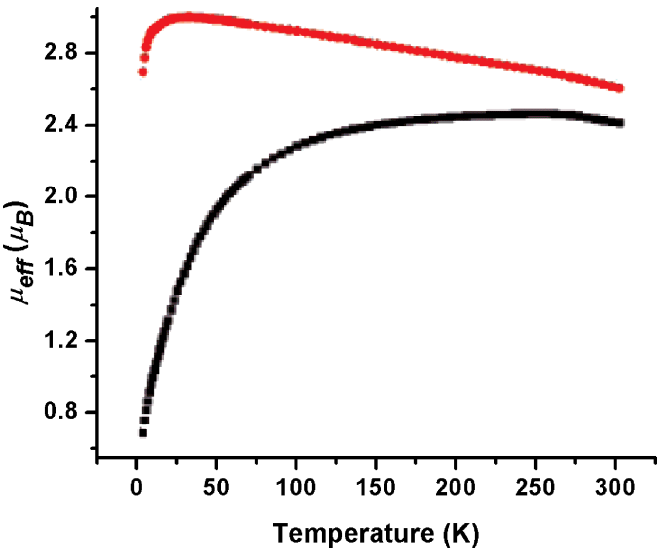


Figure 3.8. Variable-temperature magnetic data for $UFe^{II}_2(C_5H_4NSi(^tBu)Me_2)_4$ (black squares) and $[UFe^{II}Fe^{III}(C_5H_4NSi(^tBu)Me_2)_4](BPh_4)$ (red circles). Adapted from Ref 25.

decrease in the net magnetic moment as the temperature is lowered, even in systems exhibiting (weak) ferromagnetic exchange interactions. Thus, the steady increase in μ_{eff} starting at room temperature could be indicative of an extremely strong ferromagnetic exchange interaction mediated by direct orbital overlap between the metals. Note, however, that such a linear upward trend in the moment with decreasing temperature could also potentially arise from complications in applying corrections for the diamagnetic contributions of the unusual sample and/or the sample holder. If indeed the upward trend is the result of a strong ferromagnetic interaction, a simple subtraction of the UFe^{II}_2 data from the $UFe^{II}Fe^{III}$ data would not provide an appropriate means of extracting the pure exchange interaction from the overall magnetism because the added electron imposes a different ligand field on the central U^{IV} ion. Instead, access to a diamagnetic analogue, such as an isostructural species containing Co^{III} in place of Fe^{III}, could perhaps lend itself to the implementation of the subtraction method and estimation of the coupling strength for this interesting system.

3.6 Uranium–Radical Systems

Thus far, we have discussed exchange interactions between uranium and other paramagnetic metal centers; however, recent years have seen examples of uranium–radical systems showing evidence of magnetic exchange coupling. Compelling evidence of such an interaction was reported in 2005 in the radical complex $Cp^*_2U^{III}(tpy^{\cdot})$.[26] This molecule, which was prepared through a one-electron reduction of $[Cp^*_2U^{III}(tpy)]I$, features a U^{III} center coordinated by a terpyridyl ligand that houses an additional, delocalized electron. Structural analysis and NMR spectroscopy support the assignments of uranium and ligand oxidation states.

In an attempt to probe the potential exchange between the U^{III} center and the unpaired electron of the reduced ligand, magnetic susceptibility data were collected for both the radical complex and the cationic precursor complex, $[Cp^*_2U^{III}(tpy)]I$. Structural analysis revealed very similar ligand fields for the two species, enabling the use of the subtraction method, wherein the cationic complex data were subtracted from the radical complex data. The resulting $\chi_M T$ data remain essentially constant as the temperature is lowered from 300 K, before decreasing precipitously below 20 K. This interaction is attributed to antiferromagnetic coupling between the $S = {}^3/_2$ U^{III} center and the unpaired electron residing on the reduced terpyridyl ligand. While no attempt was made to quantify the coupling strength, the low temperature at which the drop in $\chi_M T$ is observed indicates that the interaction is relatively weak. One possible explanation for the exchange being weak is the large separation between the unpaired electron and the U^{III} center. While the electron is delocalized throughout the terpyridyl ligand, no good resonance form exists wherein the electron resides on a uranium-coordinated N atom. Alternatively, the drop in $\chi_M T$ may be the result of intermolecular exchange, possibly between radical ligands on neighboring molecules.

A second example of a uranium–radical complex has been found to bind and activate carbon dioxide.[27] This molecule was prepared by first encapsulating a U^{III} ion within the pocket of a bulky hexadentate ligand, $(^{Ad}ArO)_3tacn$ [$(^{Ad}ArOH)_3tacn$ = 1,4,7-tris(3-adamantyl-5-*tert*-butyl-2-hydroxybenzyl)-1,4,7-triazacyclonane], to give the electron-rich, coordinatively unsaturated complex $[(^{Ad}ArO)_3tacn]U$. Exposure of this

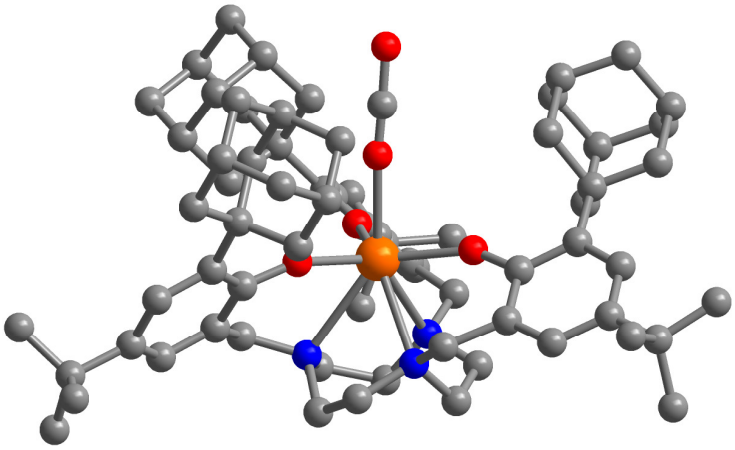


Figure 3.9. Structure of $((^{Ad}ArO)_3tacn)U(CO_2)$.[27] Orange, red, gray, and blue spheres represent U, O, C and N atoms, respectively; H atoms are omitted for clarity.

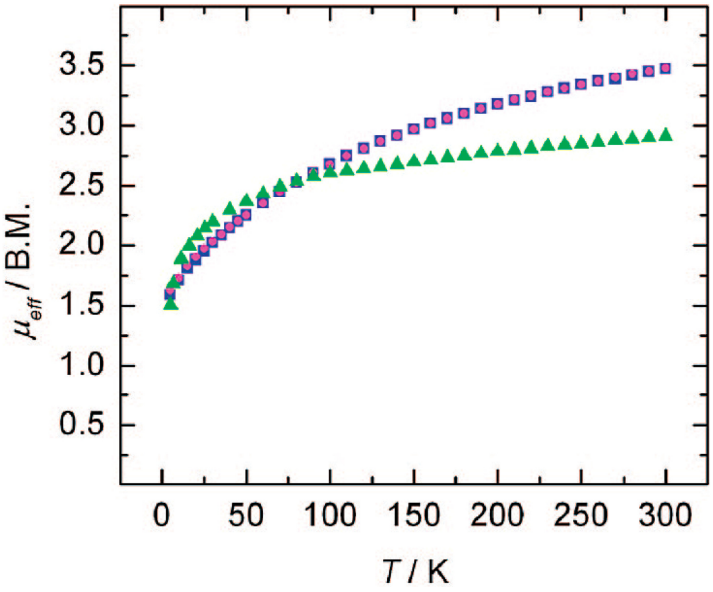


Figure 3.10. Variable-temperature magnetic moment data for $[((^{t\text{-}Bu}ArO)_3tacn)U^{IV}(OC\bullet^{t\text{-}Bu}Ph_2)]$ (magenta circles and blue squares) and $[((^{Ad}ArO)_3tacn)U^{IV}(CO_2)]$ (green triangles). The higher room-temperature moment for the former molecule is attributed to contribution from an $S = {}^3/_2$ U^{III} resonance form.

complex to an atmosphere of CO_2 initiates a one-electron transfer from the U^{III} center to the CO_2 ligand to afford $[(^{Ad}ArO)_3tacn]U^{IV}(CO_2)$, as depicted in Figure 3.9. The structure of the product reveals a remarkable η^1-OCO coordination to the U^{IV} ion, with U–C–O and O–C–O bond angles of 171.1(2)° and 178.0(3)°, respectively. The presence of an unpaired electron residing on the CO_2 carbon was inferred largely from the differences in $C–O_{terminal}$ vs $C–O_U$ bond lengths and shifts in the IR spectra compared to free CO_2, which suggest a bonding scheme comprised of the resonance forms $U^{IV}=O=C^{\bullet}–O^{-} \leftrightarrow U^{IV}–O\equiv C–O^{-}$.

The variable-temperature magnetic susceptibility data for the radical complex were compared to those taken for a related U^{IV} complex, $[(^{Ad}ArO)_3tacn]U^{IV}(N_3)$. At high temperature, the μ_{eff} vs. *T* plots for the two compounds are virtually superimposable.[28] As the temperature is decreased, however, the two curves begin to diverge at ca. 120 K. Below this temperature, the data for the azido complex drop sharply, reaching a minimum of ca. 0.7 μ_B at 5 K. This behavior is consistent with an isolated $5f^2$ U^{IV} center. The low-temperature data for the radical complex display a quite different trend. While the moment drops as the temperature is decreased, it does so more gradually than was observed for the azido analogue and reaches a minimum of ca. 1.5 μ_B at 5 K. The difference in the magnetic behavior in the two complexes is attributed to the extra electron residing on the CO_2 ligand, which accounts for the added magnetic moment at low temperature. However, the observation that the shapes of the two μ_{eff} vs. *T* curves do not deviate above 120 K may suggest the presence of an exchange interaction between the U^{IV} center and the unpaired electron on CO_2. Unfortunately, the subtraction method cannot be applied to this system because of the lack of an analogue of the radical complex that eliminates the radical but preserves the ligand field experienced by uranium. Thus, it seems unlikely that any exchange interactions between the two paramagnetic centers can be wholly extracted from the overall magnetic behavior of the molecule.

Recently, it was found that a related U^{III} species could reduce di-*tert*-butylbenzophenone to give $[((^{t\text{-}Bu}ArO)_3tacn)U^{IV}(OC^{\bullet t\text{-}Bu}Ph_2)]$.[29] The crystal data and the results of density functional theory (DFT) calculations are consistent with an overall structure comprised of four resonance forms, three containing a U^{IV} center with an unpaired electron residing on the di-*tert*-butylbenzophenone fragment, and one featuring a U^{III} center bound to a diamagnetic di-*tert*-butylbenzophenone. The temperature dependence of the magnetic susceptibility data for this radical complex shows a trend similar to that of the CO_2 complex, with the exception of a higher moment at 300 K, which is attributed to a contribution from the U^{III} resonance form (see Figure 3.10). Calculations suggest that coupling between the U^{IV} center and the radical ligand is at least physically reasonable because the computed singly occupied molecular orbital of the molecule possesses both metal and ligand character.

3.7 References

(1) (a) Sessoli, R.; Tsai, H. L.; Schake, A. R.; Wang, S.; Vincent, J. B.; Folting, K.; Gatteschi, D.; Christou, G.; Hendrickson, D. N. *J. Am. Chem. Soc.* **1993**, *115*, 1804. (b) Sessoli, R.; Gatteschi, D.; Caneschi, A.; Novak, M. A. *Nature* **1993**, *365*, 141. (c) Gatteschi D.; Sessoli R.; Villain J. *Molecular Nanomagnets*, Oxford

University Press: New York, 2006 and references therein. (d) Milios, C. J.; Vinslava, A.; Wernsdorfer, W.; Moggach, S.; Parsons, S.; Perlepes, S. P.; Christou, G.; Brechin, E. K. *J. Am. Chem. Soc.* **2007**, *129*, 2754.

(2) (a) Garanin, D. A.; Chudnovsky, E. M. *Phys. Rev. B* **1997**, *56*, 11102. (b) Leuenberger, M. N.; Loss, D. *Nature* **2001**, *410*, 789. (c) Heersche, H. B.; de Groot, Z.; Folk, J. A.; van der Zant, H. S. J.; Romeike, C.; Wegewijs, M. R.; Zobbi, L.; Barreca, D.; Tondello, E.; Cornia, A. *Phys. Rev. Lett.* **2006**, *96*, 206801. (d) Jo, M.-H.; Grose, J. E.; Liang, W.; Baheti, K.; Deshmukh, M. M.; Sokol, J. J.; Rumberger, E. M.; Hendrickson, D. N.; Long, J. R.; Park, H.; Ralph, D. C. *Nano Lett.* **2006**, *6*, 2014.

(3) (a) Powell, A. K.; Heath, S. L.; Gatteschi, D.; Pardi, L.; Sessoli, R.; Spina, G.; Del Giallo, F.; Pieralli, F. *J. Am. Chem. Soc.* **1995**, *117*, 2491. (b) Zhong, Z. J.; Seino, H.; Mizobe, Y.; Hidai, M.; Fujishima, A.; Ohkoshi, S.; Hashimoto, K. *J. Am. Chem. Soc.* **2000**, *122*, 2952. (c) Murugesu, M.; Habrych, M.; Wernsdorfer,W.; Abboud, K. A.; Christou, G. *J. Am. Chem. Soc.* **2004**, *126*, 4766. (d) Ako, A. M.; Hewitt, I. J.; Mereacre, V.; Clérac, R.; Wernsdorfer, W.; Anson, C. E.; Powell, A. K. *Angew. Chem., Int. Ed.* **2006**, *45*, 4926.

(4) (a) Osa, S.; Kido, T.; Matsumoto, N.; Re, N.; Pochaba, A.; Mrozinski, J. *J. Am. Chem. Soc.* **2004**, *126*, 420. (b) Mishra, A.; Wernsdorfer, W.; Abboud, K. A.; Christou, G. *J. Am. Chem. Soc.* **2004**, *126*, 15648. (c) Zaleski, C. M.; Depperman, E. C.; Kampf, J. W.; Kirk, M. L.; Pecoraro, V. L. *Angew. Chem., Int. Ed.* **2004**, *43*, 3912. (d) Mishra, A.; Wernsdorfer, W.; Parsons, S.; Christou, G.; Brechin, E. K. *Chem. Commun.* **2005**, 2086. (e) Mori, F.; Nyui, T.; Ishida, T.; Nogami, T.; Choi, K.-y.; Nojiri, H. *J. Am. Chem. Soc.* **2006**, *128*, 1440. (f) Tang, J.; Hewitt, I.; Madhu, N. T.; Chastanet, G.; Wernsdorfer, W.; Anson, C. E.; Benelli, C.; Sessoli, R.; Powell, A. K. *Angew. Chem., Int. Ed.* **2006**, *45*, 1729. (g) Ferbinteanu, M.; Kajiwara, T.; Choi, K.-y.; Nojiri, H.; Nakamoto, A.; Kojima, N.; Cimpoesu, F.; Fujimura, Y.; Takaishi, S.; Yamashita, M. *J. Am. Chem. Soc.* **2006**, *128*, 9008. (h) Tangoulis, V.; Figuerola, A. *Chem. Phys.* **2007**, *340*, 293. (i) Chandrasekhar, V.; Pandian, B. M.; Boomishankar, R.; Steiner, A.; Vittal, J. J.; Houri, A.; Clérac, R. *Inorg. Chem.* **2008**, *47*, 4918.

(5) (a) Ishikawa, N.; Sugita, M.; Ishikawa, T.; Koshihara, S.; Kaizu, Y. *J. Am. Chem. Soc.* **2003**, *125*, 8694. (b) Ishikawa, N.; Sugita, M.; Ishikawa, T.; Koshihara, S.; Kaizu, Y. *J. Phys. Chem. B* **2004**, *108*, 11265. (c) Ishikawa, N.; Sugita, M.; Wernsdorfer, W. *Angew. Chem., Int. Ed.* **2005**, *44*, 2931. (d) Takamatsu, S.; Ishikawa, T.; Koshihara, S.-y.; Ishikawa, N. *Inorg. Chem.* **2007**, *46*, 7250. (e) AlDamen, M. A.; Clemente-Juan, J. M.; Coronado, E.; Martí-Gastaldo, C.; Gaita-Ariño, A. *J. Am. Chem. Soc.* **2008**, *130*, ASAP.

(6) (a) Crosswhite, H. M.; Crosswhite, H.; Carnall, W. T.; Paszek, A. P. *J. Chem. Phys.* **1980**, *72*, 5103. (b) Costes, J.-P.; Dahan, F.; Dupuis, A.; Laurent, J.-P. *Chem. Eur. J.* **1998**, *4*, 1616. (c) Kahn, M. L.; Mathonière, C.; Kahn, O. *Inorg. Chem.* **1999**, *38*, 3692. (d) Benelli, C.; Gatteschi, D. *Chem. Rev.* **2002**, *102*, 2369 and references therein.

(7) Gaunt, A. J.; Reilly, S. D.; Enriquez, A. E.; Scott, B. L.; Ibers, J. A.; Sekar, P.; Ingram, K. I. M.; Kaltsoyannis, N.; Neu, M. P. *Inorg. Chem.* **2008**, *47*, 29.

(8) Rosen, R. K.; Andersen, R. A.; Edelstein, N. M. *J. Am. Chem. Soc.* **1990**, *112*, 4588.
(9) Graves, C. R.; Yang, P.; Kozimor, S. A.; Vaughn, A. E.; Clark, D. L.; Conradson, S. D.; Schelter, E. J.; Scott, B. L.; Thompson, J. D.; Hay, P. J.; Morris, D. E.; Kiplinger, J. L. *J. Am. Chem. Soc.* **2008**, *130*, 5272.
(10) (a) Siddall, T. H. *Theory and Applications of Molecular Paramagnetism*; Wiley: New York, 1976. (b) Kanellakopulos, B. In *Organometallics of the f-Elements;* Marks, T. J.; Fischer, R. D.; Eds.; NATO Advanced Study Institutes Series; D. Reidel: Dordrecht, Netherlands, 1978. (c) Edelstein, N. M.; Lander, G. H. In *The Chemistry of the Actinide and Transactinide Elements*, 3rd ed; Morss, L. R.; Edelstein, N. M.; Fuger, J.; Eds; Springer: Dordrecht, Netherlands, 2006; Vol 4, p 2225.
(11) Cotton, F. A.; Marler, D. O.; Schwotzer, W. *Inorg. Chem.* **1984**, *23*, 4211.
(12) Cotton, F. A.; Schwotzer, W. *Organometallics*. **1985**, *4*, 942.
(13) Reynolds, J. G.; Zalkin, A.; Templeton, D. H.; Edelstein, N. M.; Tempelton, L. K. *Inorg. Chem.* **1976**, *15*, 2498.
(14) (a) Berthet, J. C.; Ephritikhine, M. *Coord. Chem. Rev.* **1998**, *178*, 83. (b) Borgne, T. L.; Lance, M.; Nierlich, M.; Ephritikhine, M. *J. Organomet. Chem.* **2000**, *598*, 313.
(15) (a) Diaconescu, P. L.; Arnold, P. L.; Baker, T. A.; Mindiola, D. J.; Cummins, C. C. *J. Am. Chem. Soc.* **2000**, *122*, 6108. (b) Diaconescu, P. L.; Cummins, C. C. *J. Am. Chem. Soc.* **2002**, *124*, 7660. (c) Evans, W. J.; Kozimor, S. A.; Ziller, J. W.; Kaltzoyannis, N. *J. Am. Chem. Soc.* **2004**, *126*, 14533.
(16) Kozimor, S. A.; Bartlett, B. M.; Rinehart, J. D.; Long, J. R. *J. Am. Chem. Soc.* **2007**, *129*, 10672.
(17) Note, however, that accomplishing this substitution would involve very serious difficulties stemming from the short half-life of the available Ac isotopes.
(18) (a) Berthet, J.-C.; Marechal, J.-F. L.; Nierlich, M.; Lance, M.; Vigner, J.; M. Ephritikhine, *J. Organomet. Chem.* **1991**, *408*, 335. (b) Lukens, W. W., Jr.; Allen, P. G.; Bucher, J. J.; Edelstein, N. M.; Hudson, E. A.; Shuh, D. K.; Reich, T.; Andersen, R. A. *Organometallics* **1999**, *18*, 1253. (c) Korobkov, I.; Gambarotta, S.; Yap, G. P. A. *Organometallics.* **2001**, *20*, 2552. (d) Castro-Rodriguez, I.; Olsen, K.; Gantzel, P.; Meyer, K. *Chem. Commun.* **2002**, 2764. (e) Karmazin, L.; Mazzanti, M.; Pecaut, J. *Inorg. Chem.* **2003**, *42*, 5900. (f) Enriquez, A. E.; Scott, B. L.; Neu, M. P. *Inorg. Chem.* **2005**, *44*, 7403. (g) Salmon, L.; Thuery, P.; Asfari, Z.; Ephritikhine, M. *Dalton Trans.* **2006**, *24*, 3006. (h) Christopher, P.; Larch, F.; Cloke, G. N.; Hitchcock, P. B. *Chem. Commun.* **2008**, 82.
(19) (a) Mokry, L. M.; Dean, N. S.; Carrano, C. J. *Angew. Chem. Int. Ed.* **1996**, *35*, 1497. (b) Duval, P. B.; Burns, C. J.; Clark, D. L.; Morris, D. E.; Scott, B. L.; Thompson, J. D.; Werkema, E. L.; Jia, L.; Andersen, R. A. *Angew. Chem., Int. Ed.* **2001**, *40*, 3357. (c) Berthet J.-C.; Thuery P.; Ephritikhine M. *Chem. Commun.* **2005**, 3415. (d) Nocton, G.; Burdet, F.; Pécaut, J.; Mazzanti, M. *Angew. Chem., Int. Ed.* **2007**, *46*, 7574.
(20) Schelter, E. J.; Veauthier, J. M.; Thompson, J. D.; Scott, B. L.; John, K. D.; Morris, D. E.; Kiplinger, J. L. *J. Am. Chem. Soc.* **2006**, *128*, 2198.

(21) Veauthier, J. M.; Schelter, E. J.; Kuehl, C. J.; Clark, A. E.; Scott, B. L.; Morris, D. E.; Martin, R. L.; Thompson, J. D.; Kiplinger, J. L.; John, K. D. *Inorg. Chem.* **2005**, *44*, 5911.

(22) Schelter, E. J.; Wu, R.; Scott, B. L.; Thompson, J. D.; Morris, D. E.; Kiplinger, J. L. *Angew. Chem., Int. Ed.* **2008**, *47*, 2993.

(23) (a) Le Borgne, T.; Rivière, E.; Marrot, J.; Girerd, J.-J.; Ephritikhine, M. *Angew. Chem., Int. Ed.* **2000**, *39*, 1647. (b) Le Borgne, T.; Rivière, E.; Marrot, J.; Thuéry, P.; Girerd, J.-J.; Ephritikhine, M. *Chem. Eur. J.* **2002**, *8*, 774. (c) Salmon, L.; Thuéry, P.; Rivière, E.; Girerd, J.-J.; Ephritikhine, M. *Chem. Commun.* **2003**, 762. (d) Salmon, L.; Thuéry, P.; Rivièry, E.; Girerd, J.-J.; Ephritikhine, M. *Dalton Trans.* **2003**, 2872. (e) Salmon, L.; Thuéry, P.; Rivièry, E.; Ephritikhine, M. *Inorg. Chem.* **2006,** *45*, 83.

(24) (a) Benelli, C.; Blake, A. J.; Milne, P. E. Y.; Rawson, J. M.; Winpenny, R. E. P. *Chem. Eur. J.* **1995**, *1*, 614. (b) Costes, J.-P.; Dahan, F.; Dupuis, A. *Inorg. Chem.* **2000**, *39*, 165. (c) Costes, J.-P.; Dahan, F.; Dupuis, A. *Inorg. Chem.* **2000**, *39*, 5994. (d) Costes, J.-P.; Dahan, F.; Donnadieu, B.; Garcia-Tojal, J.; Laurent, J. P. *Eur. J. Inorg. Chem.* **2001**, 363.

(25) Monreal, M. J.; Carver, C. T.; Diaconescu, P. L. *Inorg. Chem.* **2007**, *46*, 7226.

(26) Mehdoui, T.; Berthet, J.-C.; Thue´ry, P.; Salmon, L.; Rivie`re, E.; Ephritikhine, M. *Chem.*s*Eur. J.* **2005**, *11*, 6994.

(27) Castro-Rodriguez, I.; Nakai, H.; Zakharov, L. N.; Rheingold, A. L.; Meyer, K. *Science* **2004**, *305*, 1757.

(28) Note that $\chi_M T$ provides a sensitive measure of the magnetic moment of a sample and is related to the perhaps more familiar quantity μ_{eff} as follows: $\mu_{eff} = (8\chi_M T)^{1/2}\mu_B$.

(29) Lam, O. P.; Anthon, C.; Heinemann, F. W.; O'Connor, J. M.; Meyer, K. *J. Am. Chem. Soc.* **2008**, *130*, 6567.

Chapter 4: Slow Magnetic Relaxation in a Series of Trigonal Pyramidal Non-Heme Iron(II) Pyrrolide Complexes

4.1 Introduction

Since the early 1990s, certain molecules have been shown to exhibit an energy barrier to magnetic relaxation, thereby enabling them to retain their magnetization after removal of an applied field and thus act as nanoscopic classical magnets.[1-5] This relaxation barrier arises due to a uniaxial magnetic anisotropy (D) acting on a nonzero spin ground state (S), according to the expression $U = S^2|D|$. These complexes, known as single-molecule magnets, have garnered much interest from both chemists and physicists, as such slow-relaxing species could find use in applications including high-density information storage, quantum computing, and magnetic refrigeration.[6-9] However, in order for any of these potential applications to be realized, higher relaxation barriers must be achieved. Indeed, despite the enormous effort aimed at generating single-molecule magnets with high relaxation barriers, to date, no molecule has shown magnetic hysteresis above 10 K.

The vast majority of single-molecule magnets characterized thus far have taken the form of multinuclear transition metal cluster compounds.[1-5] Recently, however, researchers have uncovered slow magnetic relaxation in mononuclear lanthanide and actinide complexes.[10-14] In these complexes, the large spin-orbit coupling in f-block ions results in highly anisotropic ground states. This discovery has led to mononuclear lanthanide phthalocyanine and actinide bis(pyrazolyl)borate complexes that demonstrate very high relaxation barriers. In principle, similar behavior should be attainable in a mononuclear transition metal complex with a high-spin ground state and uniaxial anisotropy. However, unlike their f-block counterparts which display significant spin-orbit coupling largely independent of ligand field effects, orbital angular momentum in transition metal coordination compounds is frequently quenched by geometric distortions. Furthermore, in the absence of steric protection, transition metal ions often undergo coordinative saturation to form low-spin complexes. Thus, the task of creating mononuclear transition metal based single-molecule magnets is one of enforcing coordination geometries that preserve a high-spin ground state while minimizing or preventing anisotropy-quenching distortions.

This task is ideally suited to modern molecular inorganic chemistry and its focus on the design and synthesis of geometrically constrained and sterically bulky ligands. Indeed, many metal complexes developed within this paradigm display novel or enhanced molecular reactivity,[15-19] as well as atypical spin states[20,21] and bonding configurations.[22-26] Of particular promise toward the development of single molecule magnets are low coordinate high-spin iron(II) complexes, some of which have been shown to exhibit axial zero-field splitting magnitudes up to $|D| = 50$ cm^{-1}, as in the case of the planar complex (β-diketiminate)FeCH$_3$. In view of these principles and the wealth of inorganic coordination chemistry carried out by iron in heme and non-heme protein active sites[27] and their synthetic models,[28-33] many laboratories, including ours, have been interested in exploring the structure, magnetism, and reactivity of synthetic iron complexes in lower-coordinate two-[34-38] and three-fold[21,22,39-52] environments. In this

context, we have pursued hybrid ligand scaffolds that combine attributes of heme and non-heme frameworks using trianionic tris(pyrrolyl-α-methyl)amines.[53] The addition of steric pickets to the $[tpa]^{3-}$ platform serves to enforce approximate three-fold symmetry while preventing undesirable dimerization events. Furthermore, the wide range of potential ligand variants allows for facile tuning of the steric and electronic properties of the corresponding metal complexes. We have previously disclosed the oxygen atom transfer chemistry of the iron complexes $[(tpa^{Ph})Fe]^-$ and $[(tpa^{Mes})Fe]^-$, demonstrating intramolecular aromatic C–H hydroxylation by the former and activation of nitrous oxide and intermolecular hydrogen atom abstraction by the latter.[53] In addition to this novel reactivity, this ligand scaffold enforces a three-fold coordination geometry about a high-spin $S = 2$ iron center. Importantly, this electronic structure features three electrons in the 1e orbital set, which leads to an unquenched orbital moment and thus the potential for strong magnetic anisotropy. Indeed, we recently demonstrated the efficacy of this strategy in our report of the magnetic properties of $K[(tpa^{Mes})Fe]$.[54] Magnetization measurements on this compound revealed the presence of immense uniaxial anisotropy, with an axial zero-field splitting parameter of $D = -40$ cm^{-1}. Moreover, we demonstrated that this anisotropy leads to slow relaxation effects under the presence of a small applied dc field, with an effective relaxation barrier of $U_{eff} = 42$ cm^{-1}, thereby providing the first example of a mononuclear transition metal-based single-molecule magnet.

The tunability of the $[(tpa^R)Fe]^-$ platform affords the opportunity to expand this concept to other mononuclear transition metal complexes. Herein, we report the design and synthesis of a homologous series of $[(tpa^R)Fe]^-$ complexes with various aryl and alkyl substituents where R = *tert*-butyl (**1**), mesityl (**2**), 2,4,6-triisopropylphenyl (**3**), phenyl (**4**), and 2,6-difluorophenyl (**5**), as well as the structural, electrochemical and magnetic properties of this novel series of trigonal pyramidal iron(II) complexes. Most importantly, we demonstrate the presence of strong uniaxial magnetic anisotropy in the complexes that gives rise to single-molecule magnet behavior with relaxation barriers up to $U_{eff} = 65$ cm^{-1} in the case of **1**. Moreover, our ability to vary the pendant substituents of the ligand across the series has enabled us to thoroughly examine the effect of factors such as ligand donor strength and coordination geometry on governing magnetic anisotropy and slow magnetic relaxation.

4.2 Results and Discussion

Syntheses and Structures of $[(tpa^R)Fe]^-$ Complexes. Deprotonation of the tpa^R ligands *in situ* followed by salt metathesis with $FeCl_2$ in THF provides a general route to anionic iron(II) complexes of the type $[M(solv)_n][(tpa^R)Fe]$ (M = Na, R = *tert*-butyl (**1**), phenyl (**4**); M = K, R = mesityl (**2**), 2,4,6-triisopropylphenyl (**3**), 2,6-difluorophenyl (**5**)). Counterion choice is dictated primarily by the solubility and crystallinity of the product. Potassium hydride proved to be a suitable base for the syntheses of **2**, **3** and **5**. Sodium hydride was employed in the synthesis of **4** whereas $NaN(SiMe_3)_2$ was used to furnish the desired sodium salt **1**.

Compounds **1**–**5** crystallize readily as THF or DME solvates. Single crystal X-ray diffraction (XRD) measurements reveal four-coordinate, trigonal pyramidal iron centers for each complex are shown in Figure 4.1. Although **3** crystallizes readily and in high yield, chronic twinning and disorder problems have so far impeded our efforts to obtain

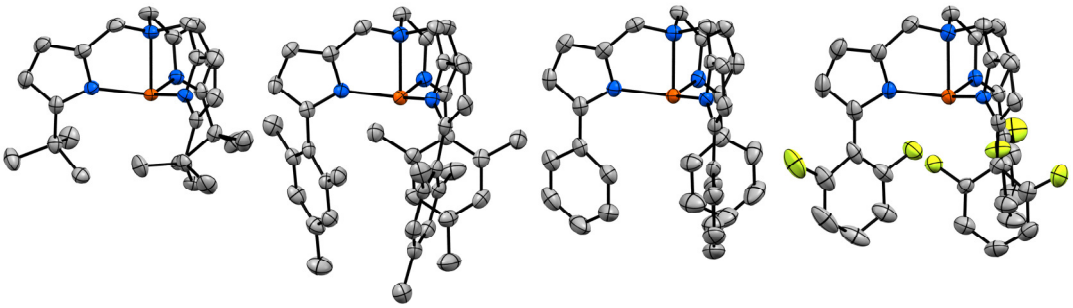


Figure 4.1. Thermal ellipsoid plots of **1**, **2**, **3** and **5**. Ellipsoids are shown at the 50% probability level. Hydrogen atoms, counterions and solvent molecules have been omitted for clarity.

Table 4.1. Summary of Bond Lengths (Å) and Angles (º) for the X-ray Structures of **1**, **2**, **4** and **5**.

	1	**2**	**4**	**5**
Fe1-N1	2.144(1)	2.172(2)	2.161(2)	2.196(2)
Fe1-N2	2.031(1)	2.008(3)	2.016(1)	2.036(2)
Fe1-N3		2.041(2)	2.013(2)	2.042(3)
Fe1-N4		2.024(3)	2.019(2)	2.038(3)
N2-Fe1-N3	118.35(6)	117.36(9)	115.56(6)	121.6(1)
N3-Fe1-N4		122.39(9)	120.22(7)	115.8(1)
N4-Fe1-N2		115.3(1)	120.27(6)	116.6(1)
Fe1-(N2,N3,N4)	0.263	0.262	0.233	0.290

satisfactory solutions to data collected on these crystals. Relevant bond lengths and angles for **1**, **2**, **4** and **5** are shown in Table 4.1. Iron–pyrrolide distances range from 2.008(3) to 2.042(3) Å for this series, consistent with anionic nitrogen ligation of high-spin iron(II). The longer axial amine–iron distances vary over a slightly larger range from 2.144(1) to 2.196(2) Å.

The *tert*-butyl derivative **1** crystallizes in the cubic space group $P2_13$ and is unique among iron(II) complexes **1–5** in that it possesses crystallographically imposed three-fold symmetry at the iron center. The iron centers in **2**, **4** and **5** exhibit slight deviations from three-fold symmetry. The most pronounced structural distortion is observed for **2**, in which a mesityl *ortho*-methyl group (C42) is rotated towards the iron center. The iron–pyrrolide bond directly opposite the iron–methyl close contact is anomalously short at 2.008(3) Å. Whereas the Fe1–C42 distance of ca. 3.1 Å is longer than what is considered typical for an agostic interaction, the related salt $[Li(THF)_4][(tpa^{Mes})Fe]$, which is structurally distinct from **2**, features a nearly identical interaction.[55] Furthermore, neither the corresponding cobalt(II) nor manganese(II) tpa^{Mes} complexes exhibit this distortion.[56] Taken together, these results suggest an electronic provenance for the iron–methyl interaction observed in the XRD structure of **2**, as there are no major distortions present in either the ligand core or periphery of complexes **4** and **5**.

Static Magnetic Properties. With structural and electrochemical data on this family of trigonal pyramidal non-heme iron(II) complexes in hand, we turned our attention to more comprehensively interrogating their magnetic properties. Dc magnetic susceptibility measurements at 300 K give values of $\chi_M T$ = 3.55, 3.32,[54] 3.68, 3.66, and 3.44 cm^3mol/K for compounds **1**-**5**, respectively (see Figures 4.2-4.5), confirming the presence of a high-spin electron configuration and an $S = 2$ spin ground state for each compound. Notably, each set of $\chi_M T$ data undergoes a downturn at low temperature, suggesting the presence of significant zero-field splitting. To investigate this possibility, we collected low-temperature magnetization data at various applied dc fields for the compounds. The resulting plot of reduced magnetization for **1**, depicted in Figure 4.6, displays a series of nonsuperimposable isofield curves that fall dramatically short of reaching the magnetization saturation of 4.00 μ_B expected for an $S = 2$ ground state with $g = 2.00$, confirming the presence of strong magnetic anisotropy. To quantify this effect, the data were modeled according to the following spin Hamiltonian:

$$\hat{H} = D\hat{S}_z^2 + E(\hat{S}_x^2 + \hat{S}_y^2) + g_{iso}\mu_B \mathbf{S}\cdot\mathbf{B} \quad (1)$$

Best fits to the data obtained using ANISOFIT 2.0[57] gave axial and transverse zero-field splitting parameters of $D = -48$ cm^{-1} and $|E| \leq 0.4$ cm^{-1}, respectively, with g = 2.28. The presence of such a strong axial anisotropy arises from the unquenched orbital angular momentum associated with a $1e^3 2e^2 a_1^1$ electronic configuration.[54] In contrast to this strong uniaxial anisotropy, the value of E is small, over two orders of magnitude smaller than D. The presence of such a large $|D/E|$ ratio may arise due to the crystallographic three-fold symmetry at the iron(II) center, which minimizes the magnetic anisotropy within the trigonal plane of the molecule. Importantly, this large negative value of D, in conjunction with the high-spin $S = 2$ ground state, demonstrates the potential of this type of mononuclear transition metal complex for exhibiting slow magnetic relaxation. Indeed, a compound exhibiting these parameters could exhibit a maximal thermal relaxation barrier of $U = S^2|D| = 192$ cm^{-1}, which would be a record barrier for a transition metal system.

Zero-field splitting parameters extracted from fits to reduced magnetization data collected for **1**-**5** are enumerated in Table 4.**2** (See Figures 4.7-4.9). For all of the compounds, best fits to the data give negative values of D, indicative of a uniaxial anisotropy and thus the possibility of slow magnetic relaxation. The series of D values ranges from $D = -48$ cm^{-1} obtained for **1** to $D = -6.2$ cm^{-1} in the case of **5**. Inspection of the trend across the series reveals a dependence of the magnitude of D on Lewis base strength, where the magnitude of D rises with increasing basicity of the ligand. This observation suggests that the magnitude of axial anisotropy may be related to the energy separation between the 1e (d_{xz} and d_{yz}) and 2e (d_{xy} and $d_{x^2-y^2}$) orbital sets, as the energy of the 2e set will increase with the σ-donating ability of the ligand. Taken together, these data establish that the trigonal pyramidal $[(tpa^R)Fe]^-$ system offers a general platform for obtaining large uniaxial zero-field splitting.

Dynamic Magnetic Properties. To investigate the potential for slow magnetic relaxation in this homologous series of high-spin iron(II) compounds, we collected variable-frequency ac susceptibility data at multiple temperatures. In the absence of an

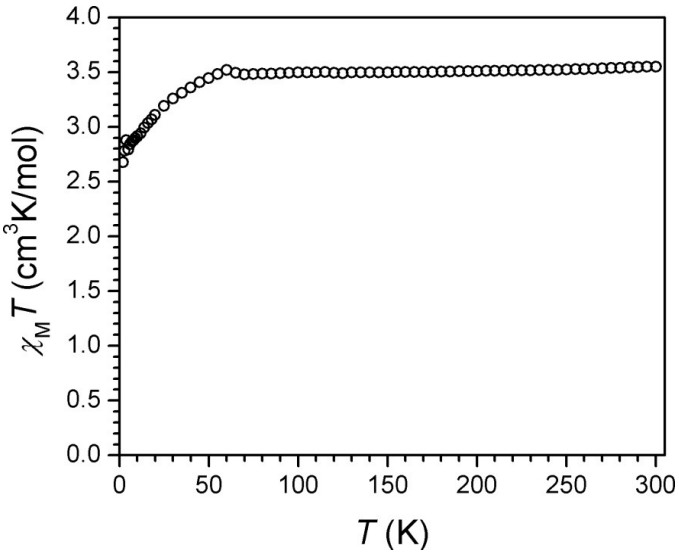


Figure 4.2. Variable-temperature magnetic susceptibility data collected for **1** under an applied dc field of 1000 Oe.

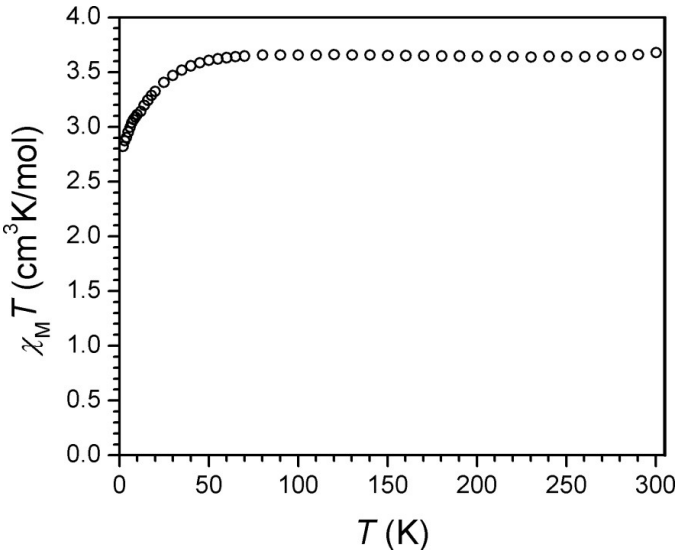


Figure 4.3. Variable-temperature magnetic susceptibility data collected for **3** under an applied dc field of 1000 Oe.

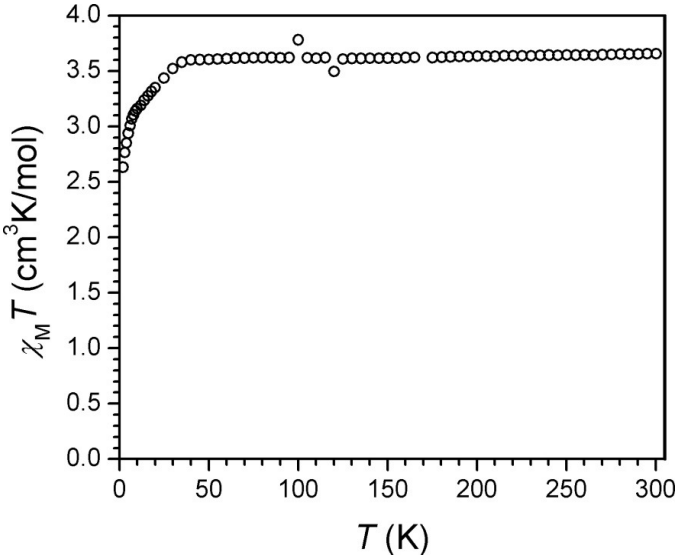


Figure 4.4. Variable-temperature magnetic susceptibility data collected for **4** under an applied dc field of 1000 Oe.

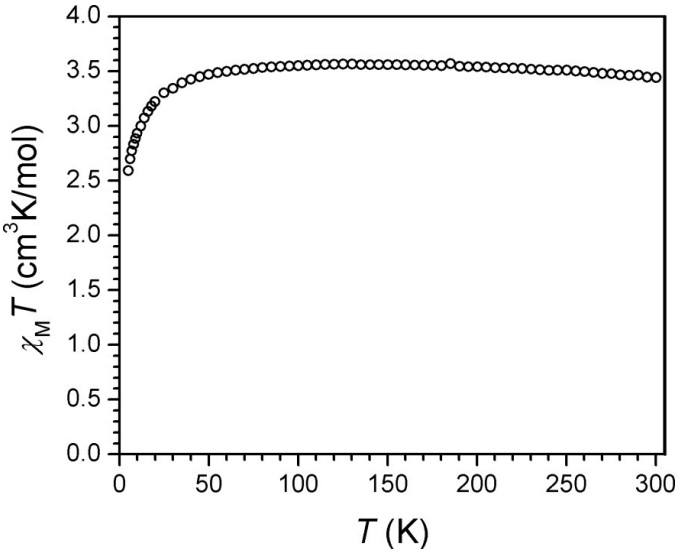


Figure 4.5. Variable-temperature magnetic susceptibility data collected for **5** under an applied dc field of 1000 Oe.

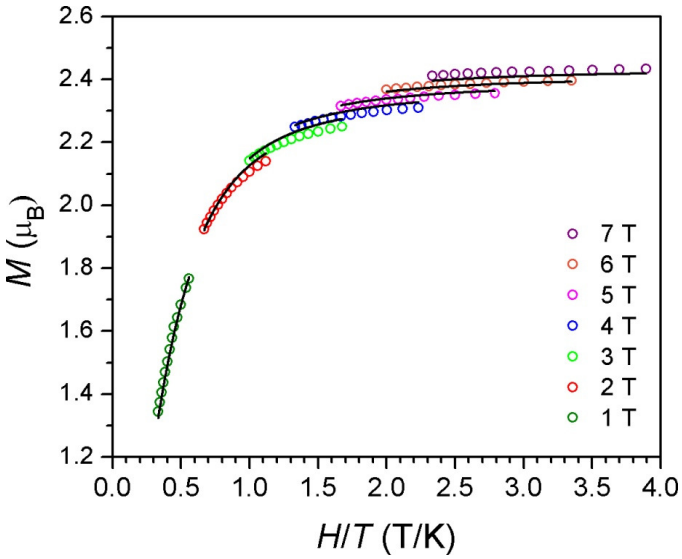


Figure 4.6. Low-temperature magnetization data for **1** collected under various applied dc fields. The black lines represent fits to the data.

Table 4.2. Summary of Magnetic Parameters for **1**–**5**.[a]

	1	**2**	**3**	**4**	**5**
g	2.28	2.23(2)[b]	2.38(1)	2.37(3)	2.02
D	−48	−44(4)	−30(2)	−26(2)	−6.2
$\|E\|_{max}$	0.4	6	4	5	0.1
U_{eff}	65	42	—	25	—

[a]All energies are given in cm^{-1}. [b]Standard deviations are provided in parentheses.

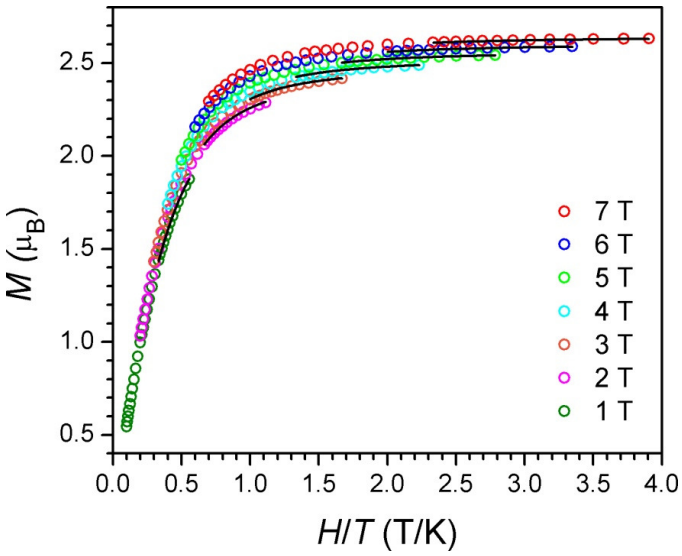


Figure 4.7. Low-temperature magnetization data for **3** collected under various applied dc fields. The black lines represent fits to the data.

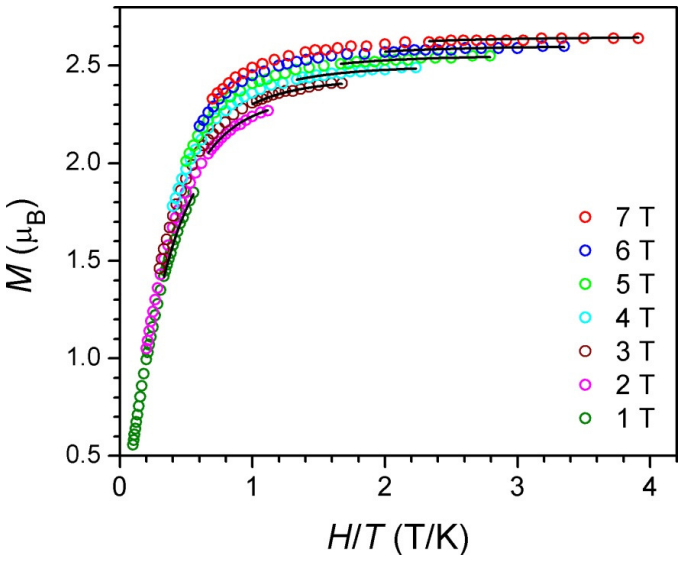


Figure 4.8. Low-temperature magnetization data for **4** collected under various applied dc fields. The black lines represent fits to the data.

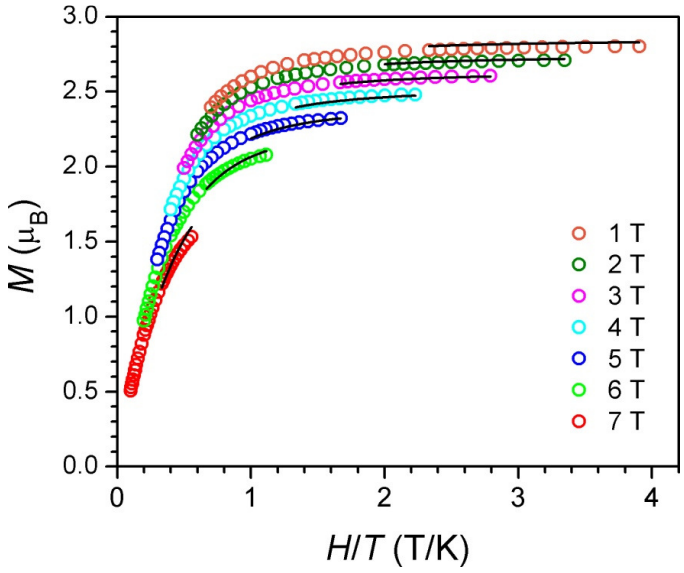


Figure 4.9. Low-temperature magnetization data for **5** collected under various applied dc fields. The black lines represent fits to the data.

applied dc field, we observe no χ_M'' signal at frequencies up to 1500 Hz and temperatures down to 1.8 K. This result is somewhat unexpected, given the large uniaxial anisotropy and $S = 2$ spin ground states determined for the compounds through static magnetic measurements. One explanation for the absence of χ_M'' signals is that quantum tunneling of the magnetization through the thermal relaxation barrier dominates other relaxation pathways in the absence of an applied dc field. Such tunneling processes may arise due to the presence of transverse magnetic anisotropy in the compounds. For a molecule exhibiting only axial anisotropy, the wavefunctions corresponding to each $\pm M_S$ pair do not overlap with one another, such that no mixing can occur between the two.[3,58] In this case, quantum tunneling is a forbidden process. If a transverse component to the magnetic anisotropy is introduced, however, mixing between these wavefunctions occurs. This mixing then enables the magnetization of the $+M_S$ level to tunnel through the anisotropy barrier to the $-M_S$ level, such that the overall relaxation time is fast. As has been observed for a number of previously reported compounds, tunneling effects can drastically reduce the relaxation time of single-molecule magnet.[14,58-62] Indeed, the smaller values of $|D/E|$ obtained for **2**–**5** support the hypothesis that quantum tunneling provides a facile relaxation pathway for the compounds. Somewhat surprisingly, despite exhibiting crystallographic three-fold symmetry and a miniscule value of E, compound **1** displays no slow relaxation under zero applied dc field. In addition to slight deviations from ideal three-fold symmetry at the iron(II) center in **1** that may be undetectable in the crystal structure due to thermal motion of the nitrogen atoms at 128 K, this lack of slow relaxation in the absence of an applied field is also likely to result from tunneling, because the tunneling probability is known to increase[58,63] with decreasing M_S and this monoiron system has a relatively small spin ground state of $S = 2$. Finally, as the magnetic measurements were performed on microcrystalline solids, fast relaxation in

zero-field may be facilitated by spin-spin interactions between neighboring iron(II) ions. Indeed, this hypothesis is consistent with the Mössbauer spectral measurements, which reveal a temperature independence of the relaxation time below 10 K (*vide infra*).

If indeed quantum tunneling effects lead to a shortcutting of the thermal relaxation barriers in the iron(II) complexes, then application of a dc field during the ac measurement should act to split the energies of the $\pm M_S$ pairs, thereby eliminating tunneling as a facile relaxation pathway and slowing down the relaxation. Indeed, just such an experiment leads to slow relaxation effects for all compounds with the exception of **5**. For instance, data collected for **1** under a 1500 Oe dc field reveal a set of temperature-dependent peaks in the plot of χ_M'' vs. ν (see Figure 4.10, bottom). In order to extract relaxation times from these peaks, we constructed Cole-Cole plots from data collected in the temperature range 1.8-6.8 K and fit them to a generalized Debye model.[64-66] For a single-molecule magnet, the relaxation time (τ) should follow a thermally-activated relaxation process where τ increases exponentially with decreasing temperature. Accordingly, the corresponding plot of $\ln(\tau)$ vs. $1/T$ should feature a linear region, with the slope of that line giving the relaxation energy barrier. Indeed, the Arrhenius plot constructed for **1** (see Figure 4.10, top) features a linear region at high temperature, with a least-squares fit giving $U_{eff} = 65$ cm^{-1} and $\tau_0 = 6.7 \times 10^{-11}$ s. The value of τ_0 provides a quantitative measure of the attempt time of relaxation from the thermal phonon bath, and the value obtained here is in accordance with other single-molecule magnets.[1-5] In addition, this value of τ_0 eliminates the possibility that phonon bottleneck effects lead to the observed slow relaxation.[67]

The large temperature range over which slow relaxation is observed for **1** at 1500 Oe provides a comprehensive map of the relaxation processes occurring within the molecule. At this applied dc field, the relaxation is dominated by spin-lattice interactions.[68,69] For instance, at high temperature, the relaxation time exhibits a clear Arrhenius dependence, with $\ln(\tau)$ increasing linearly with $1/T$ (see Figure 4.10, upper, dashed blue line). This region is likely dominated by an Orbach relaxation process, sometimes referred to as thermally-assisted quantum tunneling. Here, a spin associated with the $M_S = +2$ level absorbs a phonon and is excited to the $M_S = +1$ level. Then, the spin tunnels from the $M_S = +1$ to $M_S = -1$ level and subsequently relaxes to the $M_S = -2$ level. Note, though, that this process cannot be the sole pathway in this region, as such a scenario would give a relaxation barrier of $U_{eff} = 144$ cm^{-1} associated with climbing from the $M_S = +2$ to $M_S = +1$ level. At low temperature, $\ln(\tau)$ also exhibits a linear dependence on $1/T$, albeit with a slope of nearly zero (see Figure 4.10, upper, dashed green line). This region is likely dominated by ground state tunneling via a direct phonon-based relaxation process, as insufficient thermal energy is available for a spin to relax via a thermally-assisted mechanism. In the case of **1**, this process corresponds to tunneling from the $M_S = +2$ to $M_S = -2$ level. Because the $\ln(\tau)$ data do not show a clear transition between a high temperature Orbach region and a low temperature direct process region, a Raman relaxation mechanism was considered in order to model the intermediate data (Figure 4.10, upper, dashed purple line). In this process, the relaxation time scales with T, intermediate between the exponential (Orbach) and direct dependences on $1/T$. The crossover between Arrhenius behavior and direct tunneling through an intermediate Raman process is prevalent among mononuclear and weakly-exchange coupled

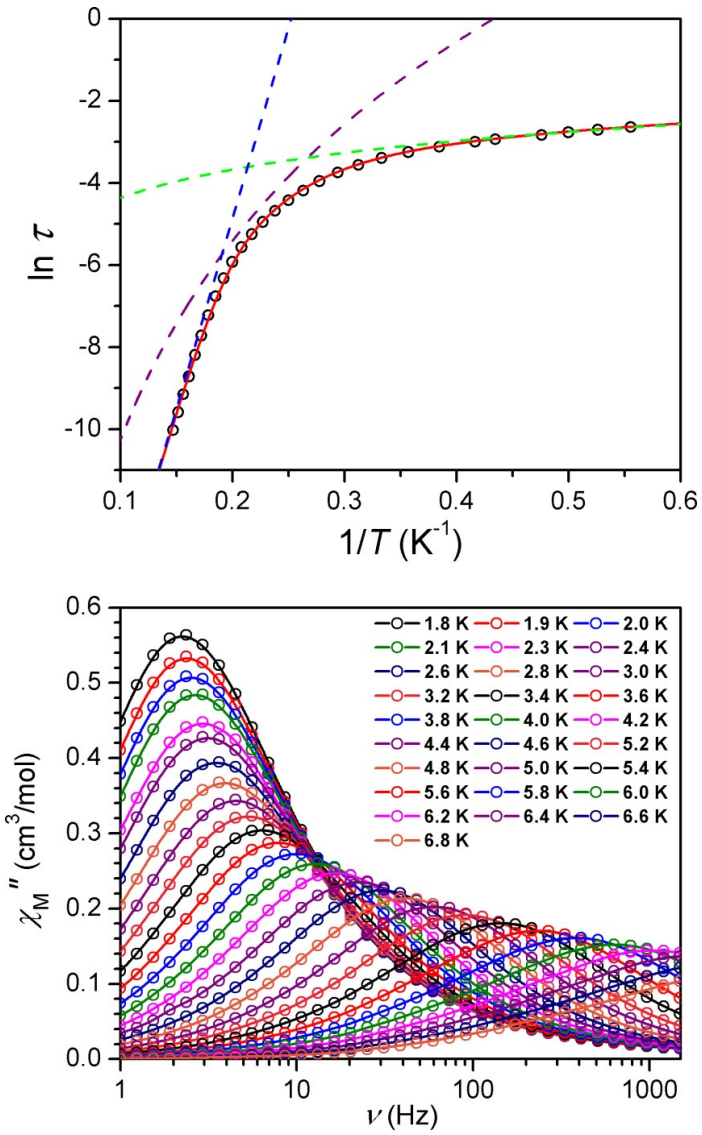


Figure 4.10. Bottom: Variable-frequency out-of-phase ac susceptibility data for **1**, collected under a 1500 Oe dc field at various temperatures. The solid lines are guides for the eye. Top: Arrhenius plot constructed from data obtained under a dc field of 1500 Oe. The dashed lines represent data fits to an Orbach (blue), Raman (purple), and direct (green) process. The solid red line represents a data fit to the three processes simultaneously.

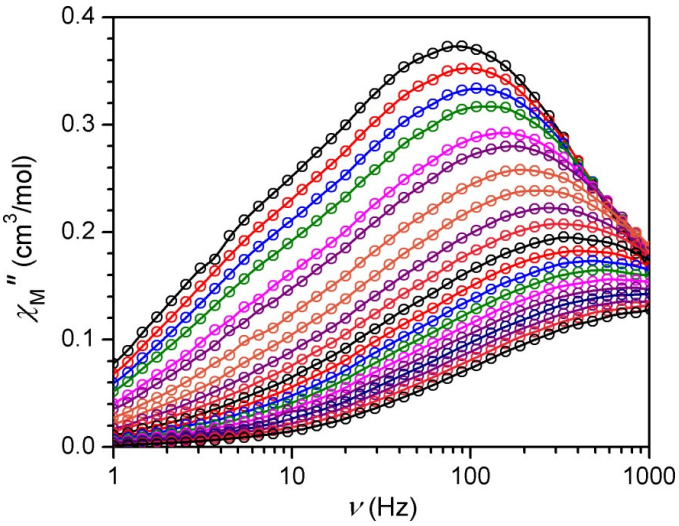


Figure 4.11. Variable-frequency out-of-phase ac susceptibility data for **3**, collected under a 1500 Oe dc field at various temperatures. The solid lines are guides for the eye.

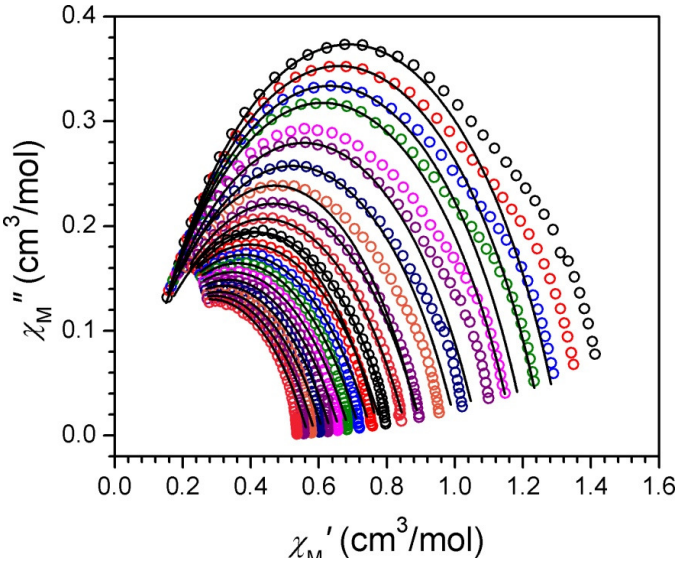


Figure 4.12. Cole-Cole plot for **3**, constructed from data collected under a 1500 Oe dc field over the temperature range 1.8 (black) to 5.2 (pink) K. Data were collected in temperature increments of 0.1 (1.8-2.4 K) and 0.2 (2.6-5.2 K) K. The solid lines are guides for the eye.

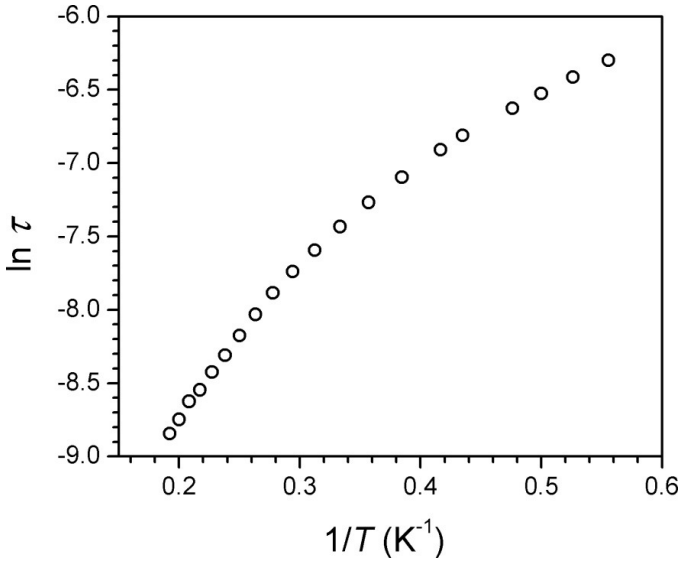


Figure 4.13. Arrhenius plot of relaxation time for **4**, constructed from data collected under a 1500 Oe dc field.

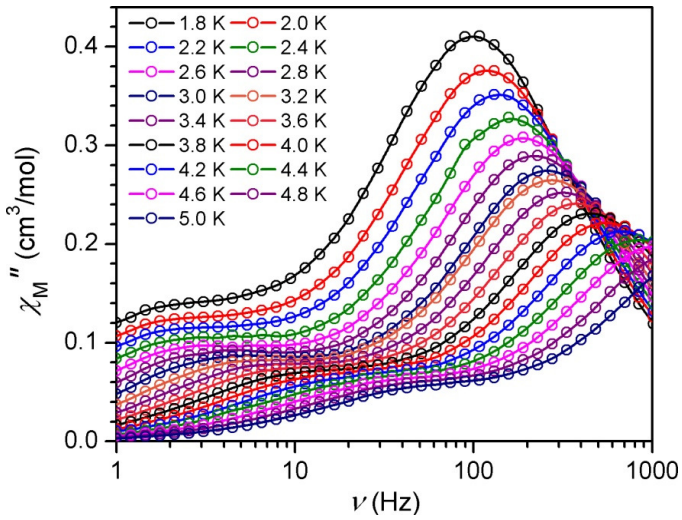


Figure 4.14. Variable-frequency out-of-phase ac susceptibility data for **4**, collected under a 1500 Oe dc field at various temperatures. The solid lines are guides for the eye.

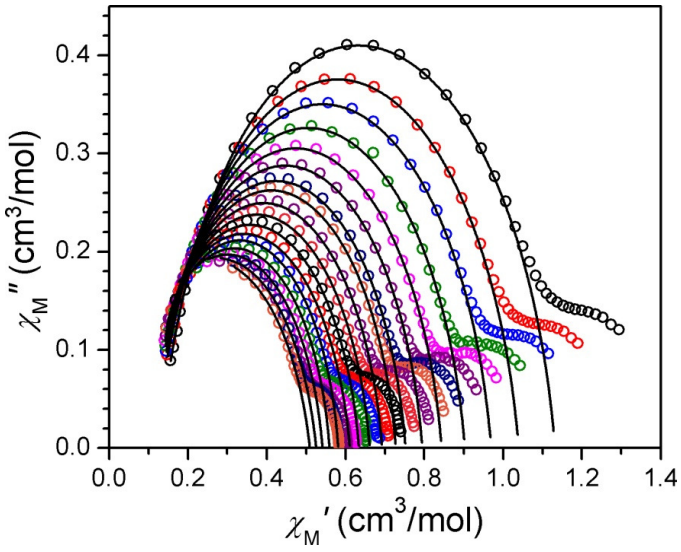


Figure 4.15. Cole-Cole plot for **4**, constructed from data collected under a 1500 Oe dc field over the temperature range 1.8 (black) to 5.0 (orange) K. Data were collected in temperature increments of 0.2 K. The solid lines are guides for the eye.

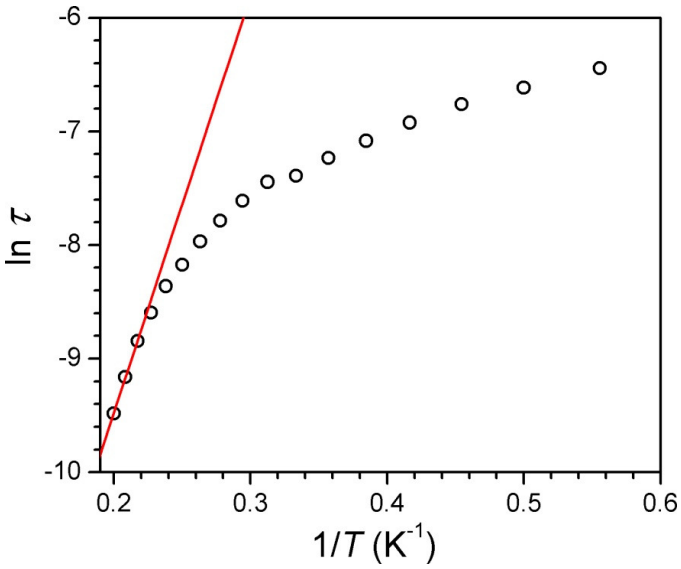


Figure 4.16. Arrhenius plot of relaxation time for **4**, constructed from data collected under a 1500 Oe dc field. The red line corresponds to a linear fit to the three highest-temperature data.

multinuclear single-molecule magnets, yet previous fitting of variable-temperature relaxation time data has included only the Orbach region.[14,54,62] Indeed, to our knowledge, this marks the first time that the temperature dependence of the relaxation time in a single-molecule magnet has been fit to a non-Orbach mechanism. (see Figure 4.10, upper, solid red line).

We conducted similar ac susceptibility measurements on the other iron(II) tpa^R compounds (see Figures 4.11-4.16). Arrhenius fits to relaxation times extracted from Cole-Cole plots give relaxation barriers of U_{eff} = 42 cm^{-1} for **2** and 25 cm^{-1} for **4**. In the case of **3**, we observe a temperature- and frequency-dependent χ_M'' signal; however, the corresponding relaxation times are not indicative of thermally-activated behavior. As such, no thermal relaxation barrier could be obtained in the measured temperature range. With the exception of **3**, the magnitude of U_{eff} increases with increasing value of D. The absence of slow relaxation observed for **5** is likely a direct consequence of the low D value obtained for the compound.

Mössbauer Spectroscopy. In view of the fast relaxation processes that dominate the magnetization dynamics of the iron(II) complexes under zero field and low temperature, we carried out zero-field Mössbauer spectroscopy measurements in order to probe these processes using a much faster timescale. For these studies, we focused our attention on compounds **1** and **4** to compare and contrast alkyl versus aryl substitution on the ancillary tpa framework. The Mössbauer spectra of **1** obtained at selected temperatures are shown in the left panel of Figure 4.17. At 220, 180, and 120 K, the spectra consist of a major sharp singlet with an isomer shift characteristic of iron(II) accounting for the majority of the sample. A minor doublet is assigned to a small amount of an iron(III) impurity. The isomer shift of δ = 0.836(2) mm/s observed for **1** at 4.2 K is consistent with a high-spin iron(II) iron in a four-coordinate environment.[70] Notably, the quadrupole splitting (ΔE_Q) observed for **1** is very small and positive. This splitting arises from two contributions to the electric field gradient: the lattice (q_{lat}) and valence (q_{val}) components. The crystallographic threefold symmetry of **1** generates a d-orbital manifold qualitatively similar to that of a tetrahedron, a geometry for which q_{val} is expected to be essentially zero. In addition, the cubic symmetry of the lattice in which **1** crystallizes likewise contributes to a highly uniform electric field gradient. The presence of a sharp singlet in this temperature range indicates that the magnetic relaxation of **1** is fast relative to the Larmor precession time of the iron-57 nuclear magnetic moment (ca. 10^{-8} s). As the temperature decreases below 60 K, the profile of **1** broadens from a singlet to an asymmetric doublet, ultimately reaching a broad complex shape at 4.2 K.

The broadening of the spectra with decreasing temperature results from the onset of slow magnetic relaxation down to 4.2 K, in accordance with the results of ac susceptibility experiments. In order to quantify this effect, the spectra were fit according to the Dattagupta and Blume formalism (see Table 4.3).[71] Here, the relaxation of the magnetic hyperfine field of the iron(II) center was best modeled as occurring in 120° steps perpendicular to the C_3 axis of the molecule, along each Fe-N_{basal} bond. Notably, the fit to the data reveals a hyperfine field of H = 5.31(6) T, a much smaller value than what is commonly observed for high-spin iron(II) complexes. This anomaly is likely a result of the large unquenched orbital angular momentum in **1**, consistent with the strong magnetic anisotropy determined through magnetization experiments. Indeed, a similar phenomenon

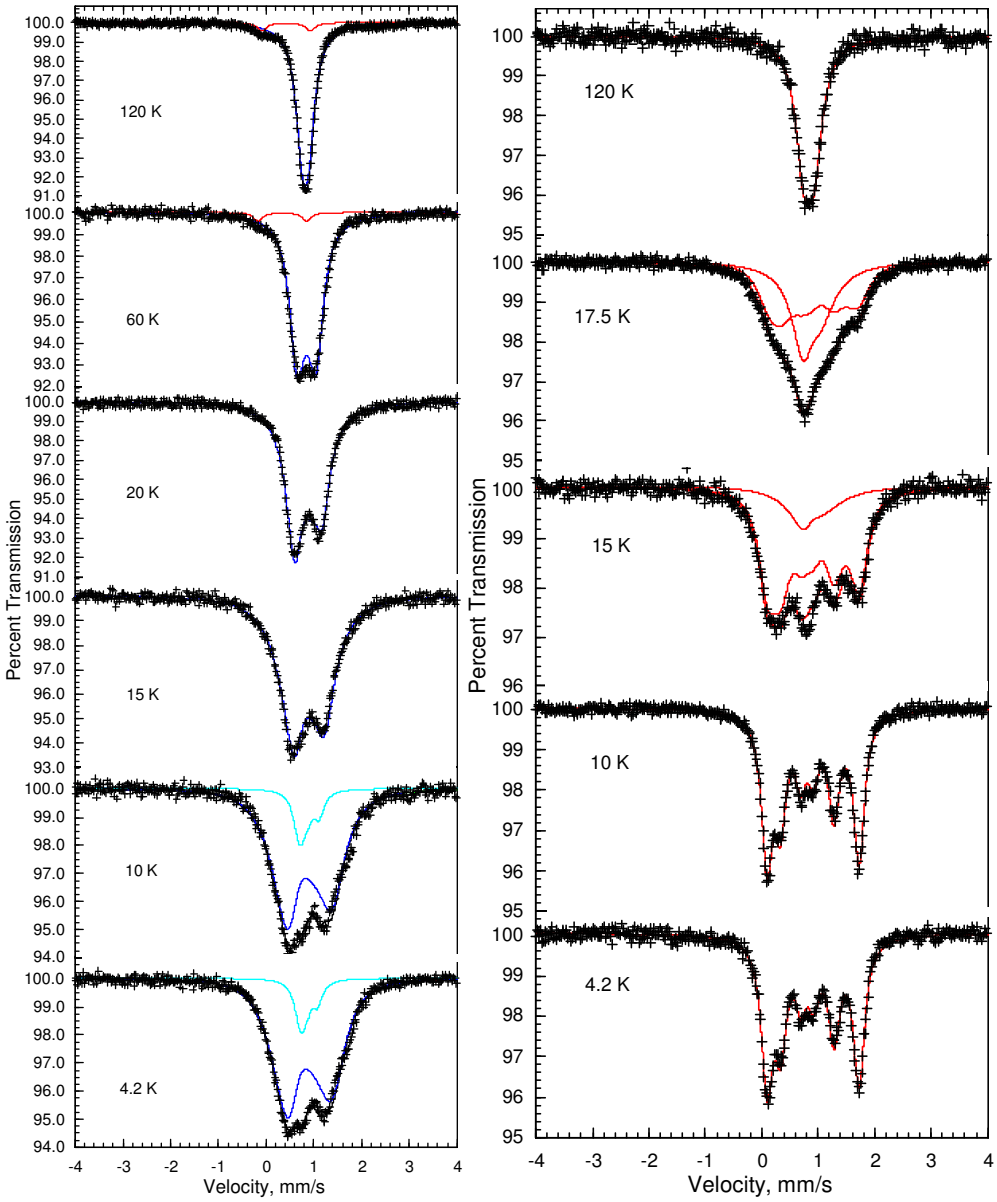


Figure 4.17. Variable-temperature Mössbauer spectra of **1** (left) and **4** (right).

Table 4.3. The Mössbauer spectral parameters[a] for the main iron(II) component in **1**.

T, K	δ, mm/s	ΔE_Q, mm/s	H, T	ν_1, MHz	Abs. Area, (%ε)(mm/s)
220	0.770(4)	+0.004(60)	3.0	53	2.75(3)
180	0.793(2)	+0.025(50)	3.2	51	3.63(3)
120	0.821(1)	+0.012(8)	3.5	49	5.42(1)
80	0.831(2)	+0.010(10)	3.8	46	6.73(3)
60	0.845(1)	+0.010(3)	4.0	35	7.86(2)
40	0.845(2)	+0.033(6)	4.5	29	9.04(4)
20	0.834(1)	+0.110	4.65	26(1)	9.27(4)
15	0.840	+0.150	5.23(11)	17(1)	9.43(5)
10	0.837(3)	+0.145	5.54(14)	12(1)	9.73(7)
4.2	0.836(2)	+0.145(8)	5.31(6)	9.9(5)	9.56(4)

[a] Γ, the linewidth at half-height was kept constant at 0.247 mm/s. δ is the isomer shift referred to α-iron at 295 K, ΔE_Q is the quadrupole splitting, H is the effective hyperfine field, ν_1 is the relaxation frequency. The absence of an error indicates that the parameter has been constrained to the reported value.

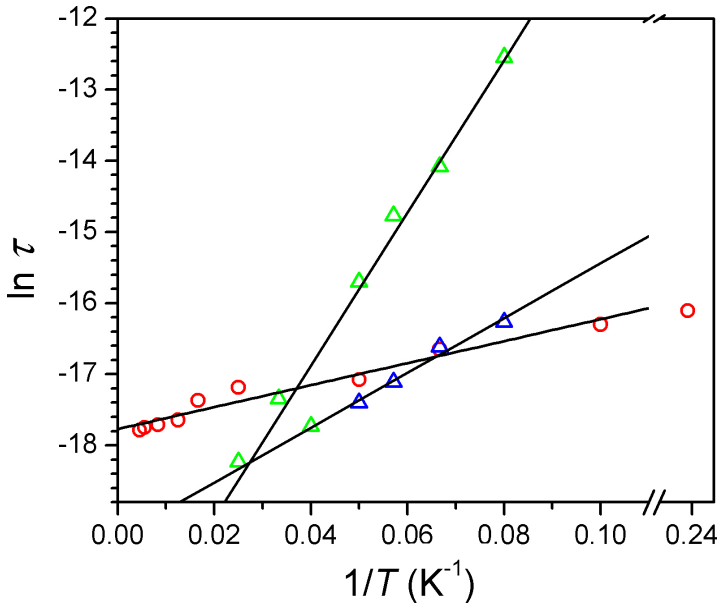


Figure 4.18. Arrhenius plot of relaxation time, as obtained from Mössbauer measurements, for **1** (red circles) and two relaxation processes for **4** (green and blue triangles). Solid black lines represent linear least-squares fits to the data.

has been observed in the mixed-valence oxalates, $(PPh_4)[Fe_2(ox)_3]$ and $(NBu_4)[Fe_2(ox)_3]$.[72,73] An Arrhenius plot of the relaxation times obtained from fitting the spectra is shown in Figure 4.18. In the temperature range 4-10 K, the frequency is essentially independent of temperature, suggesting that the relaxation process governed by spin-spin relaxation under zero applied magnetic field. In contrast, above 10 K, the relaxation frequency demonstrates a strong temperature dependence, with a linear least-squares fit to the data in the temperature range 10-220 K providing a relaxation barrier of 10(4) cm^{-1}. This result indicates that a thermally-activated Orbach mechanism dominates the relaxation process above 10 K.[74,75] Interestingly, while a similar relaxation mechanism was observed from ac susceptibility experiments, the relaxation barrier obtained here is much smaller than that of U_{eff} = 65 cm^{-1} from magnetic measurements. This difference may arise in large part due to the presence of fast relaxation processes in zero field that serve to shortcut the thermal relaxation processes. Nevertheless, this result confirms that slow magnetic relaxation does indeed occur in the absence of an applied magnetic field for **1**.

Mössbauer spectra collected for compound **4** at selected temperatures are shown in the right panel of Figure 4.17. Here, the small negative quadrupole splitting and isomer shift of δ = 0.858(2) mm/s at 4.2 K confirm the presence of high-spin iron(II) in a high-symmetry four-coordinate enivronment. In the temperature range 220-80 K, the spectra consist of a narrow doublet, indicative of fast magnetic relaxation. As the temperature is lowered, the doublet broadens to a complex peak similar to that observed for **1** below 10 K. In contrast to that observed for **1**, however, the lineshape continues to evolve until finally forming a fully resolved sextet below 10 K. The observation of this sextet demonstrates the presence of magnetic relaxation even slower than that observed in **1**. To further investigate this phenomenon, the spectra were modeled similarly to those for complex **1**, with the exception that these spectra were best fit using two separate relaxation modes (see Table 4.4). The presence of two relaxation modes may arise from a single iron(II) coordination environment or two distinct coordination environments featuring different degrees of DME desolvation. Akin to that observed for **1**, the fits reveal an unusually small hyperfine field of H = 4.95(1) T, indicative of strong magnetic anisotropy. The corresponding Arrhenius plots of relaxation time for the two modes both show a thermally-activated behavior (see Figure 18), demonstrating that the hyperfine field of the iron(II) center is relaxing via an Orbach process. Least-squares fits to the two datasets give relaxation barriers of 26(4) and 75(4) cm^{-1}. The barrier of 26(4) cm^{-1} is in accordance with that obtained from ac susceptibility data obtained for compound **4** at much lower temperatures under a dc field of 1500 Oe. In contrast, the second process, corresponding to a barrier of 75(4) cm^{-1}, is undetectable by ac measurements with or without an applied dc field. Notably, the magnitude of this barrier corresponds exactly to the energy separation between the M_S = 2 and M_S = 1 levels, considering the axial zero-field splitting parameter of $D = -26(2)$ cm^{-1} obtained from fitting magnetization data and the expression $\Delta E = (M_{S\,2})^2|D| - (M_{S1})^2|D|$. This barrier may thus represent a pure Orbach mechanism that is quenched at low temperatures or upon application of a dc field.

Table 4.4. The Mössbauer spectral parameters[a] for the main iron(II) component in **4**.

T, K	Γ, mm/s	δ, mm/s	ΔE_Q, mm/s	H, T	ν_1, MHz	ν_2, MHz	A_2, %
250	0.277(2)	0.753(2)	–0.064(5)	-	-	-	-
220	0.254(2)	0.782(2)	–0.128(5)	-	-	-	-
180	0.352(5)	0.794(2)	–0.184(5)	-	-	-	-
150	0.396(5)	0.814(2)	–0.195(5)	-	-	-	-
120	0,341(5)	0.836(2)	–0.191(5)	-	-	-	-
80	0.306(4)	0.843(2)	–0.214(5)	-	-	-	-
40	0.248	0.855(1)	–0.226(3)	3.4(1.4)	83(66)	-	7.4(1)
30	0.248	0.860(2)	–0.231(4)	2.9(3)	34(9)	-	17.7(1)
25	0.248	0.859(2)	–0.244(5)	4.8(4)	50(8)	-	45(3)
20	0.248	0.862(3)	–0.240	5.000	6.6(2.0)	36(7)	59(12)
17.5	0.248	0.862(2)	–0.240	5.000	2.6(2)	27(2)	-
15	0.248	0.860(1)	–0.240	5.000	1.301(3)	16.4(1)	-
12.5	0.248	0.858(1)	–0.240(3)	4.950(7)	0.28(2)	11.6(1)	-
10	0.239(1)	0.857(1)	–0.234(2)	4.944(4)	0	-	-
4.2	0.245(3)	0.859(1)	–0.220(4)	4.954(8)	0	-	-

[a] Γ is the linewidth at half-height, δ is the isomer shift referred to α-iron at 295 K, ΔE_Q is the quadrupole splitting,[a] H is the effective hyperfine field, ν_1 and ν_2 are the relaxation frequencies, A_2 is the percent area of the component corresponding to ν_2. The absence of an error indicates that the parameter has been constrained to the reported value. The asymmetry parameter of the electric field gradient, η, has been constrained to zero and the angle, θ, between the principal axis of the electric field gradient tensor and the hyperfine field has been fitted to 82(5)°.

High-Field Electron Paramagnetic Resonance Spectroscopy. Finally, in order to directly probe the energy separation between the M_S levels and thus the zero-field splitting of the iron(II) complexes, we carried out high-field EPR experiments on polycrystalline samples of **1**-**5**. Variable-field spectra collected for difluorophenyl-substituted complex **5** at 30 K and various frequencies (see Figure 4.19) reveal the presence of up to two transitions at each frequency, excluding the omnipresent peak at g ≈ 2 that likely stems from a small amount of iron(III)-containing impurity. The low-field peak corresponds to the forbidden $M_S = 2 \rightarrow M_S = -2$ transition, whereas the high-field peak corresponds to the allowed $M_S = -2 \rightarrow M_S = -1$ transition. We note that the $\Delta M_S = 4$ transition in iron(II) complexes may sometimes be observed even in X-Band EPR owing to the fact that the $M_S = +2$ and -2 levels are split only by approximately $3E^2/D$, while splittings between other M_S levels are of the order of E or D. To quantify the energies of the observed transitions, we used the frequency dependence of the peaks to construct a plot of resonance field vs. frequency (see Figure 4.20). The data were then fit according to the following spin Hamiltonian:

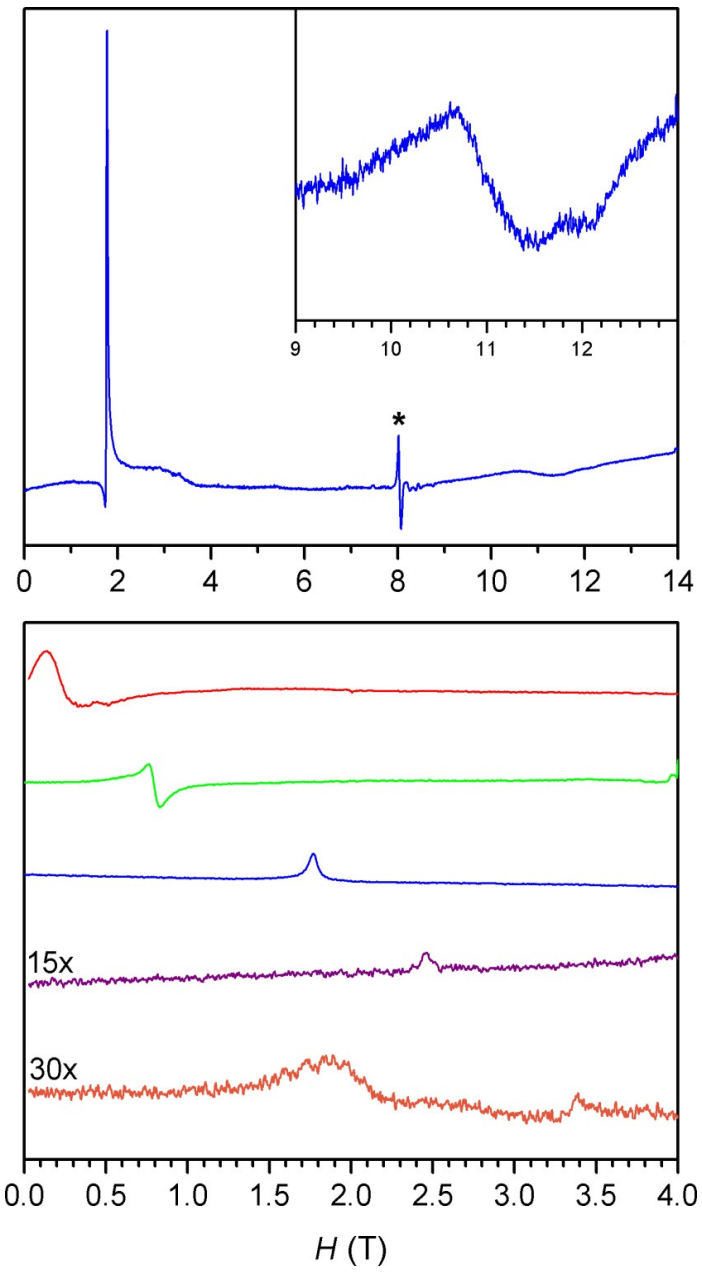


Figure 4.19. Top: Variable-field EPR spectrum for **5** collected at 10 K and 224 GHz. The asterisk denotes an impurity positioned at $g \approx 2$. Inset: Expanded view of the high-field portion of the spectrum. Bottom: Spectra for **5** collected at 30 K and frequencies of 56 (red), 112 (green), 305 (purple) and 416 (magenta) GHz.

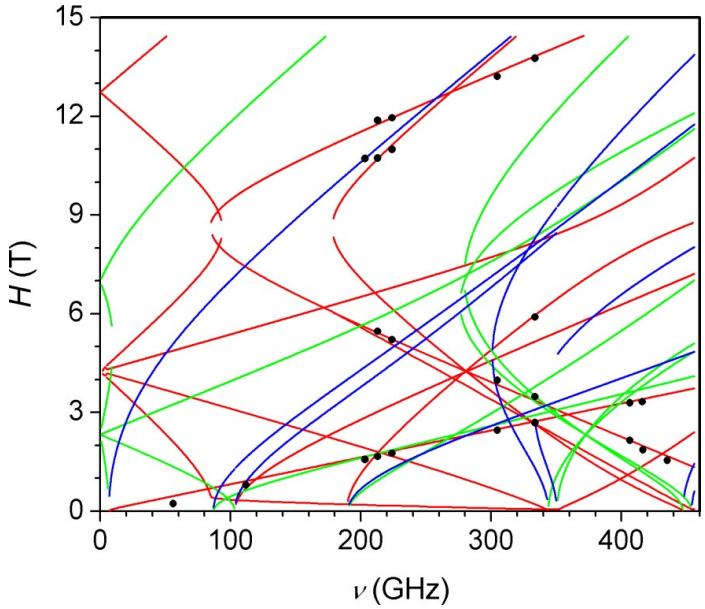


Figure 4.20. Resonant field vs. frequency plot for **5**, constructed for data obtained at 30 K. Solid lines represent fits to the data, with x (red), y (blue) and z (green) turning points, to give $|D| = 4.397(9)$ cm^{-1}, $|E| = 0.574(9)$ cm^{-1} and $g = 2.20$.

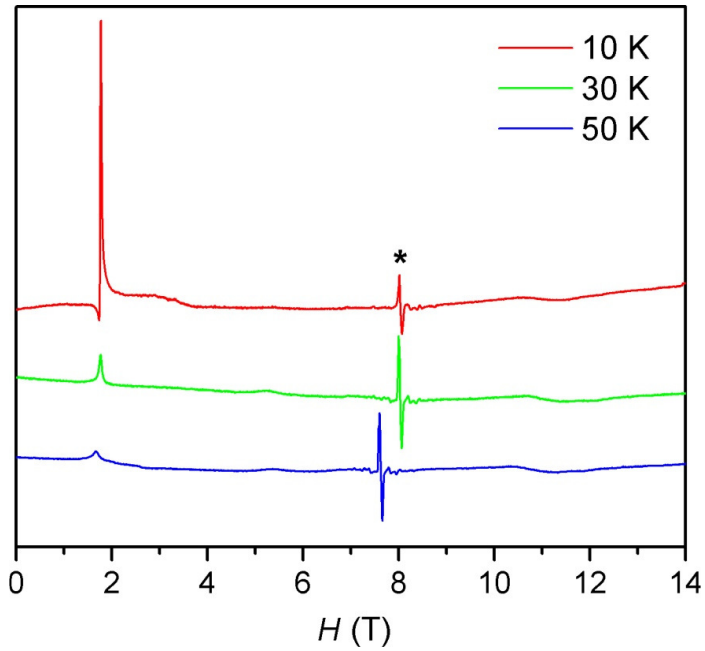


Figure 4.21. Variable-field EPR spectra for **5** collected at 224 GHz and various temperatures. The asterisk denotes an impurity positioned at $g \approx 2$.

$$\hat{H} = \mu_B B \cdot \boldsymbol{g} \cdot \boldsymbol{S} + D\,(\hat{S}_z^2 - S(S+1)/3) + E\,(\hat{S}_x^2 - \hat{S}_y^2) \quad (2)$$

Best fits to the data provided zero-field splitting parameters of $|D| = 4.397(9)$ cm^{-1} and $|E| = 0.574(9)$ cm^{-1}, with $g = 2.20$. These parameters are in good agreement with those of $D = -6.22$ cm^{-1} and $|E| = 0.1$ cm^{-1} obtained from fits to reduced magnetization data. In order to ascertain the sign of D for compound **5**, spectra were collected at 224 GHz at various temperatures. As shown in Figure 4.21, the intensity of the $\Delta M_S = 4$ transition dramatically increases as the temperature is lowered. In contrast, the intensity of the allowed $\Delta M_S = 1$ transition increases as the temperature is increased. These observations indicate the presence of an M_S manifold in which the largest values of M_S are lowest in energy, corresponding to a negative D value. This uniaxial anisotropy is consistent with the results from magnetization measurements.

High-field EPR spectra obtained for complexes **1**–**4** display the forbidden $\Delta M_S = 4$ transition, but we observe no defined peaks at magnetic fields up to 14 T and frequencies up to 600 GHz. As a transition corresponding to $M_S = 2 \rightarrow M_S = -2$ does not provide information regarding the separation between M_S levels with different absolute quantum numbers, we were unable to extract zero-field splitting parameters from these data. However, the absence of observable allowed transitions in these spectra is not surprising given the large axial zero-field splitting parameters these four $[(tpa^R)Fe]^-$ compounds relative to **5**. For instance, according to fits to magnetization data, compound **4** exhibits the next smallest magnitude of D across the series, with $D = -26(2)$ cm^{-1}. The lowest-field allowed transition expected for a molecule with this value occurs at ca. 12 T at 224 GHz. Moreover, this transition is located ca. 100 K higher in energy than the corresponding $\Delta M_S = 4$ transition at 12 T, which suggests that an experimental temperature of 100 K would be necessary to observe a peak. Indeed, data obtained at such a high temperature show a very low signal/noise ratio, such that any peak in the spectrum is likely lost in the background.

4.3 Concluding Remarks

In summary, we have described the synthesis and properties of a novel family of non-heme trigonal pyramidal iron(II) pyrrolide complexes that feature considerable magnetic anisotropy. These coordinatively unsaturated high-spin S=2 iron(II) compounds have been thoroughly characterized by X-ray crystallography, cyclic voltammetry, and Mössbauer spectroscopy. Through systematic modification of a conserved three-fold symmetric trispyrrolide tpa^R core with sterically demanding alkyl and aryl substituents, we reveal a range of large uniaxial zero-field splittings and slow magnetic relaxation for the corresponding $[(tpa^R)Fe]^-$ complexes from static and dynamic magnetic measurements under applied dc fields. In addition, high-field EPR measurements provide direct independent evidence for negative zero-field splittings in this mononuclear high-spin iron(II) platform. Moreover, through the use of more sterically encumbering alkyl pendants to prevent distortions from three-fold symmetry, we have successfully increased the barrier to spin inversion up to $U_{eff} = 65$ cm^{-1} for compound **1**. Taken together, these studies establish the first class of mononuclear transition metal complexes in which single-molecule magnet behavior has been observed and the collective structural and spectroscopic data provide a starting point for further synthetic, reactivity, and magnetic studies of this promising family of bioinspired coordination compounds.

4.4 Experimental Section

Synthetic Materials and Methods. Unless otherwise noted, all manipulations were carried out at room temperature under an atmosphere of dinitrogen in a Vacuum Atmospheres glove box or using Schlenk techniques. Pentane, dimethoxyethane (DME), tetrahydrofuran (THF) and diethyl ether were deoxygenated by sparging with dinitrogen and dried via Vacuum Atmospheres solvent purification system. Diisopropyl ether was distilled from purple sodium/benzophenone ketyl. Dry 1,2-dichloroethane was purchased from Acros, and $FeCl_2$ beads were purchased from Strem. Potassium hydride was purchased as a suspension in mineral oil, washed with pentane and used as a dry solid inside the glove box. Literature procedures were used for the preparation of ethyl pyrrole-2-carboxylate (**6**),[76] K[(tpa^{Mes})Fe] (**2**),[53] tris((5-phenyl-1*H*-pyrrol-2-yl)methyl)amine (H_3tpa^{Ph}) (**7**)[53] and tris((5-(2,4,6-triisopropylphenyl)-1*H*-pyrrol-2-yl)methyl)amine (H_3tpa^{Trip}) (**8**).[52] All other reagents and solvents were purchased from chemical suppliers and used as received. NMR spectra were recorded on Bruker spectrometers operating at 300 or 400 MHz as noted. Chemical shifts are reported in ppm and referenced to residual protiated solvent; coupling constants are reported in Hz. Mass spectra and elemental analyses were performed at the Mass Spectrometry and Microanalytical Facilities at the University of California, Berkeley.

Magnetic Measurements. Magnetic data were collected using a Quantum Design MPMS-XL SQUID magnetometer. Measurements for **1–5** were obtained for finely ground microcrystalline powders restrained in a frozen eicosane matrix within polycarbonate capsules. Dc susceptibility measurements were collected in the temperature range 2-300 K under a dc field of 1000 Oe. Dc magnetization measurements were obtained in the temperature range 1.8-10 K under dc fields of 1, 2, 3, 4, 5, 6, and 7 T. These data were fit in the temperature range 1.8-3.0 K. In general, several different values of E could be obtained and had little to no effect on the goodness-of-fit, depending only on the input values for E. As such, only the maximum values of E are reported. In addition, in cases where multiple fits of similar quality provided slightly different values of g and D, the average value is reported, with the standard deviation of these values given in parentheses. Ac susceptibility measurements were obtained in the temperature range 1.7-6.8 K under a 4 Oe ac field oscillating at frequencies of 1-1488 Hz, under an applied dc field of 1500 Oe. Dc magnetic susceptibility data were corrected for diamagnetic contributions from the sample holder and eicosane, as well as for the core diamagnetism of each sample (estimated using Pascal's constants).

Mössbauer Spectroscopy. The Mössbauer spectra of compounds **1-3** have been measured between 4.2 and 220, 250, and 280 K, respectively, in a Janis Supervaritemp cryostat with a constant-acceleration spectrometer which utilized a rhodium matrix cobalt-57 source and was calibrated at 295 K with α-iron powder. The Mössbauer spectral absorbers of **1-3** contained 60(5), 35(5), and 85(5) mg/cm^2, respectively, of powder mixed with boron nitride; the errors are high because of the difficulty of preparing the absorbers under an inert atmosphere. The statistical errors are given in parentheses in the text and tables. However, more realistic absolute errors for the isomer

shifts are ±0.005 mm/s, for the quadrupole shifts and line widths are ±0.01 mm/s, and for the relative component areas are ±1 %.

X-Ray Crystallography. Crystals were mounted on Kaptan or monofilament loops in Paratone-N hydrocarbon oil. Air-sensitive samples were transferred from the glove box to Paratone-N and mounted quickly to avoid decomposition. All data collection was performed on a Bruker (formerly Siemens) SMART diffractometer/CCD area detector equipped with a low temperature apparatus. Data integration was performed using SAINT. Preliminary data analysis and absorption correction were performed with the Bruker APEX2 software package. Structure solution by direct methods was performed using SIR2004, and the resulting solution refined using the ShelX software package. Hydrogen atoms were included in calculated positions. Table 4.5 summarizes the unit cell and structure refinement parameters forcompounds **1**, **2**, **4**, and **5**.

High-field Electron Paramagnetic Resonance Spectroscopy. High-field, high-frequency EPR spectra at temperatures ranging from ca. 3 K to 290 K were recorded on a home-built spectrometer at the Electron Magnetic Resonance facility of National High Magnetic Field Laboratory. The setup of this instrument has been described in detail previously. The instrument is a transmission-type device in which microwaves are propagated in cylindrical lightpipes. The microwaves are generated by a phase-locked Virginia Diodes source, generating a frequency of 13 ± 1 GHz and producing its harmonics of which the 2^{nd}, 4^{th}, 6^{th}, 8^{th}, 16^{th}, 24^{th} and 32^{nd} are available. A superconducting magnet (Oxford Instruments) capable of reaching a field of 17 T was employed.

Ethyl 5-*tert*-butylpyrrole-2-carboxylate (9). This compound was prepared by the modification of a literature procedure.[77] A dry, round-bottom flask was charged with a stir bar, **6** (30.0 g, 0.216 mol) and 2 L of anhydrous 1,2-dichloroethane. The flask was purged with dinitrogen and $AlCl_3$ (60.5 g, .454 mol) was added in one portion followed by the immediate addition of 2-chloro-2-methylpropane (23.7 mL, 0.216 mol). The resulting mixture was stirred under nitrogen for 2 h and then quenched in air by careful addition to a saturated solution of aqueous $NaHCO_3$ (2 L). Diethyl ether (1 L) was added and the organic layer separated. The aqueous layer was then further extracted with ether (2 x 250 mL). The combined organic portions were dried over anhydrous Na_2SO_4 and concentrated by rotary evaporation to yield a pale brown oil which crystallized upon standing to give 37.5 g (89%) of an off-white solid which was used without further purification. The spectral properties of this material were identical to those reported in the literature.[78]

2-*tert*-Butylpyrrole (10). A slurry of **9** (65.5 g, 0.335 mol) and powdered NaOH (67.0 g, 1.68 mol) in ethylene glycol (650 mL) was brought to reflux with the aid of a heating mantle. After 6 h, the reaction mixture was allowed to cool to room temperature, diluted with water (800 mL) and extracted with CH_2Cl_2 (5 x 200 mL). The organic portions were dried over anhydrous Na_2SO_4 and concentrated by rotary evaporation to yield a brown oil which was vacuum distilled into a flask cooled to –78º C to give 35.0 g (85 %) of a colorless crystalline solid. The spectral properties of this material were identical to those reported in the literature.[79]

Tris-(5-*tert*-butyl-*1H*-pyrrol-2-ylmethyl)-amine, $H_3tpa^{t\text{-}Bu}$ (6). To a solution of NH_4Cl (1.50 g, 28.0 mmol) in an ethanol/water mixture (1:1 v/v, 60 mL) was added

aqueous formaldehyde (37 wt. %, 6.80 g, 83.7 mmol) followed by a solution of **10** (10.3 g, 83.7 mmol) in ethanol (30 mL). The resulting mixture was stirred for three days at room temperature under nitrogen at which point a fine white precipitate was collected by filtration, washed with a small portion of ethanol, briefly air-dried and dissolved in CH_2Cl_2 (200 mL). The solution was washed with 20% aqueous NaOH (200 mL) and the aqueous layer extracted further with CH_2Cl_2 (2 x 100 mL). The organic portions were combined, dried over anhydrous Na_2SO_4 and concentrated to a pale yellow oil that was dried *in vacuo* to give a pale yellow foam. The foam was triturated with 5 mL of hexanes and filtered to yield 7.1 g (60%) of the title compound as a fine white powder. ^{1}H NMR (400 MHz, $CDCl_3$): δ 8.13 (s, 3 H), 5.94 (t, J = 2.8 Hz, 3 H), 5.84 (t, J = 2.8 Hz, 3 H), 3.52 (s, 6 H), 1.30 (s, 9 H); ^{13}C NMR ($CDCl_3$, 100 MHz) δ 142.1, 126.7, 107.7, 102.3, 49.8, 31.6, 30.8.

Na[(tpa$^{t\text{-Bu}}$)Fe] • THF (1). To a solution of **11** (664 mg, 1.57 mmol) in THF (10 mL) was added solid $NaN(SiMe_3)_2$ (865 mg, 4.71 mmol). After stirring for 2 h, the volatiles were removed under reduced pressure, and the colorless residue redissolved in THF (10 mL). Solid $FeCl_2$ (199 mg, 1.57 mmol) was added, and the resulting slurry stirred for 6 h. Precipitated NaCl was removed by filtration over Celite, and the filtrate concentrated under reduced pressure to a colorless glaze. Redissolution of this residue in minimal THF followed by layering with pentane deposited colorless tetrahedral crystals which were washed with pentane and dried *in vacuo* to yield 456 mg (51%) of a microcrystalline solid. Anal. Calcd for $C_{31}H_{47}FeN_4NaO$: C, 65.26; H, 8.30; N, 9.79. Found: C, 64.83; H, 8.43; N, 9.55.

K[(tpa^{Trip})Fe] • 3 DME (3). To a stirring solution of **8** (514 mg, 0.597 mmol) in THF (10 mL) was added solid KH (144 mg, 3.59 mmol) in ca. 10 portions resulting in vigorous effervescence. After stirring for 2 h, effervescence had ceased and the slurry was filtered to remove excess KH. Solid $FeCl_2$ (76 mg, 0.60 mmol) was added to the filtrate, and the resulting slurry was stirred for 6 h. Precipitated KCl was removed by filtration over Celite, and the filtrate was concentrated under reduced pressure to a colorless glaze. Dissolving this residue in minimal 1:1 DME/*i*-Pr_2O and layering with pentane deposited colorless, block-shaped crystals which were washed with pentane and dried *in vacuo* to yield 490 mg (67%) of a white powder. Anal. Calcd for $C_{72}H_{111}FeKN_4O_6$: C, 70.67; H, 9.14; N, 4.58. Found: C, 70.44; H, 9.31; N, 4.81.

Na[(tpa^{Ph})Fe] • 3 DME (4). To a stirring solution of **7** (486 mg, 1.01 mmol) in THF (10 mL) was added solid NaH (145 mg, 604 mmol) in ca. 10 portions resulting in vigorous effervescence. After stirring for 2 h, effervescence had ceased and the slurry was filtered to remove excess NaH. Solid $FeCl_2$ (128 mg, 1.01 mmol) was added to the filtrate, and the resulting slurry was stirred for 6 h. Precipitated NaCl was removed by filtration over Celite, and the filtrate was concentrated under reduced pressure to a yellow glaze. Dissolution of this residue in a minimal amount of THF followed by layering with with DME deposited yellow crystals which were washed with DME and dried *in vacuo* to afford 475 mg (57%) of yellow, microcrystalline solid. Anal. Calcd for $C_{45}H_{57}FeN_4NaO_6$: C, 65.21; H, 6.93; N, 6.76. Found: C, 65.14; H, 6.91; N, 6.86.

2-(2,6-Difluorophenyl)-1*H*-pyrrole (15). This compound was prepared by the modifcation of a literature procedure.[80] In the glove box, sodium pyrrole (1.35 g, 15.2 mmol), $ZnCl_2$ (2.07 g, 15.2 mmol) and THF (35 mL) were combined in a heavy-walled

reaction vessel and allowed to stir for 5 minutes. (Caution: vigorously exothermic.) Then 2-(di-*tert*-butylphosphino)biphenyl (31.1 mg, 0.104 mmol), Pd_2dba_3 (17.4 mg, 0.0190 mmol) and 1-bromo-2,6-difluorobenzene (0.974 g, 5.05 mmol) were added sequentially. The reaction vessel was sealed, removed from the glovebox and heated in an oil bath at 100 ºC for 48 h. Upon cooling to ambient temperature, diethyl ether (100 mL) and water (100 mL) were added to the reaction and the dark mixture filtered through celite, washing the residue with diethyl ether (30 mL). The organic portion of the filtrate was separated and the aqueous layer extracted further with diethyl ether (3 x 75 mL). The combined organic portions were dried over Na_2SO_4 and concentrated by rotary evaporation. Purification of the resultant residue by column chromatography on silica gel (5% ethyl acetate/hexanes) provided 0.485 g (54%) of the title compound as a slightly orange oil. The spectral properties of this material were identical to those reported in the literature.[81]

Tris((5-(2,6-difluorophenyl)-1*H*-pyrrol-2-yl)methyl)amine, H_3tpa^{DFP} (16). To a solution of NH_4Cl (0.183 g, 3.42 mmol) in an ethanol/water mixture (1:1 v/v, 20 mL) was added 37 wt. % aqueous formaldehyde (0.836 g, 10.3 mmol) followed by a solution of **15** (1.84 g, 10.3 mmol) in ethanol (15 mL). The resulting mixture was stirred for three days at room temperature under nitrogen at which point a fine white precipitate was collected by filtration, washed with a small portion of ethanol, briefly air-dried and dissolved in CH_2Cl_2 (100 mL). The solution was washed with 20% aqueous NaOH (100 mL) and the aqueous layer extracted further with CH_2Cl_2 (2 x 75 mL). The organic portions were combined, dried over anhydrous Na_2SO_4 and concentrated to a colorless oil that crystallized on standing to yield 0.661 g (33 %) of a colorless solid. ^{1}H NMR (400 MHz, $CDCl_3$): δ 9.23 (s, 3 H), 7.08 (m, 3 H), 6.97 (t, J = 22 Hz, 6 H), 6.84 (s, 3 H), 6.27 (s, 3 H) 3.71 (s, 6 H); ^{13}C NMR ($CDCl_3$, 100 MHz) δ 159.3 (dd, J = 9, 246 Hz), 130.1 (s), 125.8 (t, J = 12 Hz), 120.6 (s), 112.6 (s), 112.2 (d, J = 27 Hz), 110.6 (t, J = 15 Hz), 109.52 (s), 50.0 (s); ^{19}F ($CDCl_3$, 376 MHz) δ –112.6 (s). HRFABMS ($[M+1]^+$) *m/z* calcd for $C_{33}H_{25}N_4F_6$ 591.1983, found 591.1985.

K[(tpa^{DFP})Fe] • 2 DME (5). To a stirring solution of **16** (698 mg, 1.18 mmol) in THF (10 mL) was added solid KH (284 mg, 7.09 mmol) in ca. 10 portions resulting in vigorous effervescence. After stirring for 2 h, effervescence had ceased and the slurry was filtered to remove excess KH. Solid $FeCl_2$ (150 mg, 1.18 mmol) was added to the filtrate, and the resulting slurry was stirred for 6 h. Precipitated KCl was removed by filtration over Celite, and the filtrate was concentrated under reduced pressure to a yellow glaze. Dissolution of this residue in a minimal amount of DME followed by layering with pentane deposited yellow crystals which were washed with pentane and dried *in vacuo* to afford 575 mg (56%) of a yellow powder. Anal. Calcd for $C_{41}H_{41}FN_4O_4F_6KFe$: C, 57.08; H, 4.79; N, 6.49. Found: C, 57.29; H, 4.56; N, 6.58.

4.5 Acknowledgments

We thank Tyco Electronics for providing T.D.H. with a fellowship.

4.6 References

(1) Sessoli, R.; Tsai, H. L.; Schake, A. R.; Wang, S.; Vincent, J. B.; Folting, K.; Gatteschi, D.; Christou, G.; Hendrickson, D. N. *J. Am. Chem. Soc.* **1993**, *115*, 1804.

(2) Sessoli, R.; Gatteschi, D.; Caneschi, A.; Novak, M. A. *Nature* **1993**, *365*, 141.

(3) Gatteschi, D.; Sessoli, R.; Villain, J. *Molecular Nanomagnets*, 2006.
(4) Milios, C. J.; Vinslava, A.; Wernsdorfer, W.; Moggach, S.; Parsons, S.; Perlepes, S. P.; Christou, G.; Brechin, E. K. *J. Am. Chem. Soc.* **2007**, *129*, 2754.
(5) Yoshihara, D.; Karasawa, S.; Koga, N. *J. Am. Chem. Soc.* **2008**, *130*, 10460.
(6) Garanin, D. A.; Chudnovsky, E. M. *Phys Rev B* **1997**, *56*, 11102.
(7) Leuenberger, M. N.; Loss, D. *Nature* **2001**, *410*, 789.
(8) Heersche, H. B.; de Groot, Z.; Folk, J. A.; van der Zant, H. S. J.; Romeike, C.; Wegewijs, M. R.; Zobbi, L.; Barreca, D.; Tondello, E.; Cornia, A. *Phys. Rev. Lett.* **2006**, *96*.
(9) Jo, M. H.; Grose, J. E.; Baheti, K.; Deshmukh, M. M.; Sokol, J. J.; Rumberger, E. M.; Hendrickson, D. N.; Long, J. R.; Park, H.; Ralph, D. C. *Nano Lett.* **2006**, *6*, 2014.
(10) Ishikawa, N.; Sugita, M.; Ishikawa, T.; Koshihara, S.-Y.; Kaizu, Y. *J. Am. Chem. Soc.* **2003**, *125*, 8694.
(11) Ishikawa, N.; Sugita, M.; Ishikawa, T.; Koshihara, S.; Kaizu, Y. *J. Phys. Chem. B* **2004**, *108*, 11265.
(12) AlDamen, M. A.; Clemente-Juan, J. M.; Coronado, E.; Martí-Gastaldo, C.; Gaita-Ariño, A. *J. Am. Chem. Soc.* **2008**, *130*, 8874.
(13) AlDamen, M. A.; Cardona-Serra, S.; Clemente-Juan, J. M.; Coronado, E.; Gaita-Arino, A.; Marti-Gastaldo, C.; Luis, F.; Montero, O. *Inorg. Chem.* **2009**, *48*, 3467.
(14) Rinehart, J. D.; Long, J. R. *J. Am. Chem. Soc.* **2009**, *131*, 12558.
(15) Laplaza, C. E.; Cummins, C. C. *Science (Washington, DC, U. S.)* **1995**, *268*, 861.
(16) Yandulov, D. V.; Schrock, R. R. *Science (Washington, DC, U. S.)* **2003**, *301*, 76.
(17) Castro-Rodriguez, I.; Nakai, H.; Zakharov, L. N.; Rheingold, A. L.; Meyer, K. *Science (Washington, DC, U. S.)* **2004**, *305*, 1757.
(18) Fryzuk, M. D. *Acc. Chem. Res.* **2009**, *42*, 127.
(19) Knobloch, D. J.; Lobkovsky, E.; Chirik, P. J. *Nature Chem.* **2010**, *2*, 30.
(20) Jenkins, D. M.; Di Bilio, A. J.; Allen, M. J.; Betley, T. A.; Peters, J. C. *J. Am. Chem. Soc.* **2002**, *124*, 15336.
(21) England, J.; Martinho, M.; Farquhar, E. R.; Frisch, J. R.; Bominaar, E. L.; Münck, E.; Que, L. *Angew. Chem., Int. Ed.* **2009**, *48*, 3622.
(22) Brown, S. D.; Peters, J. C. *J. Am. Chem. Soc.* **2005**, *127*, 1913.
(23) Diaconescu, P. L.; Arnold, P. L.; Baker, T. A.; Mindiola, D. J.; Cummins, C. C. *J. Am. Chem. Soc.* **2000**, *122*, 6108.
(24) Mindiola, D. J.; Hillhouse, G. L. *J. Am. Chem. Soc.* **2001**, *123*, 4623.
(25) Melenkivitz, R.; Mindiola, D. J.; Hillhouse, G. L. *J. Am. Chem. Soc.* **2002**, *124*, 3846.
(26) Mindiola, D. J.; Hillhouse, G. L. *J. Am. Chem. Soc.* **2002**, *124*, 9976.
(27) Groves, J. T. *J. Inorg. Biochem.* **2006**, *100*, 434.
(28) Bukowski, M. R.; Koehntop, K. D.; Stubna, A.; Bominaar, E. L.; Halfen, J. A.; Munck, E.; Nam, W.; Que, L. *Science (Washington, DC, U. S.)* **2005**, *310*, 1000.
(29) de Oliveira, F. T.; Chanda, A.; Banerjee, D.; Shan, X. P.; Mondal, S.; Que, L.; Bominaar, E. L.; Munck, E.; Collins, T. J. *Science (Washington, DC, U. S.)* **2007**, *315*, 835.

(30) Halfen, J. A.; Mahapatra, S.; Wilkinson, E. C.; Kaderli, S.; Young, V. G.; Que, L.; Zuberbuhler, A. D.; Tolman, W. B. *Science (Washington, DC, U. S.)* **1996**, *271*, 1397.
(31) Rohde, J. U.; In, J. H.; Lim, M. H.; Brennessel, W. W.; Bukowski, M. R.; Stubna, A.; Münck, E.; Nam, W.; Que, L. *Science (Washington, DC, U. S.)* **2003**, *299*, 1037.
(32) Grapperhaus, C. A.; Mienert, B.; Bill, E.; Weyhermüller, T.; Wieghardt, K. *Inorg. Chem.* **2000**, *39*, 5306.
(33) Berry, J. F.; Bill, E.; Bothe, E.; George, S. D.; Mienert, B.; Neese, F.; Wieghardt, K. *Science (Washington, DC, U. S.)* **2006**, *312*, 1937.
(34) Holland, P. L. *Acc. Chem. Res.* **2008**, *41*, 905.
(35) Bart, S. C.; Lobkovsky, E.; Bill, E.; Chirik, P. J. *J. Am. Chem. Soc.* **2006**, *128*, 5302.
(36) Sazama, G. T.; Betley, T. A. *Inorg. Chem.* **2010**, *49*, 2512.
(37) King, E. R.; Betley, T. A. *J. Am. Chem. Soc.* **2009**, *131*, 14374.
(38) King, E. R.; Betley, T. A. *Inorg. Chem.* **2009**, *48*, 2361.
(39) Thomas, C. M.; Mankad, N. P.; Peters, J. C. *J. Am. Chem. Soc.* **2006**, *128*, 4956.
(40) Betley, T. A.; Peters, J. C. *J. Am. Chem. Soc.* **2004**, *126*, 6252.
(41) Brown, S. D.; Betley, T. A.; Peters, J. C. *J. Am. Chem. Soc.* **2003**, *125*, 322.
(42) Mukherjee, J.; Lucas, R. L.; Zart, M. K.; Powell, D. R.; Day, V. W.; Borovik, A. S. *Inorg. Chem.* **2008**, *47*, 5780.
(43) Larsen, P. L.; Gupta, R.; Powell, D. R.; Borovik, A. S. *J. Am. Chem. Soc.* **2004**, *126*, 6522.
(44) MacBeth, C. E.; Golombek, A. P.; Young, V. G.; Yang, C.; Kuczera, K.; Hendrich, M. P.; Borovik, A. S. *Science (Washington, DC, U. S.)* **2000**, *289*, 938.
(45) Popescu, C. V.; Mock, M. T.; Stoian, S. A.; Dougherty, W. G.; Yap, G. P. A.; Riordan, C. G. *Inorg. Chem.* **2009**, *48*, 8317.
(46) Mock, M. T.; Popescu, C. V.; Yap, G. P. A.; Dougherty, W. G.; Riordan, C. G. *Inorg. Chem.* **2008**, *47*, 1889.
(47) Scepaniak, J. J.; Young, J. A.; Bontchev, R. P.; Smith, J. M. *Angew. Chem., Int. Ed.* **2009**, *48*, 3158.
(48) Scepaniak, J. J.; Fulton, M. D.; Bontchev, R. P.; Duesler, E. N.; Kirk, M. L.; Smith, J. M. *J. Am. Chem. Soc.* **2008**, *130*, 10515.
(49) Nieto, I.; Ding, F.; Bontchev, R. P.; Wang, H. B.; Smith, J. M. *J. Am. Chem. Soc.* **2008**, *130*, 2716.
(50) Govindaswamy, N.; Quarless, D. A.; Koch, S. A. *J. Am. Chem. Soc.* **1995**, *117*, 8468.
(51) Nguyen, D. H.; Hsu, H. F.; Millar, M.; Koch, S. A.; Achim, C.; Bominaar, E. L.; Munck, E. *J. Am. Chem. Soc.* **1996**, *118*, 8963.
(52) Hwang, J.; Govindaswamy, K.; Koch, S. A. *Chem. Commun. (Cambridge, U. K.)* **1998**, 1667.
(53) Harman, W. H.; Chang, C. J. *J. Am. Chem. Soc.* **2007**, *129*, 15128.
(54) Freedman, D. E.; Harman, W. H.; Harris, T. D.; Long, G. J.; Chang, C. J.; Long, J. R. *J. Am. Chem. Soc.* **2010**, *132*, 1224.
(55) Harman, W. H.; Chang, C. J. *unpublished results*.

(56) Harman, W. H.; Chang, C. J. *manuscript in preparation*.
(57) Shores, M. P.; Sokol, J. J.; Long, J. R. *J. Am. Chem. Soc.* **2002**, *124*, 2279.
(58) Gatteschi, D.; Sessoli, R. *Angew. Chem., Int. Ed.* **2003**, *42*, 268.
(59) Friedman, J. R.; Sarachik, M. P.; Tejada, J.; Ziolo, R. *Phys. Rev. Lett.* **1996**, *76*, 3830.
(60) Thomas, L.; Lionti, F.; Ballou, R.; Gatteschi, D.; Sessoli, R.; Barbara, B. *Nature* **1996**, *383*, 145.
(61) Sangregorio, C.; Ohm, T.; Paulsen, C.; Sessoli, R.; Gatteschi, D. *Phys. Rev. Lett.* **1997**, *78*, 4646.
(62) Lin, P. H.; Burchell, T. J.; Clérac, R.; Murugesu, M. *Angew. Chem., Int. Ed.* **2008**, *47*, 8848.
(63) Chudnovsky, E. M.; Tejada, J. *Macroscopic Tunneling of the Magnetic Moment*, 1998.
(64) Cole, K. S.; Cole, R. H. *J. Chem. Phys.* **1941**, *9*, 341.
(65) Böttcher, C. J. F. *Theory of Electric Polarisation*, 1952.
(66) Aubin, S. M. J.; Sun, Z. M.; Pardi, L.; Krzystek, J.; Folting, K.; Brunel, L. C.; Rheingold, A. L.; Christou, G.; Hendrickson, D. N. *Inorg. Chem.* **1999**, *38*, 5329.
(67) Schenker, R.; Leuenberger, M. N.; Chaboussant, G.; Loss, D.; GuÃàdel, H. U. *Phys. Rev. B: Condens. Matter Mater. Phys.* **2005**, *72*, 184403.
(68) Abragam, A.; Bleaney, B. *Electron Paramagnetic Resonance of Transition Ions*; Clarendon Press: Oxford, U. K., 1970.
(69) Carlin, R. L. *Magnetochemistry*; Springer-Verlag: Berlin, 1986.
(70) Reiff, W. M.; Long, G. J. In *Mössbauer Spectroscopy Applied to Inorganic Chemistry*; Long, G. J., Ed.; Plenum Press: New York, 1984; Vol. 1, p 245.
(71) Dattagupta, S.; Blume, M. *Phys. Rev. B* **1974**, *10*, 4540.
(72) Ovanesyan, N. S.; Shilov, G. V.; Sanina, N. A.; Pyalling, A. A.; Atovmyan, L. O.; Bottyán, L. *Mol. Cryst. Liq. Cryst.* **1999**, *335*, 91.
(73) Bottyán, L.; Kiss, L.; Ovanesyan, N. S.; Pyalling, A. A.; Sanina, N. A.; Kashuba, A. B. *JETP Letters* **1999**, *70*, 697.
(74) Kittel, C. *Introduction to Solid State Physics*, New York, 1971.
(75) Mørup, S. in *The Time Domain in Surface and Structural Dynamics*, Long, G. J.; Grandjean, F., Eds., Kluwer, Dordrecht, 1988.
(76) Bailey, D. M.; Johnson, R. E.; Albertson, N. F. *Org. Synth.* **1988**, *50-9*, 618.
(77) Wood, J. E.; Wild, H.; Rogers, D. H.; Lyons, J.; Katz, M.; Caringal, Y.; Dally, R.; Lee, W.; Smith, R. A.; Blum, C. U. S. Patent 6,187,799, 2001.
(78) Elder, T.; Gregory, L. C.; Orozco, A.; Pflug, J. L.; Wiens, P. S.; Wilkinson, T. J. *Synth. Commun.* **1989**, *19*, 763.
(79) Spaggiari, A.; Vaccari, D.; Davoli, P.; Prati, F. *Synthesis* **2006**, 995.
(80) Rieth, R. D.; Mankad, N. P.; Calimano, E.; Sadighi, J. P. *Org. Lett.* **2004**, *6*, 3981.
(81) Kruse, C. G.; Bouw, J. P.; Vanhes, R.; Vandekuilen, A.; Denhartog, J. A. J. *Heterocycles* **1987**, *26*, 3141.

Chapter 5: Slow Magnetic Relaxation in a Series of $MRe(CN)_2$ (M = Mn, Fe, Co, Ni) Chain Compounds Incorporating $[ReCl_4(CN)_2]^{2-}$

5.1 Introduction

Nearly two decades ago, researchers discovered that certain molecules exhibit slow relaxation of the magnetization after removal of an applied dc magnetic field, a phenomenon stemming from an energy barrier to spin inversion.[1] Such species can thus behave at low temperature as classical magnets, and have come to be known as single-molecule magnets. This discovery sparked much excitement, in part because single-molecule magnets could potentially find use in applications such as high-density information storage and quantum computing.[2] However, for such applications to be realized, dramatic increases in spin-reversal barriers must be achieved. Indeed, despite the tremendous effort directed toward this goal, the highest relaxation barrier yet reported for a molecule is 67 cm^{-1}, less than one-third the thermal energy available at room temperature.[1f]

In 2001, slow relaxation of the magnetization was observed in a one-dimensional solid,[3] a phenomenon predicted by Glauber over four decades ago.[4] This solid, a radical-bridged compound of formula $Co(hfac)_2$(NITPhOMe), displays a relaxation barrier of 107 cm^{-1},[5] representing nearly a two-fold increase over the current record in molecular systems. Such a remarkable energy barrier exists for this solid despite the modest net spin generated through antiferromagnetic coupling between anisotropic Co^{II} ions (effective $S = {}^1/_2$) and nitroxide radical ligands ($S = {}^1/_2$). Spurred by this breakthrough, many researchers have recently begun targeting other one-dimensional systems that exhibit slow relaxation of the magnetization,[6] which have come to be known as single-chain magnets.[6a] Indeed, the nascent field of single-chain magnet research has already seen the formation of several new one-dimensional materials exhibiting relaxation barriers higher than any yet observed in single-molecule magnets.[3,6b-d,m]

The increase in relaxation barrier for single-chain magnets over their molecular counterparts can be attributed to an added energy component to the overall barrier in one-dimensional systems. In single-molecule magnets, the energy barrier, Δ_A, stems from a uniaxial magnetic anisotropy, D, acting on a high-spin ground state, S, such that $\Delta_A = S^2|D|$ for integer S values or $\Delta_A = (S^2 - {}^1/_4)|D|$ for half-integer S values (according to the Hamiltonian $H = DS_z^2$, where S_z is the component of S along the z direction). The same anisotropy energy barrier is also present in single-chain magnets, where each chain is composed of individual repeating anisotropic spin units.[7] In addition to this anisotropy barrier, however, single-chain magnets experience an added component to the overall relaxation barrier that stems from short-range magnetic correlation along each individual chain. The length of this correlation, ξ, increases exponentially as the temperature is lowered, where infinite chains are divided into domains of length $L = 2\xi$.[8] As such, inverting a spin within a chain requires the creation of two new domain walls. This added energy requirement for inverting the magnetization, not present in molecules, is known as the correlation energy, Δ_ξ, and corresponds physically to the energy required to create a domain wall. Thus, the total energy required to invert the magnetization in a single-chain magnet, Δ_τ, may be expressed as $\Delta_\tau = 2\Delta_\xi + \Delta_A$.[6i] This relationship, however, only

provides a valid measure of the relaxation barrier within a regime where the chain can be considered infinite. At very low temperatures, the correlation length becomes arrested by defects within the solid.[9] In this finite-size regime, the total energy needed to invert the magnetization reduces to $\Delta_\tau = \Delta_\xi + \Delta_A$, since the reversal of the magnetization becomes more probable from the ends of the finite-size chains.[6i,7] Indeed, previous investigations into the magnetization dynamics of single-chain magnets have found relaxation processes in a single compound corresponding to both infinite- and finite-size regimes by studying the relaxation time in a broad temperature range.[6p,7] One-dimensional chain structures with exchangeable components[10] could provide an important means of probing such effects, while also facilitating variation of anisotropy and magnetic exchange as a means of enhancing the relaxation barrier.

Our approach to synthesizing modular single-chain magnets of this type was initiated through the synthesis of a paramagnetic building unit well-suited for directing the formation of one-dimensional coordination solids. Rhenium(IV) was selected as a metal center owing to its $S = {}^3/_2$ spin ground-state (in an octahedral coordination environment) and the large magnetic anisotropy arising from spin-orbit coupling associated with the third-row transition ion. Indeed, previous studies have reported extremely large axial zero-field splitting parameters for mononuclear rhenium(IV) complexes,[11] as high as $D = 53$ cm^{-1} for $[ReCl_4(ox)]^{2-}$.[11b] Moreover, the building unit $[ReCl_4(ox)]^{2-}$ has been successfully incorporated into a $NiRe_3$ cluster that exhibits single-molecule magnet behavior at low temperature.[12] In addition, for directing the formation of a one-dimensional chain structure, a complex featuring only two *trans* terminal cyanide ligands is desireable. Here, we introduce just such a building unit, with the preparation of the high-anisotropy $S = {}^3/_2$ complex *trans*-$[ReCl_4(CN)_2]^{2-}$, the first structurally-characterized example of a paramagnetic molecule of the form $[MX_x(CN)_y]^{n-}$ (X^- = halide). Additionally, we report the successful incorporation of this complex into a series of cyano-bridged one-dimensional coordination solids $(DMF)_4MReCl_4(CN)_2$ (M = Mn, Fe, Co, Ni), all exhibiting slow relaxation of the magnetization.

5.2 Experimental Section

Preparation of Compounds. The compounds *cis*-$[ReCl_4(THF)_2]$[13] and $(Bu_4N)CN$[14] were synthesized according to literature procedures. Solid $(Bu_4N)CN$ was dried in vacuo ($P < 10^{-3}$ torr) for 36 h using a trap containing P_2O_5 prior to use. All other reagents were obtained from commercial sources and used without further purification. Compound **1** was prepared under a dinitrogen atmosphere using standard glovebox techniques. ***Caution!*** Although we have experienced no problems while working with them, perchlorate salts are potentially explosive and should be handled with extreme care and only in small quantities.

$(Bu_4N)_2$[*trans*-$ReCl_4(CN)_2$]·2DMA (1). Under an atmosphere of dinitrogen, solid $(Bu_4N)CN$ (0.41 g, 1.5 mmol) was added to a stirred green solution of *cis*-$[ReCl_4(THF)_2]$ in 2 mL of DMF. The resulting dark brown viscous solution was stirred for 24 h and then exposed to air. Addition of 25 mL of water to the solution resulted in the formation of a brown precipitate. The precipitate was collected by filtration, washed with water (3 × 25 mL), and allowed to dry on the filter for 30 min. The pale brown solid was then dissolved in 1.5 mL of *N*,*N*-dimethylacetamide (DMA), and the resulting dark yellow solution was

filtered through diatomaceous earth. Diffusion of diethylether vapor into the resulting filtrate yielded 0.20 g (44%) of pale blue rod-shaped crystals suitable for X-ray analysis. Absorption spectrum (MeCN): λ_{max} (ε_M) 325 (sh), 348 (4000), 362 (3200), 371 (sh), 391 (1550), 613 (3.05), 672 (2.70), 723 (3.35), 740 (2.98). IR: ν_{CN} 2120 cm^{-1}. ES^--MS (MeCN): *m*/*z* 623 ($\{(Bu_4N)[ReCl_4(CN)_2]\}^-$). Anal. Calcd. For $C_{42}H_{90}Cl_4N_6O_2Re$: C, 48.54; H, 8.73; N, 8.09. Found: C, 48.78; H, 8.83; N, 8.06.

$(DMF)_4MnReCl_4(CN)_2$ (2). A solution of $Mn(ClO_4)_2 \cdot 6H_2O$ (0.045 g, 0.13 mmol) in 1.5 mL of DMF was added to a solution of **1** (0.051 g, 0.049 mmol) in 1.5 mL of DMF. The resulting yellow solution was allowed to stand for 8 h to afford yellow plate-shaped crystals. The crystals were collected by filtration, washed with successive aliquots of DMF (3 × 1 mL), THF (3 × 5 mL), and Et_2O (3 × 5 mL), and dried in air to yield 0.030 g (83%) of product. IR: ν_{CN} 2148 cm^{-1}. Anal. Calcd. For $C_{14}H_{28}Cl_4MnN_6O_4Re$: C, 23.14; H, 3.89; N, 11.57. Found: C, 23.53; H, 4.06; N, 11.59.

$(DMF)_4FeReCl_4(CN)_2$ (3). A solution of $Fe(ClO_4)_2 \cdot 6H_2O$ (0.020 g, 0.055 mmol) in 1 mL of DMF was added to a solution of **1** (0.030 g, 0.035 mmol) in 1 mL of DMF. The resulting deep blue solution was allowed to stand for 24 h to afford blue plate-shaped crystals. The crystals were collected by filtration, washed with successive aliquots of DMF (3 × 1 mL), THF (3 × 2 mL), and Et_2O (3 × 2 mL), and dried in air to yield 0.014 g (55%) of product. IR: ν_{CN} 2143 cm^{-1}. Due to the instability of crystals of **3** outside their mother liquor, acceptable elemental analysis has not yet been obtained.

$(DMF)_4CoReCl_4(CN)_2$ (4). A solution of $Co(NO_3)_2 \cdot 6H_2O$ (0.061 g, 0.11 mmol) in 1.5 mL of DMF was added to a solution of **1** (0.061 g, 0.071 mmol) in 1.5 mL of DMF. The resulting orange solution was allowed to stand for 24 h to afford orange plate-shaped crystals. The crystals were collected by filtration, washed with successive aliquots of DMF (3 × 1 mL), THF (3 × 5 mL), and Et_2O (3 × 5 mL), and dried in air to yield 0.038 g (72%) of product. IR: ν_{CN} 2151 cm^{-1}. Anal. Calcd. For $C_{14}H_{28}Cl_4CoN_6O_4Re$: C, 23.01; H, 3.86; N, 11.51. Found: C, 23.41; H, 4.08; N, 11.36.

$(DMF)_4NiReCl_4(CN)_2$ (5). A solution of $Ni(ClO_4)_2 \cdot 6H_2O$ (0.032 g, 0.088 mmol) in 1.5 mL of DMF was added to a solution of **1** (0.041 g, 0.039 mmol) in 1.5 mL of DMF. The resulting green solution was allowed to stand for 12 days to afford a pale green microcrystalline solid. The solid was collected by filtration, washed with successive aliquots of THF (2 × 10 mL) and Et_2O (2 × 10 mL), and dried in air to yield 0.021 g (75%) of product. IR: ν_{CN} 2148 cm^{-1}. Anal. Calcd. For $C_{14}H_{28}Cl_4N_6NiO_4Re$: C, 23.04; H, 3.87; N, 11.53. Found: C, 23.44; H, 4.18; N, 11.43.

X-ray Structure Determinations. Single crystals of compounds **1**-**4** were coated with Paratone-N oil and mounted on glass fibers or Kaptan loops. The crystals were then quickly transferred to a Siemens SMART, Bruker APEX, or Bruker MICROSTAR diffractometer, and cooled in a stream of nitrogen gas. Preliminary cell data were collected, giving unit cells consistent with the triclinic Laue groups for all compounds, using the SMART[15] or APEX2[16] program package. The unit cell parameters were later refined against all data. A full hemisphere of data was collected for each compound. None of the crystals showed significant decay during data collection. Data were integrated and corrected for Lorentz and polarization effects using SAINT[17] and were corrected for absorption effects using SADABS.[18]

Table 5.1. Crystallographic Data[a] for $(Bu_4N)_2[ReCl_4(CN)_2]\cdot 2DMA$ (**1**) and $(DMF)_4MReCl_4(CN)_2$, where M = Mn (**2**), Fe (**3**), Co (**4**).

	1	**2**	**3**	**4**
formula	$C_{42}H_{90}Cl_4N_6O_2Re$	$C_{14}H_{28}Cl_4MnN_6O_4Re$	$C_{14}H_{28}Cl_4FeN_6O_4Re$	$C_{14}H_{28}Cl_4CoN_6O_4Re$
formula weight	1039.22	727.37	728.27	731.36
T, K	139	149	100	155
space group	P-1	P-1	P-1	P-1
Z	1	2	2	2
a, Å	10.5629(8)	9.9185(9)	9.8745(7)	9.957(1)
b, Å	11.9119(9)	10.712(1)	10.5846(7)	10.549(1)
c, Å	12.1271(9)	14.026(1)	13.9378(10)	13.914(1)
α, deg	64.8130(10)	68.07(1)	68.131(4)	67.882(1)
β, deg	75.0150(10)	77.78(1)	78.315(4)	86.275(1)
γ, deg	82.1510(10)	68.91(1)	69.294(4)	69.659(1)
V, Å^3	1333.24(17)	1284.7(2)	1260.38(15)	1266.0(2)
d_{calc}, g/cm^3	1.294	1.880	1.919	1.919
R_1 (wR_2), %[b]	3.37 (8.58)	3.66 (9.15)	3.06 (10.26)	4.01 (10.04)

[a]Obtained with graphite-monochromated Mo Kα (λ = 0.71073 Å) radiation for **1**, **2**, and **4**, and Cu Kα (λ = 1.5406 Å) for **3**. [b] $R_1 = \Sigma||F_o| - |F_c||/\Sigma|F_o|$, $wR_2 = \{\Sigma[w(F_o^2 - F_c^2)^2]/\Sigma[w(F_o^2)^2]\}^{1/2}$.

Space group assignments were based upon systematic absences, *E*-statistics, and successful refinement of the structures. Structures were solved by direct methods and expanded through successive difference Fourier maps. They were refined against all data using the SHELXTL program.[19] Thermal parameters for all non-hydrogen atoms were refined anisotropically in all compounds, with the exception of C1 in **3**, which was refined isotropically. Table 5.1 summarizes the unit cell and structure refinement parameters for compounds **1**-**4**.

Magnetic Susceptibility Measurements. Magnetic data were collected using a Quantum Design MPMS-XL SQUID magnetometer. Measurements for **1** and dc susceptibility measurements for **2**-**5** were obtained for finely ground microcrystalline powders restrained in a frozen eicosane matrix within polycarbonate capsules. These measurements were collected in the temperature range 1.8-300 K under a dc field of 1000 Oe. *M* vs. *H* and ac susceptibility measurements for **2**-**5** were obtained for crystals restrained in frozen mother liquors within sealed quartz tubes to prevent sample decomposition. The field dependences of the magnetization were measured at 1.8 K while sweeping the magnetic field between –7 and 7 T. ac magnetic susceptibility data were collected in zero dc field in the temperature range 1.7-100 K, under an ac field of 4 Oe, oscillating at frequencies in the range 0.5-1488 Hz. All data were corrected for diamagnetic contributions from the sample holder and eicosane, as well as for the core diamagnetism of each sample (estimated using Pascal's constants). The coherence of the

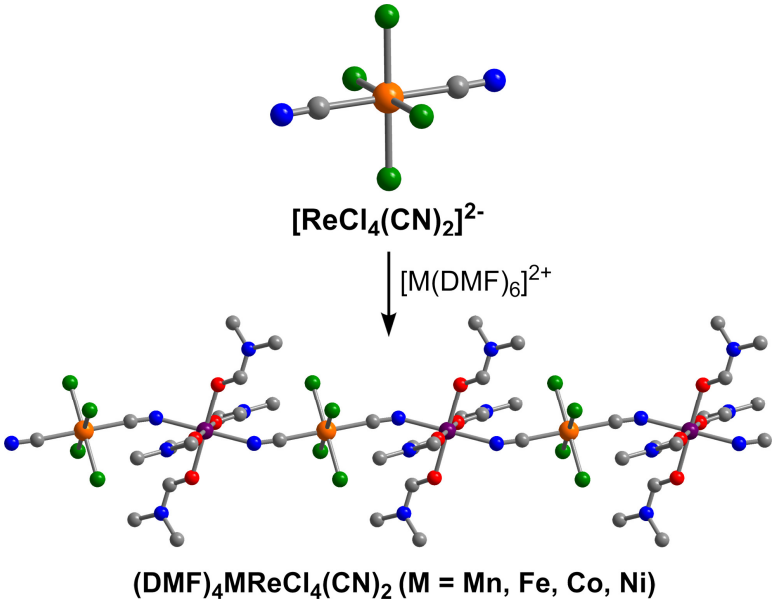


Figure 5.1. Reaction of *trans*-$[ReCl_4(CN)_2]^{2-}$ (upper) with $[M(DMF)_6]^{2+}$ (M = Mn, Fe, Ni, Co) to form the one-dimensional solids $(DMF)_4MReCl_4(CN)_2$. Orange, purple, green, red, blue, and gray spheres represent Re, M, Cl, O, N, and C atoms, respectively; H atoms have been omitted for clarity. In the structure of **1**, the $[ReCl_4(CN)_2]^{2-}$ complex resides on a crystallographic inversion center, with selected interatomic distances (Å) and angles (°) of: Re-C 2.148(4), Re-Cl 2.351(1), 2.341(1), C-N 1.123(5), Re-C-N 177.2(3), C-Re-C 180, C-Re-Cl 89.6(1), 90.4(1), Cl-Re-Cl 89.9(1), 90.1(1).

collected data for all the compounds was checked between the different techniques of measurements.

Other Physical Measurements. Absorption spectra were measured with a Hewlett-Packard 8453 spectrophotometer. Infrared spectra were obtained on a Nicolet Avatar 360 FTIR or Perkin-Elmer Spectrum 100 Optica FTIR spectrometer, each equipped with an attenuated total reflectance accessory. Carbon, hydrogen, and nitrogen analyses were obtained from the Microanalytical Laboratory of the University of California, Berkeley. X-ray powder diffraction data were collected using Cu Kα (λ = 1.5406 Å) radiation on a Siemens D5000 diffractometer.

5.3 Results and Discussion

Synthesis, Structure, and Magnetic Properties of $[ReCl_4(CN)_2]^{2-}$. The complex $[ReCl_4(CN)_2]^{2-}$ was synthesized via addition of excess $(Bu_4N)CN$ to a solution of $ReCl_4(THF)_2$ in DMF. Adding water to the solution gave a pale brown precipitate, and diffusion of diethylether vapor into a DMA solution of the solid subsequently afforded pale blue rod-shaped crystals of $(Bu_4N)_2$[*trans*-$ReCl_4(CN)_2$]·2DMA (**1**). X-ray analysis of a single crystal revealed an octahedral coordination geometry for the Re^{IV} center, which

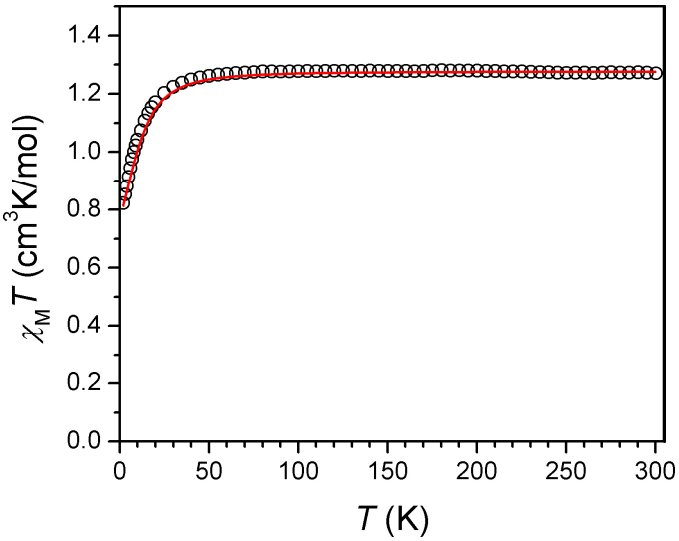


Figure 5.2. Variable-temperature magnetic susceptibility data collected for **1** under an applied dc field of 1000 Oe. The solid red line corresponds to D = -14.4 cm^{-1} and g = 1.66.

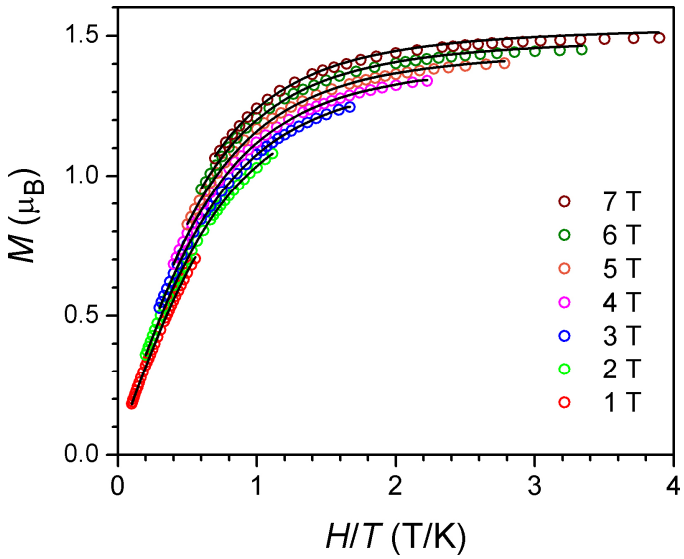


Figure 5.3. Low-temperature magnetization data for **1** collected under various applied dc fields. The black lines represent fits to the data.

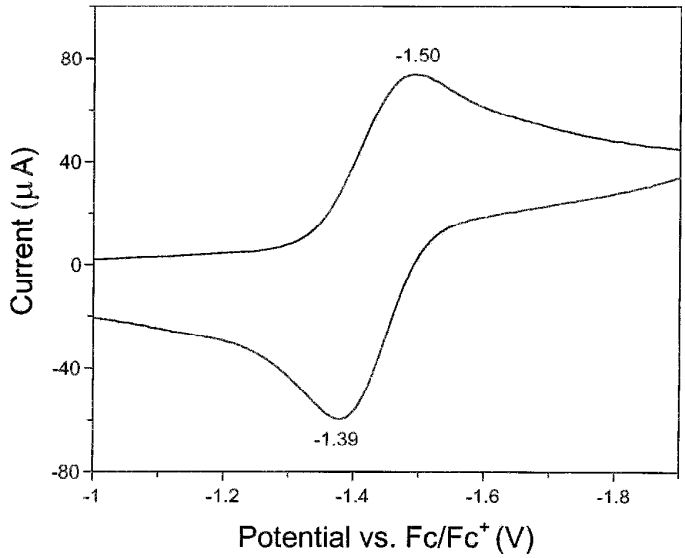


Figure 5.4. Cyclic voltammogram of **1** in acetonitrile. The measurement was performed on a platinum electrode at a scan rate of 100 mV/s, with 0.1 M $[Bu_4N](PF_6)$ as the supporting electrolyte. Potentials are referenced to the Fc/Fc^+ couple.

is ligated by four equatorial chloride ligands and two axial cyanide ligands oriented *trans* to one another (see Figure 5.1). In the structure, the Re atom resides on an inversion center, and the C-Re-Cl and Cl-Re-Cl bond angles are close to 90°. The Re-C distance of 2.148(4) Å is slightly longer than those observed for $[Re(CN)_7]^{3-}$ (2.06(1)-2.12(1) Å),[20] and the mean Re-Cl distance of 2.346(1) Å is close to that found in $[ReCl_6]^{2-}$ (2.351 Å).[21] To our knowledge, the only previous examples of structurally-characterized transition metal complexes of the type $[MX_x(CN)_y]^{n-}$ (X^- = halide) are octahedral *trans*-$[Pt(CN)_4X_2]^{2-}$ (X = Cl, Br, I)[22] and square planar *trans*-$[Au(CN)_2X_2]^-$.[23] Thus, *trans*-$[ReCl_4(CN)_2]^{2-}$ represents the first example of a paramagnetic complex with a mixture of halide and cyanide ligands.

Magnetic susceptibility data collected for **1** yield a value of $\chi_M T$ = 1.27 $cm^3 \cdot K/mol$ at 300 K, corresponding to an $S = {}^3/_2$ spin ground-state with g = 1.65 (see Figure 5.2). Upon lowering the temperature, $\chi_M T$ remains essentially constant to ca. 70 K, before dropping precipitously at lower temperatures. This downturn can be attributed to the presence of magnetic anisotropy. Additionally, the plot of reduced magnetization reveals a series of non-superimposable isofield curves, also indicative of significant anisotropy (see Figure 5.3). To quantify this effect, the isofield data were fit using ANISOFIT 2.0[24] to give a zero-field splitting parameter of $D = -14.4\ cm^{-1}$, with g = 1.66. The large magnitude of D establishes the highest value yet reported for a metal-cyanide complex of any kind, and stems from the considerable spin-orbit coupling associated with the heavy Re^{IV} center.

Since possession of a large negative D value serves as a prerequisite for slow relaxation of the magnetization, the foregoing result emphasizes the potential of **1** as a building unit for new single-molecule and single-chain magnets. Indeed, incorporation of

Table 5.2. Selected Mean Interatomic Distances (Å) and Angles (°) for $(DMF)_4MReCl_4(CN)_2$, where M = Mn (**2**), Fe (**3**), Co (**4**)

	2	**3**	**4**
Re-C	2.125(1)	2.118(1)	2.134(1)
M-N	2.228(1)	2.155(1)	2.111(1)
M-O	2.181(1)	2.134(1)	2.098(1)
Re-C-N	175.8(1)	175.4(1)	174.7(1)
M-N-C	155.8(1)	158.1(1)	159.4(1)
φ(Re-C)[a]	6.3	5.9	5.7
φ(M-N)[a]	7.5	7.0	7.1

[a] Interchain tilt angles, as described in the text.

the rhenium(IV) complex $[Re(CN)_7]^{3-}$ into molecular clusters has already led to the formation of three single-molecule magnets, among them a species exhibiting a relaxation barrier of 33 cm^{-1}, the highest yet observed for a cyano-bridged molecule.[1e,25] One considerable disadvantage to the pentagonal bipyramidal complex $[Re(CN)_7]^{3-}$, however, is its propensity to undergo a spontaneous, solvent-assisted one-electron reduction to diamagnetic $[Re(CN)_7]^{4-}$ as metal complexes are appended to it.[1e,20] In $[ReCl_4(CN)_2]^{2-}$, the presence of π-donating chloride ligands serves to stabilize the higher +4 oxidation state of the rhenium center. Indeed, the cyclic voltammogram of **1** shows a single reversible one-electron reduction occurring at $E_{1/2}$ = –1.45 V vs. $Cp_2Fe^{0/1+}$ (see Figure 5.4), a shift to a considerably more negative potential relative to $[Re(CN)_7]^{3-}$ ($E_{1/2}$ = –1.06 V vs. $Cp_2Fe^{0/1+}$).[20] In addition, even in the event of a one-electron reduction of $[ReCl_4(CN)_2]^{2-}$, the octahedral coordination environment of the Re^{III} center would render a paramagnetic t_{2g}^4 electron configuration.

Syntheses and Structures of the $M^{II}Re^{IV}(CN)_2$ Chain Compounds. The one-dimensional cyano-bridged solids $(DMF)_4MReCl_4(CN)_2$ (M = Mn (**2**), Fe (**3**), Co (**4**), Ni (**5**)) were synthesized through the simple addition of a DMF solution containing the appropriate hydrated metal salt to a DMF solution of **1**, as indicated in Figure 5.1. X-ray analyses showed the compounds to crystallize as an isostructural series in space group $P\bar{1}$ (see Table 1). For **2**-**4**, structures were obtained through single-crystal X-ray diffraction, while powder diffraction data confirm the structure of **5**. The structures consist of one-dimensional chains, wherein each chain is composed of alternating $[ReCl_4(CN)_2]^{2-}$ and $[M(DMF)_4]^{2+}$ units connected via bridging cyanide ligands. The coordination environment of each Re^{IV} center does not deviate significantly from that observed in $[ReCl_4(CN)_2]^{2-}$, while the geometry at each M^{II} center approximates an octahedron, with O-M-O and N-M-O angles near 90° (see Table 5.2). Along the sequence from **2** (M = Mn) to **3** (M = Fe) to **4** (M = Co), the mean M-N and M-O distances decrease from 2.228(1) and 2.111(1) Å, respectively, to 2.111(1) and 2.097(1) Å, as expected for the

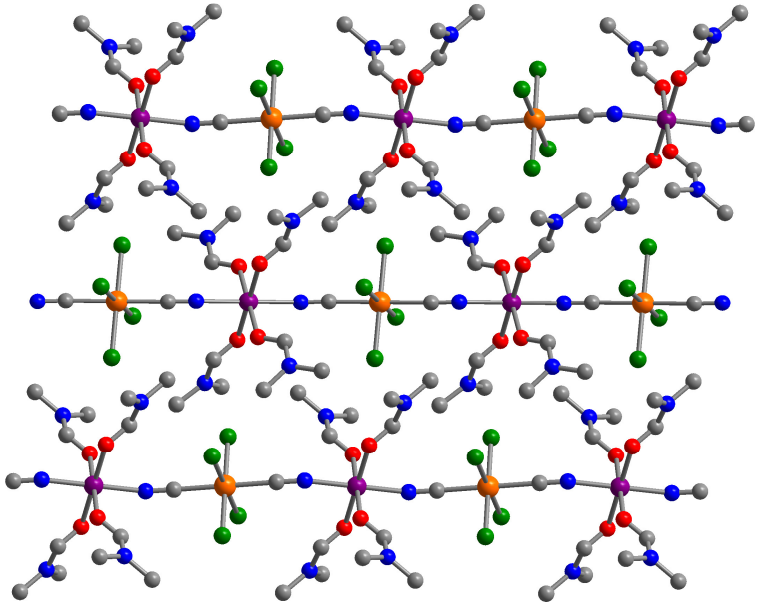


Figure 5.5. Crystal packing diagram for **2**. Orange, purple, green, red, blue, and gray spheres represent Re, Mn, Cl, O, N, and C atoms, respectively; H atoms are omitted for clarity. The closest interchain metal-metal contact is a Re···Mn distance of 7.6845(5) Å.

decreasing metal ion radii. The Re-C-N angles are all close to 180°, while the M-N-C angles deviate significantly from linearity, with mean angles ranging from 155.8(1)° in **2** to 159.4(1)° in **4**. Such bent angles are not uncommon for M^{II} centers coordinated at the nitrogen end of cyanide[1e,20,26] and, in this case, likely arise from the packing of the chains within the crystals. The structure of each solid consists of two crystallographically independent chains, wherein the Re-C bonds on neighboring chains deviate slightly from a parallel orientation, and are tilted at angles (φ) ranging from 5.7° to 6.3° relative to each other. Likewise, a similar deviation can be observed between Fe-N bonds on neighboring chains, with tilt angles lying in the range 7.0-7.5°. Despite the minor local tilting relative to one another, both chains propagate along the *b* axis of the crystal (see Figure 5.5). Compounds **2**-**4** crystallize with no lattice solvent molecules present in the unit cell. Importantly, no close metal-metal contacts are found in the crystal structure, with the shortest interchain metal-metal separations being 7.6845(5), 7.6815(5), and 7.7215(6) Å for **2**, **3**, and **4**, respectively. In addition, no hydrogen bonding interactions are evident in any of the structures.

Static Magnetic Properties of the $M^{II}Re^{IV}(CN)_2$ Chain Compounds. To probe the nature of magnetic exchange interactions in the one-dimensional solids, variable-temperature magnetic susceptibility data were collected for compounds **2**-**5**. A plot of $\chi_M T$ vs. T for **2**, collected under an applied dc field of 1000 Oe, is shown in Figure 5.6. At 300 K, $\chi_M T$ = 4.79 cm^3·K/mol, slightly lower than the expected value of $\chi_M T$ = 6.25 cm^3·K/mol for one isolated Re^{IV} center ($S = {}^3/_2$) and one isolated Mn^{II} center ($S = {}^5/_2$), with g = 2. Upon lowering the temperature, $\chi_M T$ begins a gradual decrease, reaching a

minimum of 2.58 cm^3·K/mol at 35 K, before climbing abruptly to a maximum of 19.6 cm^3·K/mol at 6 K. This behavior is indicative of antiferromagnetic coupling between the neighboring Re^{IV} and Mn^{II} centers within the chains. Thus, antiferromagnetic exchange overwhelms the competing ferromagnetic interactions, as expected for superexchange through cyanide between Re^{IV} (t_{2g}^3) and high-spin Mn^{II} ($t_{2g}^3e_g^2$) centers.[27] The noncompensation of the spins induces a ferrimagnetic arrangement along the chain, giving rise to a repeating unit with $S = 1$. As the temperature drops below 6 K, $\chi_M T$ turns down sharply owing to field saturation of the magnetization and the magnetic anisotropy of the Re^{IV} centers .

In order to quantify the strength of intrachain exchange coupling in **2**, the $\chi_M T$ vs. T data were modeled according to the following spin Hamiltonian for a chain comprised of alternating Heisenberg classical spins:

$$H = -2J\sum_{i=1}^{N}\left(S_i s_i + s_i S_{i+1}\right) \quad (1)$$

The data were fit (solid red line in Figure 3) in the temperature range 14-300 K, employing an expression previously used to describe the magnetic susceptibility of an alternating chain,[28] to give J = -5.4(4) cm^{-1}, g_{Re} = 1.80(6), and g_{Mn} = 1.96(2).

The $\chi_M T$ product for **3** shows distinctly different temperature dependence than does that of **2**, as shown in Figure 5.7. At 300 K, $\chi_M T$ is 5.46 cm^3·K/mol, close to the expected value of $\chi_M T$ = 4.88 cm^3·K/mol for one isolated Re^{IV} center ($S = {}^3/_2$) and one isolated high-spin Fe^{II} center (S = 2) with g = 2.00. As the temperature is lowered, $\chi_M T$ begins to rise, gradually at first, and then abruptly below 40 K, to attain a maximum value of 63.1 cm^3·K/mol at 12 K, before dropping sharply at lower temperature. This increase with decreasing temperature is indicative of ferromagnetic coupling between neighboring Re^{IV} (t_{2g}^3) and Fe^{II} ($t_{2g}^4e_g^2$) centers within the chains. The $\chi_M T$ vs. T data were modeled similarly to those for **2**, in the temperature range 25-300 K, to give J = +4.8(4) cm^{-1} and g = 1.96(6).[29] The occurrence of ferromagnetic coupling is somewhat unexpected, given that the antiferromagnetic interactions tend to dominate over the ferromagnetic interactions in such situations.[27]

The plot of $\chi_M T$ vs. T for **4** follows a similar trend to that observed for **3** (see Figure 5.8). At 300 K, $\chi_M T$ = 4.72 cm^3·K/mol, slightly higher than the expected value of $\chi_M T$ = 3.75 cm^3·K/mol for one isolated Re^{IV} center ($S = {}^3/_2$) and one isolated high-spin Co^{II} center ($S = {}^3/_2$) with g = 2.00. As the temperature is lowered, $\chi_M T$ increases to a maximum value of 35.8 cm^3·K/mol at 6 K, before dropping precipitously below 6 K. The increase in $\chi_M T$ with decreasing temperature is indicative of intrachain ferromagnetic coupling between Re^{IV} (t_{2g}^3) and Co^{II} ($t_{2g}^5e_g^2$) centers. Indeed, a fit to the data in the temperature range 12-300 K confirms a ferromagnetic interaction, with J = +2.4(1) cm^{-1} and g = 2.11(3). Similarly, susceptibility data collected for **5** confirm the presence of intrachain ferromagnetic coupling, as expected between metals with t_{2g}^3 and $t_{2g}^6e_g^2$ configurations, for which the unpaired electrons reside in orthogonal orbitals (see Figure 5.9). A fit to the data for **5** in the temperature range 14-300 K afforded parameters of J = +3.7(3) cm^{-1} and g = 2.04(4).

For any one-dimensional classical system, the $\chi_M T$ product in zero applied field is directly proportional to the correlation length, ξ, in zero applied field. In the particular

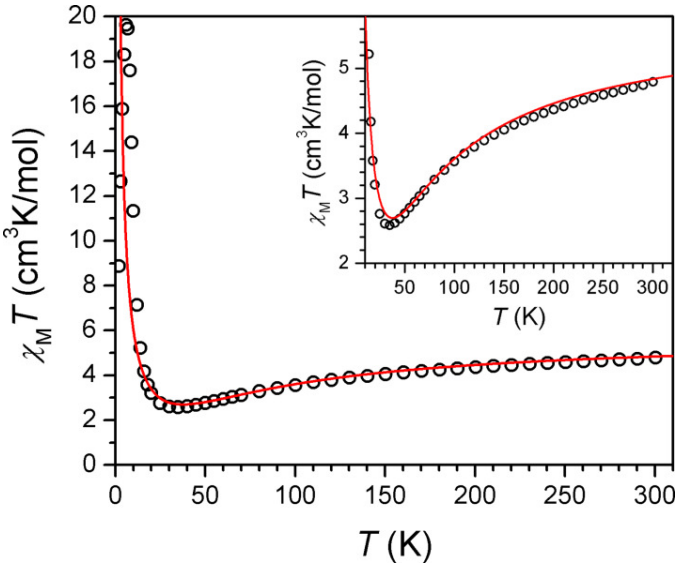


Figure 5.6. Variable-temperature dc magnetic susceptibility data for **2**, collected in an applied field of 1000 Oe. The solid red line corresponds to a fit to the data, as described in the text. Inset: Contracted view of the data and fit, highlighting the presence of intrachain antiferromagnetic coupling in **2**.

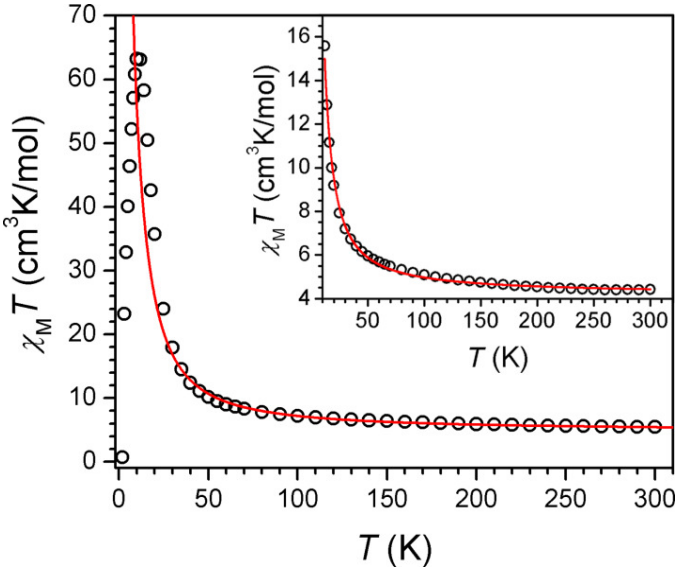


Figure 5.7. Variable-temperature dc magnetic susceptibility data for **3**, collected in an applied field of 1000 Oe. The solid red line corresponds to a fit to the data, as described in the text. Inset: Contracted view of the data and fit, highlighting the presence of intrachain ferromagnetic coupling in **3**.

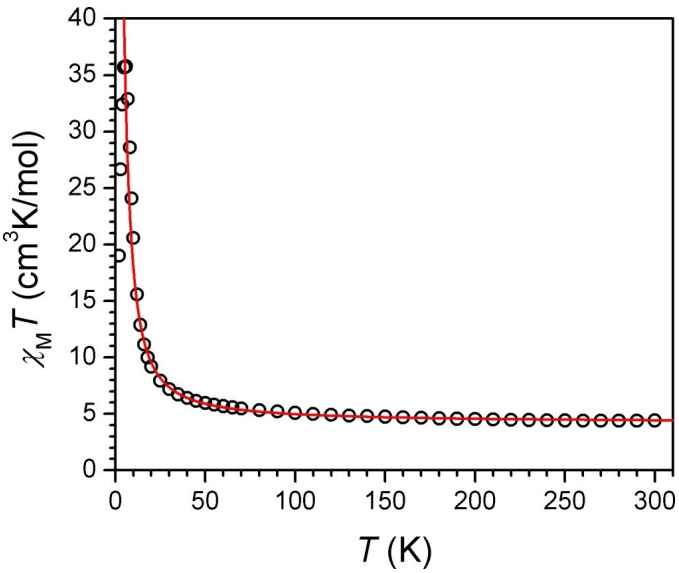


Figure 5.8. Variable-temperature dc magnetic susceptibility data for **4**, collected in an applied field of 1000 Oe. The solid red line corresponds to a fit to the data, as described in the text.

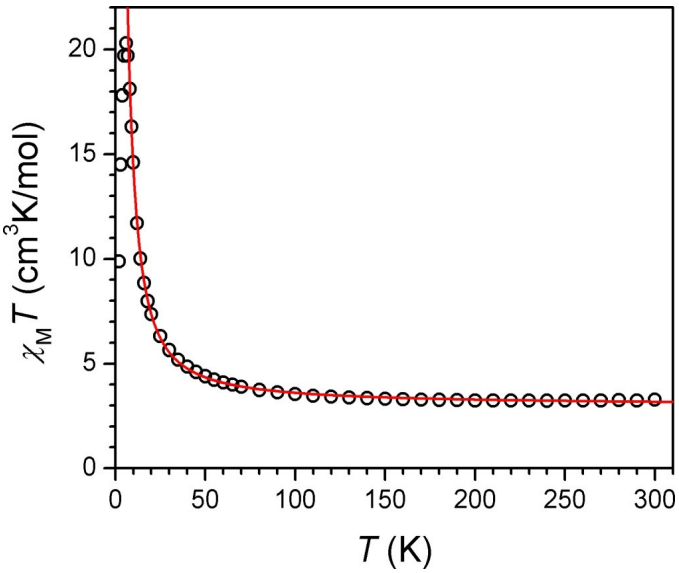


Figure 5.9. Variable-temperature dc magnetic susceptibility data for **5**, collected in an applied field of 1000 Oe. The solid line corresponds to a fit to the data, as described in the text.

case of anisotropic one-dimensional behavior, ξ, and thus $\chi_M T$, increases exponentially with decreasing temperature, according to the following equation:

$$\chi_M T/C \approx \exp(\Delta_\xi/k_B T) \quad (2)$$

where C is the effective Curie constant, Δ_ξ is the correlation energy (the energy needed to create a domain wall in the chain), and k_B is the Boltzmann constant.[6i,8,30] Following from this relationship, a plot of $\ln(\chi_M T)$ vs. $1/T$ should display a linear region, with the line of best fit exhibiting a slope corresponding to the correlation energy. Thus, to ascertain the one-dimensional nature of **2**, variable-temperature ac susceptibility data were collected in the absence of an applied dc field, with an ac field of 4 Oe oscillating at 1 Hz. Indeed, the resulting plot of $\ln(\chi_M T)$ vs. $1/T$ features a linear region in the temperature range 6.8-20 K (see Figure 5.10), yielding $\Delta_\xi = 19$ cm^{-1}, a value corresponding to the energy required to create a domain wall within the chain. Below 6.8 K, $\ln(\chi_M T)$ reaches a maximum, and then undergoes a linear decrease with decreasing temperature. The intersection of the two linear regions, occurring at ca. 6.5 K, corresponds to the crossover temperature (T^*), where the magnetic correlation becomes physically limited by crystalline defects, and temperatures below T^* comprise the finite-size regime. Similarly, the solids **3**-**5** display clear linear regions in $\ln(\chi_M T)$, followed by downturns as temperature is decreased (see Figures 5.11-13). Linear fits to the high-temperature data provide correlation energies for **3**-**5** of $\Delta_\xi = 28$, 8.5, and 8.8 cm^{-1}, with crossover temperatures of $T^* = 14$, 5.9, and 6.7 K, respectively. For one-dimensional systems falling within the Ising limit, the correlation energy is related to the intrachain coupling strength, J, and constituent spins through the equation $\Delta_\xi = 4|JS_1S_2|$.[6i] In the case of **2**, considering the value of J obtained from fitting the $\chi_M T$ vs. T data, $4|JS_1S_2| = 81$ cm^{-1}, more than four times the experimental value of Δ_ξ. Likewise, comparisons of $4|JS_1S_2|$ and Δ_ξ for the other solids indicate strong disagreement between values in **3**, **4**, and **5** (see Table 5.3). These stark disagreements demonstrate that the compounds do not fall within the Ising limit with sharp domain walls and instead possess the broad domain walls expected when the anisotropy energy is not sufficiently larger than the exchange energy. In this intermediate regime between the Ising and the Heisenberg limits, the Δ_ξ expression is still unknown and thus no direct relation with J and S is evident.

Variable-field magnetization data collected for **2** at 1.8 K between –7 and 7 T reveal complete reversibility of the magnetization (see Figure 5.14). Notably, the M vs. H curve is smooth, with the absence of any kinks, thus eliminating the possibility of a three-dimensional antiferromagnetic ordering transition down to 1.8 K. A dramatically different M vs. H curve is observed for **3** at 1.8 K, however, as sweeping the magnetic field between –7 and 7 T reveals significant hysteresis in the magnetization (see Figure 5.15). Indeed, inspection of the hysteresis loop shows a coercive field of $H_C = 1.0$ T and a remnant magnetization of $M_R = 3.77$ μ_B. This substantial slow dynamics of the magnetization, indicative of a "magnetic memory," demonstrates classical magnet-like behavior in **3**. Finally, variable-field magnetization data collected for **4** and **5** at 1.8 K between –7 and 7 T show complete reversibility of the magnetization, similar to that observed for **2** (see Figures 5.16-17).

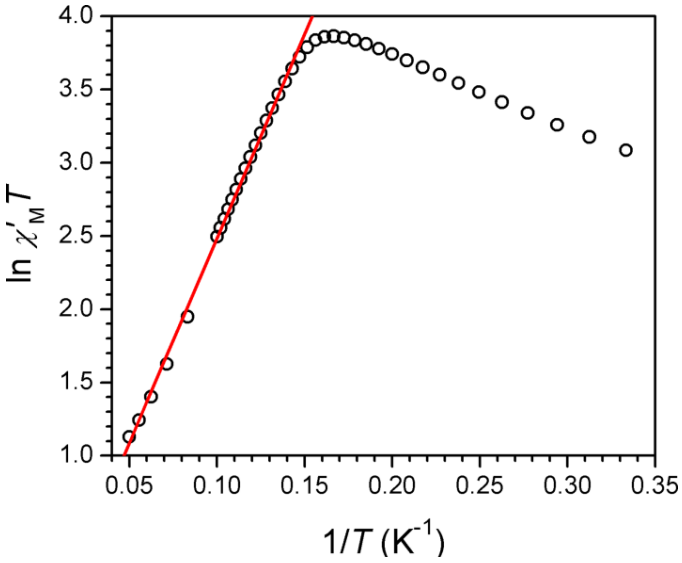


Figure 5.10. Plot of $\ln(\chi'_M T)$ vs. $1/T$ (where χ'_M is the molar component of the ac susceptibility) for **2**, collected in zero applied dc field. The solid red line corresponds to a fit to the linear portion of the data, giving $\Delta_\xi = 19$ cm^{-1}.

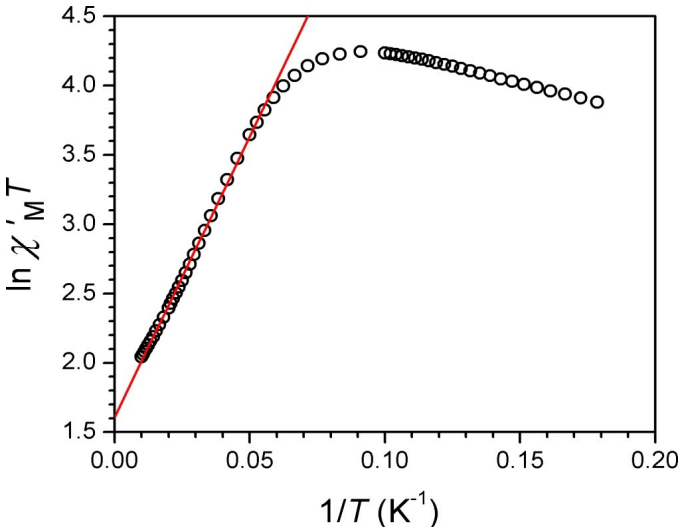


Figure 5.11. Plot of $\ln(\chi'_M T)$ vs $1/T$ for **3**, collected in zero applied dc field under an ac field of 4 Oe oscillating at 1 Hz. The solid line corresponds to a fit to the linear portion of the data, giving $\Delta_\xi = 28$ cm^{-1}.

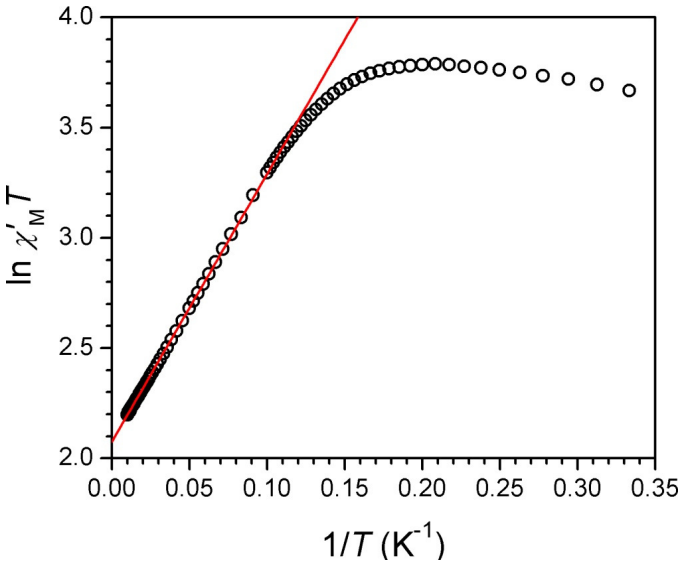


Figure 5.12. Plot of ln($\chi'_M T$) vs 1/T for **4**, collected in zero applied dc field under an ac field of 4 Oe oscillating at 1 Hz. The solid line corresponds to a fit to the linear portion of the data, giving $\Delta_\xi = 8.5$ cm^{-1}.

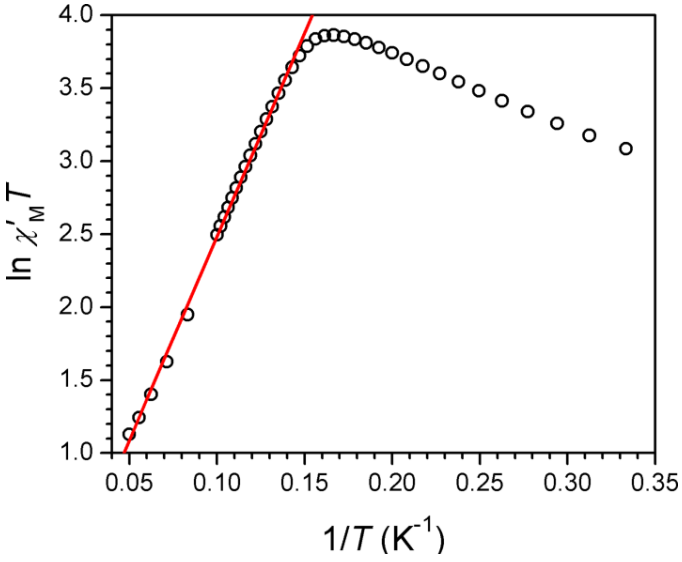


Figure 5.13. Plot of ln($\chi'_M T$) vs 1/T for **5**, collected in zero applied dc field under an ac field of 4 Oe oscillating at 1 Hz. The solid line corresponds to a fit to the linear portion of the data, giving $\Delta_\xi = 8.8$ cm^{-1}.

Table 5.3. Summary of Magnetic Data for $(DMF)_4MReCl_4(CN)_2$, where M = Mn (**2**), Fe (**3**), Co (**4**), Ni (**5**)

	J (cm^{-1})	$4\|JS_1S_2\|$ (cm^{-1})	Δ_ξ (cm^{-1})	Δ_τ (cm^{-1})	H_A (T)	H_{sat} (T)
2	–5.4(4)	81	19	31	23	13-15
3	+4.8(4)	58	28	56	18	23-25
4	+2.4(1)	22	8.5	17		
5	+3.7(3)	22	8.8	20	11	19-21

Dynamic Magnetic Properties of the $M^{II}Re^{IV}(CN)_2$ Chain Compounds. To probe the dynamics of the magnetization in the one-dimensional coordination solids, the ac magnetic susceptibility was studied as a function of both temperature and frequency. Variable-temperature ac susceptibility measurements for **2** (see Figure 5.18) reveal a strong frequency dependence of both in-phase (χ_M') and out-of-phase (χ_M'') components. From the χ_M'' data, relaxation times (τ) were extracted for each peak through the expression $\tau = 1/2\pi\nu$, where ν is the switching frequency of the ac field. Variable-frequency data collected in the temperature range 2.2-3.2 K also show highly frequency-dependent peaks (see Figure 5.19). Cole-Cole plots of χ_M'' vs. χ_M' were constructed from these data (see Figure 5.20) and were fit to a generalized Debye model to provide relaxation times at the different temperatures.[31] These fits give α values ranging from 0.12 to 0.18, indicative of a relatively narrow distribution of relaxation times.[31a] For a single-chain magnet, the temperature dependence of the relaxation time should follow an Arrhenius (or thermally-activated) behavior, where τ is enhanced exponentially as temperature is decreased.[4,5f] Thus, a plot of $\ln(\tau)$ vs. $1/T$ should be linear, with the slope being directly proportional to the relaxation energy barrier, Δ_τ. Indeed, the plot of $\ln(\tau)$ vs. $1/T$ for compound **2**, with values of τ obtained through both temperature and frequency dependences of the ac susceptibility, demonstrates a clear thermally-activated behavior, with a least-squares fit to the line giving $\Delta_\tau = 31$ cm^{-1} and $\tau_0 = 1.3 \times 10^{-10}$ s. The value of τ_0 provides a quantitative estimation of the attempt time of relaxation from the chain bath, and the value obtained here is in good agreement with those found for other reported single-chain magnets.[6] Notably, in the plot of χ_M'' vs. T, the magnitude of χ_M'' decrease with decreasing frequency. This likely occurs due to weak antiferromagnetic interchain interactions. Nevertheless, the forgoing analysis of the ac susceptibility, in conjunction with the smooth curve observed in the plot of M vs. H, clearly demonstrates the presence of one-dimensional single-chain magnet behavior with no evidence of magnetic order above 1.8 K.

The variable-frequency and variable-temperature ac susceptibility data collected for **3** also demonstrate strong frequency dependence and a corresponding Arrhenius behavior of the relaxation times (Figures 5.21-24). However, in comparison to that of **2**, the slow relaxation occurs at higher temperature, resulting in an energy barrier of $\Delta_\tau = 56$ cm^{-1}, with $\tau_0 = 1.0 \times 10^{-10}$ s (and α values in the range 0.21-0.32, indicative of a small

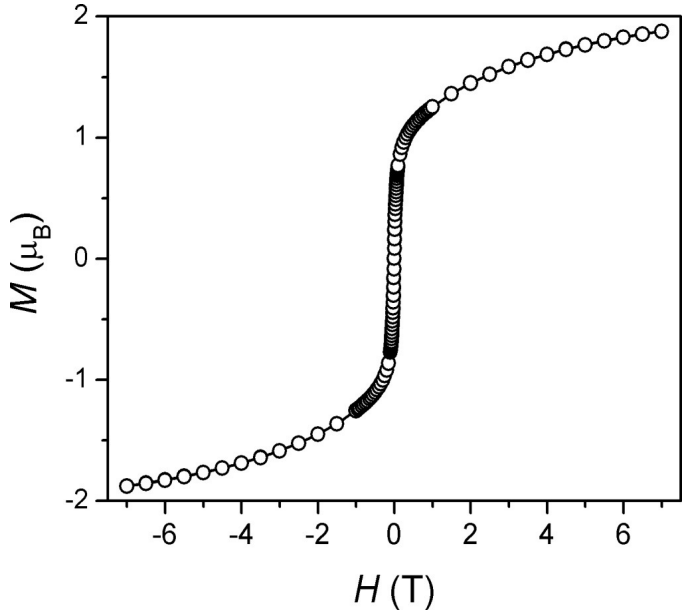


Figure 5.14. Variable-field magnetization data for **2** at 1.8 K with a mean sweep rate of 15 Oe/min.

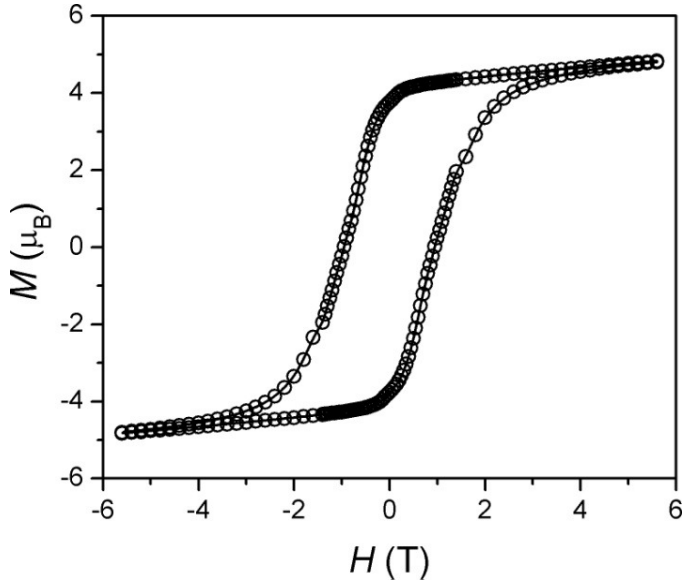


Figure 5.15. Variable-field magnetization data for **3**, collected at 1.8 K with a mean sweep rate of 150 Oe/min. This plot gives H_C = 1.0 T and M_R = 3.77 μ_B.

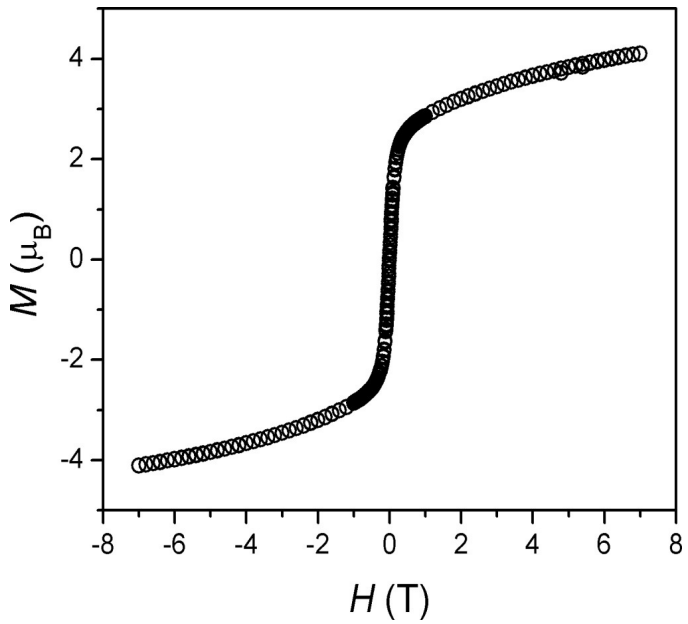


Figure 5.16. Variable-field magnetization data for **4** at 1.8 K with a mean sweep rate of 30 Oe/s.

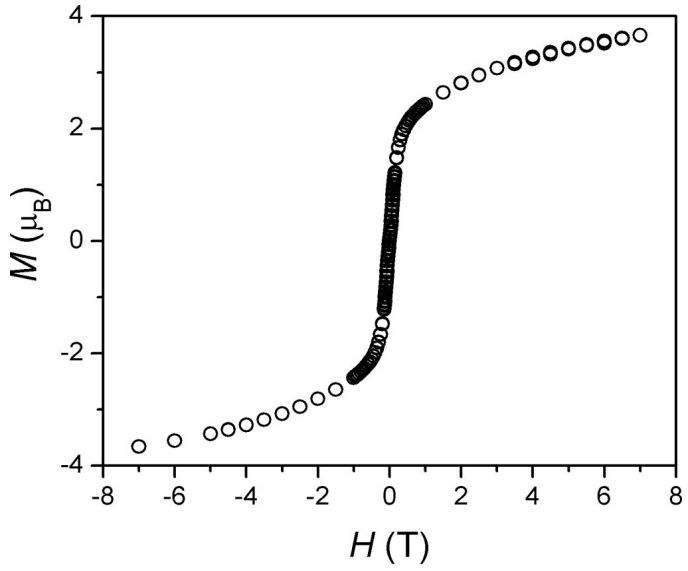


Figure 5.17. Variable-field magnetization data for **5** at 1.8 K with a mean sweep rate of 30 Oe/s.

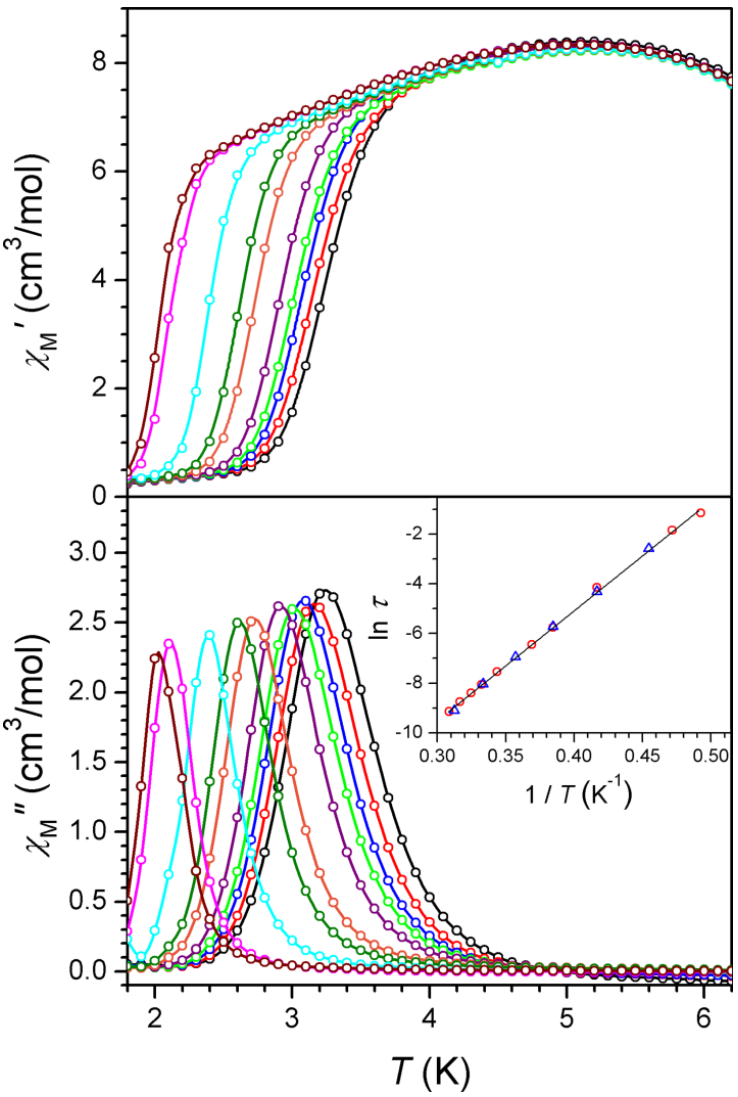


Figure 5.18. Variable-temperature in-phase (upper) and out-of-phase (lower) components of the ac magnetic susceptibility data for **2**, collected in a 4 Oe ac field oscillating at frequencies of 0.5 (maroon), 1 (magenta), 10 (cyan), 50 (green), 100 (orange), 300 (purple), 499 (bright green), 700 (blue), 1000 (red), and 1488 (black) Hz. Inset: Arrhenius plot of the relaxation time, as determined through variable-temperature (red circles) and variable-frequency ac susceptibility (blue triangles) measurements. The solid line corresponds to a linear fit to the data, giving $\Delta_\tau = 31$ cm^{-1}.

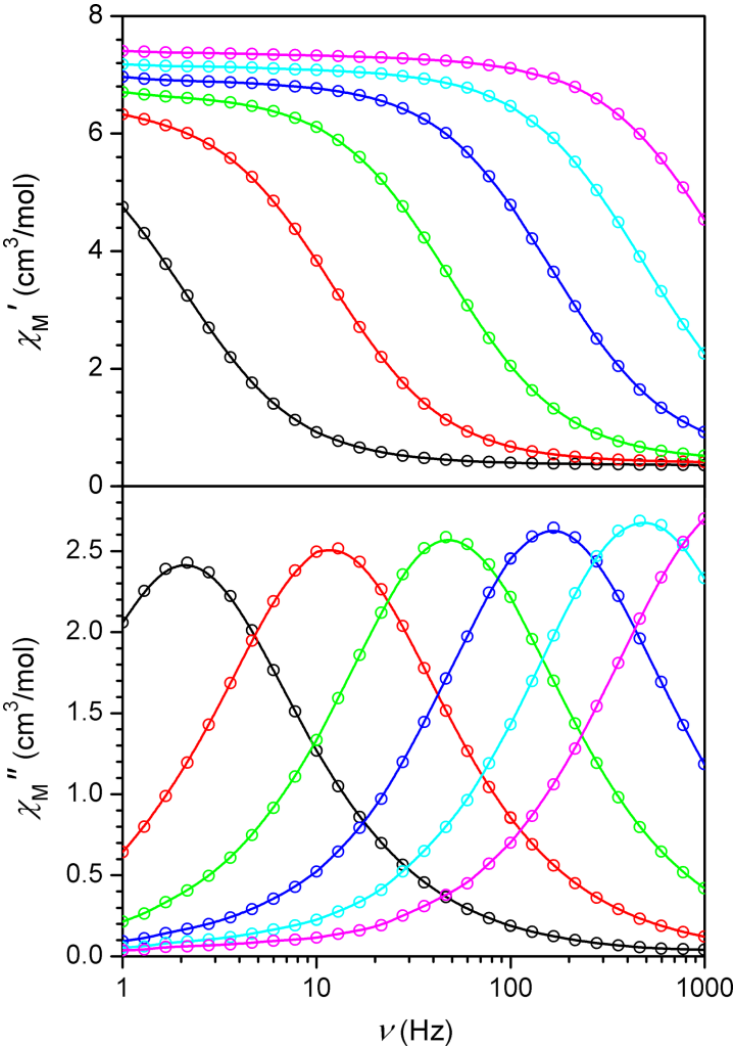


Figure 5.19. Variable-frequency in-phase (top) and out-of-phase (bottom) ac magnetic susceptibility data for **2**, collected in a 4 Oe ac field at temperatures of 2.2 (black), 2.4 (red), 2.6 (green), 2.8 (blue), 3.0 (cyan), and 3.2 (magenta) K.

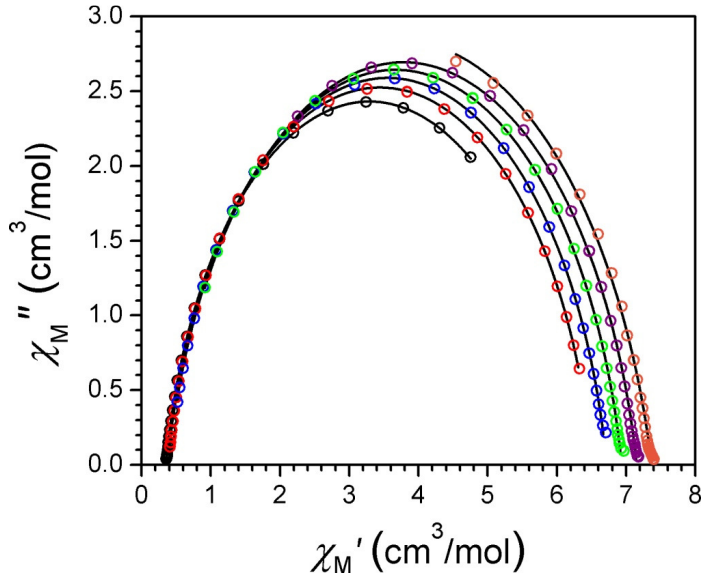


Figure 5.20. Cole-Cole plots for **2**, constructed from variable-frequency ac susceptibility data collected at temperatures of 2.0 (black), 2.2 (red), 2.4 (blue), 2.6 (green), 2.8 (purple), and 3.0 (orange) K. Solid black lines correspond to fits using a generalized Debye model.

distribution of relaxation times). This result is not surprising, given the hysteresis effect observed in the *M* vs. *H* data for **3** at 1.8 K (see Figure 15). The substantial increase in barrier over the manganese congener likely stems from a combination of (i) larger repeating unit spin ($S = {}^{7}/_{2}$ for **3** vs. $S = 1$ for **2**), (ii) slightly stronger intrachain coupling, and (iii) single-ion anisotropy stemming from unquenched orbital angular momentum in the Fe^{II} ions. This energy for **3** is among the highest for cyano-bridged single-chain magnets yet reported, and the fit to the Arrhenius plot indicates that the compound retains its magnetization for over one year at 2 K.[6b,d]

Ac susceptibility data collected for **4** and **5** confirm that both compounds also exhibit slow relaxation of magnetization (Figures 5.25-30). Fits to Arrhenius plots derived from Cole-Cole plots for the two compounds give parameters of $\Delta_\tau = 17$ cm^{-1} and $\tau_0 = 2.7 \times 10^{-9}$ s for **4**, and $\Delta_\tau = 20$ cm^{-1} and $\tau_0 = 1.7 \times 10^{-9}$ s for **5**. In addition, these fits provide α values in the range 0.19-0.31 for **4** and 0.49-0.63 for **5**, both indicative of distributions of relaxation times.

The dynamics of the magnetization in all solids was observed below their crossover temperatures, meaning that the slow dynamics occurs within the finite-size regime of relaxation.[6i] In this regime, the overall spin-reversal barrier can be expressed as the sum of the correlation and anisotropy energies, as $\Delta_\tau = \Delta_\xi + \Delta_A$.[6i] Having determined both Δ_τ and Δ_ξ values experimentally, the anisotropy energy, Δ_A, can be calculated for each compound, as $\Delta_A = \Delta_\tau - \Delta_\xi$. Within the Ising limit, the anisotropy energy can be easily linked to the anisotropy field, H_A, the field required to induce saturation of the magnetization, through the equation $2\Delta_A = M_{sat}H_A\mu_B$, where M_{sat} is the magnetization at

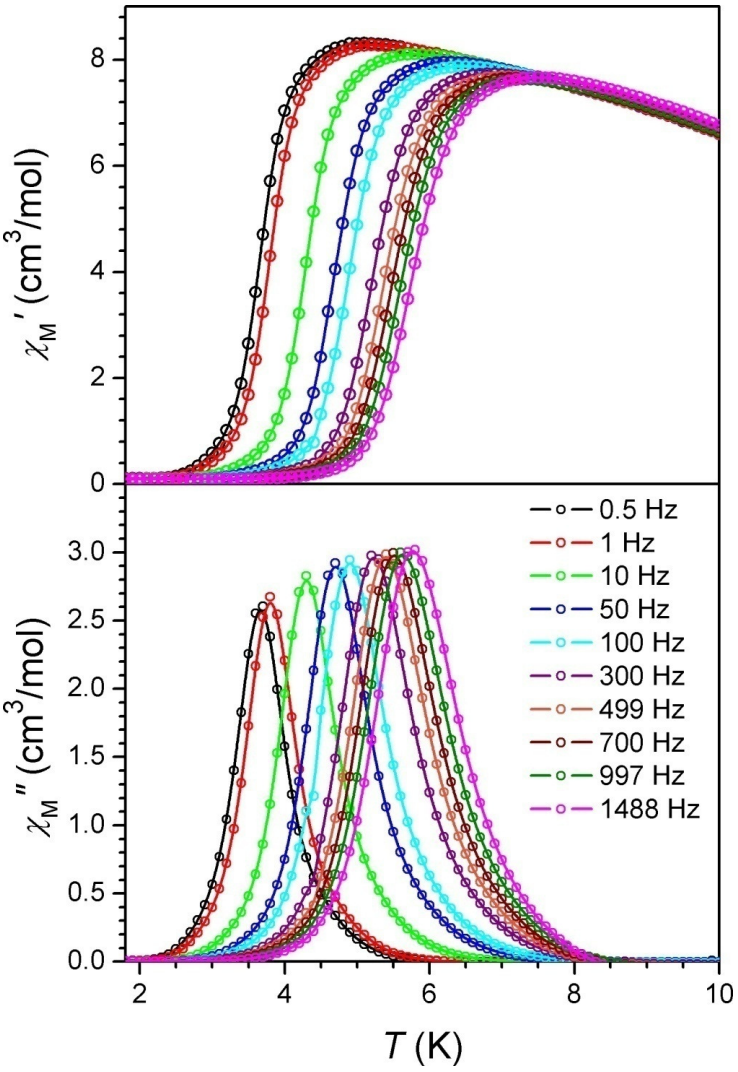


Figure 5.21. Variable-temperature in-phase (top) and out-of-phase (bottom) ac magnetic susceptibility data for **3**, collected in a 4 Oe ac field oscillating at various frequencies.

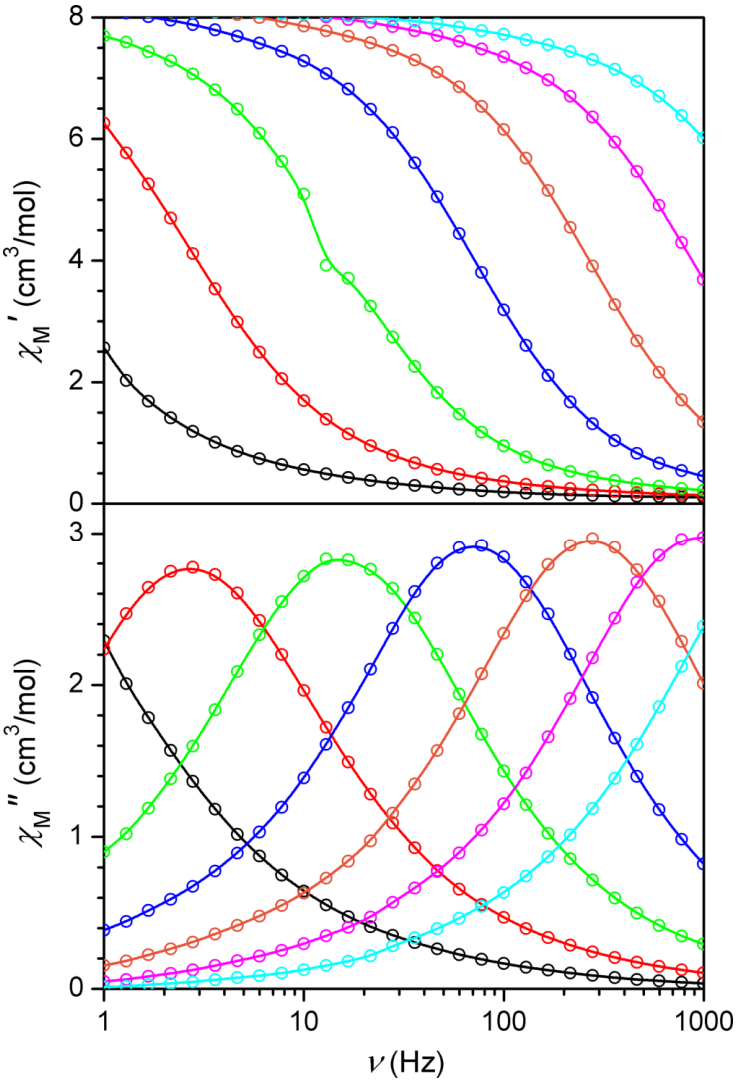


Figure 5.22. Variable-frequency in-phase (top) and out-of-phase (bottom) ac magnetic susceptibility data for **3**, collected in a 4 Oe ac field at temperatures of 3.6 (black), 4.0 (red), 4.4 (green), 4.8 (blue), 5.2 (orange), 5.6 (magenta), and 6.0 (cyan) K. Solid lines are guides for the eye.

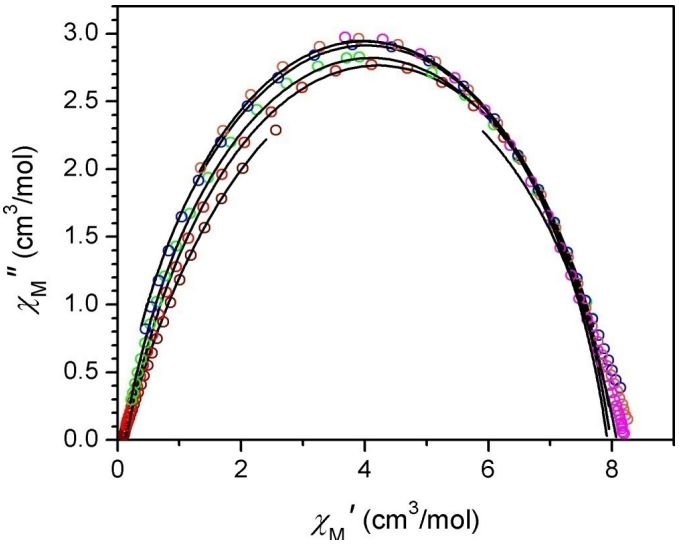


Figure 5.23. Cole-Cole plots for **3**, constructed from variable-frequency ac susceptibility data collected at temperatures of 3.6 (maroon), 4.0 (red), 4.4 (green), 4.8 (blue), 5.2 (orange), 5.6 (magenta), and 6.0 (cyan) K. Solid black lines correspond to fits using a generalized Debye model.

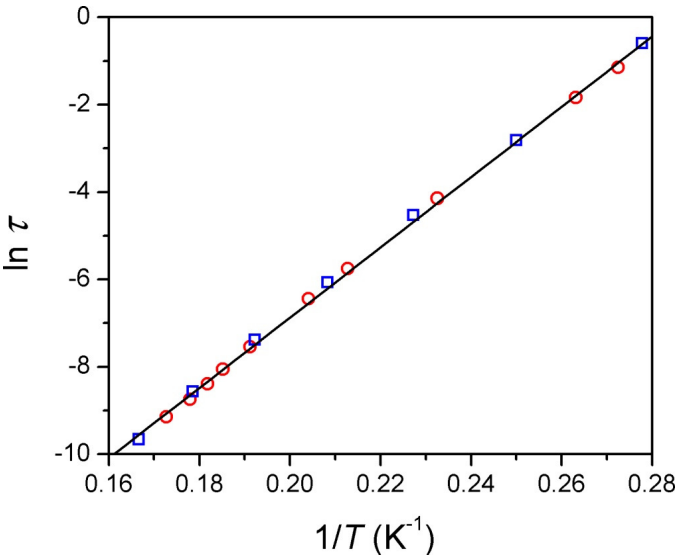


Figure 5.24. Arrhenius plot of the relaxation time for **3**, as determined through variable-temperature (red circles) and variable-frequency ac susceptibility (blue squares) measurements. The solid line corresponds to a linear fit to the data**.**

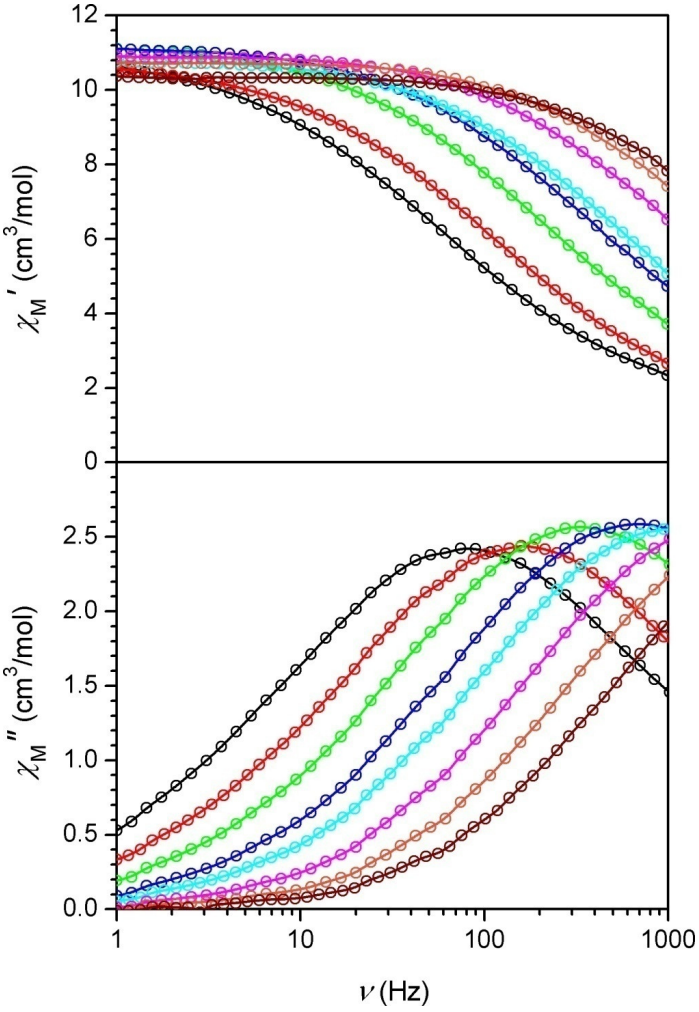


Figure 5.25. Variable-frequency in-phase (top) and out-of-phase (bottom) ac magnetic susceptibility data for **4**, collected in a 4 Oe ac field at temperatures of 1.8 (black), 1.9 (red), 2.0 (green), 2.1 (blue), 2.2 (cyan), 2.3 (magenta), 2.4 (orange), and 2.5 (maroon) K. Solid lines are guides for the eye.

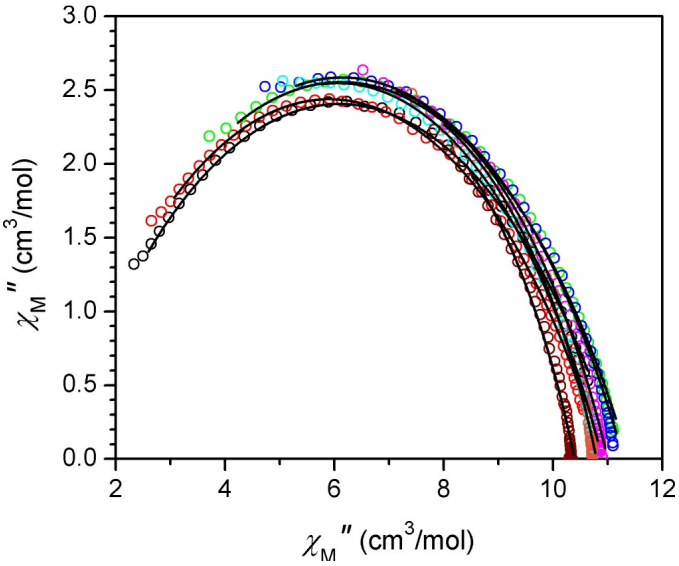


Figure 5.26. Cole-Cole plots for **4**, constructed from variable-frequency ac susceptibility data collected at temperatures of 1.8 (black), 1.9 (red), 2.0 (green), 2.1 (blue), 2.2 (cyan), 2.3 (magenta), 2.4 (orange), and 2.5 (maroon) K. Solid black lines correspond to fits using a generalized Debye model.

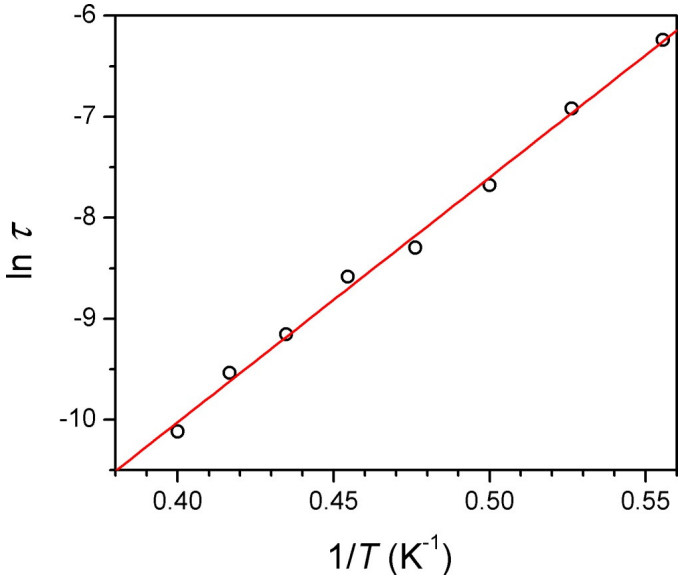


Figure 5.27. Arrhenius plot of the relaxation time for **4**, as determined through variable-frequency ac susceptibility measurements. The solid line corresponds to a linear fit to the data**.**

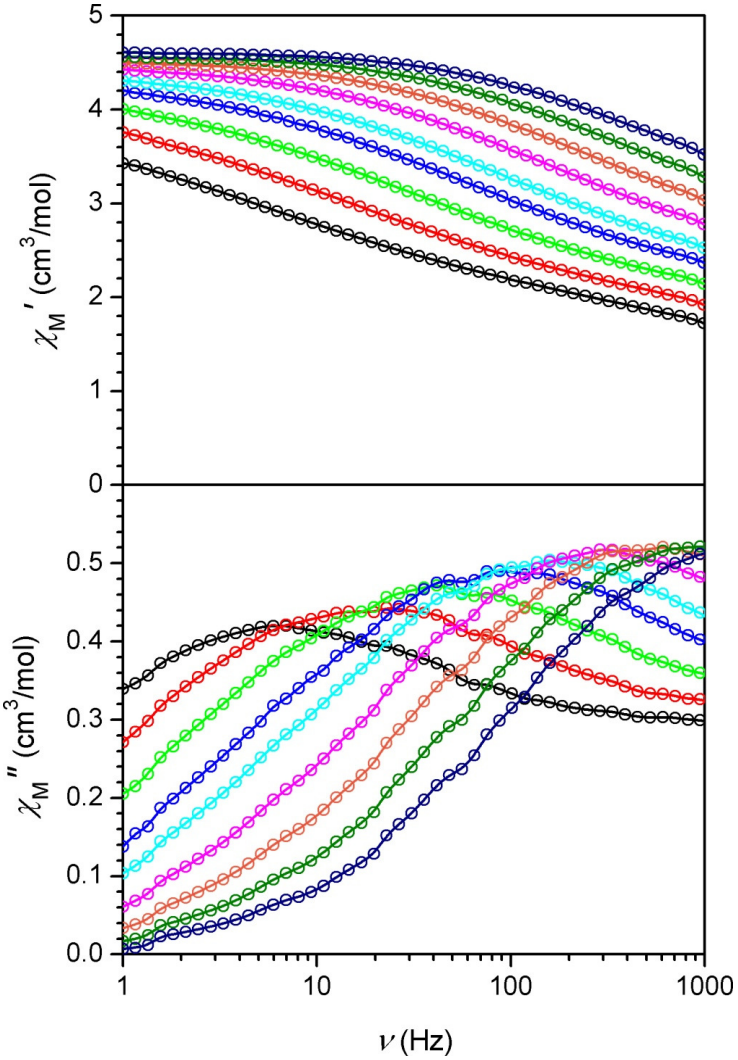


Figure 5.28. Variable-frequency in-phase (top) and out-of-phase (bottom) ac magnetic susceptibility data for **5**, collected in a 4 Oe ac field at temperatures of 1.8 (black), 1.9 (red), 2.0 (green), 2.1 (blue), 2.2 (cyan), 2.3 (magenta), 2.4 (orange), 2.5 (olive), and 2.6 (dark blue) K. Solid lines are guides for the eye.

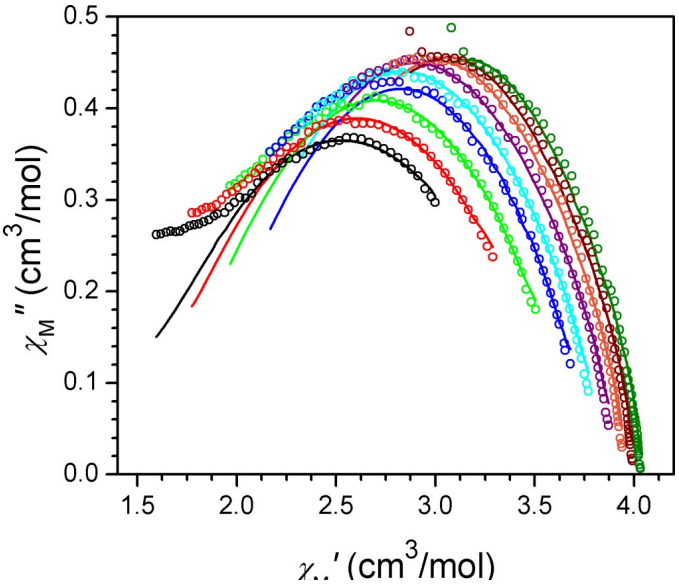


Figure 5.29. Cole-Cole plots for **5**, constructed from variable-frequency ac susceptibility data collected at temperatures of 1.8 (black), 1.9 (red), 2.0 (green), 2.1 (blue), 2.2 (cyan), 2.3 (purple), 2.4 (orange), 2.5 (maroon), and 2.6 (olive) K.

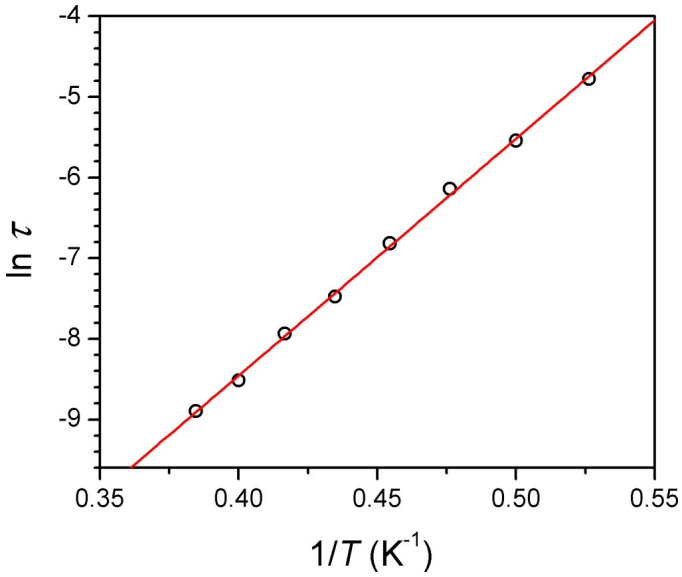


Figure 5.30. Arrhenius plot of the relaxation time of **5**, as determined through variable-frequency ac susceptibility measurements. The solid red line corresponds to a linear fit to the data**.**

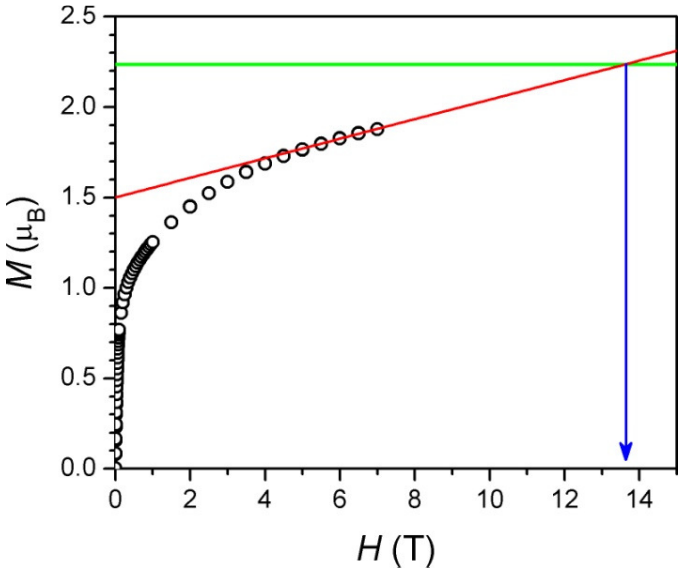


Figure 5.31. Variable-field magnetization data for **2**, collected at 1.8 K. The solid red line corresponds to a fit to the linear portion of the data, the green horizontal line at M = 2.23 μ_B corresponds to the expected magnetization saturation, and the blue vertical line at $H \approx 14$ T denotes the magnitude of the saturation field (H_{sat}).

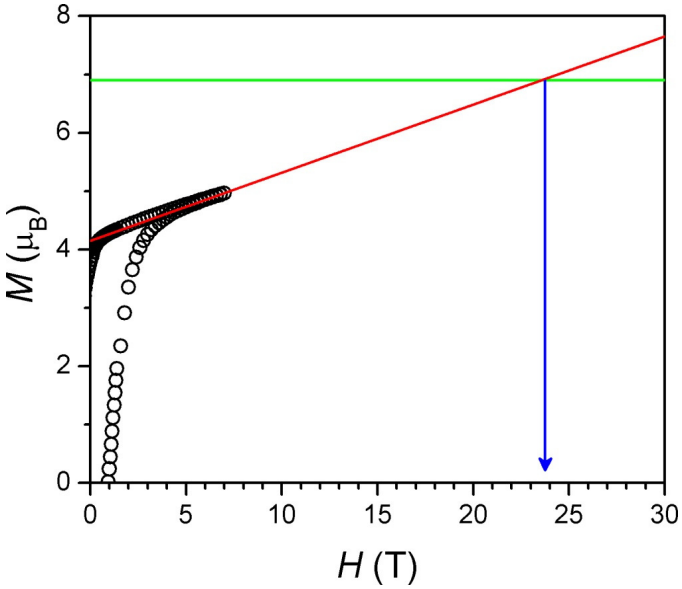


Figure 5.32. Variable-field magnetization data for **3**, collected at 1.8 K. The solid red line corresponds to a fit to the linear portion of the data, the green horizontal line at M = 6.90 μ_B corresponds to the expected magnetization saturation, and the blue vertical line at $H \approx 24$ T denotes the magnitude of the saturation field (H_{sat}).

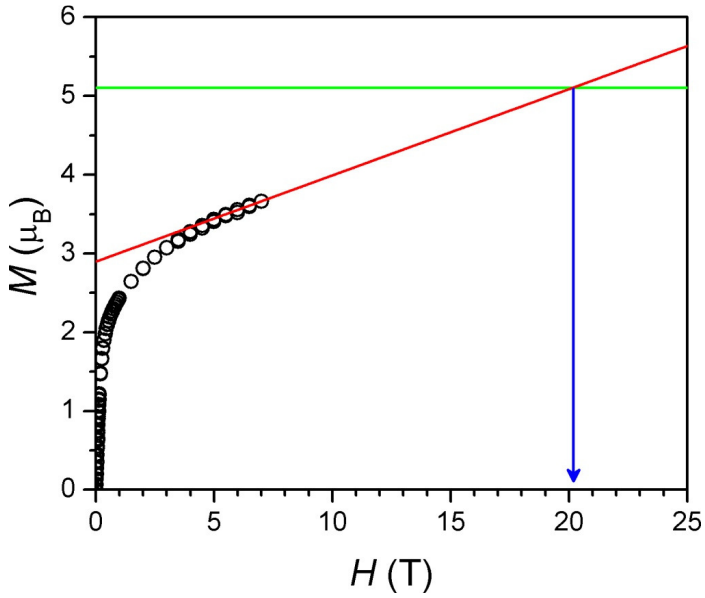


Figure 5.33. Variable-field magnetization data for **5**, collected at 1.8 K. The solid red line corresponds to a fit to the linear portion of the data, the green horizontal line at M = 5.11 μ_B corresponds to the expected magnetization saturation, and the blue vertical line at $H \approx 20$ T denotes the magnitude of the saturation field (H_{sat}).

saturation.[7] As shown in Figures 5.30, 5.31, and 5.32, the saturation of the magnetization cannot be attained experimentally due to the large anisotropy of these systems. Nevertheless, M_{sat} can be determined analytically through the expression $M_{sat} = |g_1S_1+g_2S_2|/N\mu_B$ for ferromagnetically coupled paramagnetic centers (as in the cases of **3** and **5**) or $M_{sat} = |g_1S_1-g_2S_2|/N\mu_B$ for antiferromagnetically coupled centers (as in **2**). We note that the calculation of M_{sat} was not possible for **4** due to the inability to accurately determine the gS product for the Co^{II} ions.[32] Thus, by experimentally determining the anisotropy field for **2**, **3**, and **5** (referred to as H_{sat} to differentiate from the calculated H_A), then subsequently comparing that value to the calculated H_A, it is possible to confirm that these systems do not fall into the Ising limit, as observed in the dc susceptibility measurements. For instance, the obtained values of Δ_τ = 31 cm^{-1} and Δ_ξ = 19 cm^{-1} for **2** give Δ_A = 12 cm^{-1}, corresponding to H_A = 23 T. A plot of M vs. H for **2** at 1.8 K (see Figure 5.31) reveals the presence of significant magnetic anisotropy, as the magnetization has failed to saturate at fields up to 7 T. Nevertheless, extrapolating the linear portion of the curve to its intersection with the calculated M_{sat} = 2.2 μ_B provides H_{sat} = 13-15 T.[33] The value of H_{sat} obtained here is clearly much lower than H_A, thereby confirming that **2** does not fall within the Ising limit, consistent with the disagreement between Δ_ξ and $4|JS_1S_2|$. This result demonstrates the lack of an analytical expression for Δ_A, as in the case of Δ_ξ. Similar calculations were made for **3** and **5** using M vs. H data (see Figures 5.32-33), and in both cases, poor agreement was found between H_A and H_{sat}, thus indicating non-Ising behavior (see Table 5.3). These results further highlight the current

limitation of the single-chain magnet models when the system does not fall in the Ising limit (i.e., when the anisotropy energy is significantly smaller than the exchange energy). In this case, analytical expressions for Δ_A, Δ_ξ and Δ_τ are absent, even while the $\Delta_\tau = 2\Delta_\xi + \Delta_A$ and $\Delta_\tau = \Delta_\xi + \Delta_A$ relations remain valid for any system in its infinite- and finite-size regime, respectively.[6i]

5.4 Conclusions and Outlook

The foregoing results demonstrate the utility of the new $S = {}^3/_2$, high-anisotropy cyanometalate complex *trans*-$[ReCl_4(CN)_2]^{2-}$ as a building unit for one-dimensional materials that exhibit slow magnetic relaxation. The resulting coordination solids represent the first transmetallic series of cyano-bridged single-chain magnets,[10] enabling a detailed investigation of how adjustment of the exchange coupling and anisotropy via metal-based substitutions affect the relaxation dynamics. Future efforts will focus on extending the coordination chemistry of $[ReCl_4(CN)_2]^{2-}$ to second- and third-row metals, which exhibit large anisotropy stemming from spin-orbit coupling and whose diffuse orbitals promote strong magnetic exchange coupling, in an attempt to isolate one-dimensional solids with increased relaxation barriers. Additionally, extension of this system to copper(II) may also lead to higher barriers, since M-CN-Cu^{II} exchange interactions are known to be considerably stronger than those of other first-row metals.[34] It is our hope that such efforts will result in new single-chain magnets exhibiting large relaxation barriers, opening the way for potential applications at more practical temperatures.

5.5 Acknowledgments

This research was supported by NSF Grant No. CHE-0617063, the IMI Program of the National Science Foundation under Award No. DMR04-09848, the France-Berkeley Fund, the University of Bordeaux, the CNRS, the ANR (No. NT09_469563, AC-MAGnets project), the Region Aquitaine, the GIS Advanced Materials in Aquitaine (COMET Project), and MAGMANet (No. NMP3-CT-2005-515767). We thank Tyco Electronics for providing T.D.H. with a graduate fellowship and Prof. Corine Mathonie`re for helpful discussions and experimental assistance.

5.6 References and Notes

(1) (a) Sessoli, R.; Tsai, H. L.; Schake, A. R.; Wang, S.; Vincent, J. B.; Folting, K.; Gatteschi, D.; Christou, G.; Hendrickson, D. N. *J. Am. Chem. Soc.* **1993**, *115*, 1804. (b) Sessoli, R.; Gatteschi, D.; Caneschi, A.; Novak, M. A. *Nature* **1993**, *365*, 141. (c) Gatteschi D.; Sessoli R.; Villain J. *Molecular Nanomagnets*, Oxford University Press: New York, 2006 and references therein. (d) Milios, C. J.; Vinslava, A.; Wernsdorfer, W.; Moggach, S.; Parsons, S.; Perlepes, S. P.; Christou, G.; Brechin, E. K. *J. Am. Chem. Soc.* **2007**, *129*, 2754. (e) Freedman, D. E.; Jenkins, D. M.; Iavarone, A. T.; Long, J. R. *J. Am. Chem. Soc.* **2008**, *130*, 2884. (f) Yoshihara, D.; Karasawa, S.; Koga, N. *J. Am. Chem. Soc.* **2008**, *130*, 10460.

(2) (a) Garanin, D. A.; Chudnovsky, E. M. *Phys. Rev. B* **1997**, *56*, 11102. (b) Leuenberger, M. N.; Loss, D. *Nature* **2001**, *410*, 789. (c) Heersche, H. B.; de

Groot, Z.; Folk, J. A.; van der Zant, H. S. J.; Romeike, C.; Wegewijs, M. R.; Zobbi, L.; Barreca, D.; Tondello, E.; Cornia, A. *Phys. Rev. Lett.* **2006**, *96*, 206801. (d) Jo, M.-H.; Grose, J. E.; Liang, W.; Baheti, K.; Deshmukh, M. M.; Sokol, J. J.; Rumberger, E. M.; Hendrickson, D. N.; Long, J. R.; Park, H.; Ralph, D. C. *Nano Lett.* **2006**, *6*, 2014.

(3) Caneschi, A.; Gatteschi, D.; Lalioti, N.; Sangregorio, C.; Sessoli, R.; Venturi, G.; Vindigni, A.; Rettori, A.; Pini, M. G.; Novak, M. A. *Angew. Chem., Int. Ed.* **2001**, *40*, 1760.

(4) Glauber, R. J. *J. Math. Phys.* **1963**, *4*, 294.

(5) A wavenumber as a unit of energy is related to the Kelvin through the following expression: $E(\mathrm{cm}^{-1})/k_B = E(\mathrm{K})$, where k_B is the Boltzmann constant, such that 1 cm^{-1} = 1.44 K.

(6) (a) Clérac, R.; Miyasaka, H.; Yamashita, M.; Coulon, C. *J. Am. Chem. Soc.* **2002**, *124*, 12837. (b) Lescouëzec, R.; Vaissermann, J.; Ruiz-Pérez, C.; Lloret, F.; Carrasco, R.; Julve, M.; Verdaguer, M.; Dromzée, Y.; Gatteschi, D.; Wernsdorfer, W. *Angew. Chem., Int. Ed.* **2003**, *42*, 1483. (c) Liu, T. F.; Fu, D.; Gao, S.; Zhang, Y. Z.; Sun, H. L.; Su, G.; Liu, Y. J. *J. Am. Chem. Soc.* **2003**, *125*, 13976. (d) Wang, S.; Zuo, J.-L.; Gao, S.; Song, Y.; Zhou, H.-C.; Zhang, Y.-Z.; You, X.-Z. *J. Am. Chem. Soc.* **2004**, *126*, 8900. (e) Pardo, E.; Ruiz-Garcia, R.; Lloret, F.; Faus, J.; Julve, M.; Journaux, Y.; Delgado, F.; Ruiz-Perez, C. *Adv. Mater.* **2004**, *16*, 1597. (f) Ferbinteanu, M.; Miyasaka, H.; Wernsdorfer, W.; Nakata, K.; Sugiura, K.; Yamashita, M.; Coulon, C.; Clérac, R. *J. Am. Chem. Soc.* **2005**, *127*, 3090. (g) Sun, Z.-M.; Prosvirin, A. V.; Zhao, H.-H.; Mao, J.-G.; Dunbar, K. R. *J. Appl. Phys.* **2005**, *97*, 10B305/1. (h) Kajiwara, T.; Nakano, M.; Kaneko, Y.; Takaishi, S.; Ito, T.; Yamashita, M.; Igashira-Kamiyama, A.; Nojiri, H.; Ono, Y.; Kojima, N. *J. Am. Chem. Soc.* **2005**, *127*, 10150. (i) Coulon, C.; Miyasaka, H.; Clérac, R. *Struct. Bonding (Berlin)* **2006**, *122*, 163. (j) Bernot, K.; Bogani, L.; Caneschi, A.; Gatteschi, D.; Sessoli, R. *J. Am. Chem. Soc.* **2006**, *128*, 7947. (k) Miyasaka, H.; Madanbashi, T.; Sugimoto, K.; Nakazawa, Y.; Wernsdorfer, W.; Sugiura, K.; Yamashita, M.; Coulon, C.; Clérac, R. *Chem.–Eur. J.* **2006**, *12*, 7028. (l) Xu, H.-B.; Wang, B.-W.; Pan, F.; Wang, Z.-M.; Gao, S. *Angew. Chem., Int. Ed.* **2007**, *46*, 7388. (m) Ishii, N.; Okamura, Y.; Chiba, S.; Nogami, T.; Ishida, T. *J. Am. Chem. Soc.* **2008**, *130*, 24. (n) Przybylak, S. W.; Tuna, F.; Teat, S. J.; Winpenny, R. E. P. *Chem. Commun.* **2008**, *17*, 1983. (o) Coronado, E.; Galán-Mascarós, J. R.; Martí-Gastaldo, C. *J. Am. Chem. Soc.* **2008**, *130*, 14987. (p) Miyasaka, H.; Julve, M.; Yamashita, M.; Clérac, R. *Inorg. Chem.* **2009**, *48*, 3420 and references therein. (q) Coulon, C.; Clérac, R.; Wernsdorfer, W.; Colin, T.; Miyasaka, H. *Phys. Rev. Lett.* **2009**, *102*, 167204. (r) Visinescu, D.; Madalan, A. M.; Andruh, M.; Duhayon, C.; Sutter, J.-P.; Ungur, L.; Van den Heuvel, W.; Chibotaru, L. F. *Chem.–Eur. J.* **2009**, *15*, 11808.

(7) Coulon, C.; Clérac, R.; Lecren, L.; Wernsdorfer, W.; Miyasaka, H. *Phys. Rev. B* **2004**, *69*, 132408.

(8) Loveluck, J. M.; Lovesey, S. W.; Aubry, S. *J. Phys. C: Solid State Phys.* **1975**, *8*, 3841.

(9) (a) Imry, Y.; Montano, P. A.; Hone, D. *Phys. Rev. B* **1975**, *12*, 253. (b) Leal de Silva, J. K.; Moreira, A. G.; Soares, M. S.; Sá Barreto, F. C. *Phys. Rev. B* **1995**, *52*, 4527. (c) Luscombe, J. H.; Luban, M.; Reynolds, J. P. *Phys. Rev. E* **1996**, *53*, 5852.
(10) Bernot, K.; Bogani, L.; Caneschi, A.; Gatteschi, D.; Sessoli, R. *J. Am. Chem. Soc.* **2006**, *128*, 7947.
(11) (a) Tomkiewicz, A.; Villain, F.; Mrozinski, J. *J. Mol. Struct.* **2000**, *555*, 383. (b) Tomkiewicz, A.; Bartczak, T. J.; Kruszynski, R.; Mrozinski, J. *J. Mol. Struct.* **2001**, *595*, 225. (c) Martínez-Lillo, J.; Armentano, D.; De Munno, G.; Lloret, F.; Julve, M.; Faus, J. *Inorg. Chim. Acta.* **2006**, *359*, 4343.
(12) (a) Martínez-Lillo, J.; Armentano, D.; De Munno, G.; Wernsdorfer, W.; Julve, M.; Lloret, F.; Faus, J. *J. Am. Chem. Soc.* **2006**, *128*, 14219. (b) Martínez-Lillo, J.; Armentano, D.; De Munno, G.; Wernsdorfer, W.; Clemente-Juan, J. M.; Krzystek, J.; Lloret, F.; Julve, M.; Faus, J. *Inorg. Chem.* **2009**, *48*, 3027.
(13) Allen, E. A.; Johnson, N. P.; Rosevear, D. T.; Wilkinson, W. *J. Chem. Soc. A.* **1969**, 788.
(14) Kobler, H.; Munz, R.; Al Gasser, G.; Simchen, G. *Justus Liebigs Ann. Chem.* **1978**, 1937.
(15) *SMART Software Users Guide, Version 5.1*; Bruker Analytical X-Ray Systems, Inc: Madison, WI, 1999.
(16) *APEX2 v.2009*; Bruker Analytical X-Ray Systems, Inc: Madison, WI, 2009.
(17) *SAINT Software Users Guide, Version 7.0*; Bruker Analytical X-Ray Systems, Inc: Madison, WI, 1999.
(18) Sheldrick, G. M. *SADABS, Version 2.03*; Bruker Analytical X-Ray Systems, Inc: Madison, WI, 2000.
(19) Sheldrick, G. M. *SHELXTL, Version 6.12*; Bruker Analytical X-Ray Systems, Inc: Madison, WI, 2000.
(20) Bennett, M. V.; Long, J. R. *J. Am. Chem. Soc.* **2003**, *125*, 2394.
(21) Adman, E.; Margulis, T. N. *Inorg. Chem.* **1967**, *6*, 210.
(22) Geiser, U.; Anderson, B. A.; Murray, A.; Pipan, C. M.; Rohl, C. A.; Vogt, B. A.; Wang, H. H.; Williams, J. M.; Kang, D. B.; Whangbo, M. H. *Mol. Cryst. Liq. Cryst.* **1990**, *181*, 105.
(23) Muehle, C.; Karpov, A.; Nuss, J.; Jansen, M. *Z. Naturforsch., B: Chem. Sci.* **2004**, *59*, 567.
(24) Shores, M. P.; Sokol, J. J.; Long, J. R. *J. Am. Chem. Soc.* **2002**, *124*, 2279.
(25) These results will appear in a future publication.
(26) (a) Naumov, N. G.; Artemkina, S. B.; Virovets, A. V.; Fedorov, V. E. *J. Solid State Chem.* **2000**, *153*, 195. (b) Mironov, Y. V.; Fedorov, V. E.; Ijjaali, I.; Ibers, J. A. *Inorg. Chem.* **2001**, *40*, 6320. (c) Brylev, K. A.; Mironov, Y. V.; Naumov, N. G.; Fedorov, V. E.; Ibers, J. A. *Inorg. Chem.* **2004**, *43*, 4833.
(27) (a) Entley, W. R.; Trentway, C. R.; Girolami, G. S. *Mol. Cryst. Liq. Cryst.* **1995**, *273*, 153. (b) Weihe, H.; Güdel, H. U. *Comments Inorg. Chem.* **2000**, *22*, 75.
(28) (a) Drillon, M.; Coronado, E.; Beltran, D.; Georges, R. *Chem. Phys.* **1983**, *79*, 449. (b) Georges, R.; Borras-Almenar, J. J.; Coronado, E.; Curely, J.; Drillon, M. *Magnetism: Molecules to Materials I: Models and Experiments*, Eds. Miller, J. S.;

Drillon, M., Wiley-VCH: Verlag, 2002. The expression used to describe the magnetic susceptibility follows:

$$\chi_0 = \frac{N_A \mu_B^2}{6 k_B T}\left[\left(M_a + M_b\right)^2 \frac{1+P}{1-P} + \left(M_a - M_b\right)^2 \frac{1-P}{1+P} \right], \text{ where } M_i = g_i \sqrt{S_i\left(S_i+1\right)},$$

$$P = \coth\left(\frac{2J\sqrt{S_a\left(S_a+1\right)S_b\left(S_b+1\right)}}{k_B T} \right) - \left(\frac{k_B T}{2J\sqrt{S_a\left(S_a+1\right)S_b\left(S_b+1\right)}} \right), \; S_a = S_{\mathrm{Re}} \text{ and } S_b = S_M$$

(29) The $\chi_M T$ vs. T data for **3**-**5** were fit applying the constraint $g_{Re} = g_M$, otherwise the fitting procedure was unable to independently and accurately determine the two g parameters.

(30) Nakamura, K; Sasada, T., *J. Phys. C: Solid State Phys.* **1978**, *11*, 331.

(31) (a) Cole, K. S.; Cole, R. H. *J. Chem. Phys.* **1941**, *9*, 341. (b) Boettcher, C. J. F. *Theory of Electric Polarisation*; Elsevier: Amsterdam, 1952. (c) Aubin, S. M.; Sun, Z.; Pardi, L.; Krzystek, J.; Folting, K.; Brunel, L.-J.; Rheingold, A. L.; Christou, G.; Hendrickson, D. N. *Inorg. Chem.* **1999**, *38*, 5329.

(32) Octahedral Co^{II} centers often behave as effective $S_{eff} = {}^1/_2$ systems at low temperature (see references below), and the g value obtained from fitting the $\chi_M T$ vs. T data considered a Co^{II} spin of $S = {}^3/_2$. Thus, a calculation of M_{sat} using that value of g is not physically reliable. (a) Kahn, O. *Molecular Magnetism*, VCH: New York, 1993 and references therein. (b) Plater, M. J.; Foreman, M. R. J.; Coronado, E.; Gómez-García, C. J.; Slawin, A. M. Z. *J. Chem. Soc., Dalton Trans.* **1999**, 4209. (c) Brechin, E. K.; Cador, O.; Caneschi, A.; Cadiou, C.; Harris, S. G.; Parsons, S.; Vonci, M.; Winpenny, R. E. P. *Chem. Commun*. **2002**, 1860.

(33) In our estimation of H_{sat}, we provide a range of fields due to the inherent imprecision in extrapolating the magnetization to its expected saturation.

(34) (a) Rodríguez-Fortea, A.; Alemany, P.; Alvarez, S.; Ruiz, E.; Scuiller, A.; Decroix, C.; Marvaud, V.; Vaissermann, J.; Verdaguer, M.; Rosenman, I.; Julve, M. *Inorg. Chem.* **2001**, *40*, 5868. (b) Marvaud, V.; Decroix, C.; Scuiller, A.; Guyard-Duhayon, C.; Vaissermann, J.; Gonnet, F.; Verdaguer, M. *Chem. Eur. J.* **2003**, *9*, 1678. (c) Shatruk, M.; Avendano, C.; Dunbar, K. *Progress in Inorganic Chemistry*, Ed. K. D. Karlin, John Wiley & Sons, Amsterdam, 2009 and references therein.

Chapter 6: Record Ferromagnetic Exchange through Cyanide and Elucidation of the Magnetic Phase Diagram for a $Cu^{II}Re^{IV}(CN)_2$ Chain Compound

4.1 Introduction

Less than a decade ago, slow magnetization dynamics was discovered in one-dimensional coordination solids.[1] These solids, known as single-chain magnets, often display relaxation barriers that are considerably higher than those observed in their single-molecule magnet counterparts,[2] suggesting their greater potential in applications such as high-density information storage and quantum computing.[3] Toward this end, we have employed a building block approach to assemble new single-chain magnets from high-spin, high-anisotropy mononuclear transition metal complexes that feature axial terminal cyanide ligands that can bridge other metal ions to direct the formation of one-dimensional solids.[1b,1g,4] Recently, we reported the synthesis of the $S = {}^3/_2$, high-anisotropy complex $[ReCl_4(CN)_2]^{2-}$, the first example of a paramagnetic molecule of the form $[MX_x(CN)_y]^{n-}$, along with its successful incorporation into a series of single-chain magnets of the type $(DMF)_4MReCl_4(CN)_2$ (M = Mn, Fe, Co, Ni).[4] The slow magnetization dynamics in these solids occurs despite weak intrachain coupling between the Re^{IV} and M^{II} centers, as the magnitude of this coupling, J, has been shown to partially govern the overall relaxation barrier ($\Delta_\tau = (8J + D)S^2$).[5] Thus, increasing the strength of this exchange should result in an increase in barrier height. Toward this end, we have begun targeting chain compounds wherein $[ReCl_4(CN)_2]^{2-}$ units are bridged via Cu^{II} centers. This effort stems from the observation that M-CN-Cu^{II} exchange interactions are often considerably stronger than those of other first-row metals, owing to the presence of a single electron residing in a $d_{x^2-y^2}$ orbital, along the direction of exchange coupling through the cyanide ligand.[6] Herein, we report the formation of a one-dimensional solid, $(Bu_4N)[TpCuReCl_4(CN)_2]$ (Tp^- = hydrotris(pyrazol-1-yl)borate), the second type of magnetic compound assembled from $[ReCl_4(CN)_2]^{2-}$, which demonstrates extremely strong ferromagnetic coupling along the chains. In addition, we have elucidated the metamagnetic behavior of the compound, which arises from a magnetic phase transition at 11.4 K to give an antiferromagnetic ground state stemming from weak π-π interactions between neighboring chains.

6.2 Experimental Section

The compound $(Bu_4N)_2[ReCl_4(CN)_2]$•2DMA was prepared as previously reported.[4] All other reagents were obtained from commercial sources and used without further purification. ***Caution!*** *Although we have experienced no problems while working with them, perchlorate salts are potentially explosive and should be handled with extreme care and only in small quantities.*

$(Bu_4N)[TpCuReCl_4(CN)_2]\cdot 1.33CH_3CN$ (**1**). A solution of KTp (0.012 g, 0.049 mmol) in 6 mL of absolute ethanol was added dropwise to a vigorously stirred solution of $[Cu(ClO_4)_2]\cdot 6H_2O$ (0.024 g, 0.065 mmol) in 6 mL of absolute ethanol, resulting in a pale blue solution and white precipitate. After stirring for 5 min, the white solid was removed

via filtration through diatomaceous earth. The pale blue filtrate was then cooled to 0 °C in an ice water bath. A solution of $(Bu_4N)_2[ReCl_4(CN)_2]\cdot 2DMA$ (0.050 g, 0.048 mmol) in 6 mL acetonitrile was chilled to 0 °C) and added dropwise to afford a pale green solution. After stirring for 10 minutes, the solution was filtered through diatomaceous earth to remove a small amount of insoluble green material, and the filtrate was quickly transferred to a 200 mL glass jar in a 3 °C refrigerator, while allowed to concentrate via evaporation. After 2 days, green blade-shaped crystals (21 mg, 46%) of product had formed. IR: ν_{BH} 2521 cm^{-1}; ν_{CN} 2246, 2289, 2120 cm^{-1}. Due to the instability of crystals of **1** outside their mother liquor, acceptable elemental analysis has not been obtained. As such, all magnetic measurements were conducted on samples of crystals restrained in their frozen mother liquor.

X-ray analysis for **1** ($C_{29.66}H_{10}BCl_4CuN_{10.33}Re$, fw = 953.69) at T = 175 K: space group $P2_1/c$, a = 11.4534(7), b = 16.2945(10), c = 22.1655(13) Å, β = 90.6770(10)°, V = 4136.4(4) $Å^3$, Z = 4, μ = 4.638 mm^{-1}, R_{int} = 0.0187, 60769 reflections measured, 6336 independent reflections, R_1 = 0.0684, wR_2 = 0.1889.ompound **1** was prepared according to a literature procedure. All manipulations were carried out under a pure nitrogen atmosphere.

X-ray Structure Determinations. A single crystal of compound **1** was coated with Paratone-N oil and mounted on a Kaptan loop. The crystal was then quickly transferred to a Bruker Platinum 200 Instrument at the Advanced Light Source at the Lawrence Berkeley National Laboratory, and cooled in a stream of nitrogen. Preliminary cell data were collected to give a unit cell consistent with the tetragonal Laue group, and the unit cell parameters were later refined against all data. A full hemisphere of data was collected, and the crystal didn't show significant decay during data collection. Data were integrated and corrected for Lorentz and polarization effects using SAINT v7.34 and were corrected for absorption effects using SADABS 2.10. Space group assignments were based upon systematic absences, E statistics, and successful refinement of the structures. The structure was solved by direct methods and expanded through successive difference Fourier maps. It was refined against all data using the SHELXTL 5.0 software package. Thermal parameters for all non-hydrogen atoms pertaining to the chain were refined anisotropically. Due to crystal disorder, tetrabutylammonium cations and lattice acetonitrile molecules were refined isotropically.

Magnetic Susceptibility Measurements. Magnetic data were collected using a Quantum Design MPMS-XL SQUID magnetometer. Measurements for **1** were obtained for crystals (6.8 mg) restrained in their frozen mother liquor within a sealed straw to prevent desolvation of the solid. These measurements were collected in the temperature range 1.8-300 K and in the field range -7−7 T. An M vs H measurement was performed at 100 K to confirm the absence of ferromagnetic impurities. Ac magnetic susceptibility data were collected in zero dc field in the temperature range 1.8-10 K, under an ac field of 3 Oe, oscillating at frequencies in the range 1-1488 Hz. Ac measurements show a complete absence of any out-of-phase ac susceptiblity component above 1.8 K at frequencies to 1500 Hz. The magnetic data were corrected for the sample holder, as well as for core diamagnetism of the sample, according to Pascal's constants.

Other Physical Measurements. Infrared spectra were obtained on a Perkin-Elmer Spectrum 100 Optica FTIR spectrometer, equipped with an attenuated total reflectance accessory (ATR).

Theoretical Modeling of the Magnetic Behavior.
Part 1, Mapping the problem into a Seiden chain:[10]

The unit cell for one chain is composed of two anisotropic spins, $\vec{S}_1$ and $\vec{S}_2$, and two isotropic spins, $\vec{s}_1$ and $\vec{s}_2$. However, ignoring the anisotropy implies that all the spins $\vec{S}_k$ or $\vec{s}_k$ become equivalent. At this approximation, the single chain description becomes equivalent to a regular chain built as an alternation of $\vec{S}$ and $\vec{s}$ spins.
Considering now the interchain couplings, the interchain Hamiltonian is given by the following equation using the notations of Figure 6.5 (*i* and *j* are indexes for the spin, *i*, in the chain numbered *j*):

$$H_{\perp} = -2J_{\perp}\sum_{i,j}\vec{s}_{1,i,j}\vec{s}_{1,i,j+1} - 2J_{\perp}\sum_{i,j}\vec{s}_{2,i,j}\vec{s}_{2,i,j-1}$$

At the mean field approximation, this Hamiltonian is reduced to:

$$H_{\perp} = -4J_{\perp}\langle\vec{s}_1\rangle\sum_{i,j}\vec{s}_{1,i,j} - 4J_{\perp}\langle\vec{s}_2\rangle\sum_{i,j}\vec{s}_{2,i,j}$$

By symmetry, the average values for the two kinds of isotropic spins, $<\vec{s}_1>$ and $<\vec{s}_2>$, are equal. The quasi-one dimensional problem can thus be described using a reduced unit cell composed of only one spin $\vec{S}$ and one spin $\vec{s}$ for the isotropic case. This approximation has been used below to derive the expression of the transition temperature. Within this description, the mean field Hamiltonian can be expressed as:

$$H_{mf} = -4J_{\perp}\langle\vec{s}\rangle\sum_{i,j}\vec{s}_{i,j} = -\frac{4J_{\perp}}{(g_s\mu_B)^2}\langle\vec{\mu}_s\rangle\sum_{i,j}\vec{\mu}_{s_{i,j}}$$

Or, introducing the effective field seen by isotropic $\vec{s}$ spins:

$$H_{mf} = -\vec{H}_{eff}\sum_{i,j}\vec{\mu}_{s_{i,j}}$$

with:

$$\vec{H}_{eff} = \frac{4J_{\perp}}{(g_s\mu_B)^2}\langle\vec{\mu}_s\rangle$$

Part 2, Determination of the transition temperature:

In a quasi-one-dimensional (1D) description, the mean field transverse Hamiltonian can be introduced to determine the transition temperature (see Part 1, Scalapino, D. J.; Imry, Y.; Pincus, P. *Phys. Rev. B* **1975**, *11*, 2042). As the experimental data demonstrate the presence of an antiferromagnetic ground state, antiferromagnetic interchain couplings and therefore a negative interchain exchange (using the notation of Part 1) can be introduced in the model. In this case, the second order phase transition towards the ordered antiferromagnetic phase is determined from the divergence of the staggered magnetic susceptibility. This problem can be mapped into an equivalent problem changing the sign of the interchain exchange and searching for the divergence of the static susceptibility. Following Seiden's work,[10] this susceptibility in the 1D case (Eq. 26 in reference 10) is:

$$\chi = \frac{1}{k_B T}\sum_{i,j}\left\langle \left(\mu_{S_i}^z + \mu_{s_i}^z\right)\left(\mu_{S_j}^z + \mu_{s_j}^z\right)\right\rangle$$

for which the thermodynamic average is taken in zero applied field. As $\vec{S}$ are classical spins (i.e. $\vec{S}$ and $\vec{s}$ commute), this expression can be readily separated into two parts to deduce separately the thermodynamic average of each kind of spins:

$$\left\langle \mu_S^z \right\rangle = \frac{1}{k_B T}\sum_{i,j}\left\langle \mu_{S_i}^z \left(\mu_{S_j}^z H + \mu_{s_j}^z H\right)\right\rangle \text{ and } \left\langle \mu_s^z \right\rangle = \frac{1}{k_B T}\sum_{i,j}\left\langle \mu_{s_i}^z \left(\mu_{S_j}^z H + \mu_{s_j}^z H\right)\right\rangle$$

These two equations can be transposed in the quasi-one dimensional case at the mean field approximation, introducing the effective field:

$$\left\langle \mu_S^z \right\rangle = \frac{1}{k_B T}\sum_{i,j}\left\langle \mu_{S_i}^z \left(\mu_{S_j}^z H + \mu_{s_j}^z \left(H + H_{eff}\right)\right)\right\rangle \text{ and}$$

$$\left\langle \mu_s^z \right\rangle = \frac{1}{k_B T}\sum_{i,j}\left\langle \mu_{s_i}^z \left(\mu_{S_j}^z H + \mu_{s_j}^z \left(H + H_{eff}\right)\right)\right\rangle$$

with the effective field that has been previously calculated:

$$H_{eff} = \frac{4|J_\perp|}{(g_s\mu_B)^2}\left\langle \mu_s^z \right\rangle = \lambda\left\langle \mu_s^z \right\rangle$$

The next step is to introduce the correlation functions calculated by Seiden:[10] $S_{\alpha\gamma} = \sum_{i,j}\left\langle \mu_{\alpha_i}^z \mu_{\gamma_j}^z \right\rangle$

with the $\alpha\gamma$ index stands for *ss*, *Ss* or *SS*. Then:

$$\left\langle \mu_S^z \right\rangle = \frac{1}{k_B T}\left(S_{SS}H + S_{Ss}H + \lambda S_{Ss}\left\langle \mu_s^z \right\rangle\right) \text{ and } \left\langle \mu_s^z \right\rangle = \frac{1}{k_B T}\left(S_{Ss}H + S_{ss}H + \lambda S_{ss}\left\langle \mu_s^z \right\rangle\right)$$

this gives: $\left\langle \mu_s^z \right\rangle = \frac{\left(S_{Ss} + S_{ss}\right)}{k_B T - \lambda S_{ss}}H$ and $\left\langle \mu_S^z \right\rangle = \frac{\left(S_{SS} + S_{Ss}\right)}{k_B T}H + \frac{1}{k_B T}\frac{\lambda S_{Ss}\left(S_{Ss} + S_{ss}\right)H}{k_B T - \lambda S_{ss}}$

The magnetic phase transition is located at the divergence of the magnetic susceptibility:

$$\chi = \frac{\left\langle \mu_S^z \right\rangle + \left\langle \mu_s^z \right\rangle}{H} = \frac{\left(S_{SS} + S_{Ss}\right)}{k_B T} + \frac{\left(1 + \frac{\lambda S_{Ss}}{k_B T}\right)\left(S_{Ss} + S_{ss}\right)}{k_B T - \lambda S_{ss}}$$

Then, the transition temperature is given (either with ferromagnetic or antiferromagnetic interchain couplings) by:

$$\lambda S_{ss}\left(T_C\right) = k_B T_C \text{ or } \frac{4|J_\perp|}{(g_s\mu_B)^2}S_{ss}\left(T_C\right) = k_B T_C$$

To give an explicit expression of the transition temperature, the expression of S_{ss} can be deduced from Eq. 27 of reference 10:

$$\frac{S_{ss}(T)}{(g_s\mu_B)^2} = \frac{2\Lambda^2 s^2}{1-\delta}$$

with at low temperature (Eq. 24 in reference 10): $\Lambda^2 \approx 1$ and $1-\delta \approx \frac{2k_BT}{J_P S}$ using the notations of Seiden,[10] except for the definition of the intrachain exchange that is written $2J_{//}$ in this work while it is equal to the coupling constant J introduced by Seiden.[10]

Finally, the equation giving the transition temperature is:

$$k_B T_C = 2\sqrt{|J_\perp| J_P S s^2}$$

For $S = 3/2$ and $s = 1/2$, this gives: $k_B T_C = \sqrt{3|J_\perp| J_P / 2}$

Part 3, Calculation of the transverse susceptibilities:

Figure 6.5 shows the equilibrium value of the spins in absence of an applied magnetic field or when a field is applied along the ***x*** direction above the transition field. In this direction, the magnetic field induces a sudden rotation of the magnetic moment at the transition field, H_C. On the other hand, applying the magnetic field along ***y*** or ***z*** implies a continuous rotation of the magnetic moments. The consequence at low temperature is a vanishing initial magnetic susceptibility (when the applied magnetic field is small) along ***x***, while the initial susceptibility remains finite down to $T = 0$ K when the magnetic field is applied along ***y*** or ***z***. The aim of this part is the calculation of these two components of the magnetic susceptibility.

Quite generally, the equilibrium state at $T = 0$ K is deduced from the minimization of the total magnetic energy. Three energy terms of the total magnetic energy should be considered: the exchange energy (coming from both intrachain and interchain magnetic couplings), the anisotropy energy and the Zeeman energy (the coupling with the external field). The expression of the intrachain exchange energy per unit cell is:

$$E_{eP} = -2J_P\left(\vec{S}_1\vec{s}_1 + \vec{S}_1\vec{s}_2 + \vec{S}_2\vec{s}_1 + \vec{S}_2\vec{s}_2\right)$$

By symmetry, the equilibrium value for the two isotropic spins will be the same and thus introducing $\vec{s}_1 = \vec{s}_2 = \vec{s}$ gives:

$$E_{eP} = -4J_P\left(\vec{S}_1 + \vec{S}_2\right)\vec{s}$$

Introducing the isotropic spins $\vec{s}$ and $\vec{s}'$ for each of the two magnetic sublattices, the interchain exchange energy is (the coupling constant being negative):

$$E_{e\perp} = -2J_\perp \vec{s}\cdot\vec{s}'$$

Finally, the anisotropy energy is given by the following relation (see Figure 6.5):

$$E_a = |D|\left(S^2 - \left(\vec{S}_1\vec{\Delta}_1\right)^2\right) + |D|\left(S^2 - \left(\vec{S}_2\vec{\Delta}_2\right)^2\right)$$

In this description, the different spins should be understood as average values. Therefore, both kinds of spins should be described as classical spins to estimate the different susceptibility components.

For clarity, we will separately consider the calculation when the magnetic field is applied along ***y*** and ***z*** as defined in Figure 6.5.

1) The magnetic field is applied along the y axis:

In this case, the spins are located in the (***x***, ***y***) plane. Let us first introduce the equilibrium solution in absence of magnetic field. From the minimization of the total magnetic energy at zero field, the isotropic spins, $\vec{s}$, are aligned along ***x***, while the angle between ***x*** and $\vec{S}_1$ and $\vec{S}_2$ are respectively $\theta_1 = \theta_e$ and $\theta_2 = -\theta_e$ with:

$$4J_P Ss\sin(\theta_e) = |D|S^2\sin(2\alpha - 2\theta_e)$$

Taking ω as the angle between $\vec{s}$ and the ***x*** axis or by symmetry between $\vec{s}'$ and -***x***, $\theta_1 = \theta_e + \varepsilon_1$ and $\theta_2 = -\theta_e + \varepsilon_2$, the expression of the intrachain exchange energy is now:

$$E_{eP} = -4J_P Ss\left(\cos(\theta_e + \varepsilon_1 - \omega) + \cos(-\theta_e + \varepsilon_2 - \omega)\right)$$

Introducing: $k = \dfrac{\varepsilon_1 + \varepsilon_2}{2}$ and $d = \dfrac{\varepsilon_1 - \varepsilon_2}{2}$, an equivalent relation is:

$$E_{eP} = -8J_P Ss\cos(\theta_e + d)\cos(k - \omega)$$

and also

$$E_{e\perp} = 2J_\perp\cos(2\omega)$$

Using the same notation, the anisotropy energy reads:

$$E_a = |D|S^2\left(\sin^2(\theta_e - \alpha + \varepsilon_1) + \sin^2(-\theta_e + \alpha + \varepsilon_2)\right)$$

or

$$E_a = 2|D|S^2\sin^2(\theta_e - \alpha + d) + 2|D|S^2\cos 2(\theta_e - \alpha + d)\sin^2 k$$

Finally, introducing the magnetic moment μ_S and μ_s for the anisotropic and isotropic spins respectively, the Zeeman energy is:

$$E_Z = -\mu_S H\left(\sin(\theta_e + \varepsilon_1) + \sin(-\theta_e + \varepsilon_2)\right) - 2\mu_s H\sin\omega$$

or

$$E_Z = -2\mu_S H\cos(\theta_e + d)\sin k - 2\mu_s H\sin\omega$$

A general calculation for any field value would require the minimization of the total magnetic energy with respect to the three angle parameters, *k*, *d* and ω. In order to estimate the initial susceptibility, a simplified calculation can be used considering only the first order development of the Zeeman energy, while the other energy terms should be developed up to second order. In this case, the Zeeman energy becomes:

$$E_Z = -2\mu_S Hk\cos\theta_e - 2\mu_s H\omega$$

As E_Z is independent of *d*, the minimum of energy is obtained for $d = 0$ and the development of the two exchange and anisotropy terms can be made considering only the two remaining angles. Then, omitting constant terms (that will disappear after derivation), the sum of these three terms developed at second order gives:

$$E_m = 4J_P s(k - \omega)^2\cos\theta_e + 4|J_\perp|\omega^2 + 2|D|S^2k^2\cos(2\theta_e - 2\alpha)$$

The minimization of the sum $E_Z + E_m$ gives the equilibrium value of *k* and ω through a set of two linear equations. The magnetic moment per (*S*, *s*) pair is then deduced from:

$$\mu = \mu_S k\cos\theta_e + \mu_s\omega$$

Then, the initial susceptibility is given by μ/H. Introducing $a = 4J_P Ss\cos\theta_e + 2|D|S^2\cos(2\theta_e - 2\alpha)$ and $b = 4J_P Ss\cos\theta_e + 4|J_\perp|$, we readily obtain the susceptibility being normalized by (*S*, *s*) pair:

$$\chi_{yy} = \frac{b\mu_S^2\cos^2\theta_e + 8J_P Ss\mu_S\mu_s\cos^2\theta_e + a\mu_s^2}{ab - (4J_P Ss\cos\theta_e)^2}$$

Note that a simplified form of this expression can be deduced assuming that $J_{//}$ is large compared with $|D|$ and $|J_\perp|$. In this case, θ_e is small and cos(θ_e) can also been approximated to **1**. This approximation will be shown to be consistent with experimental data. It gives the simplified expression:

$$\chi_{yy} \approx \frac{(\mu_S + \mu_s)^2}{|D|S^2 \cos(2\theta_e - 2\alpha) + 2|J_\perp|}$$

As usual, the transverse susceptibility is proportional to the inverse of the sum of an anisotropy and exchange term. Here, the relevant exchange comes from the interchain coupling while the effective anisotropy energy in this plane is $|D|S^2 \cos(2\theta_e - 2\alpha)$, i.e. is strongly reduced by the canting topology of the chain.

2) The magnetic field is applied along z:

The same calculation can be done applying the magnetic field along the ***z*** direction. Here, the symmetry immediately implies $\vec{s}_1 = \vec{s}_2 = \vec{s}$ at equilibrium. Moreover, the ***y*** component of $\vec{s}$ should also vanish. In order to make this calculation, it is necessary to introduce the coordinates of the different spins as: $\vec{S}_i = S\begin{pmatrix} \cos\theta_i \cos\phi_i & \sin\theta_i \cos\phi_i & \sin\phi_i \end{pmatrix}$ with i = 1 or 2, $\theta_1 = \theta_e + \varepsilon_1$, $\theta_2 = -\theta_e + \varepsilon_2$ and $\vec{s} = s\begin{pmatrix} \cos\omega & 0 & \sin\omega \end{pmatrix}$.

It is worth mentioning that the three angles ε_i, ϕ and ω should be small at low field. Using these notations, the intrachain exchange energy per unit cell reads:

$$E_{eP} = -4J_P Ss(\cos\theta_1 \cos\phi_1 \cos\omega + \sin\phi_1 \sin\omega) - 4J_P Ss(\cos\theta_2 \cos\phi_2 \cos\omega + \sin\phi_2 \sin\omega)$$

and the interchain exchange energy has the same expression as in the previous case.

The anisotropy energy can be written introducing the coordinates of the anisotropy axes:

$$\vec{\Delta}_i = \begin{pmatrix} \cos\alpha & \pm\sin\alpha & 0 \end{pmatrix}$$

This gives: $\vec{S}_1\vec{\Delta}_1 = S\cos\phi_1 \cos(\theta_1 - \alpha)$ and $\vec{S}_2\vec{\Delta}_2 = S\cos\phi_2 \cos(\theta_2 + \alpha)$. Then, the anisotropy energy per unit cell reads:

$$E_a = |D|S^2\left[1 - (\cos^2\phi_1 \cos^2(\theta_1 - \alpha)) + 1 - (\cos^2\phi_2 \cos^2(\theta_2 + \alpha))\right]$$

Finally, the Zeeman energy is: $E_Z = -\mu_S H(\sin\phi_1 + \sin\phi_2) - 2\mu_s H \sin\omega$.

Since the Zeeman term is independent of θ_i, the minimization will give $\varepsilon_i = 0$. Moreover, the ϕ_1 and ϕ_2 dependences are the same and thus the equilibrium values of these two angles will be the same, ϕ (i.e. $\vec{S}_1 = \vec{S}_2 = \vec{S}$). Thus the sum of the exchange terms gives:

$$E_e = -8J_P Ss(\cos\theta_e \cos\phi\cos\omega + \sin\phi\sin\omega) + 2J_\perp \cos(2\omega)$$

while the anisotropy energy is: $E_a = 2|D|S^2\left[1 - (\cos^2\phi\cos^2(\theta_e - \alpha))\right]$.

The magnetic energy depends only on two angles, ϕ and ω and the procedure becomes similar to the one developed in the previous case. Omitting constant terms, the quadratic development of $E_m = E_e + E_a$ gives:

$$E_m = 4J_P Ss(\phi^2 + \omega^2)\cos\theta_e - 8J_P Ss\phi\omega + 4|J_\perp|\omega^2 + 2|D|S^2\phi^2\cos^2(\theta_e - \alpha)$$

while a first order development of the Zeeman term gives: $E_Z = -2\mu_S H\phi - 2\mu_s H\omega$.
The rest of the calculation is similar to the one developed in the ***y*** direction. In particular, using the same approximations ($\cos(\theta_e) = 1$ and large value of $J_{//}$), the expression to be minimized is similar, simply changing $\cos(2\theta_e - 2\alpha)$ into $\cos^2(\theta_e - \alpha)$. Then, the corresponding susceptibility is:

$$\chi_{zz} \approx \frac{(\mu_S + \mu_s)^2}{|D|S^2 \cos^2(\theta_e - \alpha) + 2|J_\perp|}$$

3) Powder susceptibility at low field:

On a powder sample, the measured susceptibility is equal to $\chi_p = \frac{1}{3}(\chi_{xx} + \chi_{yy} + \chi_{zz})$. As the susceptibility along ***x*** is zero at low fields, the powder susceptibility at this approximation is:

$$\chi_p \approx \frac{(\mu_S + \mu_s)^2}{3}\left(\frac{1}{|D|S^2 \cos(2\theta_e - 2\alpha) + 2|J_\perp|} + \frac{1}{|D|S^2 \cos^2(\theta_e - \alpha) + 2|J_\perp|}\right)$$

To compare with the experimental results, the equilibrium value θ_e should be introduced in the above expression. This angle is obtained from:

$$4J_{//}Ss\sin(\theta_e) = |D|S^2 \sin(2\alpha - 2\theta_e)$$

In the limit where $J_{//}$ is large, a simplified expression can be deduced:

$$\sin(\theta_e) \approx \frac{|D|S^2 \sin 2\alpha}{4J_{//}Ss + 2|D|S^2 \cos 2\alpha}$$

Then, this equation can be used to obtain explicit expressions of the cosine factors found in the χ_p susceptibility:

$$\cos(2\theta_e - 2\alpha) \approx \cos 2\alpha + \frac{|D|S^2 \sin^2 2\alpha}{2J_{//}Ss + |D|S^2 \cos 2\alpha}$$

and:

$$\cos(\theta_e - \alpha) \approx \cos\alpha + \frac{|D|S^2 \sin\alpha \sin 2\alpha}{4J_{//}Ss + 2|D|S^2 \cos 2\alpha}$$

As the two exchange constants, $J_\perp$ and $J_\parallel$, are already known and $\alpha = 38.7°$, the comparison with the experimental result ($\chi_p = 0.19$ cm^3/mol) gives an estimation of the anisotropy energy at $DS^2/k_B \approx -20$ K or $D/k_B \approx -9$ K.

4.3 Results and Discussion

The compound $(Bu_4N)[TpCuReCl_4(CN)_2]\cdot 1.33CH_3CN$ (**1**) was synthesized through addition of $[ReCl_4(CN)_2]^{2-}$ to a solution containing $[Cu(H_2O)_6]^{2+}$ and KTp in a mixture of ethanol and acetonitrile at 0 °C, followed by crystallization at -25 °C to afford green plate-shaped crystals suitable for X-ray diffraction. The structure of **1**, depicted in Figure 6.1, consists of one-dimensional zig-zag chains that propagate along the *b* axis, where each chain is composed of alternating $[ReCl_4(CN)_2]^{2-}$ and $[TpCu]^+$ units, bridged through cyanide. To our knowledge, **1** represents the first structurally-characterized

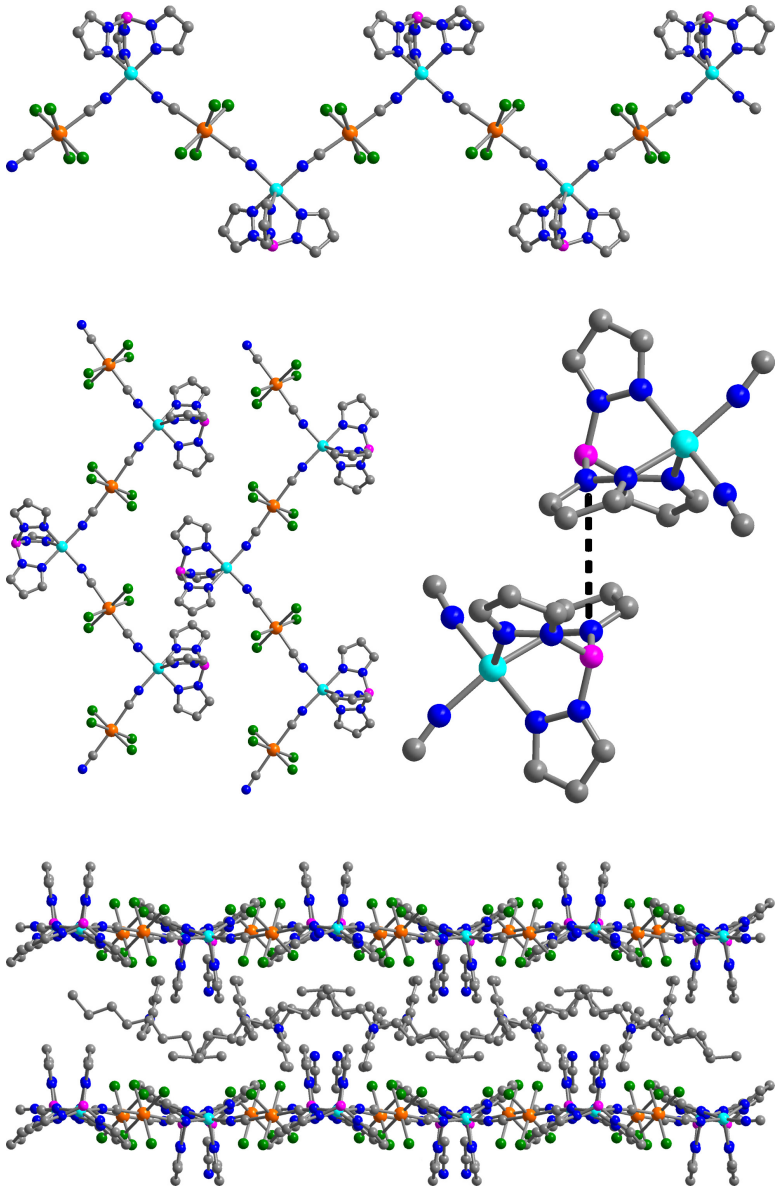


Figure 6.1. Upper: Crystal structure of $(Bu_4N)[TpCuReCl_4(CN)_2]$, as observed in **1**. Orange, cyan, green, purple, gray, and blue spheres represent Re, Cu, Cl, B, C, and N atoms, respectively; H atoms are omitted for clarity. Middle Left: View along the *a* axis, illustrating the arrangement of neighboring chains to form a two-dimensional sheet. Middle Right: View of π-π stacking between pyrazolate rings of neighboring chains, where d = 3.4985(2) Å. Lower: View along the *c* axis, where the sheets of chains are separated by Bu_4N^+ cations, with a shortest intersheet metal-metal distance of 11.4534(7) Å.

example of a cyanide bridge between rhenium and copper not supported by a $Re_{6-n}Os_nQ_8$ (n = 0, 1, 2)[7] or Re_4Q_4[8] (Q = chalcogenide) cluster core. The coordination environment of each Re^{IV} center does not deviate significantly from that in $[ReCl_4(CN)_2]^{2-}$, and each Cu^{II} center approximates a square pyramidal coordination geometry. Each Cu^{II} center exhibits a significant Jahn-Teller elongation along the $Cu\text{-}N_{apical}$ bond and subsequent contraction along the $Cu\text{-}N_{basal}$ and CuN_{CN} bonds, giving rise to bond distances of $d_{Cu\text{-}N(apical)}$ = 2.1828(1) Å, $d_{Cu\text{-}N(CN)}$ = 2.0130(1) Å (mean), and $d_{Cu\text{-}N(basal)}$ = 1.9839(1) Å (mean).The mean Re-C-N angles do not deviate significantly from linearity, while the Cu-N-C angles are slightly more bent, with a mean angle of 168.96(1)°. Note, however, that the Cu-N-C angles are considerably less bent than those found in $(DMF)_4MReCl_4(CN)_2$, where the mean M-N-C angle of 158.l(1)°). This substantial increase enhances the orthogonality of the $d_{\pi(Re)}$ and $d_{\sigma(Cu)}$ orbitals and should thus promote stronger ferromagnetic exchange. Along the *c* axis, neighboring chains are linked through π-π stacking of pyrazolate rings, with a ring centroid separation of 3.4985(2) Å (see Figure 1, middle), resulting in the formation of two-dimensional sheets of chains lying in the *bc* plane. Along the *a* axis, these sheets are well separated from one another by tetrabutylammonium cations and lattice acetonitrile molecules (see Figure 1, lower), with a shortest intersheet metal-metal distance of $d_{Cu\text{-}Cu}$ = 11.4534(7) Å.

To probe the magnetic exchange coupling in **1**, variable-temperature magnetic susceptibility data were collected. A plot of $\chi_M T$ vs. T, recorded in an applied dc field of 1000 Oe, is shown in Figure 2. At 300 K, $\chi_M T$ = 2.0 cm^3·K/mol, slightly higher than the value expected for one isolated Re^{IV} center ($S = {}^3/_2$, $g \approx 1.65$)[4] and one isolated Cu^{II} center ($S = {}^1/_2$, $g \approx 2.0$). Upon lowering the temperature from 300 K, $\chi_M T$ begins a gradual increase, then climbs abruptly below 80 K to a reach a maximum of 9.6 cm^3·K/mol at 12 K. This behavior is indicative of intrachain ferromagnetic coupling between the Re^{IV} ($t_{2g}{}^3$) and Cu^{II} ($e^4b_2{}^2b_1{}^2a_1{}^1$) centers, as expected for superexchange through cyanide.[9] In order to quantify the strength of intrachain exchange coupling in **1**, the $\chi_M T$ data were modeled considering a Heisenberg chain comprised of alternating isotropic classical ($S_i = {}^3/_2$) and quantum ($s_i = {}^1/_2$) spins.[10] The data were fit in the temperature range 12-300 K, employing a Seiden expression previously used to describe the magnetic susceptibility of an alternating chain,[10,11] to give $J_{\|}/k_B$ = +41(2) K (+29 cm^{-1}) and g_{av} = 1.74(1). To our knowledge, this value of $J_{\|}$ represents the strongest ferromagnetic superexchange interaction yet reported through cyanide. Such strong magnetic coupling arises from the presence of a d^9 electron configuration with local C_{4v} symmetry. The square pyramidal coordination of the Cu^{II} center serves to lower the energy of the $d_z{}^2$ orbital relative to the $d_{x^2-y^2}$ orbital, thereby localizing the unpaired electron along the $Cu\text{-}N_{CN}$ bond, in the direction of magnetic exchange.

Below 12 K at 1000 Oe, $\chi_M T$ undergoes a precipitous decline, reaching a minimum of 0.5 cm^3·K/mol at 1.8 K (see Figure 2). To probe this downturn, variable-temperature susceptibility measurements were conducted under various applied dc fields (see Figure 2, inset). The maximum of the magnetic susceptibility shifts to lower temperature with increasing applied field, until the data reach a plateau at $H \geq 4500$ Oe. This strong field dependence of the susceptibility suggests the presence of a magnetic phase transition below 12 K. To further investigate that possibility, variable-field magnetization data were collected at multiple temperatures (see Figure 6.3). Indeed, the

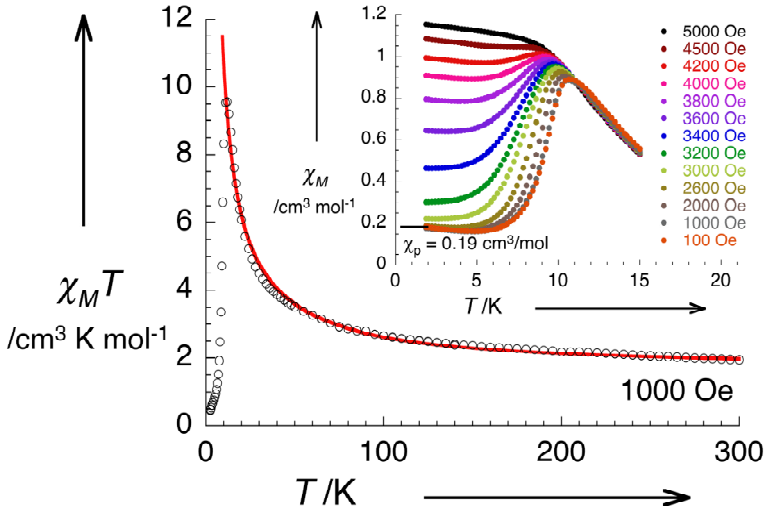


Figure 6.2. Variable-temperature magnetic susceptibility data for **1** (where χ_M is the molar magnetic susceptibility obtained as $\chi_M = M/H$), collected under a dc field of 1000 Oe. The solid red line corresponds to a fit to the data, as described in the text. Inset: Variable-temperature magnetic susceptibility data for **1**, collected under various applied dc fields.

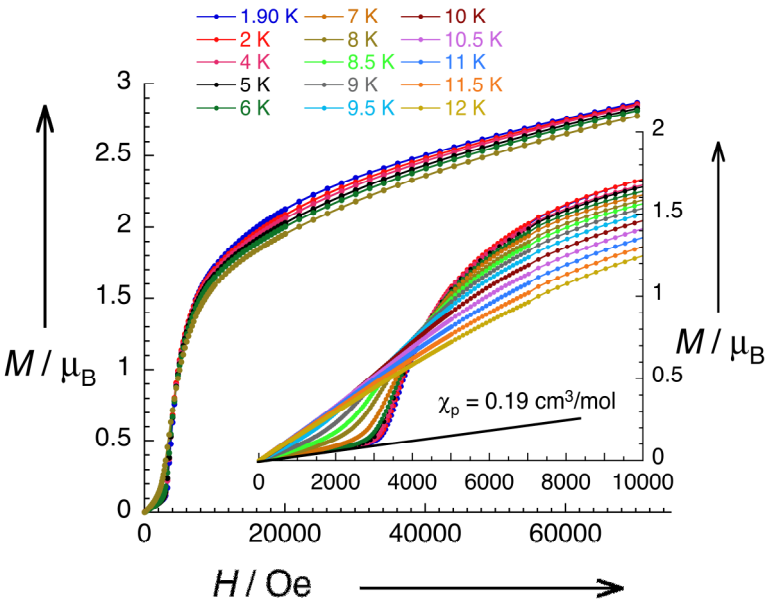


Figure 6.3. Variable-field magnetization data for **1**, collected at various temperatures. Inset: Expanded view of the data, highlighting inflection point that shifts to lower field with increasing temperature.

magnetization curve exhibits a temperature-dependent inflection point, corresponding to a maximum in the field dependence of the susceptibility, $\chi_M = dM/dH$ (see Figure 6.4), that is associated with a characteristic field, H_C. By combining the maxima observed in the $\chi_M(T)$ and $\chi_M(H)$ data, a (T,H) phase diagram can be constructed (see Figure 6.5), providing a complete map of the temperature dependence of H_C. Note that the phase transition curve extrapolates to $T = 0$ K at approximately $H_C(0) = 3600$ Oe and vanishes near $T_N = 11.4$ K.

The phase diagram in Figure 4 is typical of an antiferromagnet with a metamagnetic behavior, such that the $H_C(T)$ line corresponds to an antiferromagnetic/paramagnetic phase transition that occurs when the magnetic field is applied along the easy direction of the magnetization (defined as the x magnetic axis along the chains).[11] The occurrence of long-range magnetic order likely stems from the presence of transverse π-π interactions, with magnitude $J_\perp$, between Cu^{II} centers through the pyrazolate rings on neighboring chains (see Figure 6.1). Indeed, previous reports have described similar metamagnetic behavior in one-dimensional coordination solids arising from π-π stacking of aromatic rings on adjacent chains.[12] At $T = 0$ K, the magnetic field necessary to align the chain magnetization of the two antiferromagnetic sublattices, and thereby overcome the ordering, is $H_C(0) = 3600$ Oe. Thus, by equating the Zeeman and transverse (interchain) exchange energies, $2|J_\perp|s^2 = (g_S S + g_s s)\mu_B H_C(0)$, the value of the interchain exchange parameter can be obtained. Indeed, this treatment reveals a value of $J_\perp/k_B = -1.7$ K (-1.2 cm^{-1}), with $g_s = 2.0$ and $g_S = 1.65$.[4]

Considering $J_\perp$ treated at the mean field approximation within the context of the Seiden model,[10] the critical or Néel temperature, T_N, between the paramagnetic phase and the antiferromagnetic superstructure depicted in Figure 6.5, can be analytically expressed as $k_B T_N = 2\sqrt{|J_\perp| J_\parallel S s^2}$.[11] Insertion of $J_\perp$ and $J_\parallel$ into this equation provides a critical temperature of $T_N = 10.2$ K, significantly smaller than the experimental value of 11.4 K. This discrepancy arises from the intrinsic Ising-like anisotropy of the $[ReCl_4(CN)_2]^{2-}$ unit, which has been shown to possess an axial zero-field splitting parameter of $D/k_B = -20.7$ K (-14.4 cm^{-1}) as a tetrabutylammonium salt.[4] In order to estimate the anisotropy strength for each $[ReCl_4(CN)_2]^{2-}$ unit along the zig-zag chain, the theoretical powder susceptibility (at 0 K and in the weak field approximation) was calculated[11] and compared to the experimental data ($\chi_p = 0.19$ cm^3/mol) seen below 2000 Oe and at 1.8 K on the χ_M vs. T or M vs. H data (see Figures 6.2 and 6.3). Considering the two exchange constants, $J_\parallel/k_B = +41$ K and $J_\perp/k_B = -1.7$ K, along with the zig-zag angle of the chain, $\alpha = 38.7°$ (as defined in Figure 6.5), the local anisotropy energy of each $S = {}^3/_2$ $[ReCl_4(CN)_2]^{2-}$ unit is estimated to be $DS^2/k_B \approx -20$ K (-14 cm^{-1}) or $D/k_B \approx -9$ K (-6 cm^{-1}).[11] Thus, the presence of this anisotropy explains the observed difference between the theoretical Heisenberg and experimental values of T_N. Importantly, while this value of D is quite large, the effective anisotropy of the chain is much smaller due to its canting topology and an α angle close to 45°.[11] This weak effective anisotropy explains the absence of single-chain magnet behavior, or related magnet-like properties within an ordered antiferromagnetic phase of single-chain magnets.[13]

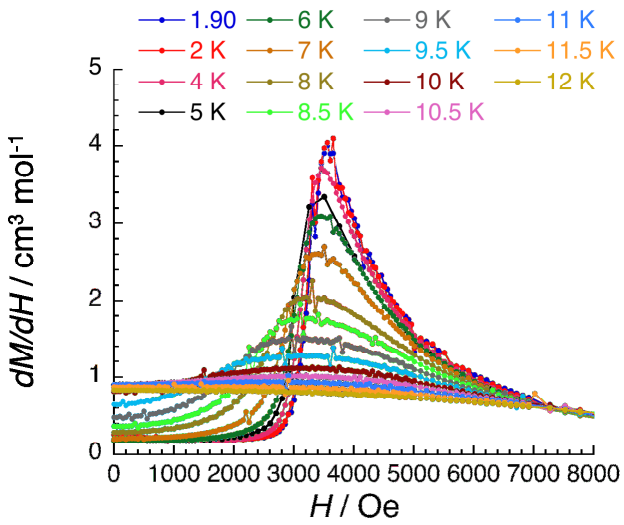


Figure 6.4. Variable-field magnetic susceptibility data for **1**, as calculated from $\chi = dM/dH$, collected at multiple temperatures. The peak maxima mark the characteristic field of the antiferromagnetic/paramagnetic phase transition.

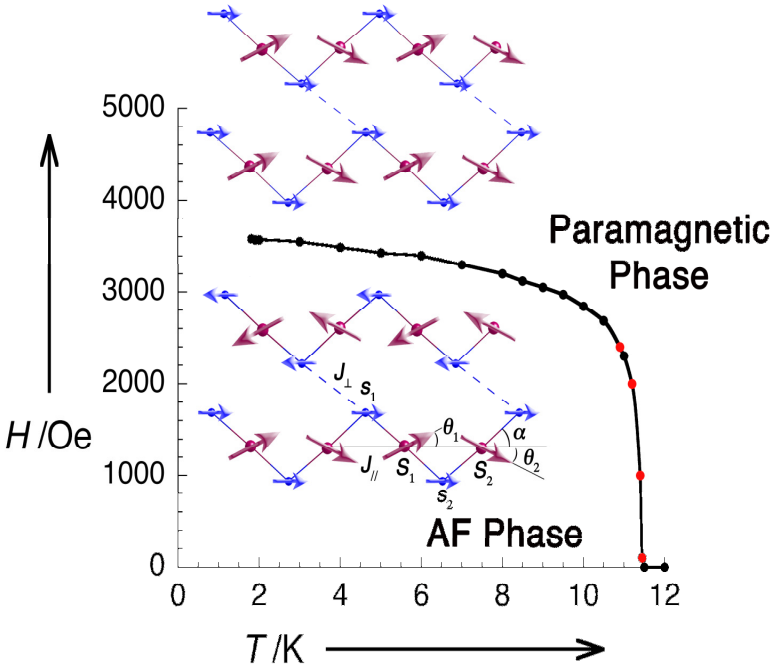


Figure 6.5. Magnetic phase diagram for **1**, constructed from variable-field (black circles) and variable-temperature (red circles) magnetic susceptibility data. The solid black line is a guide for the eye. Inset: Schematic diagrams of the magnetic superstructure in the *bc* plane within the antiferromagnetic (bottom) and paramagnetic (top) phases. Purple and blue spheres/arrows represent Re^{IV} and Cu^{II} centers, respectively, with the arrows representing the anisotropy vectors. The solid purple/blue lines and dashed blue lines represent the direction of magnetic intrachain and interchain exchange, respectively.

6.4 Conclusions and Outlook

The foregoing results describe the synthesis of the one-dimensional coordination solid $(Bu_4N)[TpCuReCl_4(CN)_2]$ from the complex $[ReCl_4(CN)_2]^{2-}$. Within the solid, individual chains display ferromagnetic coupling between Re^{IV} and Cu^{II} centers of unprecedented strength through the cyanide bridge, thus demonstrating the utility of the Re^{IV}-CN-Cu^{II} linkage in constructing strongly-coupled magnetic materials. In addition, we demonstrate experimentally and theoretically that the zig-zag arrangement of the local tensors of magnetic anisotropy around the Re^{IV} ions dramatically reduces the effective magnetic anisotropy of the chain and thus explains the absence of slow relaxation despite the strong one-dimensional exchange. Work is underway to construct other one-dimensional solids based on the Re^{IV}-CN-Cu^{II} linkage that feature a more linear arrangement of chains, such that the local anisotropy tensors do not cancel. In addition, future work will target related solids containing more separated chains to preclude magnetic ordering at low temperature. It is our expectation that these synthetic efforts will enable utilization of strong ferromagnetic coupling in the assembly of new single-chain magnets with large relaxation energy barriers.

6.5 References and Notes

(1) (a) Caneschi, A.; Gatteschi, D.; Lalioti, N.; Sangregorio, C.; Sessoli, R.; Venturi, G.; Vindigni, A.; Rettori, A.; Pini, M. G.; Novak, M. A. *Angew. Chem.* **2001**, *113*, 1810; *Angew. Chem., Int. Ed.* **2001**, *40*, 1760. (b) Clérac, R.; Miyasaka, H.; Yamashita, M.; Coulon, C. *J. Am. Chem. Soc.* **2002**, *124*, 12837. (c) Lescouëzec, R.; Vaissermann, J.; Ruiz-Pérez, C.; Lloret, F.; Carrasco, R.; Julve, M.; Verdaguer, M.; Dromzée, Y.; Gatteschi, D.; Wernsdorfer, W. *Angew. Chem.* **2003**, *115*, 1521; *Angew. Chem., Int. Ed.* **2003**, *42*, 1483. (d) Liu, T. F.; Fu, D.; Gao, S.; Zhang, Y. Z.; Sun, H. L.; Su, G.; Liu, Y. J. *J. Am. Chem. Soc.* **2003**, *125*, 13976. (e) Bernot, K.; Bogani, L.; Caneschi, A.; Gatteschi, D.; Sessoli, R. *J. Am. Chem. Soc.* **2006**, *128*, 7947. (f) Coulon, C.; Miyasaka, H.; Clérac, R. *Struct. Bonding* (Berlin) **2006**, *122*, 163 and references therein. (g) Ishii, N.; Okamura, Y.; Chiba, S.; Nogami, T.; Ishida, T. *J. Am. Chem. Soc.* **2008**, *130,* 24. (h) Miyasaka, H.; Julve, M.; Yamashita, M.; Clérac, R. *Inorg. Chem.* **2009**, *48*, 3420 and references therein.

(2) (a) Sessoli, R.; Tsai, H. L.; Schake, A. R.; Wang, S.; Vincent, J. B.; Folting, K.; Gatteschi, D.; Christou, G.; Hendrickson, D. N. *J. Am. Chem. Soc.* **1993**, *115*, 1804. (b) Sessoli, R.; Gatteschi, D.; Caneschi, A.; Novak, M. A. *Nature* **1993**, *365*, 141. (c) Gatteschi, D.; Sessoli, R.; Villain, J. in *Molecular Nanomagnets*, Oxford University Press: New York, 2006 and references therein. (d) Milios, C. J.; Vinslava, A.; Wernsdorfer, W.; Moggach, S.; Parsons, S.; Perlepes, S. P.; Christou, G.; Brechin, E. K. *J. Am. Chem. Soc.* **2007**, *129*, 2754. (e) Freedman, D. E.; Jenkins, D. M.; Iavarone, A. T.; Long, J. R. *J. Am. Chem. Soc.* **2008**, *130*, 2884. (f) Yoshihara, D.; Karasawa, S.; Koga, N. *J. Am. Chem. Soc.* **2008**, *130*, 10460.

(3) (a) Garanin, D. A.; Chudnovsky, E. M. *Phys. Rev. B*, **1997**, *56*, 11102. (b) Leuenberger, M. N.; Loss, D. *Nature* **2001**, *410*, 789. (c) Heersche, H. B.; de

Groot, Z.; Folk, J. A.; van der Zant, H. S. J.; Romeike, C.; Wegewijs, M. R.; Zobbi, L.; Barreca, D.; Tondello, E.; Cornia, A. *Phys. Rev. Lett.* **2006**, *96*, 20680. (d) Jo, M.-H.; Grose, J. E.; Liang, W.; Baheti, K.; Deshmukh, M. M.; Sokol, J. J.; Rumberger, E. M.; Hendrickson, D. N.; Long, J. R.; Park, H.; Ralph, D. C. *Nano Lett.*, **2006**, *6*, 2014.

(4) Harris, T. D.; Bennett, M. V.; Clérac, R.; Long, J. R. *J. Am. Chem. Soc.*, **2010**, *132*, 3980.

(5) This equation applies in the infinite-size regime for an Ising-type single-chain magnet with the following definition of the Hamiltonian:

$$H = -2J\sum_{-\infty}^{+\infty}\vec{S}_i\vec{S}_{i+1} + D\sum_{-\infty}^{+\infty}\vec{S}_{iz}^2$$

and in the $|D/J| > {}^4/_3$ Ising limit, where Δ_τ is the overall relaxation barrier, and S and D are the spin ground state and magnetic anisotropy parameter of the repeating unit, respectively. See C. Coulon, R. Clérac, L. Lecren, W. Wernsdorfer, H. Miyasaka, *Phys. Rev. B*, **2004**, *69,* 132408.

(6) (a) Rodríguez-Fortea, A.; Alemany, P.; Alvarez, S.; Ruiz, E.; Scuiller, A.; Decroix, C.; Marvaud, V.; Vaissermann, J.; Verdaguer, M.; Rosenman, I.; Julve, M. *Inorg. Chem.* **2001**, *40*, 5868. (b) Marvaud, V.; Decroix, C.; Scuiller, A.; Guyard-Duhayon, C.; Vaissermann, J.; Gonnet, F.; Verdaguer, M. *Chem. Eur. J.*, **2003**, *9,* 1678. (c) Shatruk, M.; Avendano, C.; Dunbar, K. in *Progress in Inorganic Chemistry*, ed. K. D. Karlin, John Wiley & Sons, Amsterdam, **2009**, *vol. 56*, pp. 155 and references therein.

(7) (a) Tulsky, E. G.; Crawford, N. R. M.; Baudron, S. A.; Batail, P.; Long, J. R. *J. Am. Chem. Soc.* **2003**, *125*, 15543. (b) Mironov, Y. V.; Naumov, N. G.; Brylev, K. A.; Efremova, O. A.; Fedorov, V. E.; Hegetschweiler, K. *Angew. Chem.* **2004**, *116*, 1317; *Angew. Chem., Int. Ed.* **2004**, *43*, 1297. (c) Mironov, Y. V.; Naumov, N. G.; Brylev, K. A.; Efremova, O. A.; Fedorov, V. E.; Hegetschweiler, K. *Koord. Khim.* **2005**, *31*, 289. (d) Brylev, K. A.; Pilet, G.; Naumov, N. G.; Perrin, A.; Fedorov, V. E. *Eur. J. Inorg. Chem.* **2005**, 461. (e) Naumov, N. G.; Mironov, Y. V.; Brylev, K. A.; Fedorov, V. E. *Zh. Strukt. Khim.* **2006**, *47*, 782. (f) Xu, L.; Kim, Y.; Kim, S.-J.; Kim, H. J.; Kim, C. *Inorg. Chem. Commun.* **2007**, *10*, 586.

(8) (a) Mironov, Y. V.; Fedorov, V. E.; Ijjaali, I.; Ibers, J. A. *Inorg. Chem.* **2001**, *40*, 6320. (b) Mironov, Y. V.; Efremova, O. A.; Naumov, D. Y.; Sheldrick, W. S.; Fedorov, V. E. *Eur. J. Inorg. Chem.* **2003**, 2591. (c) Mironov, Y. V.; Efremova, O. A.; Solodovnikov, S. F.; Naumov, N. G.; Sheldrick, W. S.; Perrin, A.; Fedorov, V. E. *Izv. Akad. Nauk SSSR, Ser. Khim.* **2004**, 2040. (d) Efremova, O. A.; Mironov, Y. V.; Naumov, D. Y.; Kozlova, S. G.; Fedorov, V. E. *Polyhedron* **2006**, *25*, 1233. (e) Efremova, O. A.; Mironov, Y. V.; Naumov, D. Y.; Fedorov, V. E. *Zh. Strukt. Khim.* **2006**, *47*, 754.

(9) (a) Entley, W. R.; Trentway, C. R.; Girolami, G. S. *Mol. Cryst. Liq. Cryst.* **1995**, *273*, 153. (b) Weihe, H.; Güdel, H. U. *Comments Inorg. Chem.* **2000**, *22*, 75.

(10) Seiden, J. *J. Physique Lett* **1983**, *44*, L947. The following Hamiltonian is used in this analysis:

$$H_P = -2J_P\sum_{i=1}^{N}\left(\left(\vec{s}_i + \vec{s}_{i+1}\right)\cdot\vec{S}_i\right)$$

(11) See Experimental Section for theoretical background.
(12) (a) Yoon, J. H.; Kim, H. C.; Hong, C. S. *Inorg. Chem.* **2005**, *44*, 7714. (b) Wen, H.-R.; Wang, C.-F.; Song, Y.; Gao, S.; Zuo, J.-L.; You, X.-Z. *Inorg. Chem.* **2006**, *45*, 8942. (c) Yoon, J. H.; Lim, J. H.; Choi, S. W.; Kim, H. C.; Hong, C. S. *Inorg. Chem.* **2007**, *46*, 1529. (d) Wang, S.; Ferbinteanu, M.; Yamashita, M. *Inorg. Chem.* **2007**, *46*, 610. (e) Choi, S. W.; Kwak, H. Y.; Yoon, J. H.; Kim, H. C.; Koh, E. K.; Hong, C. S. *Inorg. Chem.*, **2008**, *47*, 10214.
(13) (a) Coulon, C. ; Clérac, R. ; Wernsdorfer, W. ; Colin, T. ; Miyasaka, H. *Phys. Rev. Lett.* **2009**, 102, 167204/1–4. (b) Miyasaka, H. ; Takayama, K. ; Saitoh, A. ; Furukawa, S. ; Yamashita, M. ; Clérac, R. *Chem. Eur. J.* **2010**, 3656.

Chapter 7: Trinuclear $M_2Re(CN)_2$ (M = Mn, Ni) Clusters Incorporating $[ReCl_4(CN)_2]^{2-}$

7.1 Introduction

Over the past two decades, a number of molecules[1] and chain compounds have been shown to exhibit magnetic bistability at low temperatures.[2] This bistability, evinced by slow magnetic relaxation in the compounds upon removal of an applied field, arises due to combination of nonzero spin ground state (*S*), uniaxial zero-field splitting (*D*) and, in the case of multinuclear species, magnetic exchange coupling (*J*). Molecules and chain compounds demonstrating this behavior have been termed single-molecule and single-chain magnets, respectively, and could potentially find use in applications such as high-density information storage, quantum computing, and magnetic refrigeration.[3] However, in order for any of these applications to be realized, we must be able to generate high energy barriers to spin relaxation in single-molecule and single-chain magnets.

Despite the effort directed toward the isolation of single-molecule and single-chain magnets with large relaxation barriers, no such compound has been shown to demonstrate magnetic hysteresis above 10 K. The relatively limited progress toward this end owes in part to a reliance on serendipity to generate new slow relaxing species. Indeed, to date the vast majority of systems exhibiting slow relaxation featured oxo-bridged Mn^{III} fragments.[1,2] While the Jahn-Teller elongation of the Mn^{III}-O bond affords the requisite magnetic anisotropy to induce slow relaxation, the preparation of these compounds often depends vary intimately on subtle changes in reaction conditions and are generally difficult to predict and control. The cyanide ligand offers a promising alternative as a bridging ligand. Whereas the oxo functionality can connect anywhere from two to six metal centers in a wide range of coordination geometries, cyanide preferentially binds only two metal centers in a near linear fashion. Moreover, the linear M-C-N and M′-N-C bond angles enable one to accurately predict a priori the sign and relative strength of *J*.[4]

The structural and magnetic predictability afforded by the cyanide ligand lends itself to a building block approach to generate multinuclear clusters and chain compounds, where a mononuclear cyanometalate precursor is employed to direct the formation of larger cyano-bridged architecture. Here, the number of terminal cyanide ligands of the building unit dictates the structure of the final product. Recently, we reported the synthesis of a new $S = {}^3/_2$ cyanometalate building unit, $[ReCl_4(CN)_2]^{2-}$, which exhibits an unprecedented magnitude of uniaxial magnetic anisotropy for a cyanide complex, with an axial zero-field splitting parameter of $D = -14.4$ cm^{-1}.[5] Indeed, we demonstrated the utility of this complex in directing the formation of a series of chain compounds of formulae $(DMF)_4MReCl_4(CN)_2$ (M = Mn, Fe, Co, Ni), each of which shows slow magnetic relaxation at low temperature. In addition to constructing chain compounds with $[ReCl_4(CN)_2]^{2-}$, this precursor can be envisioned as the central unit of a linear trinuclear cluster, where each cyanide ligand binds a single coordination site of a pendant metal complex. Herein, we report the synthesis of two such clusters, $[(PY5Me_2)_2M_2ReCl_4(CN)_2]^{2+}$ (M = Mn (**1**), Ni (**2**)); $PY5Me_2$ = 2,6-bis(1,1-bis(2-pyridyl)ethyl)pyridine), each featuring a high-spin $S = {}^7/_2$ ground state, resulting from

intracluster ferromagnetic and antiferromagnetic exchange, respectively, and strong magnetic anisotropy.

7.2 Experimental Section

Preparation of Compounds. Unless otherwise noted, all procedures were performed under an inert N_2 atmosphere using standard glove box techniques. The ligand 2,6-bis(1,1-bis(2-pyridyl)ethyl)pyridine ($PY5Me_2$)[6] and the compounds $(Bu_4N)_2[ReCl_4(CN)_2]\cdot 2DMA$[5] and $[(PY5Me_2)M(MeCN)](PF_6)_2$ (M = Mn,[1e] Ni,[7]) were synthesized as previously described. The solvated DMA molecules were removed from the compound $(Bu_4N)_2[ReCl_4(CN)_2]\cdot 2DMA$ by heating under vacuum for 16 h at 60 °C. Acetonitrile and diethylether were dried by circulation over alumina for 16 h prior to use, and were then deoxygenated by sparging with N_2 for at least 1 h. All other reagents were obtained from commercial vendors and used without further purification.

$[(PY5Me_2)_2Mn_2ReCl_4(CN)_2](PF_6)_2\cdot 3MeCN$ (**1**·3MeCN). A solution containing $(Bu_4N)_2[ReCl_4(CN)_2]$ (0.040 g, 0.046 mmol) in 4 mL of MeCN was added dropwise to a solution containing $[(PY5Me_2)M(MeCN)](PF_6)_2$ (0.070 g, 0.094 mmol) in 4 mL of MeCN to give an orange solution. The solution was swirled then allowed to stand for 5 minutes to give a white precipitate, which was subsequently removed via filtration through diatomaceous earth. Diffusion of Et_2O vapor into this filtrate afforded orange rod-shaped crystals. The crystals were collected by filtration, washed with Et_2O (2 × 1 mL), and dried under nitrogen to yield 0.020 g (24%) of product. IR (neat): ν_{CN} = 2288, 2247, 2162 cm^{-1}. Anal. Calcd. for $C_{66}H_{59}Cl_4F_{12}Mn_2N_{15}P_2Re$: C,44.28; H, 3.32; N, 11.74 %. Found: C, 44.07; H, 3.21; N, 11.97 %.

$[(PY5Me_2)_2Ni_2ReCl_4(CN)_2](PF_6)_2\cdot 2MeCN\cdot Et_2O$ (**3**·2MeCN·Et_2O). A solution containing $(Bu_4N)_2[ReCl_4(CN)_2]$ (0.013 g, 0.046 mmol) in 2 mL of MeCN was added dropwise to a solution containing $[(PY5Me_2)M(MeCN)](PF_6)_2$ (0.026 g, 0.094 mmol) in 2 mL of MeCN to give a yellow solution. Diffusion of Et_2O vapor into this filtrate afforded orange block-shaped crystals. The crystals were collected by filtration, washed with Et_2O (2 × 1 mL), and dried under nitrogen to yield 0.017 g (47%) of product. IR (neat): ν_{CN} = 2247, 2156 cm^{-1}. Anal. Calcd. for $C_{68}H_{66}Cl_4F_{12}N_{14}Ni_2OP_2Re$: C,44.61; H, 3.63; N, 10.71 %. Found: C, 44.60; H, 3.26; N, 10.86 %.

X-ray Structure Determinations. X-ray diffraction analyses were performed on a single crystal of **1** coated with Paratone-N oil and mounted on Kaptan loops. The crystals were frozen under a stream of N_2 during measurements. Data were collected using a Bruker X8 APEX diffractometer equipped with a Bruker MICROSTAR X-ray source, APEX-II detector, and a Cu anode (λ = 1.5406 Å). Raw data were integrated and corrected for Lorentz and polarization effects using Bruker APEX2 v. 2009.1.[8] Absorption corrections were applied using SADABS.[9] Space group assignments were determined by examination of systematic absences, E statistics, and successive refinement of the structures. Crystal structures were solved by direct with the aid of successive difference Fourier maps in SHELXL.[10] None of the crystals showed significant decay during data collection. Thermal parameters were refined anisotropically for all non-hydrogen atoms in the main body.

Magnetic Susceptibility Measurements. Magnetic data were collected using a Quantum Design MPMS-XL magnetometer. Measurements were obtained on finely

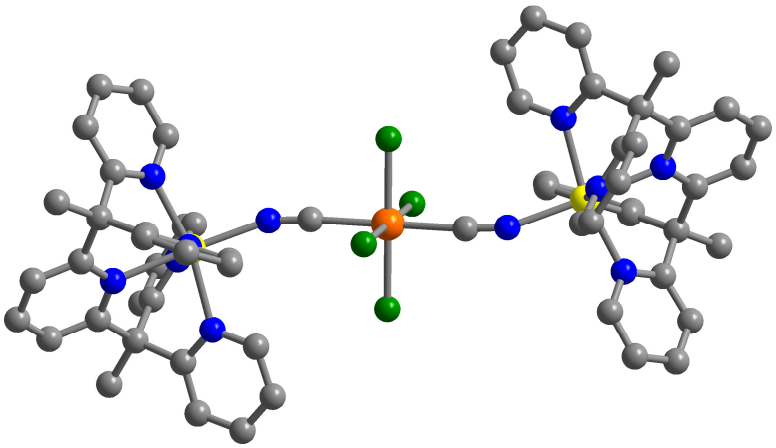


Figure 7.1. Crystal structure of **1**. Orange, yellow, green, blue, and gray spheres represent Re, Mn, Cl, N, and C atoms, respectively; H atoms are omitted for clarity.

ground microcrystalline powders restrained in a polyethylene bag. Dc magnetic susceptibility data were collected in the temperature range of 2-300 K under an applied field of 1000 Oe. Dc magnetization data were collected in the temperature range 1.8-10 K at fields from 1 to 7 T. All data were corrected for diamagnetic contributions from the sample holder, as well as for core diamagnetism that was estimated using Pascal's constants.

Other Physical Measurements. Infrared spectra were obtained on a Perkin-Elmer Spectrum 100 Optica FTIR spectrometer furnished with an attenuated total reflectance accessory (ATR). Elemental (C, H, and N) analyses were performed at the Microanalytical Laboratory of the University of California, Berkeley.

7.3 Results and Discussion

Syntheses and Structures of M_2Re Clusters. The trinuclear cyano-bridged clusters $[(PY5Me_2)_2M_2ReCl_4(CN)_2]^{2+}$ (M = Mn (**1**), Ni (**2**)) were synthesized through addition of a solution containing $[ReCl_4(CN)_2]^{2-}$ to a solution containing the appropriate precursor $[(PY5Me_2)M(MeCN)]^{2+}$ complex. Subsequent diffusion of diethyl ether vapor into the resulting solution afforded each cluster as a crystalline product. Single-crystal X-ray analysis on **1** of revealed the presence of a linear trinuclear cluster, where a $[ReCl_4(CN)_2]^{2-}$ unit occupies the central position, bridged through cyanide to two pendant $[(PY5Me_2)Mn]^{2+}$ groups (see Figure 7.1). In the space group $P2_1/c$, the Re^{IV} ion resides on a crystallographic inversion center, in a coordination environment that does not significantly deviate from that of $[ReCl_4(CN)_2]^{2-}$.[5] The coordination environment of each Mn^{II} ion approximates an octahedron, and bond distances and angles are very close to those found in $[(PY5Me_2)M(MeCN)]^{2+}$.[1e] The structure of **1** features a Re-C-N angle close to linear at 174.981(7)°, however the Mn-N-C angle is very bent at 154.120(7)°. Such a significant deviation is frequently observed for metal ions coordinated through the nitrogen terminus of cyanide, and it likely results from a combination of crystal packing effects and steric conflicts between $PY5Me_2$ ligands.[1e,5,7,11]

Magnetic Properties of the M_2Re Clusters. In order to probe the magnetic exchange coupling in the clusters, variable-temperature dc susceptibility measurements were carried out under an applied field of 1000 Oe. A plot of $\chi_M T$ vs. T for **1** is shown in Figure 7.2. At 300 K, $\chi_M T$ = 9.53 cm^3K/mol, slightly lower than the expected value of $\chi_M T$ = 10.63 cm^3K/mol for one isolated Re^{IV} center and two isolated high-spin Mn^{II} centers ($S = {}^5/_2$) centers, with g = 2.00. Upon lowering the temperature, $\chi_M T$ undergoes a gradual decline to a minimum value of 3.51 cm^3K/mol at 9 K, before undergoing a rise at lower temperature. The drop in $\chi_M T$ with lowering temperature indicates the presence of intracluster antiferromagnetic coupling between Re^{IV} and Mn^{II} ions. The slight rise in $\chi_M T$ below 9 K results from a noncompensation of magnetic moments of one Re^{IV} ion ($S = {}^3/_2$) and two Mn^{II} ions (S_{total} = 5), which will ultimately lead to an $S = {}^7/_2$ ground state and a corresponding maximum in $\chi_M T$ of 7.88 cm^3K/mol. The observation that $\chi_M T$ falls well short of this value down to 2 K demonstrates qualitatively the presence of very weak exchange interactions.

In order to quantify the exchange coupling in **8**, the $\chi_M T$ data were modeled with the following isotropic spin Hamiltonian (Equation 1):

$$\hat{H} = -2J[\hat{S}_{Re} \bullet (\hat{S}_{Mn(1)} + \hat{S}_{Mn(2)})] \quad (1)$$

In the temperature range 40-300 K, the data were fit using MAGFIT 3.1[12] to give a coupling constant of $J = -2.7\ cm^{-1}$ with g = 1.98. This small value of J is in accordance with the failure of the $\chi_M T$ data to reach the expected value for an $S = {}^7/_2$ ground state. Moreover, this weak exchange stems from competing ferromagnetic ($d_{Re(\pi)}$ and $d_{Mn(\sigma)}$) and antiferromagnetic ($d_{Re(\pi)}$ and $d_{Mn(\pi)}$) interactions.

The plot of $\chi_M T$ vs. T obtained for **2** demonstrates a markedly different temperature dependence than that observed for **1** (see Figure 7.3). At 300 K, $\chi_M T$ = 4.00 cm^3K/mol, close to the expected value of $\chi_M T$ = 3.88 cm^3K/mol for one isolated Re^{IV} center ($S = {}^3/_2$) and two isolated Ni^{II} centers (S = 1). As the temperature is decreased from 300 K, $\chi_M T$ increases monotonically to a maximum of 7.01 cm^3K/mol at 14 K. The increase in $\chi_M T$ with decreasing temperature is indicative of ferromagnetic coupling between the Re^{IV} and Ni^{II} centers, expected for superexchange through cyanide between Re^{IV} ($t_{2g}{}^3$) and Ni^{II} ($t_{2g}{}^6e_g{}^2$) ions, giving rise to a spin ground state of $S = {}^7/_2$. Notably, the $\chi_M T$ data fail to reach the value of $\chi_M T$ = 7.88 cm^3K/mol expected for an $S = {}^7/_2$ ground state and undergo a downturn below 14 K, owing to the magnetic anisotropy of the Re^{IV} center. To quantify this behavior, the data were modeling according to the isotropic spin Hamiltonian shown in Equation 2:

$$\hat{H} = -2J[\hat{S}_{Re} \bullet (\hat{S}_{Ni(1)} + \hat{S}_{Ni(2)})] \quad (2)$$

A simulation of the data obtained using MAGPAK[13] afforded an exchange constant of $J = +11(1)\ cm^{-1}$, with g = 1.90 and $D = -6\ cm^{-1}$. While the axial zero-field splitting parameter was necessary to reproduce the downturn at low temperature, we note that other effects such a intercluster antiferromagnetic exchange may contribute the downturn. As such, this value of D should be considered as an estimate.

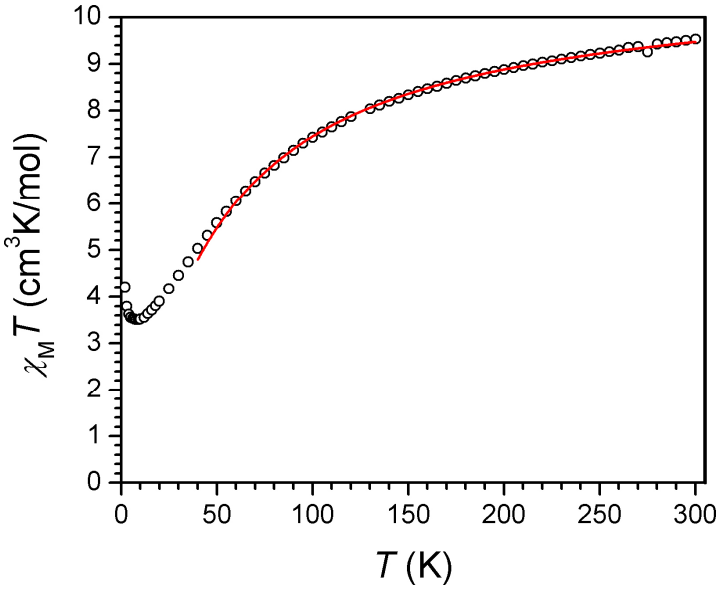


Figure 7.2. Variable-temperature dc magnetic susceptibility data for **1**, collected in an applied field of 1000 Oe. The solid red line corresponds to a fit to the data, as described in the text.

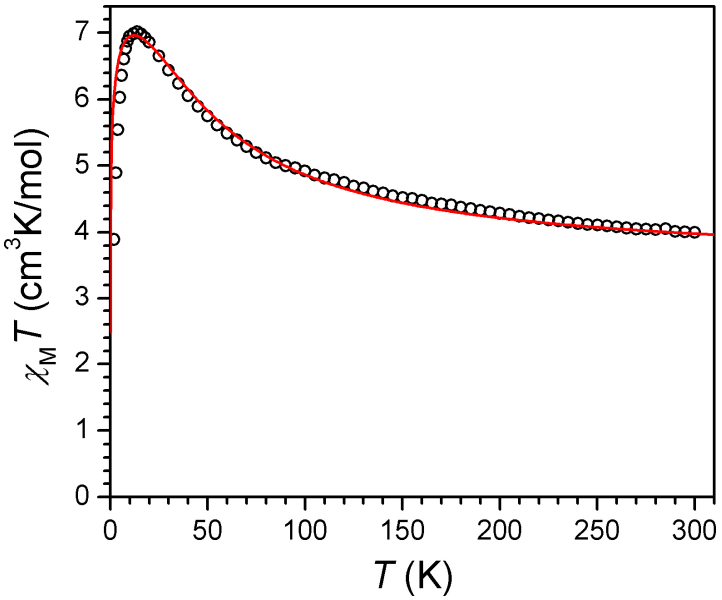


Figure 7.3. Variable-temperature dc magnetic susceptibility data for **2**, collected in an applied field of 1000 Oe. The solid red line corresponds to a fit to the data, as described in the text.

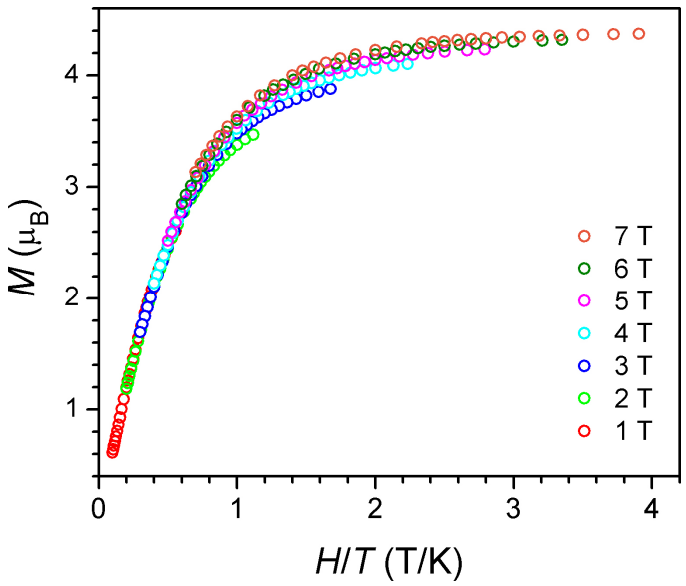


Figure 7.4. Low-temperature magnetization data for **1** collected under various applied dc fields.

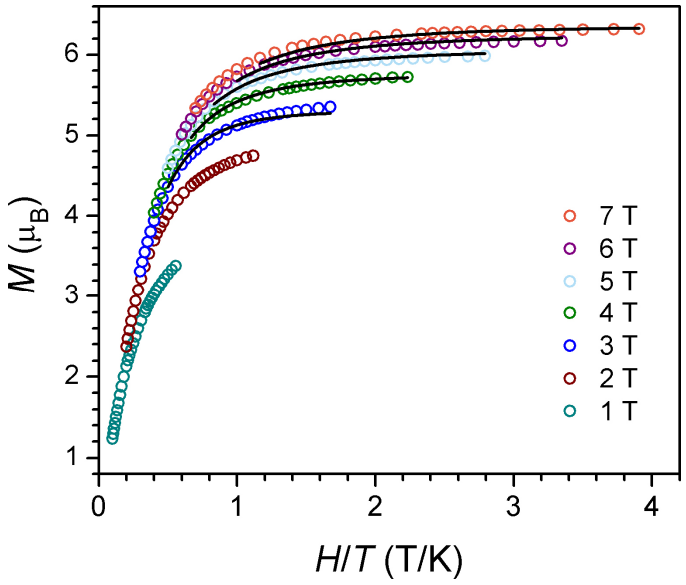


Figure 7.5. Low-temperature magnetization data for **2** collected under various applied dc fields. The black lines represent fits to the data, as described in the text.

To further probe the strength of magnetic anisotropy in **1** and **2**, variable-temperature magnetization data were collected under a range of applied dc fields. The resulting plots of reduced magnetization for the compounds reveal the presence of non-superimposable isofield curves (see Figures 7.4 and 7.5) as expected for molecules exhibiting significant zero-field splitting of the spin ground state. In the case of **1**, the data fall drastically short of the expected magnetization saturation of 7.00 μ_B expected for a molecule possessing an $S = {}^7/_2$ ground state and $g = 2.00$ (see Figure 7.4). This marked discrepancy results from a poorly isolated ground state spin, such that population of excited states corresponding to $S < {}^7/_2$ leads to a low value of magnetization. As a result, the isofield curves cannot be reliably fit and thus zero-field splitting parameters cannot be obtained. The observation of low-lying spin excited states is not surprising, given the weak exchange constant of $J = -2.7$ cm^{-1} obtained from susceptibility fits.

The plot of reduced magnetization data constructed for complex **2** also shows a set of non-superimposable isofield lines (Figure 7.5). In contrast, however, these data can be fit successfully using ANISOFIT 2.0[14] to obtain axial and transverse zero-field splitting parameters of $D = -0.76$ cm^{-1} and $|E| = 0.00004$ cm^{-1}, respectively, with $g = 1.90$. The presence of a negative D value illustrates that the cluster possessing a uniaxial, or "easy axis" anisotropy, and thus can give rise to single-molecule magnet behavior. Indeed, based on this value and an $S = {}^7/_2$ ground state, this molecule should possess a magnetic relaxation barrier of up to $U = S^2|D| = 9.1$ cm^{-1}. We note, however, that observation of such of small relaxation barrier requires access to temperatures lower and frequencies higher than those attainable by our ac susceptometer.

7.4 Conclusions and Outlook

The foregoing results demonstrate the utility of the complex $[ReCl_4(CN)_2]^{2-}$ in directing the formation of the magnetically anisotropic clusters, as evidenced in assembly of new linear trinuclear clusters of formulae $[(PY5Me_2)_2M_2ReCl_4(CN)_2]^{2+}$ (M = Mn, Ni). Dc magnetic susceptibility measurements reveal the presence of intracluster antiferromagnetic and ferromagnetic coupling in **1** and **2**, respectively, each giving rise to an $S = {}^7/_2$ ground state. In addition, magnetization measurements demonstrate the presence of considerable magnetic anisotropy, with fits to the data giving an axial zero-field splitting parameter of $D = -0.76$ cm^{-1} for **2**. Future work will focus on incorporating high-spin iron(II)-containing units as the pendant units of similar trinuclear clusters. In addition, substitution of second- and third-row metals into the pendant fragments will be investigated, as such species may lend stronger anisotropy and exchange coupling to the overall cluster.

7.5 Acknowledgements

This work was supported by NSF Grant No. CHE-0617063. We thank Tyco Electronics for providing T.D.H. with a predoctoral fellowship.

7.6 References

(1) (a) Sessoli, R.; Tsai, H. L.; Schake, A. R.; Wang, S.; Vincent, J. B.; Folting, K.; Gatteschi, D.; Christou, G.; Hendrickson, D. N. *J. Am. Chem. Soc.* **1993**, *115*,

1804. (b) Sessoli, R.; Gatteschi, D.; Caneschi, A.; Novak, M. A. *Nature* **1993**, *365*, 141. (c) Gatteschi D.; Sessoli R.; Villain J. *Molecular Nanomagnets*, Oxford University Press: New York, 2006 and references therein. (d) Milios, C. J.; Vinslava, A.; Wernsdorfer, W.; Moggach, S.; Parsons, S.; Perlepes, S. P.; Christou, G.; Brechin, E. K. *J. Am. Chem. Soc.* **2007**, *129*, 2754. (e) Freedman, D. E.; Jenkins, D. M.; Iavarone, A. T.; Long, J. R. *J. Am. Chem. Soc.* **2008**, *130*, 2884. (f) Yoshihara, D.; Karasawa, S.; Koga, N. *J. Am. Chem. Soc.* **2008**, *130*, 10460.

(2) (a) Caneschi, A.; Gatteschi, D.; Lalioti, N.; Sangregorio, C.; Sessoli, R.; Venturi, G.; Vindigni, A.; Rettori, A.; Pini, M. G.; Novak, M. A. *Angew. Chem., Int. Ed.* **2001**, *40*, 1760. (b) Clérac, R.; Miyasaka, H.; Yamashita, M.; Coulon, C. *J. Am. Chem. Soc.* **2002**, *124*, 12837. (c) Lescouëzec, R.; Vaissermann, J.; Ruiz-Pérez, C.; Lloret, F.; Carrasco, R.; Julve, M.; Verdaguer, M.; Dromzée, Y.; Gatteschi, D.; Wernsdorfer, W. *Angew. Chem., Int. Ed.* **2003**, *42*, 1483. (d) Wang, S.; Zuo, J.-L.; Gao, S.; Song, Y.; Zhou, H.-C.; Zhang, Y.-Z.; You, X.-Z. *J. Am. Chem. Soc.* **2004**, *126*, 8900. (f) Ferbinteanu, M.; Miyasaka, H.; Wernsdorfer, W.; Nakata, K.; Sugiura, K.; Yamashita, M.; Coulon, C.; Clérac, R. *J. Am. Chem. Soc.* **2005**, *127*, 3090. (p) Miyasaka, H.; Julve, M.; Yamashita, M.; Clérac, R. *Inorg. Chem.* **2009**, *48*, 3420 and references therein.

(3) (a) Garanin, D. A.; Chudnovsky, E. M. *Phys. Rev. B* **1997**, *56*, 11102. (b) Leuenberger, M. N.; Loss, D. *Nature* **2001**, *410*, 789. (c) Heersche, H. B.; de Groot, Z.; Folk, J. A.; van der Zant, H. S. J.; Romeike, C.; Wegewijs, M. R.; Zobbi, L.; Barreca, D.; Tondello, E.; Cornia, A. *Phys. Rev. Lett.* **2006**, *96*, 206801. (d) Jo, M.-H.; Grose, J. E.; Liang, W.; Baheti, K.; Deshmukh, M. M.; Sokol, J. J.; Rumberger, E. M.; Hendrickson, D. N.; Long, J. R.; Park, H.; Ralph, D. C. *Nano Lett.* **2006**, *6*, 2014.

(4) (a) Entley, W. R.; Trentway, C. R.; Girolami, G. S. *Mol. Cryst. Liq. Cryst.* **1995**, *273*, 153. (b) Weihe, H.; Güdel, H. U. *Comments Inorg. Chem.* **2000**, *22*, 75.

(5) Harris, T. D.; Bennett, M. V.; Clérac, R.; Long, J. R. *J. Am. Chem. Soc*. **2010**, *132*, 3980.

(6) Bechlars, B.; D'Alessandro, D. M.; Jenkins, D. M.; Iavarone, A. T.; Glover, S. D.; Kubiak, C. P.; Long, J. R. *Nat. Chem.,* **2010**, *Advance Online Publication*.

(7) Zadrozny, J. M.; Freedman, D. E.; Jenkins, D. M.; Harris, T. D.; Iavarone, A. T.; Harte, E.; Mathonière, C.; Clérac, R.; Long, J. R., *submitted*.

(8) *APEX2 v.2009*; Bruker Analytical X–Ray Systems, Inc: Madison, WI, 2009.

(9) Sheldrick, G. M. *SADABS, Version 2.03*; Bruker Analytical X–Ray Systems, Inc: Madison, WI, 2000.

(10) Sheldrick, G. M. *SHELXTL, Version 6.12*; Bruker Analytical X–Ray Systems, Inc: Madison, WI, 2000.

(11) (a) Naumov, N. G.; Artemkina, S. B.; Virovets, A. V.; Fedorov, V. E. *J. Solid State Chem.* **2000**, *153*, 195. (b) Mironov, Y. V.; Fedorov, V. E.; Ijjaali, I.; Ibers, J. A. *Inorg. Chem.* **2001**, *40*, 6320. (c) Brylev, K. A.; Mironov, Y. V.; Naumov, N. G.; Fedorov, V. E.; Ibers, J. A. *Inorg. Chem.* **2004**, *43*, 4833.

(12) Schmitt, E. A. Ph.D. Thesis. University of Illinois at Urbana-Champaign, 1995.

(13) Borrás-Almenar, J. J.; Clemente-Juan, J. M.; Coronado, E.; Tsukerblat, B. S. *J.*

Comput. Chem. **2001**, *22*, 985.
(14) Shores, M. P.; Sokol, J. J.; Long, J. R. *J. Am. Chem. Soc.* **2002**, *124*, 2279.